CLEAN SKY 2
JTI-CS2-2020-CFP11-THT-13: Sustainability of Hybrid-Electric Aircraft System Architectures

GAUGING THE ENVIRONMENTAL SUSTAINABILITY OF ELECTRIC AIRCRAFT SYSTEMS

D2.2

Deliverable No.	GENESIS D2.2
Deliverable Title	Medium-term technology analysis covering all main technologies in T2.1 - T2.6
Deliverable Date	31/05/2021
Version	1
Deliverable Type	Report
Dissemination level	Public
Link to scientific publication and/or repository	NA

Written By	Markus Meindl (FAU-LEE), Bruno Lemoine (BFH), Dr. Priscilla Caliandro (BFH), Dr. Erdem Akay (TUD), Sergio Turteltaub (TUD), Thomas Wannemacher (PMFC), Dr. Nils Baumann (PMFC), Alexe Guiguemdé (MHT), Mario Di Stasio (UNINA), Manuela Ruocco (SMARTUP), Fabrizio Nicolosi (UNINA), Agostino De Marco (UNINA), Pierluigi Della Vecchia (UNINA)
Checked by	Alexis Laurent (DTU), Karen Saavedra Rubio (DTU), Nils Thonemann (DTU); Mario Distasio (UNINA), Valerio Marciello (UNINA), Fabrizio Nicolosi (UNINA)
Contact person	M.M (markus.meindl@fau.de)
Status	Submitted

About project GENESIS

In a global context, where modern societies need to move towards more environmental sustainability, the aviation sector has an important role to play. Transition to reduce its environmental footprint (i.e., impacts on ecosystems, human health, and natural resources) stemming from activities in the entire value chain of aircraft has become high on political and industrial agenda. This transition must go hand in hand with the technological transformation of aircraft systems, moving away from the use of fossil-based fuels to alternative energy sources, like biofuels, hydrogen, or electricity via batteries.

Project GENESIS, funded by the EU Commission under the Clean Sky 2 Programme, aims to tackle some of these challenges. GENESIS stands for "Gauging the environmental sustainability of electric and hybrid aircraft". Its main purpose is to develop a technology and sustainability roadmap to support the ambitions of the European aviation industry for transitioning towards environmentally sustainable and competitive electric and hybrid aircraft systems. Several powertrain technology alternatives are explored, including conventional, batteries, fuel cells and hybrid combinations of them, all with three time perspectives over the period 2025-2055.

Organized around a multidisciplinary and complementary expertise of its consortium members, GENESIS has the following key objectives (each reflecting the WP1-3 structure of GENESIS):

1. Develop a conceptual design, associated with top level aircraft requirements and scenarios, for all-electric and hybrid 50 PAX regional class aircraft.
2. Perform technology foresight analyses on key elements of the aircraft system, focusing on the powertrain architecture and energy storage alternatives.
3. Build life cycle inventories for each relevant technology process within the aircraft life cycle (from resource extraction, through manufacturing and use, up to end-of-life), and use them to perform prospective life cycle assessments of future aircraft system configurations and scenarios.

Overview and role of this deliverable within the GENESIS project

This document describes the medium-term technology analysis for all main technologies in T2.1 - T2.6. GENESIS is an ambitious and innovative project that aims to gauge electric aircraft's environmental sustainability in a foresight perspective and provide a technology roadmap for a sustainable transition toward electric aircraft systems. The main task of WP2 is to perform technology foresight analyses on key elements of the powertrain structure and support systems in three time perspectives (short-term 2025-2035; medium-term 2035-2045, and long-term 2045-2055). This document focuses on the medium-term (2035-2045) technology foresight evaluations for the powertrain components and the energy storage, including ground-based energy supply. The technology foresight analysis highlights knowledge gaps, technological challenges, and potential solutions to meet 50 passenger regional aircraft requirements. The analyses will feed back into the aircraft conceptual design for potential refinements. They will also serve as inputs for the generation of LCI data and economic evaluation.

Table of contents

List of figures and tables

List of abbreviations

Abbreviation	Meaning
AC	Alternating Current
ACC	Accurec Recycling GmbH
AIB	Aluminum-ion Battery
APU	Auxiliary Power Unit
ARMS	Ampere Root Mean Square
BEV	Battery Electric Vehicle
BFH	Bern University of Applied Science / Berner Fachhochschule
BMS	Battery Management System
BOL	Beginning of Life
BOP	Beginning of Plant
BPP	Bipolar Plate
BV	Breakdown Voltage
CAPEX	Capital Expenditures
CCM	Catalyst-Coated Membrane
CCS	Combined Charging System
CID	Current interrupt devices
CTC	Cell-to-Chassis
CTP	Cell-to-Pack
CO	Carbon Monoxide
DAB	Dual Active Bridge
DC	Direct Current
DEP	Distributed Electric Propulsion
DoD	Depth-of-Discharge
EI	Emission Index
EIS	Entry Into Service
EM	Electric Motor
EMC	Electromagnetic Compatibility
EMI	Electromagnetic Interference
EoL	End of Life
ESL	Equivalent Series Inductance
ESR	Equivalent Series Resistance
EU	European Union
EV	Electric Vehicle
FAT	Factory Acceptance Test
FAU-LEE	Friedrich Alexander University - Lehrstuhl für Leistungslektronik
FB	Full-Bridge
FC	Fuel Cell
FCEV	Fuel Cell Electric Vehicle
FT	Fischer-Tropsch
GaN	Gallium nitride
GDL	Gas diffusion layers

GENESIS	Gauging the ENvironmental sustainability of electrIc aircraft Systems
GT	Gas Turbine
HMI	Human Machine Interface
HP	High Pressure
HV	High Voltage
HV DC	High Voltage Direct Current
ICE	Internal Combustion Engine
I.D	Inner diameter
IEC	International Electrotechnical Commission
IGBT	Insulated-Gate Bipolar Transistor
IM	Induction Motor
IoT	Internet of Things
ISA	International Standard Atmosphere
ISO	International Organization for Standardization
JFET	Junction-fet
LCA	Life Cycle Assessments
LCI	Life Cycle Inventories
LCO	Lithium cobalt oxide
LFP	Lithium iron phosphate
LIB	Lithium-ion batteries
Li_2S	Lithium sulfide
Li-S	Lithium-sulfur
LMO	Lithium manganese oxide
LMNO	Lithium manganese-nickel oxides
LP	Low Pressure
LT	Lithium titanate
LT-PEM	Low temperature Polymer Electrolyte Membrane Fuel Cells
LTO	Lithium titanate oxide
LV	Low Voltage
MCS	Megawatt Charging System
MEA	Membrane Electrode Assembly
MHT	MAHYTEC
MIE	Minimum Ignition Energy
MJ	Megajoule
MOSFET	Metal Oxide Semiconductor Field-Effect Transistors
MPL	Microporous Layer
MW	Megawatt
NASA	National Aeronautics and Space Administration
NCA	Nickel cobalt aluminium
NCR	Nickel cobalt echargeable
Ni	Nickel
NMC	Nickel manganese cobalt
NOx	Nitrogen Oxides
O.D.	Outer diameter

OPEX	Operating Expenses
OPR	Overall Pressure Ratio
PAX	Passenger
PEMFC	Polymer Electrolyte Membrane Fuel Cell
PLECS	Piecewise Linear Electrical Circuit Simulation
PMFC	Proton Motor Fuel Cell GmbH
PMSM	Permanent Magnet Synchronous Motor
PSFB	Phase-Shifted Full-Bridge
PT	Power Turbine
PTC	Positive temperature coefficient
PWM	Pulse-Width Modulation
RHIA	Rotterdam The Hague Airport
RM	Reluctance Motor
RMS	Root Mean Square
SBB	Solid-state batteries
SFC	Specific Fuel Consumption
SiB	Sodium-ion Battery
SiC	Silicon carbide
SiC MOSFET	Silicon carbide power semiconductor
SL	Sea Level
SMARTUP	Smartup Engineering S.r.l
SoC	State-of-charge
SoH	State-of-Health
SoR	State-of-Resistance
SOFC	Solid Oxide Fuel Cell
SPD	Shaft Power Delivered
SSE	Solid-State Electrolytes
T	Task
TCO	Total cost of ownership
TLAR	Top-level Aircraft Requirements
TRL	Technology Readiness Level
UNINA	University of Naples Federico II
VDC	DC Voltage
VDS	Drain-Source Voltage
VRMS	Voltage Root Mean Square
WBG	Wide-Band gap
WP	Work Package
YSZ	Yttria stabilized zirconia
ZCS	Zero Current Switching
ZVS	Zero Voltage Switching

Executive Summary

The deliverable D2.2 "Medium-term technology analysis covering all main technologies in task 2.1-2.6 (T2.1- T2.6)" is a public document of the GENESIS project, produced in the context of work package 2 (WP2). GENESIS is an ambitious and innovative project that aims to gauge electric aircraft's environmental sustainability in a foresight perspective and provide a technology roadmap for a sustainable transition towards electric aircraft systems. The main task of WP2 is to perform technology foresight analyses on key elements of the powertrain structure and support systems in three time perspectives (short-term 2025-2035, medium-term 2035-2045, and long-term 2045-2055). This document focuses on the medium-term (2035-2045, reference year 2040) technology foresight evaluations for the powertrain components and the energy storage, including ground-based energy supply. The technology foresight analysis highlights knowledge gaps, technological challenges, and potential solutions to meet the requirements for a 50 passenger regional aircraft. The analyses will feed back into the aircraft conceptual design for potential refinements. They will also serve as inputs for the generation of LCI data and economic evaluation.

The electric architecture of a hybrid electric aircraft powertrain with all key technology components mapped to their respective partner and the supportive infrastructure needed during its operation is shown in Figure 1. Here, the system boundaries and interconnections between the aircraft powertrain, energy storage, and the ground-based energy supply components are highlighted.
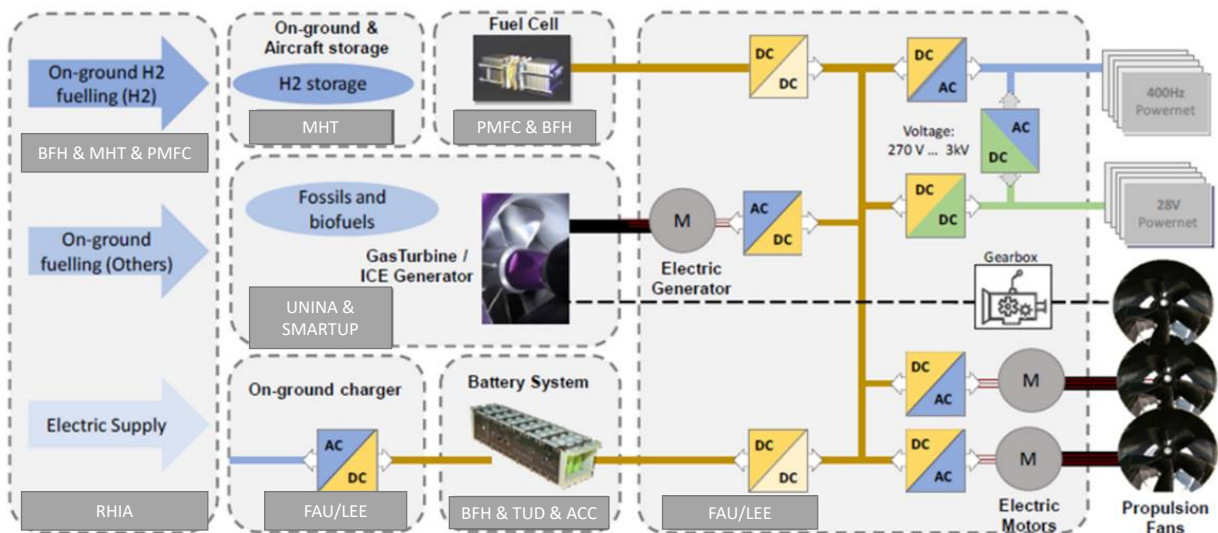
Figure 1. The electric architecture of a hybrid electric aircraft powertrain, mapping key technology components and supporting infrastructure to their respective partners in WP2.

Each chapter of the deliverable is dedicated to one key element in the aircraft powertrain. Chapter 2 presents the battery technology analysis investigating different chemistries, battery structures, and recycling possibilities. Li-S (lithium-sulfur) and SSBs (solid-state-batteries) batteries are possible options for the medium-term horizon. The specific energy density for solid-state batteries (SBB) is expected to rise from 572 Wh/kg in 2035, to 650 Wh/kg in 2045, allowing a significant weight reduction over the years. However, that is to low in the mid-term scenario for a fully electric aircraft in the regional class, which is demanded in the Top-level Aircraft Requirements (TLAR). Therefore, a hybrid electric solution with a gas turbine is needed for the medium-term perspective. Chapter 3 focuses on the fuel cell technology analysis (T2.2), and different options for technological development are mentioned. Solid oxide fuel cells (SOFCs) and polymer electrolyte membrane fuel cells (PEMFCs) are the two most promising candidates. However, with a power density of 1 kW/kg, they lay below the minimum value of 2 kW/kg at which fuel cells can be utilized for an aircraft

application. Opportunities for fuel cell technology development and hydrogen tanks are given in Chapter 3. Fuel cell technology is expected to be ready for the medium-term horizon (2035-2045). Chapter 4 is centered on gas turbine engines and provides a a surrogate model for a gas turbine engine for the medium-term scenario with performance, emissions, weight, main dimensions, and cost evaluation. Testing of the model is also provided. Chapter 5 includes technology analysis for all power electronics converters. First, the high-volage direct current (HV DC) bus voltage and power semiconductors are discussed. The voltage was also set in the medium-term to 800 V and it was illustrated that silicon carbide (SiC) wide-bandgap power semiconductors should be used for all power electronics converters. Then all converters, i.e., motor and generator traction drive inverter, bidirectional battery DC/DC converter, fuel cell DC/DC converter, DC/AC grid converter, and isolated DC/DC converter for low voltage supply are investigated in detail. For each converter type, the efficiency and power density values were determined. Chapter 6 explores the topic of electric drives. First, two different optimization possibilities for the Permanent Magnet Synchronous Motor (PMSM) of the medium-term scenario are mentioned with the result that a Halbach magnet arrangement and direct cooled stator windings are the best options for the medium-term horizon. Furthermore, a possible design of the primary and secondary electric machines is presented. Finally, Chapter 7 describes the possibilities of the on-ground energy supply focusing on the electric supply at Rotterdam The Hague Airport (RTHA), battery storage possibilities, ultra-fast DC charging stations, and system simulations. The DC ultra-fast chargers need to provide a maximum output power of 820 kW, and they will be built with silicon carbide-based building blocks of 100 kW power. If possible, it is recommended to use a DC-based distribution network in a (zonally structured) ring topology to save converters and thus losses. Two scenarios were considered in the medium-term, and data was collected for each scenario. The first scenario deals with the gas turbine and battery as a hybrid propulsion system. In the second scenario, the gas turbine is replaced by the fuel cell and forms the hybrid propulsion system for the aircraft together with the battery. Table 1 summarizes the recommended main technologies for all key technology components for the medium-term perspective.

Key technology components	Recommended technologies for the medium-term perspective	Main technical parameters and values	Technology readiness level (TRL)
Batteries (Task 2.1)	Li-S, SSBs and Semi-integrated structural Batteries are possible opinions	Li-S: Expected specific energy densitiy: 750 Wh/kg SBB Expected specific energy densitiy: 650 Wh/kg $LiFePO_4$ based chemistry with carbon fiber electrode and glass fiber seperator. Expected specific energy densitiy: 106 Wh/kg	Li-S: Current TRL: 5; Expected TRL: 8 – 9; SSBs: Current: TRL: 4; Expected TRL: 8 – 9; Structual batteries: Current TRL: 1 – 2; Expected TRL: 3 – 4;
Fuel cells (Task 2.2)	Low temperature Polymer Electrolyte Membrane (LT-PEM) Fuel Cell	Actual power density: 1 kW/kg Needed power density: > 2 kW/kg	SOFC: Current TRL: 5 - 6; Expected TRL: 8 – 9; SO-Electrolyzer: Current TRL: 4 - 6; Expected TRL: 8 – 9; PEMFC: Current TRL: 7 – 8; Expected TRL: 8 – 9;
Gas turbines (Task 2.3)	Conventional gas turbine (shaft power of 1800 kW) sized according to the application with the usage of up to 100 % biofuel	Fuel consumption: 0.223 kg/(kWh)-max. take-off-rating Dry mass: 260 kg Maximum diameter: 530 mm	Current TRL: 7 - 8; Expected TRL: 8 – 9;
Power electronics converters (Task 2.4)	Silicon carbide (SiC) power semiconductors, multi-phase/interleaved topologies, estimation of Gallium nitride (GaN)-MOSFETs	HV DC bus voltage: 800 V Inverter efficiency: ≈ 99 % SiC: Inverter power density: 63 kW/kg GaN: Inverter power density: 94.2 kW/kg	SiC: Current TRL: 7 - 8; Expected TRL: 8 – 9; GaN: Current TRL: 6 - 7; Expected TRL: 8 – 9;
Electric drives (Task 2.5)	Multiphase permanent magnet synchronous machine (PMSM) with Halbach array and direct cooled stator windings	Efficiency: ≈ 92 % Total power density: 13.5-15.2 kW/kg Mass for 600 kW motor: 40 - 45 kg	Current TRL: 6 - 7; Expected TRL: 9;
On-ground infrastructure (Task 2.6)	AC-based distribution grid in a (zonal structured) ring topology, silicon carbide-based DC fast charges	DC charging power: 2x 820 kW Hydrogen infrastructure and tanks under discussion – no TRL could be provided in this deliverable.	Fast-charging-station: Current TRL: 9; Expected TRL: 9;

1. Introduction

1.1. Structure and objectives

GENESIS is an ambitious and innovative project that aims to gauge electric aircraft's environmental sustainability in a foresight perspective and provide a technology roadmap for a sustainable transition toward electric aircraft systems.

This deliverable D2.2, produced in the context of work package 2 (WP2), specifically focuses on the medium-term (2035-2045) technology foresight evaluations for the powertrain components, energy storage, and on-ground energy supply. WP2 consists of six specific tasks (T2.1 to T2.6), each dealing with a technological key component of the electric aircraft system (batteries, fuel cells, gas turbines, power electronics, electric drives, and on-ground infrastructures).
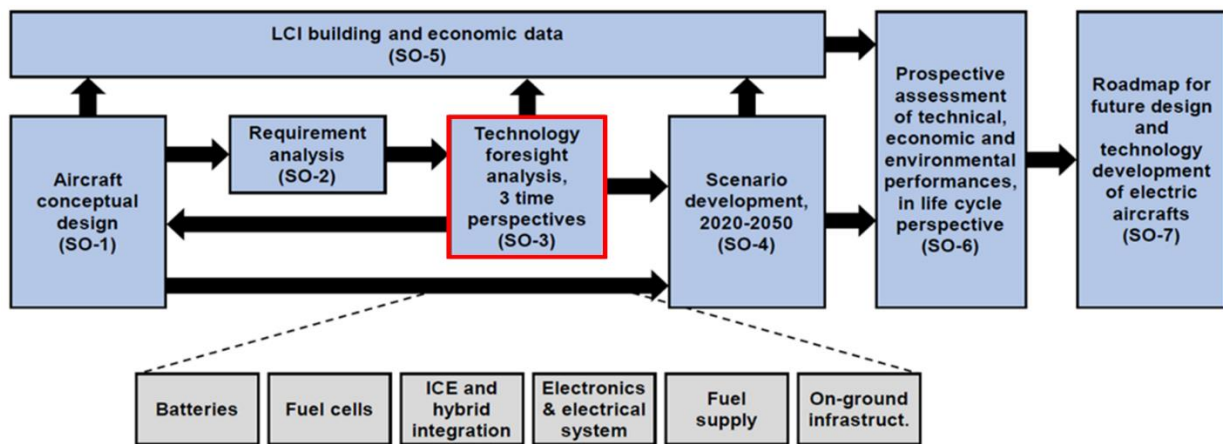
Figure 2. Conceptual framework of GENESIS, with interconnections between specific objectives (SO)

The electric architecture of a hybrid electric aircraft powertrain with all key technology components mapped to their respective partner and the supportive infrastructure needed during its operation.

Each chapter of the deliverable is dedicated to one specific task and key element in the aircraft powertrain. Chapter 2 presents the battery technology analysis (T2.1), investigating different chemistries and battery structures. Chapter 3 focuses on the fuel cell technology analysis (T2.2), and different options for a technological development are mentioned. Chapter 4 is centered on gas turbine engines (T2.3) and describes an approach to model a gas turbine engine for the medium-term scenario regarding performance emissions, weight, main dimensions, and costs. Validation of the model is also provided. Chapter 5 includes technology analysis for all power electronics converters (T2.4). First, the choice of the HV DC bus voltage and power semiconductors is discussed. Then all converters, i.e., motor and generator traction drive inverter, bidirectional battery DC/DC converter, fuel cell DC/DC converter, DC/AC grid converter, and isolated DC/DC converter for low voltage supply are investigated in detail. Chapter 6 explores the electric drives (T2.5) and provides a design of the primary and secondary electric machines. Finally, Chapter 7 describes the possibilities of the on-ground energy supply (T2.6), focusing on the electric on-ground energy supply and ultra-fast DC charging stations. Chapter 8 provides a conclusion and gives an outlook.

Table 2 shows the contributions of all partners with the corresponding authors.

Table 2. Partner contributions

Chapter	Topic	Author (Partner)
1	Introduction	Markus Meindl (FAU-LEE)
2.1 – 2.7	Battery technology analysis	Bruno Lemoine (BFH) Dr. Priscilla Caliandro (BFH)
2.8	Structual Battery Technologies	Dr. Erdem Akay (TUD) Sergio Turteltaub (TUD)
3.1 - 3.4	Fuel cell technologies	Bruno Lemonie (BFH)
3.6	PEM fuel cells	Thomas Wannemacher (PMFC), Dr. Nils Baumann (PMFC)
3.5	Hydrogen storage	Alexe Guiguemde (MHT)
4	Turbine / ICE generator set	Mario Di Stasio (UNINA), Manuela Ruocco (SMARTUP) Fabrizio Nicolosi (UNINA) Agostino De Marco (UNINA) Pierluigi Della Vecchia (UNINA)
5.	Power electronics converters	Markus Meindl (FAU-LEE)
6	Electric drives	Markus Meindl (FAU-LEE)
7.	On-ground energy supply	Markus Meindl (FAU-LEE) Cor de Ruiter (RHIA)
8	Conclusions and outlook	Markus Meindl (FAU-LEE)

1.2. Basic aircraft configuration and powertrain architecture

In the GENESIS deliverable D1.1, the basic top-level aircraft requirements (TLAR) for a hybrid electric 50 passenger regional class aircraft were defined. The requirements for the powertrain components are shown in Table 3. A safety margin was applied for unpredicted mass penalties and assumptions about technology level. For the short-term horizon (2025-2035), there will be two gas turbines and no fuel cell system. Two scenarios will be discussed for the medium-term horizon (2035-2045). One scenario is considering gas turbines (GT/Hybrid) for the primary propulsion system and a battery system for the secondary propulsion system. The second scenario is sonsidering a fuel cell system and a battery system (FC/Hybrid) with only one propulsion system. For the long-term horizon (2045-2055), should be the fuel cell system and a bigger battery pack sufficient [1].

Table 3. Power demand of powertrain components for different time frames [1]

Powertrain Component	Number of units	Reference Power in kW	
		Short-Term GT/Hybrid	Medium-Term GT/Hybrid
Gas turbine	2	1800	1400
Battery pack	2	550	950
Primary electric machine	2	1200	1500
Secondary electric machine	8	600	750
Powertrain Component	Number of units	Reference Power in kW	
		Medium-Term FC/Hybrid	Long-Term FC/Hybrid
Fuel cell system	2	1400	1400
Battery pack	2	1000	1000
E-drive-power machine	10	500	500

In deliverable D1.1, it was concluded that for the short-term horizon, an architecture with distributed electric propulsion (DEP) and tip-mounted propellers is the most promising solution for the aircraft design [1]. The same configuration is also used in the NASA X-57 Maxwell technology demonstrator (see Figure 3). For the GT/Hybrid scenario in the medium-term horizon, the regional aircraft in the GENESIS project will also four small high lift motors (secondary electric machines) under each wing like in the short-term horizon. These motors are only used during the take-off phase. There is a big cruise motor (primary electric machine) at each wing tip that is used in all flight situations. In the second scenario for the medium-term horizon, the aircraft will have five e-drive power motors with the same power levels, as depicted in Figure 4.

Figure 3. Concept of NASA's X-57 Maxwell aircraft with distributed electric propulsion [2]

Figure 4. Concept of a finite element model of electric hybrid aircraft designs [3]

For the electric powertrain, a serial/parallel partial hybrid configuration was chosen [1]. Figure 5 shows the GT/Hybrid scenario basic aircraft configuration with the powertrain and power electronics components derived from the top-level aircraft requirements (TLAR) for the medium-term horizon 2035-2045. It contains all existing power electronics systems and machines for one-half of the aircraft. The aircraft is symmetrically built, so the other half of the aircraft is identical. More details about the different power electronics converter and their function can be found in Chapter 5.

Figure 6 to Figure 8 show the power distribution and power flow during the take-off, the climbing, and the cruise phase. The power flow diagrams show that the electrical power from the battery system enters a bidirectional battery DC/DC converter, which transfers power from the battery with a maximum voltage of 681 V to the internal 800V DC bus. The DC/AC grid converter and the isolating DC/DC converter supply the 400 Hz and 28 V power nets, respectively. During take-off (see Figure 6), power is also transferred from the 800 V DC bus via the motor traction drive inverters to the electric motors, which will convert the electrical power into mechanical power to move the secondary propulsion fans. For the GT/hybrid scenario in the medium-term horizon, the latter is used during the take-off and climb phase. The mechanical power of the gas turbine is delivered to a gearbox, which drives the primary propulsion propeller. In the take-off phase (Figure 6), the gas turbine drives the electric generator via the gearbox. In this case, the generator traction drive inverter supplies the electric energy from the generator to the internal 800V DC bus by rectifying the AC voltages. In the climb and cruise phase, the generator is used as a motor and electric energy from the battery system is also used to drive the main propeller via the generator drive inverter and the battery DC/DC converter. It has not been deined whether or not a gear box will required during the climb and cruise phase, thus, the efficiency losses from the gearbox were not considered, or the efficiency of the gearbox was assumed to be 100% for this preliminary assessment. To complete the drivetrain, the gearbox has been included in the illustrations.
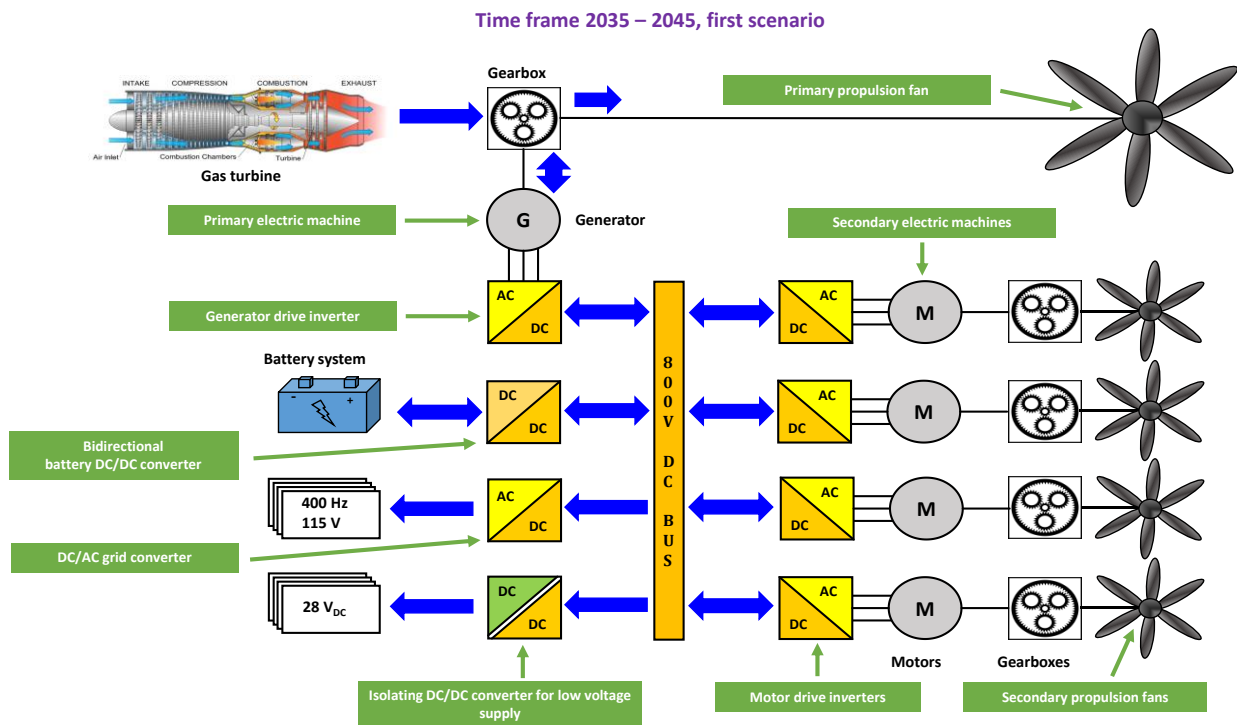
Figure 5. Powertrain and power electronics architecture for the GT/hybrid scenario in the medium-term horizon (2035-2045) [4]
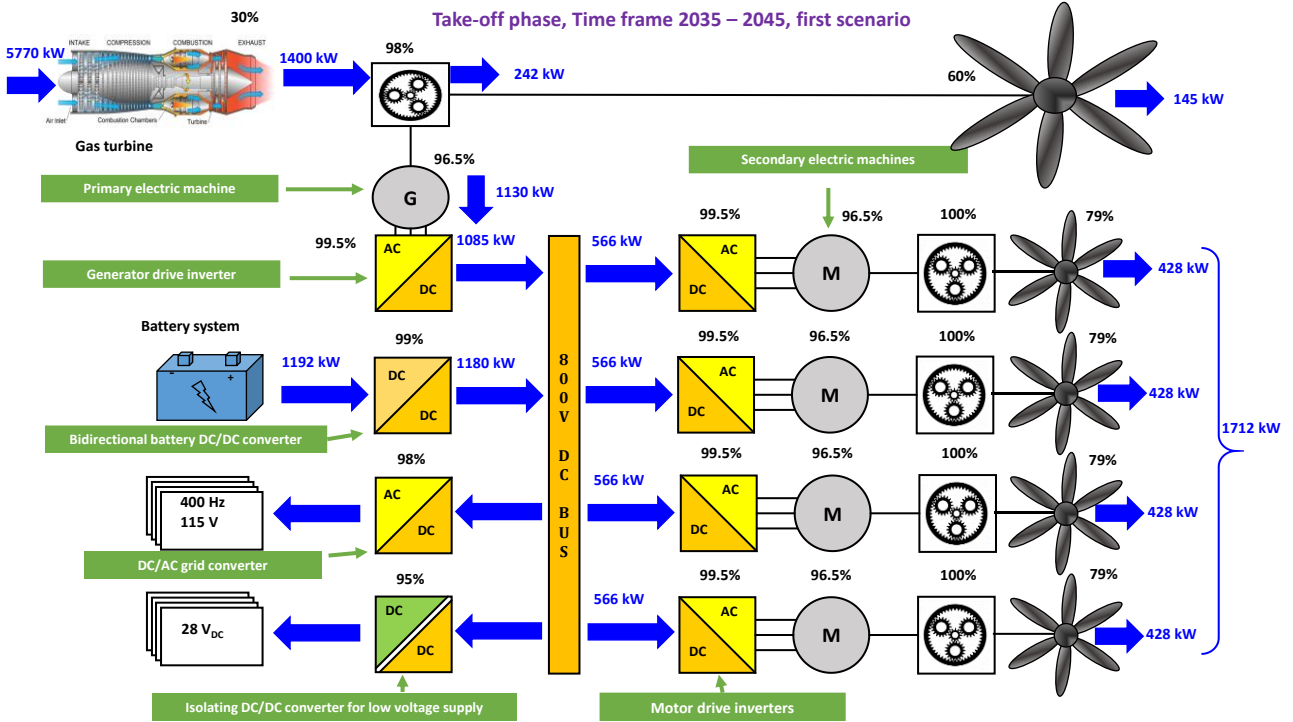
Figure 6. Power flow during the take-off phase, GT/hybrid scenario [4]
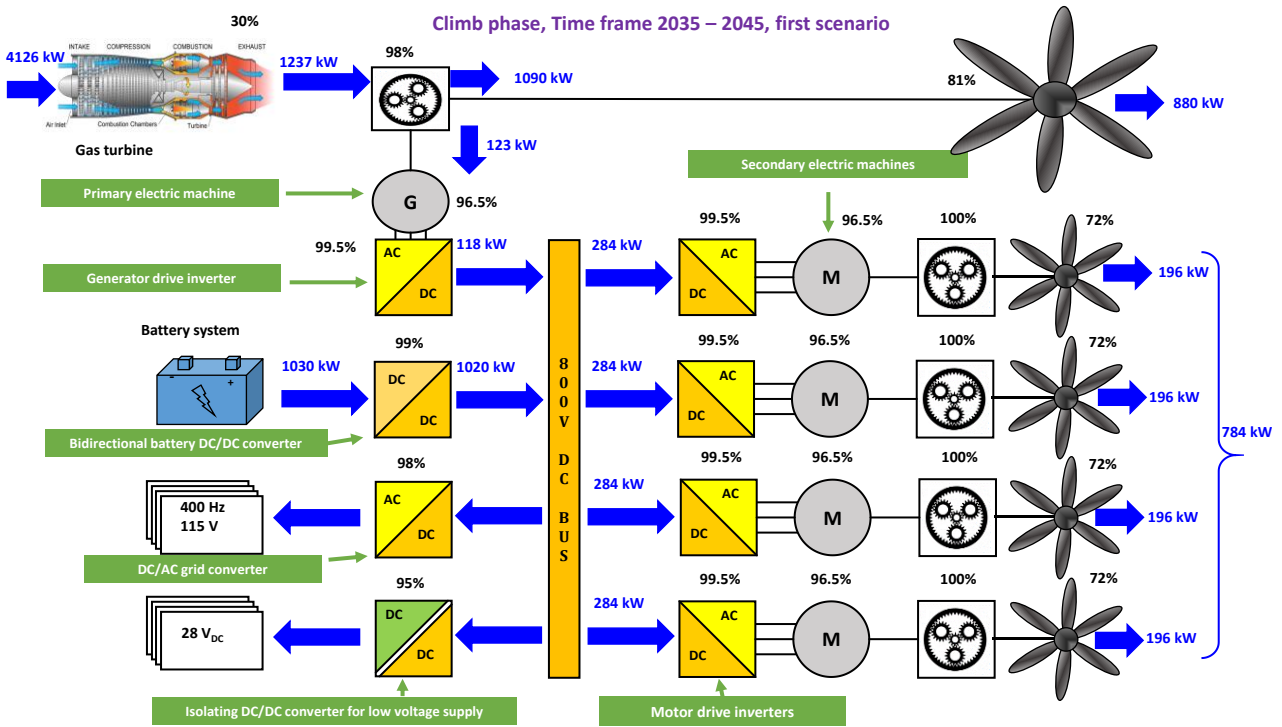
Figure 7. Power flow during the climb phase, GT/hybrid scenario [4]
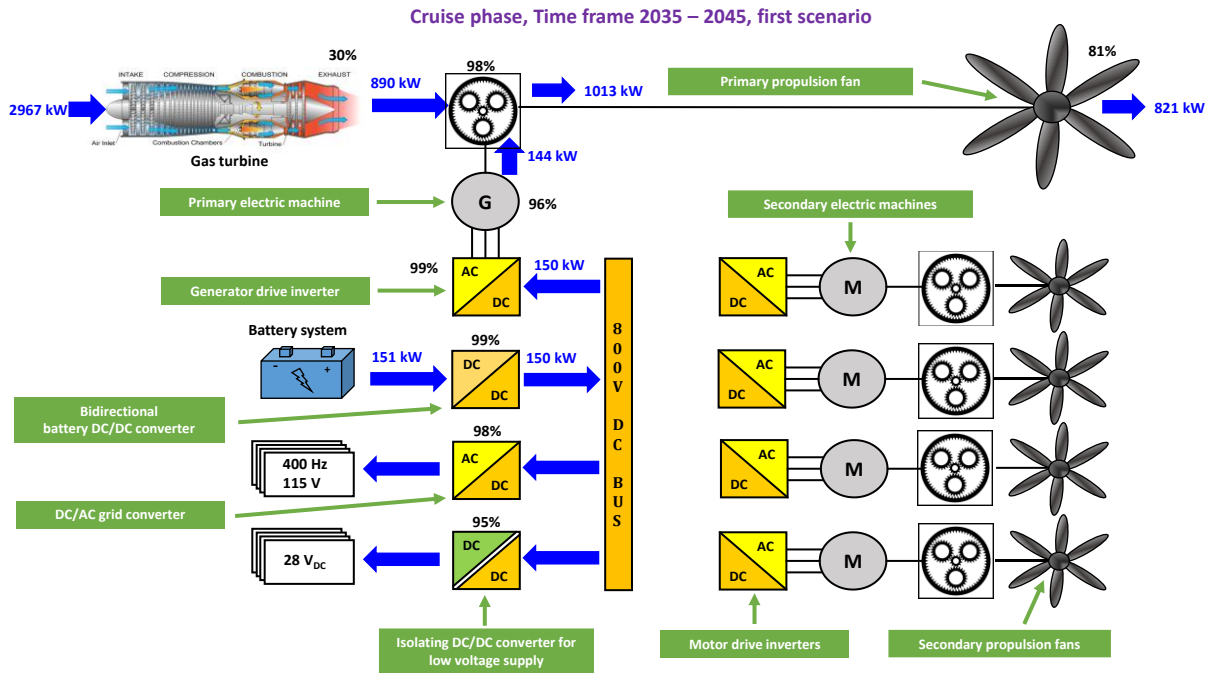
Figure 8. Power flow during the cruise phase, GT/hybrid scenario [4]

Figure 9 shows the configuration of the FC/hybrid scenario with the powertrain and power electronics components derived from the TLAR for the medium-term horizon 2035-2045. It depicts all existing power electronics systems and machines for one-half of the aircraft. More details about the different power electronics converter and their function can also be found in Chapter 5.

Figure 10 to Figure 12 show the power distribution and flow during the take-off, the climbing, and the cruise phase. The power flow diagrams show that the battery system provides the electrical power, like in the GT/hybrid scenario, and the FCsystem which replaces the GT power.

During all three phases, power is transferred from the 800 V DC bus via the motor traction drive inverters to the electric motors, which will convert the electrical power into mechanical power to move all five propellers with the same power. The power is distributed equally to all propellers used during the take-off, climb, and cruise phases. The chemical power of the FC is delivered to an FC-DC/DC converter, which supplies the DC bus.

In the take-off phase (Figure 10) and climb phase (Figure 11), the FC provides most of the power demand to the internal 800V DC bus. The battery supports the internal 800V DC bus with the remaining power needed. In the take-off phase, the battery must support 909 kW while in the climb phase, 667 kW is enough. During the cruise phase, the power demand is lower, thus, the power needed by the FC and battery system drops to 1293 kW and 399 kW, respectively. One thing to point out is that the efficiency of the propellers increases from the take-off phase to the climb phase (Figures 11-13). It has not been deined whether or not a gear box will required during the climb and cruise phase, thus, the efficiency losses from the gearbox were not considered, or the efficiency of the gearbox was assumed to be 100% for this preliminary assessment. To complete the drivetrain, the gearbox has been included in the illustrations.
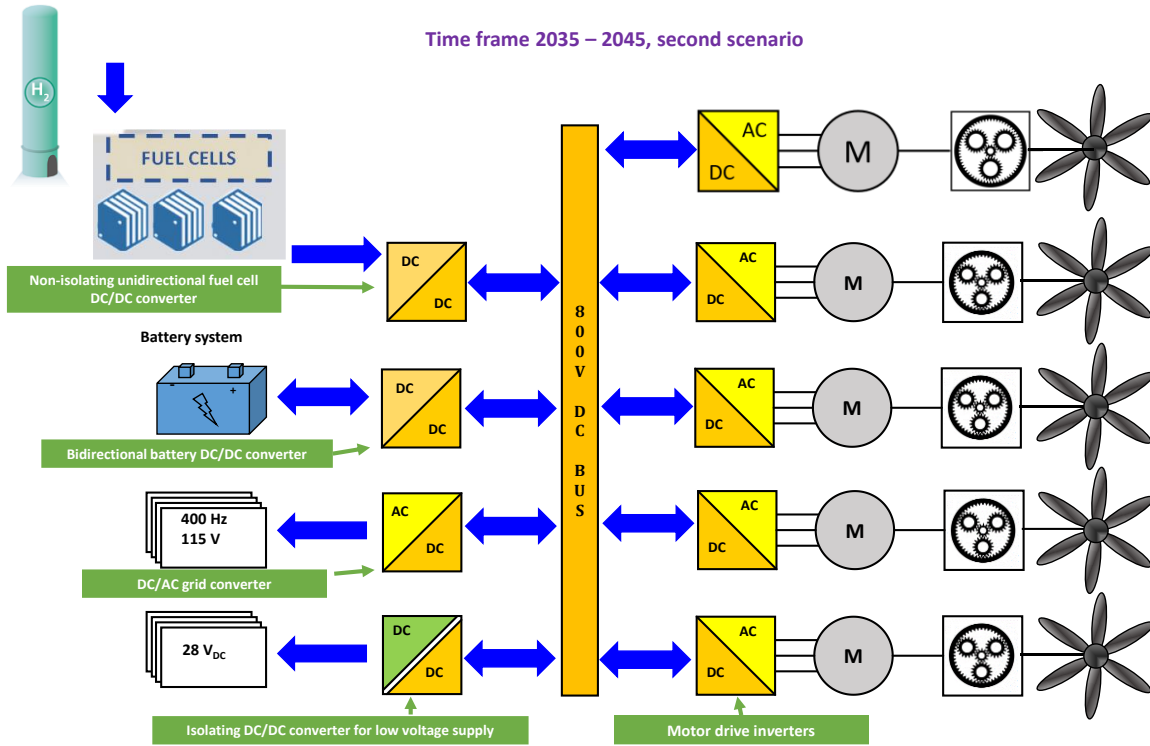
Figure 9. Powertrain and power electronics architecture for the FC/hybrid scenario in the medium-term horizon (2035-2045) [4]
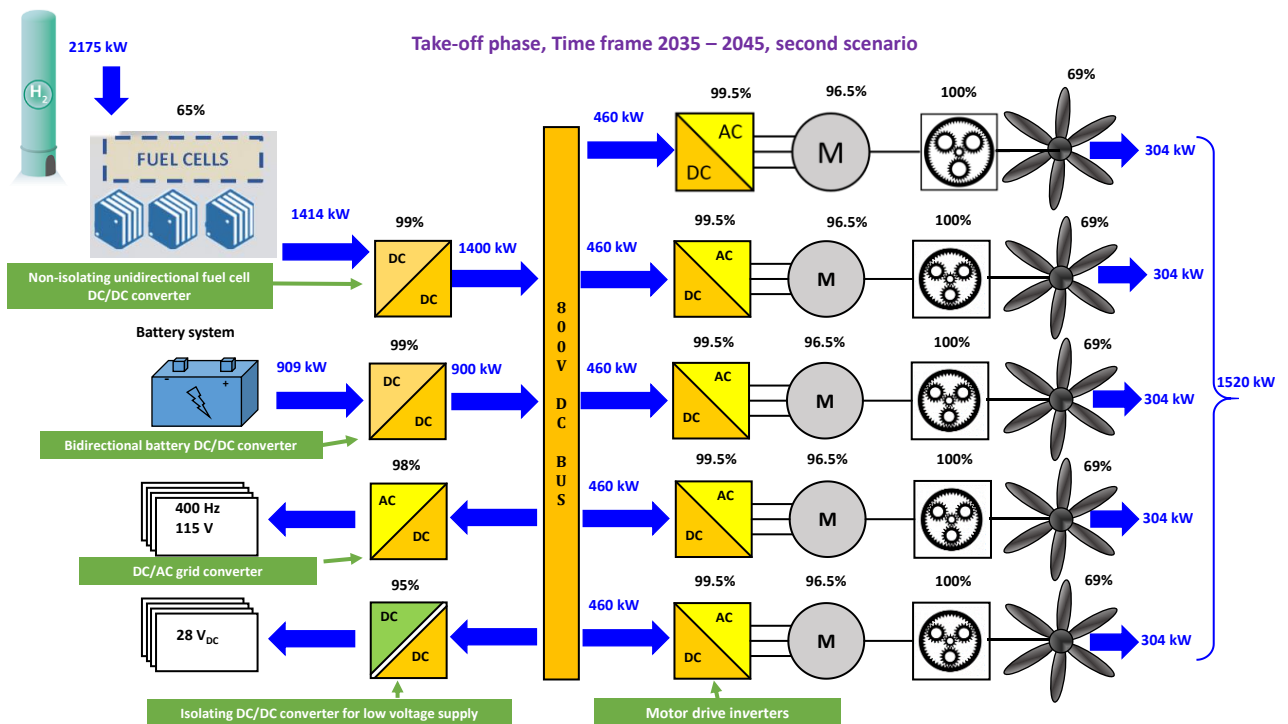
Figure 10. Power flow during the take-off phase, FC/hybrid scenario [4]
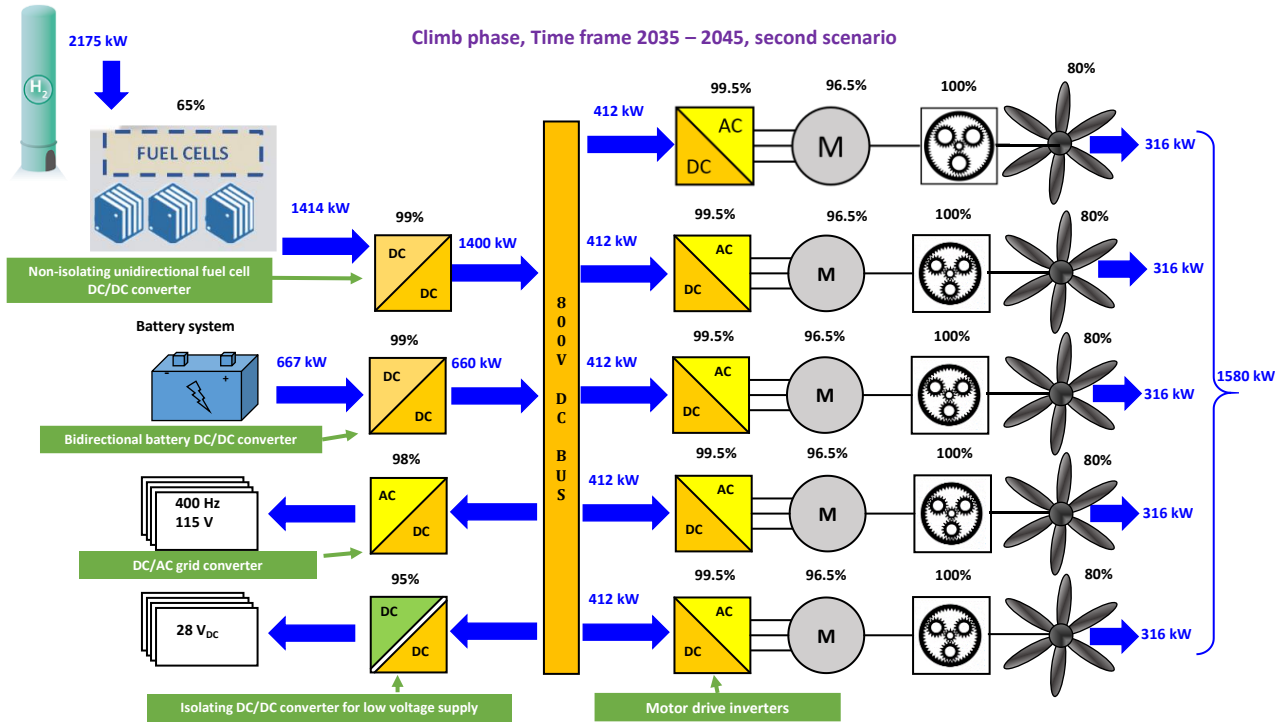
Figure 11. Power flow during the climb phase, FC/hybrid scenario [4]
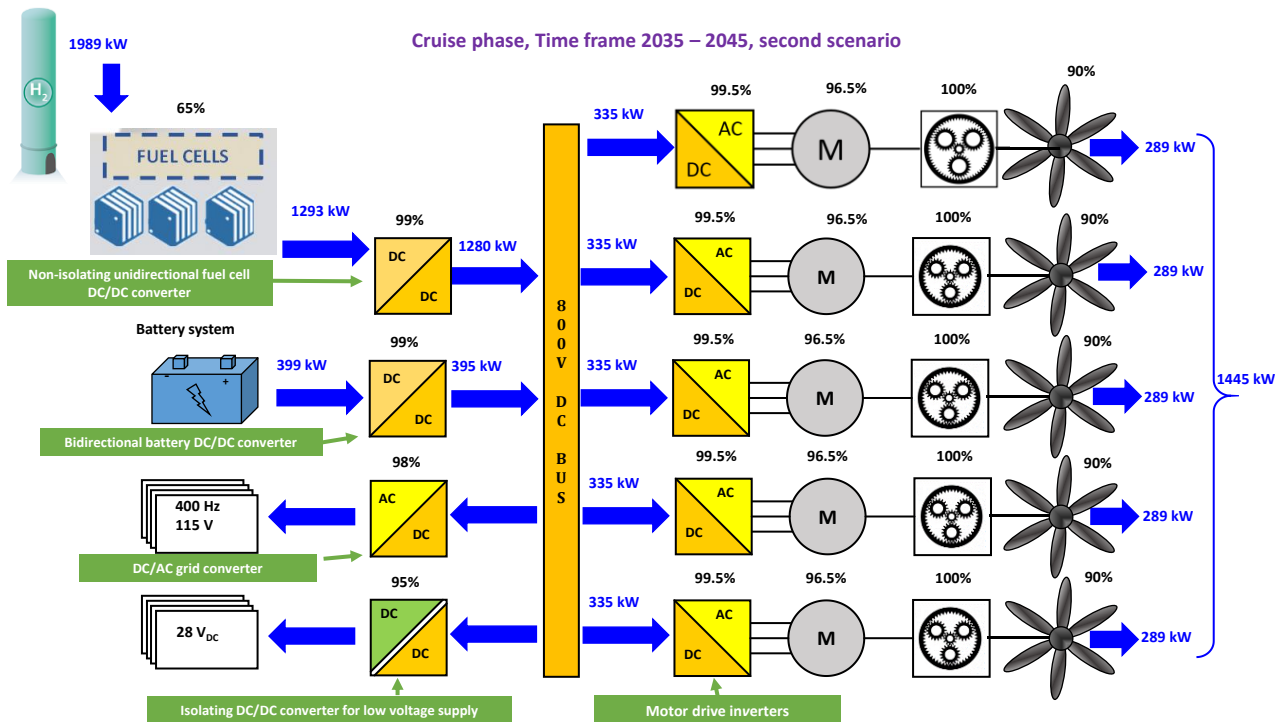
Figure 12. Power flow during the cruise phase, FC/hybrid scenario [4]

2. Battery technology analysis

2.1. Lithium metal anodes

Today's electric systems are almost exclusively powered by lithium-ion batteries (LIBs) but the path to surpass conventional systems requires batteries to reach higher performances. Indeed, electric vehicles (EVs) still show limitations compared to gasoline cars to become dominant in the global automotive market [5]. The importance of energy storage technologies is increasing rapidly as it is a major topic to face the issues of climate change in our society. Technological improvements must happen to allow the decarbonization of many applications such as the mobility sector.

Many promising technologies are investigated in detail to fulfill the extreme requirements of hybrid and electric aircraft. With LIBs approaching their intrinsic specific energy limit with graphite-based anodes, lithium metal anodes have been attracting renewed interest thanks to their high-capacity anode [6] [7]. Furthermore, increased safety, higher cell voltages or lower costs will be major keys to enable the widespread usage of batteries in aircraft.

Metallic lithium anodes have been extremely attractive thanks to the high theoretical energy density ($3861 \ mAh * g^{-1}$) and the most negative standard reduction potential [8]. However, lithium anodes have major limitations that need to be addressed before further commercialization. The first one is related to the volumetric changes while performing a charge and discharge cycle. These changes induce stresses at the interfaces which lead to a low cycle life [7]. This effect is usually mitigated by tuning the morphology or structure of the anode . This solution is already being used to incorporate a small percentage of silicon (5-10%) into a porous graphite structure to maximize both the performances along with the lifetime of li-ion cell. However, due to the weight of the host graphite structure, the maximum theoretical energy density cannot be reached.

Another significant issue with lithium metal anodes relies on the high chemical reactivity of the anode which takes root from the low standard reduction potential of lithium [7]. This phenomenon can lead to dendrites which causes internal short circuits during operation. The chemical reactivity is also a major topic related to mass production of lithium metal anodes as the lithium anode reacts with residual traces of chemicals and forms a passivation layer even under inert conditions.

Lithium metal anodes can be used in all of the three next generation of batteries: solid-state batteries (SSBs), lithium-sulfur (Li-S) and lithium-oxygen (Li-O$_2$ or Li-Air) batteries [7] [9] [10]. Currently, each of them is at a different technology readiness level (TRL). Li-S have been developed at laboratory scale and projects of developing first applications are happening [11]). SSBs instead have been studied under plenty of research projects and are a focal point of the research of batteries, however, pilot manufacturing lines have not been started yet. On the other hand, Li-O$_2$ batteries show great theoretical performances but are currently at the very early stages of research [12]. Therefore, only SSBs and Li-S are considered for GENESIS medium-term horizon (2035-2045). Li-O$_2$ batteries are expected to be the chosen technology for the long-term horizon but will not be covered in this report.

2.2. Introduction and limitations of solid state batteries

The recent developments in EVs have established a massive interest in developing safer batteries while maintaining high energy density. The risk of fires and explosions is a major topic of discussion and can often be linked to the use of liquid electrolytes. Indeed, they are flammable, volatile and lack the mechanical strength to suppress the growth of dendrites. Therefore, numerous researchers are devoted to investigate the replacement of liquid electrolytes with solid-state lithium-ions conductors. Solid electrolyte which features higher thermal and mechanical stability could suppress the growth of dendrites and improve the safety and cycle life of a battery cell. In addition,

solid state electrolyte would enable the incorporation of lithium metal anodes (~3.850 Ah*kg^{-1}) replacing current carbon anodes (~370 Ah*kg^{-1}). This feature alone would increase drastically the theoretical performances that lithium batteries could reach [9], [13]. For all these reasons, SSBs are expected to be one of the most promising pathways to decarbonize and electrify many applications. However, the current performances of SSBs are preventing its usage in commercial applications as they have a low areal capacity (<1 mAh*kg^{-1} , which is lower than LIBs) and extremely low cycle life (<100s cycles).

2.2.1. Performances

Solid state battery represents a new technology; however, it is interesting to note that its working principle is very similar to LIBs. Indeed, the on-going developments on cathode active materials from LIBs are expected to be completely transferrable to solid state batteries. Therefore, similarly, High-nickel (Ni) content and Li-rich oxides cathodes should become the mainstream solutions in the future. The final choice of the specific cathode chemistry would depend on the applications requirements. However, an aircraft requires high specific power and high specific energy. These demands could be fulfilled by cathode materials such as lithium-manganese-nickel oxides (LMNO) and nickel-manganese-cobalt (NMC).

Current Solid-State Electrolytes (SSEs) are classified in three main categories: inorganic oxides, inorganic sulfides, and organic polymers. Organic polymers electrolytes have been proven difficult to use because of their low ionic conductivity and poor mechanical properties which often require high ambient operating temperatures (around 60-80°C).

Inorganic solid electrolytes, and particularly sulfide based crystalline materials, are considered the most attractive solution due to their high thermal stability, ionic conductivity, and cyclability. They can achieve high ionic conductivity at room temperature and high Li-ion transference number. However, they also present some limitations such as a high interfacial impedance (caused by a poor contact at the electrode/electrolyte interface) and electrochemical instability towards lithium metal. Inorganic oxides electrolytes show similar characteristics and performances, but usually require more expensive materials and exhibit higher interfacial resistance [14].

The interface between solid electrolytes and electrodes is being greatly investigated and, particularly the wettability between Li-metal and the SSEs. In addition, lithium surface morphology and volumetric expansion during cycles lead to the formation of gaps in the interface and further increase the interfacial resistance. Finally, the manufacturing cost of the electrolytes is a major issue to overcome.

Thus, solving those aspects it is expected to lead to a rapid adoption of the SSBs in the industry as manufacturing process should remain similar and the implementation of this new technology will require similar components and systems than for LIBs. Plenty of future goals and targets have been set for SSBs for 2030 and, they are specifically expected to combine high energy density (>500 Wh/kg) with high safety [7]. Developments of new materials to produce the perfect solid electrolyte are needed to reach such values but, recent improvements [12], [15], lead to believe that this threshold of 500 Wh/kg would be soon within reach which would drastically accelerate the transition to a fossil energy free society.

In spite of great efforts from academia and industries for achieving commercially viable Lithium metal batteries, only few practical demonstrations have been reported. SolidPower, a spinoff of the university of Boulder reported to have made a laboratory scale cells to 400-500Wh/kg capable of withstanding 5000 charge cycles with inorganic solid separator [12], [15]. Four potential targets of the aircraft industry would be addressed with SSBs such as improved safety, longer lifetime as well as higher energy and power density.

The discharge curves for different C-rates of a LMNO-graphite solid state battery can be seen in Figure 13. It can be seen that it is not affected too significantly by the increase of C-rates. This cell has been developed with graphite anode, but it is expected to see similar discharge curves for lithium metal anodes. The main difference will come from the capacity retrieved in the case of a lithium metal anode.
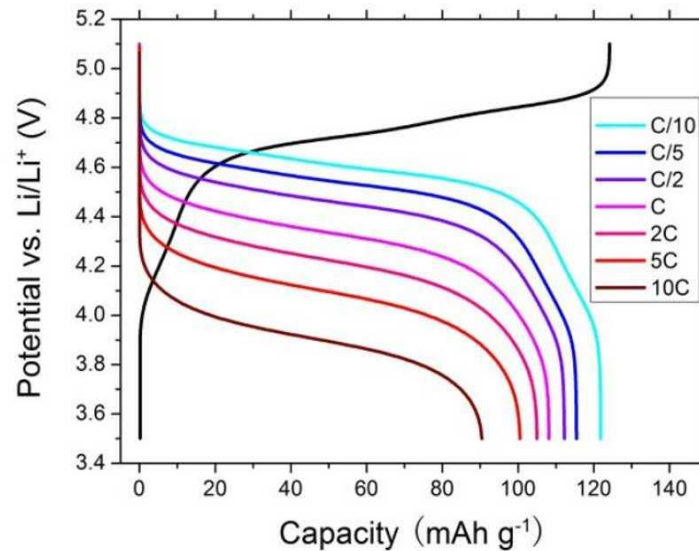
(a)

Figure 13. SSBs LMNO-graphite voltage curves [16]

2.3.   Lithium Sulfur

Li-S batteries have received increased attention thanks to the high theoretical energy density (~2700 Wh/kg) which is 5 times higher than lithium ion. While this value is greatly reduced in reality, the technology has already demonstrated great performances of 470 Wh/kg in a technologically relevant cell format [11]. These performances are extremely needed to enable new applications such as aviation and large EV.

Additionally, sulfur is abundant, cost effective and environmentally friendly which could have a great impact at reducing emissions of the aircraft industry [14]. The benefit of cost reduction will also greatly speed up the commercialization and widespread of such technology. Some forecasts suggest that with comparable performances, the cost of a Li-S cell would be just half the one of a Li-ion cell. Indeed, cathode materials are a major reason for the high cost of LIBs (Nickel, Cobalt, Aluminum…) [10].

2.3.1. Performances

Li-S cells use lithium metal anodes, liquid electrolytes and conversion cathodes based on elemental sulfur mixed with carbon. During a discharge, sulfur is converted to lithium sulfide (Li_2S) involving several electrochemical steps. During a charge, Li_2S in the cathode is converted back to elemental sulfur and lithium is plated on the anode [7] [10].

To make Li-S commercially available and improve the current performances, many challenges are to be faced. The practical gravimetric and volumetric energy densities are difficult to increase because of the high electrolyte to sulfur (E/S) ratio, the high anode to cathode capacity ratio (N/P – negative/positive electrode), the low areal loading of cathodes and the use of high-content porous carbon in the cathodes. The reduction of excessive carbon, electrolyte, and lithium without sacrificing

electrochemical performances is one of the key challenges. Production challenges also arise due to the high loading sulfur cathodes with low porosity and the need to scale up the technologies.

Nowadays, most research focus is on electrochemical problems and not on real applications conditions which makes the transition between academia to industry difficult. From the academic perspective, there is the need to guarantee the fast conversion between electric/ionic insulating sulfur and its discharge product (Li_2S) as well as to mitigate the volume expansion (~80%) during the conversion of S to Li_2S. This expansion leads to structural failure of the sulfur electrodes similarly as the lithium metal anode. Finally, ether-based electrolytes can promote the conversion between S and Li_2S, but the dissolution and diffusion of lithium polysulfide intermediate (LiPSs) leads to the presence of side chemicals instead of active species with lithium. This "Shuttle effect" results in irreversible consumption of both Li and S accompanied by the polarization increase and electrolyte decomposition.

Li-S cells offer significant safety benefits over the current Li-ion technology. The conversion reaction, which forms new materials during a cycle, eliminates the need for host Li-ions and reduces the risks of catastrophic failures. Additionally, during operation, the highly reactive lithium anode is passivated with sulfide materials which reduce the risk of dangerous failure. However, thermal runaway remains a possibility, but, at significantly lower magnitude than in Li-ion batteries. The conversion mechanism also enables Li-S to be stored in a fully discharged state which enables easy and safe transportation.

Li-S with high capacity and rather acceptable cycle life have been widely reported, but significant improvements are needed to realize the widespread possible applications of Li-S batteries. Concerning the aircraft industry, Li-S batteries could be a very interesting solution for specific high energy demanding phases such as cruise and descent. The high energy density will be extremely advantageous; however, the very low power density means that the system will likely need to be hybridized to fulfill the power demanding phases efficiently.

The early applications of Li-S batteries will likely be niche market such as satellites, drones or in the defense sector. The current cost of lithium sulfur cell is very high due to the electrolyte. However, the cost is expected to drop thanks to both technological and economic advancements. A more detailed analysis of the projected costs will be described in section 2.5.2.

The design of the anode of a Li-S cell has a crucial role to play on the performances of the cells defining the cycle life, power capability, and energy efficiency [7]. The main limiting factors are related to the presence of inactive materials due to the host structure that represents a high mass and volumetric fraction in a Li-S cell.

As battery technology is being widely adopted, the impact of the raw materials is becoming an increasing concern. Sulfur is considered a "limitless resource" and does not pose any major health risks which will likely make Li-S a significant technology of the future [12], [15].

The discharge behavior of a Li-S cell can be seen in Figure 14. Two different discharge regimes can be identified, and the impact of C-rates is much more pronounced than for SSBs. It is expected that Li-S cells will improve and be able to perform efficiently at 1.5C and used at maximum of 2C.
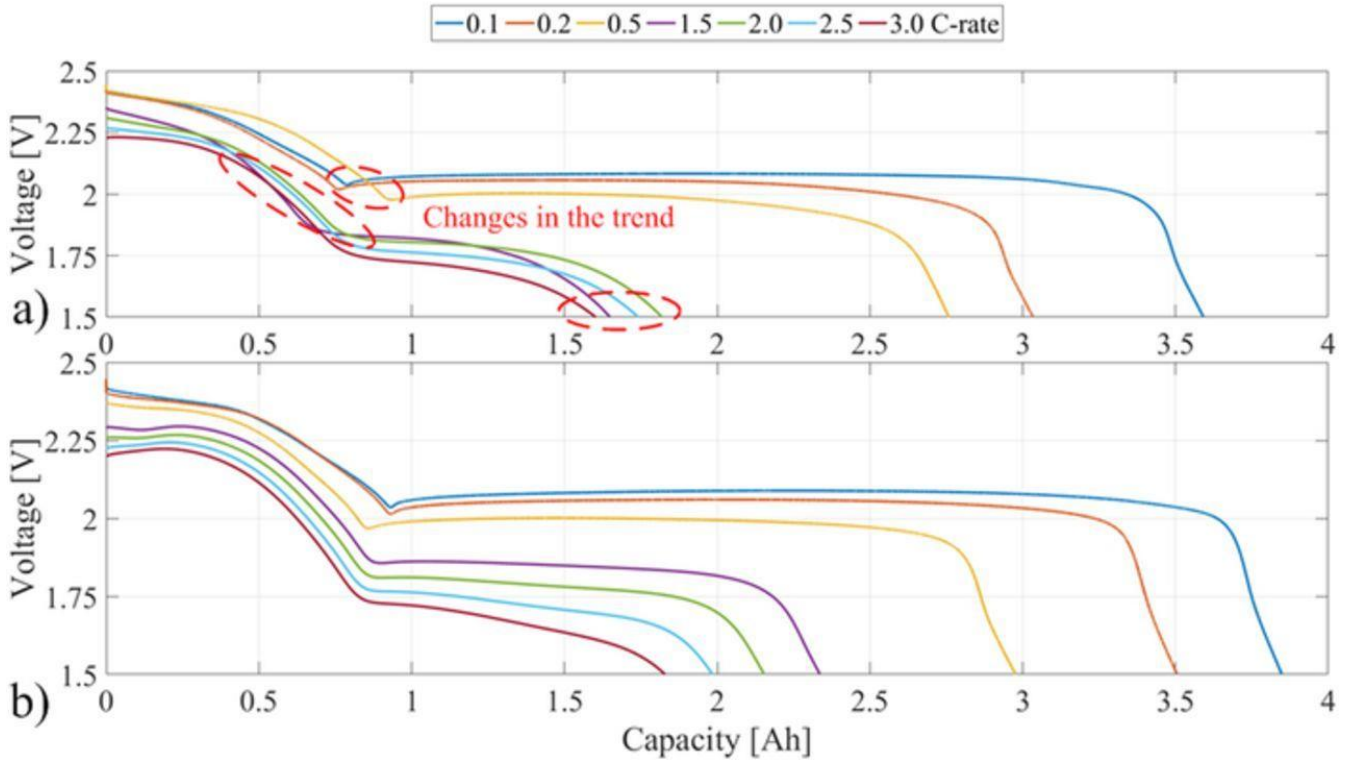
Figure 14. Voltage discharge curves for Li-S at different C-rates: (a) without the pre-conditioning cycle, (b) with the pre-conditioning cycle before every charge (0.1 C-rate) [17].

2.4. Battery management system

The battery management system (BMS) refers to the management scheme that monitors, controls and optimizes the performances of an energy storage system [18]. The aircraft industry is well known for the harsh safety requirements applied in order to prevent any probability of accidents. Therefore, the developments of hybrid or electric aircraft would need the improvements of BMS which can guarantee the safe usage of the batteries. The main objectives of the BMS are to improve the performances of the battery, optimizing the temperature of the battery pack, integrating safety features required, and assuring the right procedure is followed in case of abnormal behavior [19]. The BMS also needs to be a functional unit that interacts with outside systems such as the grid, the aircraft controller unit or the charging system. Finally, in case of a failure of a module, it should be responsible to disconnect the module from the rest of the battery to prevent thermal runaways and fires. All these functions are essential in the case of an aircraft.

Figure 15. BMS board [20].

2.4.1. Components and topology

A BMS is not a standalone product and in order to be active, it must be integrated within another system. Its objective is to manage and distribute in a safe method the power of the battery to the different interfaces such as the aircraft or the grid. Figure 16 shows the different BMS topologies. These different components can be integrated in different topology where each brings its own challenges [19].
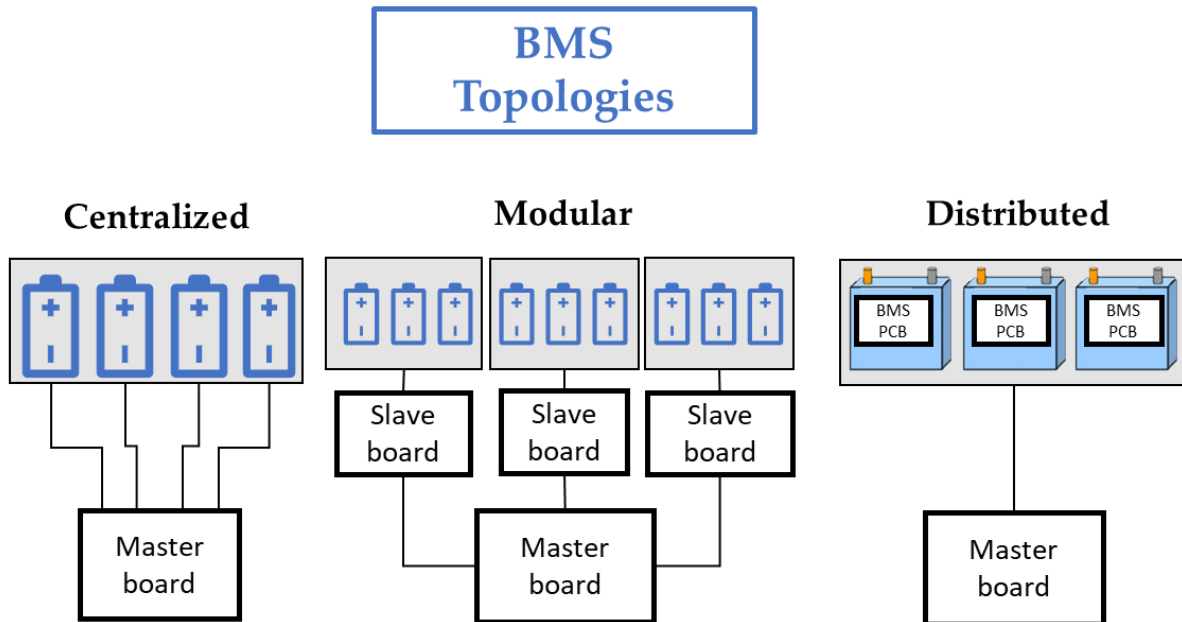
Figure 16. BMS topologies.

- Centralized BMSs are controlled by single unit assembled through numerous amounts of wires to reach every modules/cells. This is an economical approach, but not modular and the weight of the cables is significant which prevents the use of this configuration in aircraft.
- Distributed BMSs are composed of multiple control units, each dedicated to one battery cell and linked together by a single communication cable. This is the costliest approach but easier to install and a rather elegant set-up. However, the battery packs in aircrafts will feature thousands of cells which is going to be an issue to up-scale the set-up.
- Modular BMSs are composed of multiple control units where each deal with a module, they are interconnected and can interact together. They can all record some variables and transmit it to the master board which handles the communications with externals systems. These systems include more hardware and needs better software. However, it gains in flexibility as each module can be considered as a separated unit. It easily can integrate redundancy which is a major concern in the aircraft industry.

2.4.2. Functionalities

Figure 17. BMS main functionalities.

The BMS is responsible for the monitoring of many variables like the voltage, current or the temperature. The data is then used in complex software to calculate major battery quantities such as the State-of-Charge (SoC), State-of-Health (SoH), State-of-Resistance (SoR) and the Depth-of-Discharge (DoD). These quantities give valuable information on the current state of the battery and its degradation. An efficient and accurate BMS greatly impacts the lifetime of the battery, particularly with the cell balancing procedure which is a major factor of battery pack degradation. Indeed, the weakest cell (lowest SOH) in a set of series connected cells will dominate the behavior of the overall string. For this reason, two methods called passive and active balancing are usually performed by the BMS to equalize the SOC of each cell before or during operation [21].

The BMS should apply strict charging and discharging methods to preserve the battery and make the process as efficient as possible. It defines the limits to maintain proper SOC and avoid over-discharge or overcharge. A faulty battery charging system or voltage regulator can cause overvoltage and lead to venting and the release of flammable species. Safeguards includes detection operating modes, setting fault criteria in case of abnormal use of the battery, predicting overvoltage or overcurrent and determining isolation fault. Indeed, for high voltage systems like battery for aircrafts, it is very important to think about protecting workers as such battery could lead to fatal accidents.

The BMS should apply strict charging and discharging methods to preserve the battery and make the process as efficient as possible. It defines the limits to maintain proper SOC and avoid over-discharge or overcharge. A faulty battery charging system or voltage regulator can cause overvoltage and lead to venting and the release of flammable species. Safeguards include detection operating modes, setting fault criteria in case of abnormal use of the battery, predicting overvoltage or overcurrent, and determining isolation fault. Indeed, for high voltage systems like batteries for aircraft, it is very important to think about protecting workers as such batteries could lead to fatal accidents.

The BMS is also present to minimize the impact of a failure of the battery system which can consist of disconnecting or cooling down a cell. The BMS is deciding when venting is necessary in the case that a cell or a module is behaving abnormally. The venting will happen to release the pressure to avoid an explosion of the battery pack (BP). Finally, as described previously, it is also responsible for communicating and providing energy to the other systems.

However, current BMSs show rather significant limitations on important topics. BMSs have limited data logging and storing functions which are extremely noteworthy to improve fleet managements or to detect faulty systems. For these reasons, new BMSs will likely feature technologies such as Internet

of Things (IoTs) to perform cloud data analysis on large data volumes. Additionally, SOCs and SOH calculations in commercial applications are usually very basic and with large errors. New models are being developed to predict in real time more accurately such variables.

Batteries are also lacking standards to facilitate the wide usage in multiple fields. Currently, national standards and guidelines are missing in applications such as EVs, electric aircraft or even transport of batteries. BMS testing is often a topic which is not addressed. Reliability is the major concern in aircraft and there will be the need to develop simpler BMS that are able to interact with each other and be redundant in case of failures.

2.4.3. Possible improvements

Current BMSs are mostly described as "Black boxes", they are difficult to understand or simply to adapt. In the next 5 to 20 years, the mass commercialization of batteries in EVs and in home storages should lead to breakthroughs in terms of safety or functionalities. First of all, safety strategies will be implemented widely like nonflammable, solid barriers or the implementation of insulated materials between two electrodes to reduce the likelihood of external short circuits or to reduce their impact.

Components such as current interrupt devices (CID) will prevent current flow in abnormal conditions to prevent gas generation. Positive temperature coefficient (PTC) will be designed to protects the battery from external short circuits. During short circuits, a PTC will heat itself and increase its resistance drastically which will result in blocking the excess current. Safety vents and thermal fuses shutdown separator will also be incorporated to prevent thermal runaway or limit the impact.

New types of sensors are also going to appear widely in the next 20 years such as integrated internal temperature sensors or passive electrochemical impedance spectroscopy measurements made from the flight power profile. Gas sensors could also be interesting to track volatile compounds that may result from a cell venting. Specifically, for pouch cells, sensors might be able to monitor the venting of the cells through mechanical sensors.

Resiliency among the system is also crucial to respond to different failure scenarios. Specifically in the case of aircraft, redundancy is a major concern and the BMS will need to be designed to fulfill a "fail safe philosophy". Modular BMSs could be a rather simple approach to integrate redundancy where multiple control units can behave like the main control board and guarantee safe operation in case of failure.

2.5. System requirements to meet medium-term expected performances (2040)

The previous sections gave an introduction to the different energy storage technologies presenting their fundamentals, challenges, and advantages. Therefore, this section will focus on the conceptual design of the energy storage system of the aircraft according to the performances expected in 2040.

2.5.1. Upscaling technology performances

As discussed in sections 2.2 and 2.3, the two technologies that we expect to be widely used in 2040 are Li-S and SSBs. Before giving values of performances needed to size the system, it is extremely important to understand that predicting the performances is a very tricky task. Indeed, the forecasts are made on technologies not available yet or only at the laboratory scale. New practical limits could be discovered, and currently unknown technologies might be discovered and become the standard in the next 20 years. Additionally, the predictions on Li-ion batteries made in the past 10 years were massively out of scope, even outside possible uncertainty limits [22]. Therefore, the values given here are based on laboratory scale cells and on theoretical limits of the different technologies to limit errors due to upscaling the technology. These values should not be seen as "true values" but rather give a basis to design our systems.

Table 4 gives the forecasts performances for SSBs and Li-S in 2040 for three different scenarios (pessimistic, expected, optimistic).

Table 4. Performances of Li-S and SSBs for the medium term (2035-2045).

Technology	SSBs			Li-S		
Values	Pessimistic	Expected	Optimistic	Pessimistic	Expected	Optimistic
Energy density [Wh/kg]	550	650	750	650	750	900
Power density [W/kg]	2200	2600	3000	975	1125	1350
Volumetric Energy Density [Wh/l]		1430			1050	
Volumetric Energy Density [Wh/l]		1430			1050	

Power density in the case of batteries is a rather difficult quantity to determine. Indeed, depending on the manufacturing process and on the exact chemical composition, the usable C-rate can be widely different from cell to cell. Therefore, in this report, it is considered that the power density for Li-S is based on 1.5 C-rate and that the cell cannot be used safely above 2C. In the case of SSBs, two different chemistries are considered to be used in 2040. NMC cathode, if the energy density were to be the limiting factor, and LMNO (high voltage cells) otherwise. In both cases, SSBs are expected to be able to be used at higher C-rates with a significant lifetime in 2040. The power density was calculated with a 4C rate, and we consider that the operation range should not exceed 5C. Current Li-ion cells are used in some very specific applications at greater C-rates, but those values could not be expected in aircraft where safety and longevity are major concerns.

In Figure 18, the Ragone plot of the battery performances reported in Table 4 can be seen.
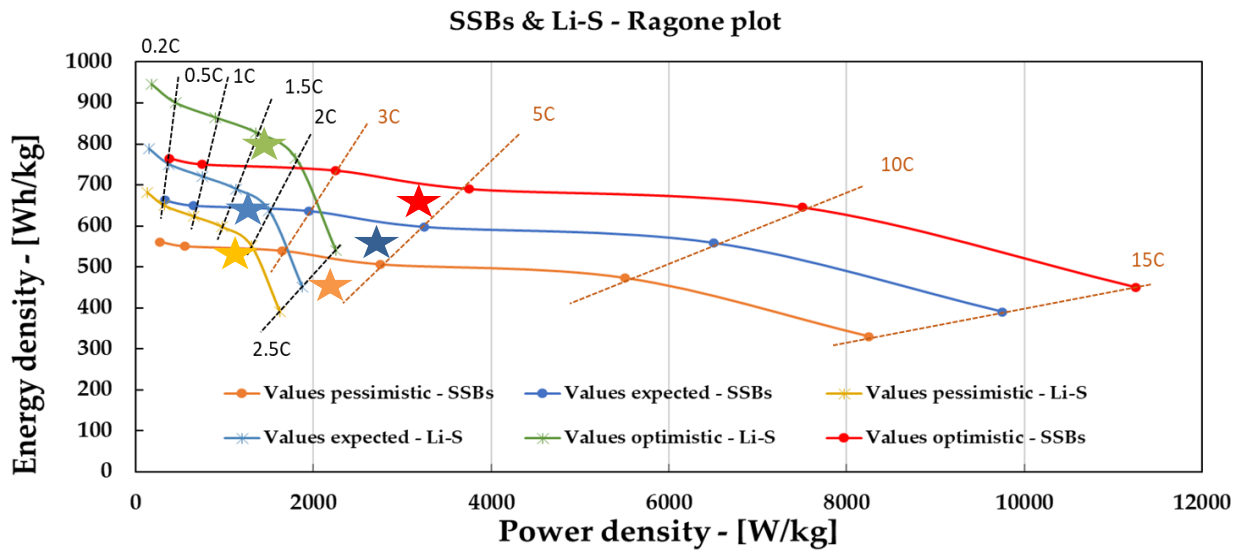
Figure 18. Ragone plot for battery energy and power densities.

The sizing values (corresponding to the nominal working point) for Li-S and SSB are represented for the 3 forecasts (pessimist-expected-optimistic) with a star marker. However, it has to be noted that during operation (and depending on the flight mission) the power and energy density of the proposed system size can be tuned. More specifically, for any storage system, there is a tradeoff between power and energy density.

While in operation, the capacity that a battery will depend on the power demand which will define a specific C-rate for the battery. In Figure 18 each point represents a specific C-rate (0.1C, 1C …) which is associated to a specific energy value that the battery can provide. The points located on the top left corner represent the maximum energy density retrievable by the energy system when used at low C-rate (<0.5C). By moving to the bottom right corner (high C-rates), the same system is used at higher powers and therefore, the energy retrievable decreases. Additionally, the stars represent the recommended operation C-rate for each technology: 1.5C and 4C for Li-S and SSBs respectively.

The plot has been shared with WP1 partners; they considered the characteristic curves of these two battery technologies in their design tool, allowing to search, thanks to an iterative process, the optimal size of the batteries for the propulsive system of the aircraft.

The values previously mentioned refer to the performances at the cell level for each technology. However, in operation, cells are assembled into a battery pack. The cell to pack transition will lead to lower final performances. An interesting analysis was performed in 2020 by Löbberding et al. and showed that the highest gravimetric cell to pack ratios for EVs were already reaching 74.2% and 52.8 % for pouch and prismatic cells [23]. Furthermore, only recently, the cell to pack ratio was considered a significant topic as it allows EVs to gain precious additional kilometres. Those advancements will definitely be applicable to aircraft where great considerations will be placed on minimizing the weight or volume of the system. Major innovations are expected to be developed such as the Cell-to-Pack (CTP) approach, where cells are assembled together without the need for a module structure, or Cell-to-Chassis (CTC), where cells are directly integrated to form the outside structure of the EV preventing the need for a chassis structure in these specific locations.

With these evolutions entering rapidly the market thanks to the fast development of new EVs, it can be expected that knowledge on BPs formation will expand rapidly. For these reasons, Table 5 shows the cell weight ratio compared to the overall weight of the BP. Knowledge on BP manufacturing is expected to improve in the next 10 years to reach a gravimetric and volumetric efficiency of 80% and 60% respectively in 2030, and then, 90% and 75%, in 2050.

Table 5. Cells weight and volume ratio.

Timeline	Cell weight ratio [%]	Cell volume ratio [%]
2025-2035	80%	60%
2035-2045	90%	70%
2050+	90%	75%

Finally, other discoveries are expected to happen such as structural batteries. However, these technologies are currently considered as an additional energy system and will not be consider in the design of the BP.

2.5.2. Costs evolution

Cost has a major role to play in the adoption of a new technology. The forecasts for multiple battery technologies have been assessed by Mauler et al. through 53 studies on either Li-ion, SSBs and Li-S batteries [24] Concerning SSBs and Li-S, the costs in 2030 are expected at 116 and 110 $/kWh respectively. Recent studies show confidence in a more stable battery market growth and across time regardless on raw material price developments. However, significant uncertainties remain on technological and chronological levels. Additionally, other parameters were not implemented which could have a major impact on cost reduction. Concepts such as CTP, CTC or tabless design should significantly decrease the overall cost of battery packs. Further research on anode free cell which should reduce the cost-intensive lithium foil processing and the necessity of lithium excess are not implemented as well. However, they found that significant risks were associated with the lithium metal anode where the price vary significantly depending on the study. Figure 19 shows the expected costs evolution for the 4 technologies of batteries from 2030 to 2050.
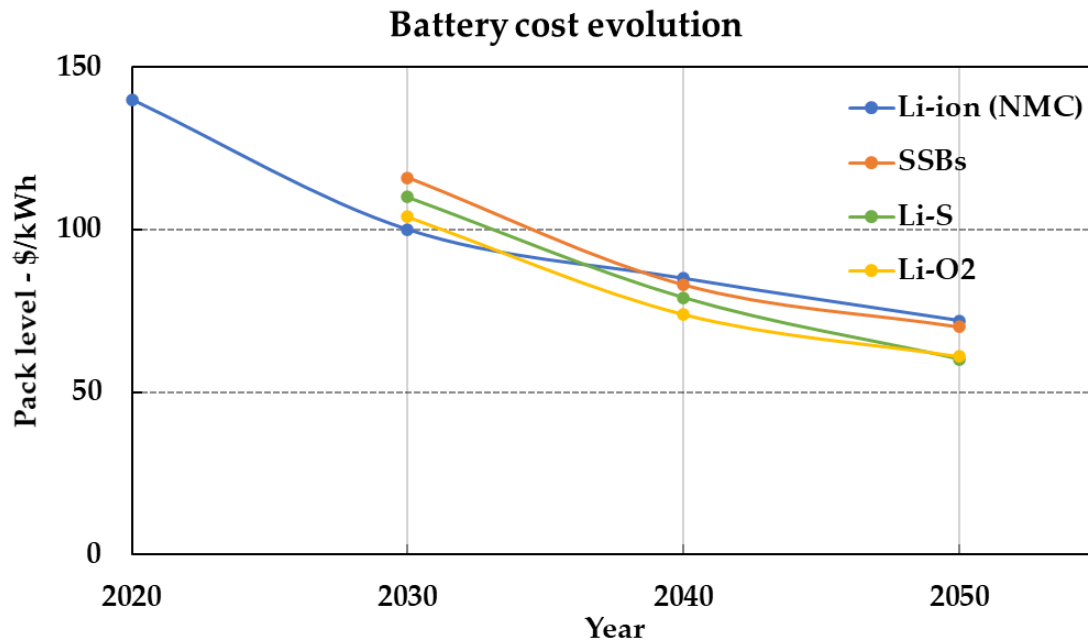
Figure 19. Costs evolution of the different technologies.

2.5.2.1.   Li-S – costs developments

Developments concerning the cathode and electrolytes could have a drastic impact on the cost of Li-S cells. In order to develop cost effective cells, different point of emphasize must be addressed. It

includes reducing the amount of conductive carbon, increasing the sulfur content, reducing the quantity of electrolyte and disminishing the thickness of anodes [25]. In parallel, the mass commercialization of Li-S cells should decrease drastically the cost associated to the production of the electrolyte. In the event that the volume of Li-S electrolyte would reach similar values of li-ion electrolytes, Li-S cells cost could go down to 60 $/kWh [12] [15].

The first deployment of Li-S cells is likely to happen in applications with high energy density requirements like heavy vehicles used for transport. Future improvements in power density and volumetric energy density would enable Li-S cells in light commercial vehicles. Finally, the expected low cost of the materials may also allow Li-S to be competitive to lithium iron phosphate (LFP) and sodium-ion cells in stationary storage applications.

2.5.2.2.   SSBs – cost developments

The first wave in the expansion of SSBs application will happen for niche applications such as medical implants or consumer electronics. Further diffusion will happen in the late 2020s in the EVs and later in the aircraft market [12], [15]. Nowadays, only very small, low power SSBs are commercially viable as upscaling shows safety and lifecycle issues. Some of the decrease in costs will be similar to Li-ion concerning the cathode materials or battery pack structure. On the other hand, lithium metal anodes will be seeing similar costs reduction than Li-S. The cost of manufacturing the sulfide electrolyte will play a major role in quick expansion of SSBs in multiple industries.

2.6.   Battery system targets

2.6.1. Scenarios

In the Clean Sky 2 GENESIS project, two missions (design and typical) have been defined for each timeline according to different aircraft scenarios:

- Short-term – Hybrid electric (H.E) Aircraft
- Medium-term - H.E. Aircraft
- Medium-term - Fuel Cell Aircraft

Table 6 summarizes the different scenario characteristics related to the battery usage. These values are considered in section 2.7 to size and design the battery pack.

Table 6. Aircraft mission scenarios- Battery requirements and specifications for each mission and aircraft configuration scenario

Requirements		Phase	Mean Power [kW]	Peak Power [kW]	Time [min]	Energy [kWh]
Short-term - H.E Aircraft						
Design						
Battery weight [kg]	1500.0	Take off	1070	1070	0.42	7.5
Required energy density [Wh/kg]	340.9	Climb	300	405	23.51	117.6
Required power density [W/kg]	713.3	Cruise	170	201	100.27	284.1
					Total	**409.1**
Typical						
Battery weight [kg]	1500.0	Take off	1340	1340	0.39	8.7
Required energy density [Wh/kg]	339.6	Climb	785	990	19.59	256.3
Required power density [W/kg]	893.3	Cruise	255	365	33.53	142.5
					Total	**407.5**
Medium-term - H.E. Aircraft						
Design						
Battery weight [kg]	1250.0	Take off	1180	1180	0.35	6.9
Required energy density [Wh/kg]	394.7	Climb	750	1020	11.35	141.9
Required power density [W/kg]	944.0	Cruise	125	150	118.05	245.9
					Total	**394.7**
Typical						
Battery weight [kg]	1250.0	Take off	975	975	0.37	6.0
Energy density [Wh/kg]	492.0	Climb	700	1225	12.14	141.6
	780.0	Cruise	850	1040	24.31	344.4
					Total	**492.0**
Medium-term - Fuel Cell Aircraft						
Design						
Battery weight [kg]	2000.0	Take off	900	900	0.33	4.9
Required energy density [Wh/kg]	427.0	Climb	500	660	13.21	110.1
Required power density [W/kg]	450.0	Cruise	330	395	103.33	568.3
					Total	**683.3**
Typical						
Battery weight [kg]	2000.0	Take off	1790	1790	0.32	9.6
Required energy density [Wh/kg]	457.0	Climb	1225	1470	11.57	236.2
Required power density [W/kg]	895.0	Cruise	1275	1525	22.84	485.4
					Total	**731.2**

First of all, it seems that the energy and power densities required in every scenario should be attainable by 2040. This means that hybrid and fully electric regional aircraft should be feasible according to the battery requirements. Better energy densities could improve ranges or reduce the usage of the gas turbine engines, which would improve the sustainability of the aircraft.

2.6.2. Thermal management

When discussing about designing a battery for an aircraft, the thermal management represents a significant aspect to consider. Figure 20 shows the evolution of the ambient temperature during the mission. It can be noticed that the temperature oscillates between 30°C and -10°C. These temperatures are rather common in many applications and should not present many difficulties to handle at the battery pack level. Additionally, the different aircraft systems could provide the necessary cooling or heating values needed to keep the battery inside the operation range. Indeed, the battery heat losses along with the fuel cells and gas turbine hot exhaust air should be enough to sustain the heat demand of the battery during the flight mission. Furthermore, the air conditioning unit from the aircraft could provide the decrease of temperature (~10°C) to cool down the battery when the aircraft is on the ground charging. Finally, the large flux of air during the take-off or climb phases should also be enough to cool down the battery to acceptable temperatures. The specific thermal design of the battery pack will be investigated in more details later in a future report of the GENESIS project.
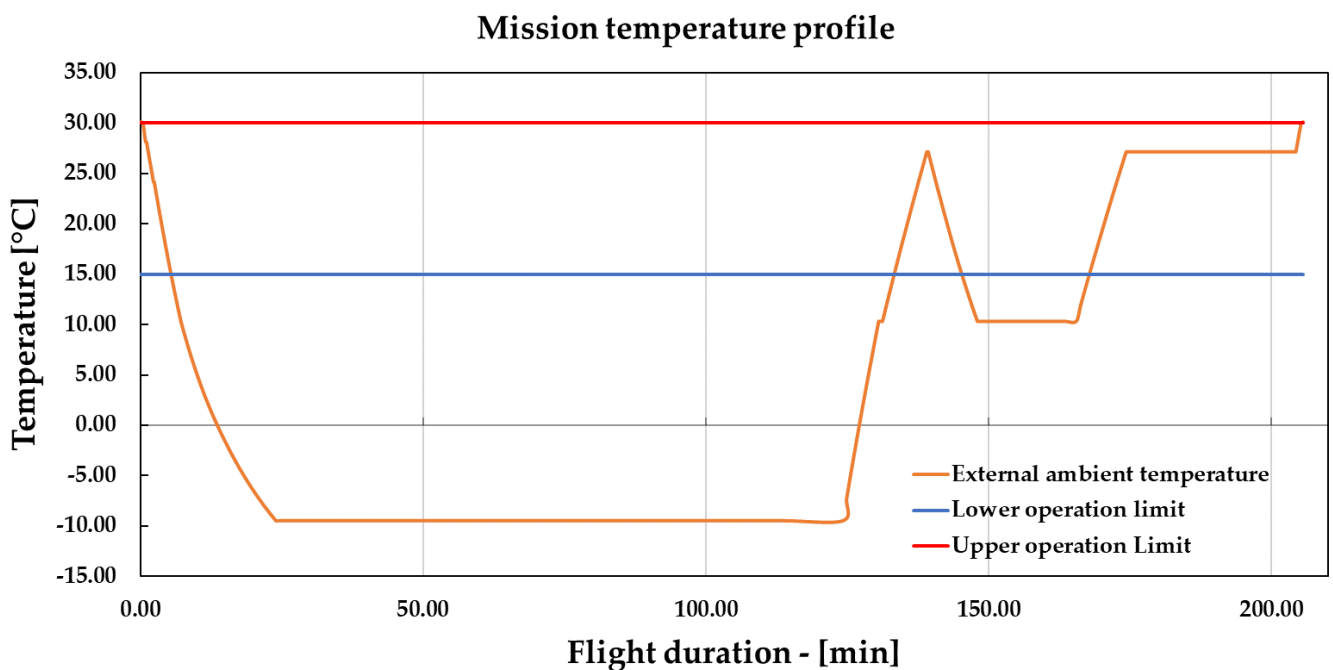
Figure 20. Mission temperature profile and battery operation window.

2.7. Sizing of the battery for the aircraft.

In this section, it will be considered that the energy and power demand for the battery energy system will be provided completely by a single technology (either SSBs or Li-S). The most optimized configuration will be defined in a future report as well. However, it could be very plausible that the best solution features a hybrid battery system composed of SSBs for power demands and Li-S batteries for energy related aspects.

Concerning the design of the battery pack, it was decided to use standard pouch cell format and to adapt the performances to the ones in 2040 (according to our forecast). Pouch cells show great performances, are easier to handle thermally, and are already widely used in the industry. The different battery formats have been discussed in more detail in a previous GENESIS report, deliverable 2.1 – Short-term technology analysis.

Table 7. Pouch cell characteristics.

		Timeline – medium-term	
		SSB	**Li-S**
TRL	Current [-]	4	5
	Future [-]	7 - 8	8 - 9
Voltage [V]	Nominal	4.4	2.1
	Maximum	4.8	2.5
	Minimum	3.5	1.7
Format	Weight - [g]	530	530
	Volume - [L]	0.245	0.392
Energy density [Wh/kg]	Pessimistic	550	650
	Expected	650	750
	Optimistic	750	900
Energy [Wh]	Pessimistic	292	345
	Expected	345	398
	Optimistic	398	477
Capacity [Ah]	Pessimistic	66	164
	Expected	78	189
	Optimistic	90	227
Power density [W/kg]	Pessimistic	2200	975
	Expected	2600	1125
	Optimistic	3000	1350
Volumetric densities	Energy [Wh/L] - Expected	1408	1015
	Power [W/L] - Expected	5631	1523

Starting from the values of the pouch cell a "potential" battery pack, answering the requirements of the mission, was designed. Some information was defined subjectively such as a nominal battery voltage of 600 V for the short and medium term aircraft scenarios and 1000 V for the long-term fuel cell aircraft. A lower battery voltage has been defined to reduce the number of cells connected as the behavior of a string connected in series is determined by the weakest cell. Table 8 shows the values for the expected battery performances. The main findings of Table 8 are:

- Li-S-BP represents a better solution for the medium term (1017.6kg versus 1236.7kg) but will be a slightly heavier solution than the SSB-BP for the longterm (1625.3kg versus 1696kg) .
- Li-S-BP would require a much larger volume, 38% and 68% more for the medium and long term scenarios respectively.
- The C-rate for the Li-S-BP reaches 1.8C for the medium term. It might be useful to increase the capacity of the BP in order to optimize the lifetime and decrease the potential costs.
- The number of cells required to reach the nominal voltage for the SSB-BP is less than half the cells needed for the Li-S-BP.

Conclusions:

In this section, two technologies have been investigated and upscaled to achieve the requirements of the medium term scenario (2035-2045). Li-S and SSBs were the chosen technology because of the high theoretical performances, a relatively high technology readiness level and the strong interest from academia and industry. The performances of a specific pouch cell have been extrapolated from battery evolution forecasts and literature data to design conceptual battery packs fulfilling the requirements. Battery management systems have also been investigated in order to define the major functions and their possible improvements in order to fulfill the harsh requirements of the aircraft industry.

Table 8. Battery pack (BP) design.

Battery Technology	SSBs		Li-S	
Scenarios Aircraft	Medium Term H.E. Aircraft	Medium term Fuel Cell Aircraft	Medium Term H.E. Aircraft	Medium term Fuel Cell Aircraft
Aircraft bus voltage - [V]	800	1500	800	1500
BP nominal voltage target - [V]	600	1000	600	1000
# of cells in series	137	228	286	477
# of cells in parallel	14	12	6	5
Total # of cells	1918	2736	1716	2385
Voltage nominal - [V]	602.8	1003.2	600.6	1001.7
Voltage maximum - [V]	650.8	1083	715	1192.5
Voltage minimum - [V]	479.5	798	486.2	810.9
Weight - cells - [kg]	1016.5	1450.1	909.5	1264.1
Volume - cells - [l]	469.4	669.6	671.9	933.9
Battery pack configuration				
# of modules in Series	2	2	2	2
# of modules in Parallel	3	3	2	2
Series cells per module	69	114	143	239
Parallel cells per module	5	4	3	3
Module configuration	69S5P	114S4P	143S3P	239S3P
BP – Energy - [kWh]	707.9	942.6	682.1	1137.6
BP - Power - [kW]	2831.8	3770.2	1023.2	1706.5
BP - Maximum C-rate	1.7	1.9	1.8	1.6
BP - Weight - [kg]	1236.7	1625.3	1017.6	1696
BP - Volume - [l]	723.7	956.5	959.9	1604.2
BP - Gravimetric energy density - [Wh/kg]	572.5	579.9	670.3	670.8
BP - Volumetric energy density - [Wh/l]	978.3	985.4	710.6	709.1
BP - Gravimetric power density - [W/kg]	2289.9	2319.7	1005.5	1006.2
BP - Volumetric power density - [W/l]	3913.1	3941.6	1066	1063.7

2.8. Structural Batteries Technologies

2.8.1. Introduction

An all-electric battery-based aircraft design is technologically challenging since existing battery systems are not suitable to store the required on-board energy [26] [27]. This is mainly due to their low energy density per unit mass compared to, e.g., kerosene. To reach the required specific energies, new chemistries are being developed to increase the energy stored while the mass is kept approximately the same. An alternative strategy that has gained traction over the last years is the concept of structural batteries in which the functions of energy storage and mechanical load-bearing functions are combined, thus effectively reducing the overall combined weights for the same electrical and mechanical functions [26]. This technology is currently at a relatively low TRL, so it is only being considered for the medium- and long-term horizons (2035 and 2050+). The aspects of structural batteries are fundamentally different than the traditional packaging arrangements of batteries (battery cells/pack) since it pertains to both the structure and the chemistries and thus it is treated in the GENESIS project as a separate battery technology. Distinct design scenarios for structural batteries are analyzed: a low voltage configuration for non-propulsion applications and a high-voltage configuration for assistance in propulsion.

A structural battery is multifunctional since it is the combination of both structural and electrochemical constituents that is designed to perform as a load-bearing structural element and an energy storage medium at the same time. There are different approaches to the structural battery concept in literature, however the most prominent one is using the fiber reinforcement and matrix elements of the composites as an active electrochemical material [28]. Thus, multifunctionality of the structural battery constituents is indispensable to achieve an effective structural battery system. A classical lithium-ion battery has four interior components, namely anode, cathode, electrolyte, and separator. To make useful structural batteries out of composites, it is necessary to accommodate all these components and utilize them for both structural and electrochemical purposes. Several studies have indicated that carbon fibers can be utilized as the active electrodes and the current collector, polymeric matrix materials can be used as the electrolyte, and glass fibers can act as the separator in between the electrodes [26] [28] [29] [30] [31] [32] [33] [34] [35] [36]. The multifunctional use of fiber reinforcements and matrix materials makes it possible to use load-bearing structures for storing energy simultaneously, which enables the use of structural battery systems in electric vehicles and aircraft. By achieving this, the use of regular battery cells can be reduced (or ideally eliminated) within the future all-electric aircraft, which will possibly have a significant impact on the efficiency by decreasing its operational weight.

2.8.2. Conceptual Design of a Structural Battery System

The design of a structural battery system requires two distinctive phases. The first phase is the structural design of the battery system. In this phase, the global structural properties of the laminate that contains a structural battery should be achieved to meet the boundary condition requirements. The second phase is the electrical design phase of the battery system, where the layout of the battery distribution should be decided to reach the electrical design requirements such as voltage and capacity. In some cases, an iterative approach might be needed to achieve the structural and electrical goals after the first cycle of each phase.

2.8.2.1. Structural Design Phase

Classical lamination theory is used to design the structural properties of the proposed structural battery system, since this system is fundamentally a laminated composite [37] [38]. For the analysis presented here, a python-based design code was developed to carry out the structural calculations of the battery system. The structural design algorithm mainly follows the process given in Figure 21. If

the design requirements cannot be met in the end of the calculations, the process returns to the initial step for performing the subsequent structural design iteration.
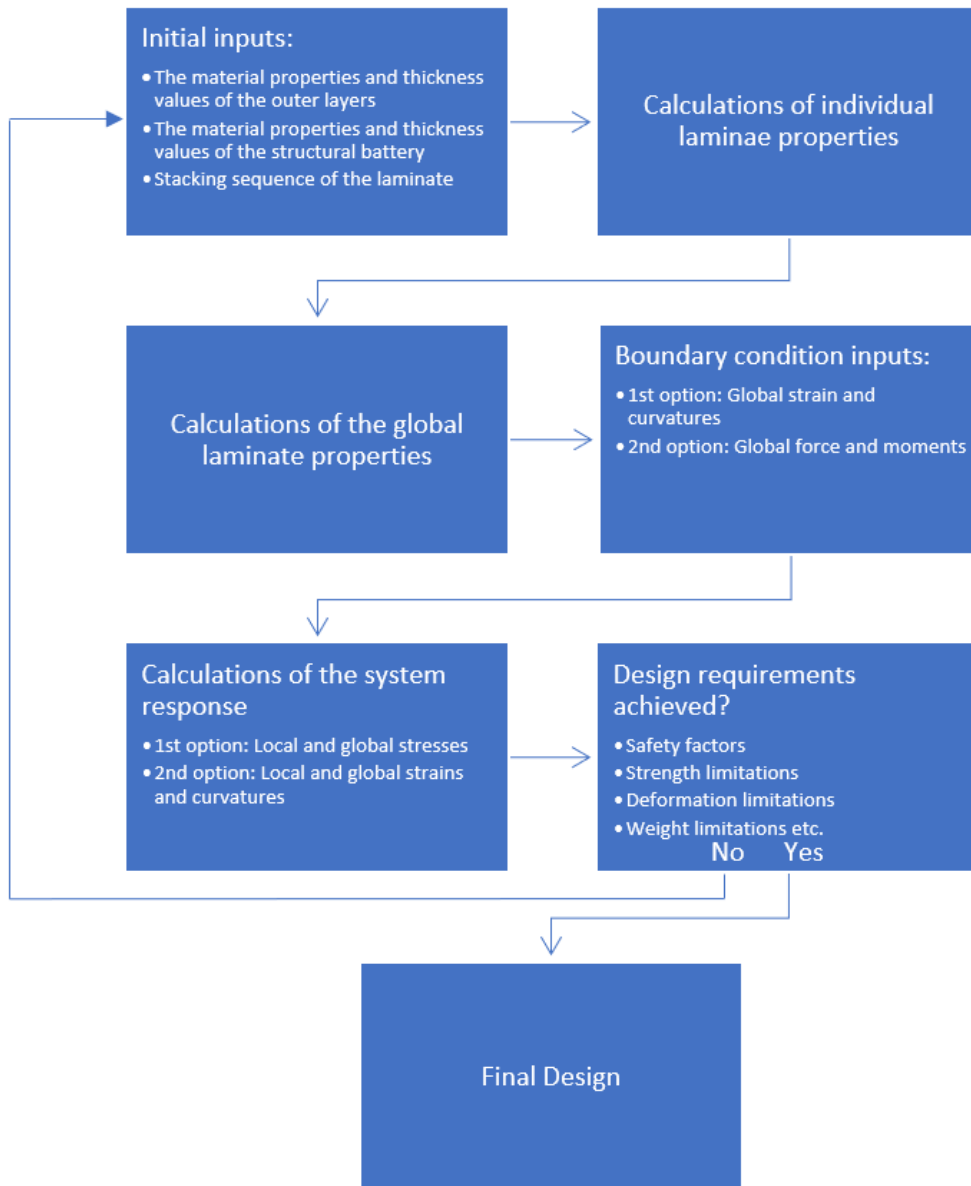
Figure 21. Structural design process of a structural battery

2.8.2.2. Electrical Design Phase

Electrical design of the structural battery system is driven by upscaling the possible single cell design depending upon the requirements of GENESIS' medium-term electric aircraft. The electrical design is also handled through the same python code by creating a separate module. The algorithm process is given in Figure 22.
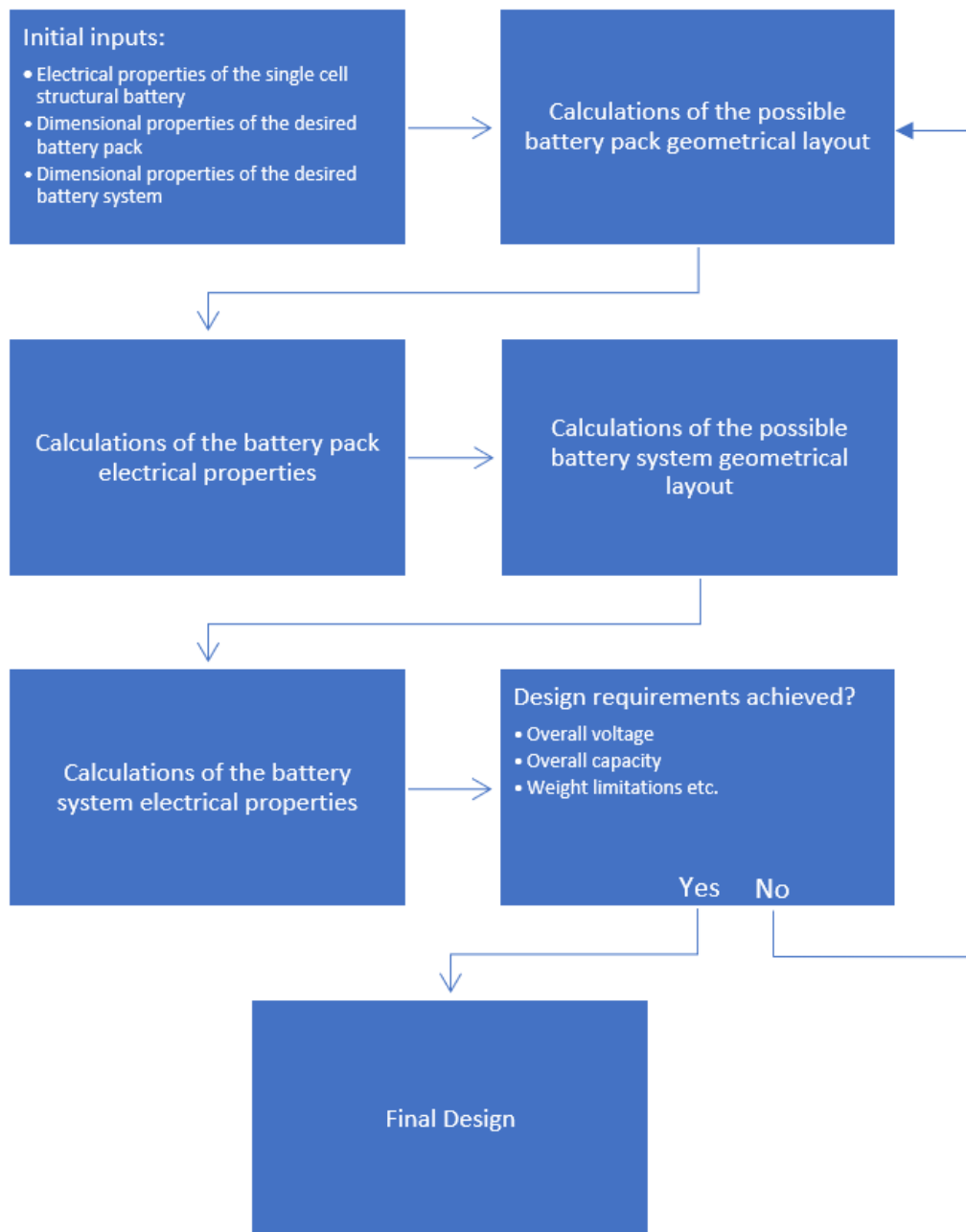
Figure 22. Electrical design process of a structural battery

2.8.3. Semi-Integrated Structural Battery

Ideally, the battery function should be fully integrated into the composite structure to maximize the multifunctionality of the structural battery; in other words, all the structural elements (i.e., fibers and matrix material) in a structural system should be actively used for storing the energy. However, the current level of structural battery technology is still quite immature, which implies that only the long-term aircraft design of the GENESIS project will probably be able to accommodate a fully integrated structural battery system. On the other hand, current research studies indicate that a semi-integrated structural battery (i.e., a structural battery that utilizes a small percentage of structural fibers and matrix material) may be possible to be implemented into the medium-term design [26] [28]. A possible application of a semi-integrated structural battery is illustrated in Figure 23. In this figure, a single cell structural battery, which utilizes two carbon fiber plies as the electrodes, a glass fiber ply as the separator, a polymeric matrix material as the electrolyte, and two carbon fiber stripes as the

current collectors, is embedded into a load-bearing structural laminate. In this single cell semi-integrated design, the outer composite layers of the laminate carry most of the structural load and seal the embedded structural battery from the environment. However, these outer layers do not contain any active materials, thus they don't have any multifunctional properties. The single cell structural battery on the other hand, has a smaller area compared to the entire laminate, and it is structurally weaker than the upper and lower composite layers, therefore its structural contribution to the entire laminate is negligible.
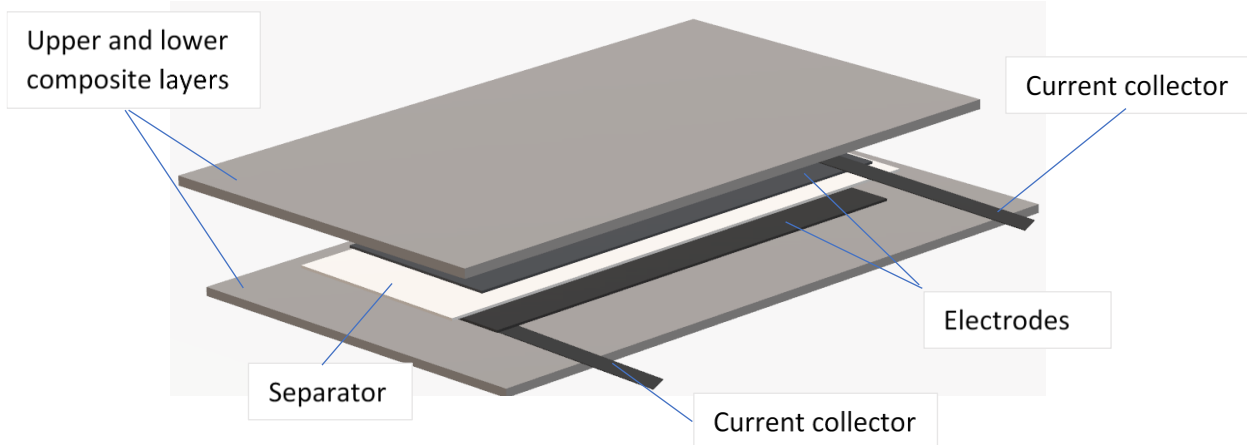
Figure 23. **Single cell semi-integrated structural battery design**

2.8.4. Semi-Integrated Structural Battery System for GENESIS Medium-Term Aircraft

The medium-term electric aircraft design of the GENESIS project utilizes a hybrid propulsion system, where the on-board battery systems (i.e., conventional batteries) are solely reserved for supplying energy to the propulsion needs. On the other hand, there are additional systems in a commercial airliner that require electrical energy such as the cabin lights, the entertainment systems, and the galleys. Therefore, the application of the semi-integrated structural battery system can provide the needed energy to operate the aforementioned systems. Additionally, factors like the TRL, certification requirements, and safety restrictions may possibly complicate the integration of the structural batteries with primary structural elements of the aircraft. In this context, the interior of the fuselage was chosen to accommodate the structural battery system for implementation of this technology to the uncritical *secondary* structures for medium-term electric aircraft design of GENESIS project. It is considered that aircraft interior panels, such as floorings, aisles, entry ways, service doors, under seats, baggage bays, and galleys may be suitable for semi-integrated structural battery applications [39]. These components are usually made of sandwich composites, which accommodate two face sheets (i.e., upper and lower face laminates) bonded to a lightweight core material to provide high flexural stiffness and strength-to-weight ratios. For instance, sandwich floor panels are generally designed in certain sizes, and they are attached to the floor rails as seen in Figure 24 to meet the load requirements while allowing easy installation and replacement. Typical sandwich panels that are designed for commercial aircraft are composed of carbon fiber/epoxy or glass fiber/epoxy face sheets and aramid honeycomb core material.

Figure 24 Installation of a sandwich aircraft floor panel [40]

Embraer ERJ145 can be taken as a comparable aircraft for this study to estimate the possible surface area that can be utilized as semi-integrated structural battery, since it is also a 50 pax regional aircraft, similar to the designed electric aircraft within the scope of the GENESIS project. The total area of the sandwich panels within the cabin of this aircraft is estimated as 75 m^2 according to the airport planning manualTable 9 [41] Table 9 reports data taken from this manual. During this estimation, 100% of the floor area and 50% of the surface area of the other volumes were taken into account. Since these sandwich panels have two laminates (i.e., face sheets) on both sides, the usable face sheet area for the structural battery integration can be estimated as 150.6 m^2 by doubling the estimated sandwich panel area.

Table 9. Example sandwich panel area estimation for 50 pax aircraft (Embraer ERJ145)

	Given dimensions	**Estimated surface area**
Cabin floor width and length	2.1 m x 23.22 m	48.8 m^2
Cargo bay	9.21 m^3	14.2 m^2
Overhead bin	1.9 m^3	4.6 m^2
Wardrobe	0.93 m^3	2.9 m^2
Stowage compartment	0.45 m^3	1.8 m^2
Galley	0.99 m^3	3.0 m^2
Total Estimated Area		150.6 m^2

2.8.4.1. Semi-integrated structural battery pack in a sandwich panel

For this study, a sandwich panel with glass fiber/epoxy face sheets was considered. To achieve a reference semi-integrated structural battery, the size of the sandwich panel was chosen as 1000mm x 1000 mm, where it includes 9 equally spaced 80 mm x 900 mm structural battery cells as seen in Figure 25Since these cells were assumed to be manufactured by using LiFePO$_4$ chemistry, a single cell in this design has a nominal voltage of 3.2 V. By connecting 9 cells in series the entire face sheet's nominal voltage reaches up to 28.8 V, which was reported as sufficient to run cabin electronics [42]. In this configuration, single face sheet can accommodate 0.648 m^2 of structural battery which corresponds to 64.8 % of the hosting sandwich panel area. By connecting the face sheets on both sides of this single sandwich panel in parallel, the capacity of the single sandwich panel will be doubled.
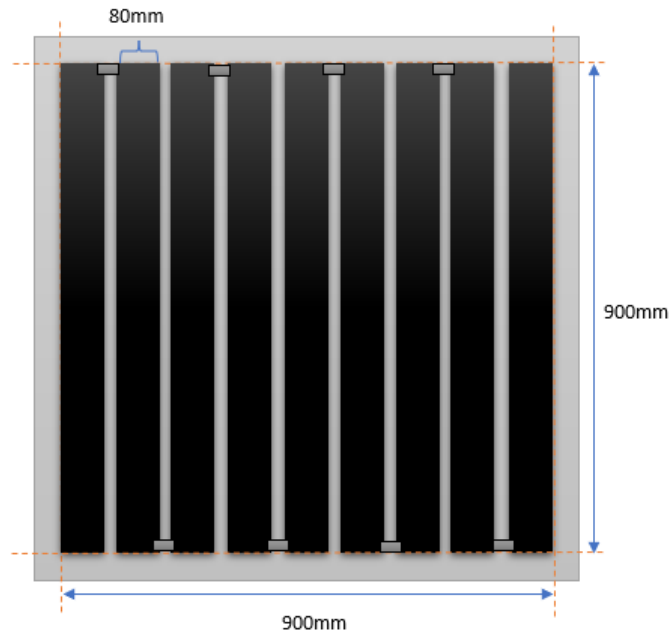
Figure 25. Semi-integrated structural battery layout within a sandwich panel face sheet

Chosen materials for this structural battery design are given in Table 10, utilized electrical properties for the structural battery design are given in Table 11 and the calculated electrical properties of a single sandwich panel are given in Table 12. It should be noted that the parameters given in Table 11 are measured values according to the used active material weight in literature [26]. Even though the calculated weight of the structural battery in this study includes the glass-fiber separator (i.e., the inactive component of structural battery), since the implementation of this technology is considered for 2035, it is assumed that the technological developments in structural battery active materials will most probably compensate the difference.

Table 10. Composite material properties of semi-integrated structural battery

Component / item	Type / value
Face sheet laminate	Glass fiber / epoxy
Structural battery anode	Carbon fiber T800
Structural battery cathode	$LiFePO_4$ coated aluminum foil
Structural battery separator	Glass fiber
Structural battery electrolyte	Epoxy with ion conductive supplement
Current collectors	Carbon fiber T800

Table 11. Electro-chemical properties of semi-integrated structural battery [43]

Property	Type / value
Chemistry	$LiFePO_4$
Nominal cell voltage	3.2V
Energy density	106 Wh/kg
Specific power	34.7 W/kg
Mass per unit area	0.46kg/m^2 for 0.27mm thickness

Table 12. Calculated single sandwich panel structural battery (SB) pack properties

Property	Type / value
Configuration	9S2P
Nominal voltage	28.8 V
Capacity	2.2 Ah
Energy	63.2 Wh
Power	20.7 W
Approximately mass of SB pack	0.6 kg

2.8.4.2. Semi-integrated structural battery system

The entire fuselage interior was assumed to have 75 m2 of usable sandwich panel area for structural battery integration. Therefore, it can be assumed that this size of surface area can host 75 sandwich structural battery packs. Since the nominal voltage of a single sandwich panel battery pack is sufficient for running the interior electric equipment, all of these panels can be configured in parallel connection. The resultant performance of the entire structural battery system is given in Table 13. It should be noted that the current collector' mass values are also included to the mass estimations of the whole SB system.

Table 13. Entire semi-integrated structural battery (SB) system properties

Property	Type / value
Configuration	75 parallel battery packs
Nominal voltage	28.8 V
Capacity	164.6 Ah
Energy	4739.5 Wh
Power	1551.5 W
Apprx. total mass of SB system	44.71 kg

For a commercial aircraft, power requirement per passenger in the cabin is calculated as 42 W in literature [42]. Since the GENESIS electric aircraft is designed for 50 passengers, the total required power reaches 2.1 kW, which is higher than the calculated power (i.e., 1.54 kW) of the entire structural battery system. The most applicable way of increasing the power and capacity properties of the structural battery is increasing the thickness of the structural battery, since it affects the mass of the active material linearly. For this purpose, a 50 % of increase in the structural battery thickness (i.e., from 0.27 to 0.405 mm) would increase the active material mass by the same ratio. If the configuration and battery areas are all kept the same, then the capacity and power would also increase by the same ratio. Therefore, the following properties can be achieved by using 50 % more active material as given in Table 14.

Table 14. Entire semi-integrated structural battery (SB) system properties

Property	Type / value
Configuration	75 parallel battery packs
Nominal voltage	28.8 V
Capacity	246.8 Ah
Energy	7109.2 Wh
Power	2327.3 W
Apprx. total mass of SB system	67.07 kg

2.8.4.3.   Semi-integrated structural battery system: HV-Configuration

Since the electro-chemical materials used for the semi-integrated structural battery design have limited properties, reaching high voltage values without compromising other parameters was not possible by only using thin composite face-sheets of the sandwich panels. On the other hand, the propulsion system of the medium-term design utilizes significantly higher voltage values. Therefore, a volume maximization approach was considered to see the possible contribution of the structural battery design for high voltage needs. For this purpose, the whole thickness (i.e., 10 mm) of the core material was taken into account to integrate the SB system. In this approach, 50 cells were integrated into the core material of a single sandwich panel to reach 160 V per pack (i.e., per panel) by using identical structural battery electro-chemicals. The same overall sandwich panel area (i.e., 75 m^2) was also used for this configuration as it was in the previous scenario. To reach 800 V in total, five panels were connected in series, and a fifteen parallel connection was achieved to use the entire available area. Calculated single sandwich panel performance for high voltage configuration is given in Table 7. The entire high-voltage semi-integrated structural battery properties are also given in Table 16.

Table 15. Single high-voltage semi-integrated structural battery (SB) pack properties s

Property	Type / value
Configuration	50 S
Nominal voltage	160 V
Capacity	6.9 Ah
Energy	1107.4 Wh
Power	362.5 W
Apprx. mass of SB pack	10.5 kg

Table 16. Entire high-voltage semi-integrated structural battery (SB) system properties

Property	Type / value
Configuration	5 series and 15 parallel
Nominal voltage	800 V
Capacity	103.8 Ah
Energy	83057.2 Wh
Power	27189.5 W
Apprx. mass of SB pack	783.6 kg

2.8.5. Conclusions

In this study, a possible semi-integrated structural battery system was investigated for regional commercial aircraft. The chosen structural elements for structural battery integration were mainly composed of glass fiber / aramid honeycomb sandwich structures. During the study, the structural contribution of the electrodes was neglected due to the discontinuous nature of the multi-cell system. The structural battery properties were taken from the literature that are derived from physical measurements under certain conditions. Studied semi-integrated structural battery system seemed to be promising by assuming that the electro-chemical properties of the active materials will be improved by the time of the medium-term design application (i.e., 2035) [43].

3. Fuel cell technology analysis

3.1. Introduction

SOFCs are showing excellent electrical efficiency (>60%) which comes close to the theoretical efficiency 75-80%. Furthermore, the residual energy from the unused fuel and hot exhaust air can be harnessed by a GT-generator system to boost the efficiency. Fuel utilization is around 85% to maximize the performances whereas the remaining lost heat located in the unused hydrogen could be harnessed through heat exchangers.

The gravitational power density is highly linked to the surface power density due to the very thin anode, cathode and electrolyte already implemented. Metal supported cells are on the forefront of power performances with companies such as Ceres or Elcogen. By observing recent technological evolution in surface power densities, ambitious developments of stack power densities are foreseeable in the medium and long-term which could make them viable option for mobility applications.

3.2. Technological challenges

PEM fuel cells have a massive head start on SOFC's for mobility applications due to their exhaustive research during the last 25 years. On the other hand, SOFC's have not been considered a viable power source alternative for a long time, which resulted in a lack of research and developments to improve power densities. However, recently, studies have been investigating the replacement of APU's in commercial airplanes through SOFC-GT (Gas-turbine) systems which boost the fuel efficiency of the ancillary power generation, yet they still lack the implementation in real world applications [44].

In order to reach mass market utilization, multiple technological gaps need to be addressed. There is the need to avoid thermal stress buildup in the thin layer electrodes and electrolyte as it means that the fuel cell stack must be slowly preheated before operation. Currently, problems such as cracking

or interfacial delamination still arise when heating the cell stack too rapidly and creating thermal gradients in the cell.

Additionally, interfacial stresses arise during thermal cycling due to differential thermal expansion coefficients of anode, electrolyte, and cathode. It reduces the robustness of SOFC stacks due to accelerated degradation. As opposed to PEMFC, SOFC's must use high temperature resistant materials such as nickel as anode, yttria-stabilized zirconia (YSZ) ceramic oxide as electrolyte, and metallic cathode. All these come with an inherent high gravimetric density. Challenges have been observed around the engineering of high temperature gas seals at the perimeter of the fuel cell. Due to the high temperature difference between working temperature and ambient temperature, thermal expansion and compression pose problems to the reliability of SOFC stacks. Several aspects of the SOFC still need to be optimized to reduce cell and stack weight.

Extensive testing to validate long term reliability under various environmental conditions (low external temperature, vibration) have not been performed yet due to the lack of industrial applications.

Although an approximation for a SOFC system for mobile applications is that the stack weight will reach ~ 75% of the whole system weight [45], weight reduction of the balance-of-plant can further increase the chances of a successful implementation of SOFC in aircraft.

3.3. Forecasts predictions

The following table states the different performances that are already reachable at the laboratory scales.

Table 17. SOFC laboratory performances reached [46], [47], [48], [49], [50]

Parameter	Value
$\eta_{\text{electric}}(LHV)$	74%
$\eta_{Combined\ Heat\ Power}(LHV)$	>90%
Surface power density – cell level	Measured 1.6 W/cm^2 @0.9V Extrapolated 3.1 W/cm^2 @0.7V
Gravimetric power density – stack level	1.2 - 1.88 kW/kg
Volumetric power density – stack level	3 kW/l

It can be seen that extremely high values have been already reached at the stack level in laboratory. However, one of the main issues concerning fuel cells is the transfer of knowledge and upscaling between the laboratory and the industry. Additionally, lots of targets and future forecasts do not separate technologies of FCs which makes it difficult to have a good understanding of which one is considered. With the values from Table 17 and different forecasts, we were able to give an estimation of the SOFC performances for different horizons in Table 18. It must be mentioned that similarly as batteries, it is very difficult to predict the evolution of fuel cells performances. Particularly concerning SOFC which is gaining a newly found interest which accentuates the very high uncertainty of predictions over large timelines.

Table 18. SOFC performances evolution.

Parameter	Horizon 2025-2035	Horizon 2035-2045	Horizon 2050+
Grav. power density (stack) – [kW/kg]	0.5	1.5	2.5
Vol. power density (stack) – [kW/l]	1	2	3
Grav. power density (system) – [kW/l]	0.2	1.125	1.875
Vol. power density (system) – [kW/kg]	0.5	1	1.5

The cost has also been investigated and Figure 26 shows the cost evolution of SOFC systems per kW installed. It shows that a significant decrease is expected to happen in the next 30 years to reach a system of 800 $/kW in 2050.
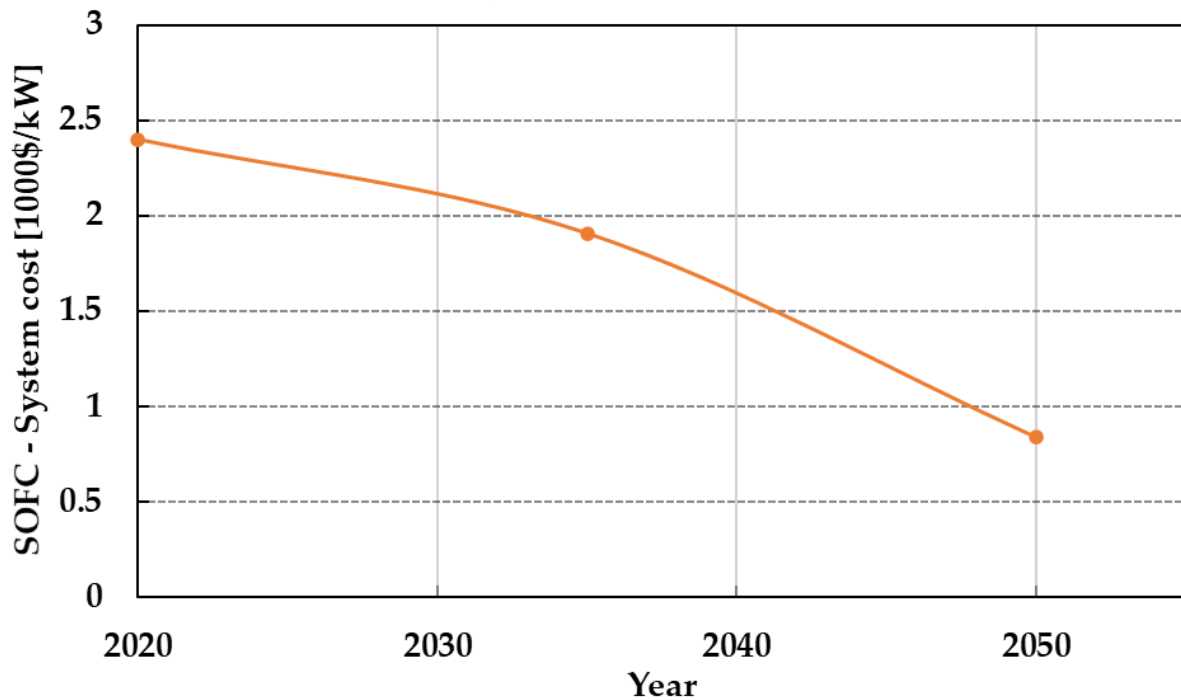
Figure 26. Cost evolution of SOFC systems [51].

Figure 27 shows the cost evolution of the production of electricity depending on the fuel source. As it can be seen, the cost is not expected to drastically change between 2020 and 2035 and even increase in the specific case of H_2. However, in 2050, the cost per kWh from H_2 will significantly decrease to reach 0.14 $/kWh.
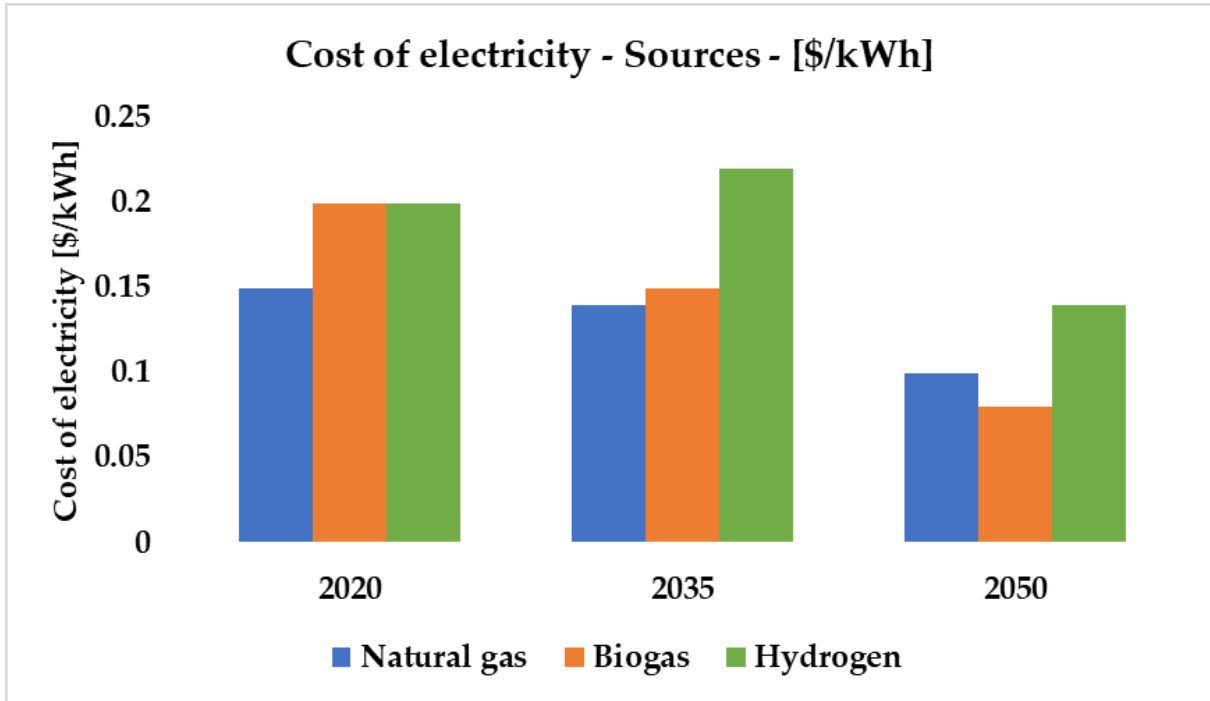
Figure 27. Cost evolution of the production of electricity depending on the fuel source.

3.4. Fuel cell system targets

In the case of a fuel-cell aircraft for medium-term – fuel cell aircraft scenario, the maximum peak power is 1400kW and the maximum on-board weight of the fuel cell plant is 1400 kg.

Table 19. Aircraft mission scenarios- fuel cell requirements.

Phase	Peak Power [kW]	Time [min]	Energy consumed [kWh]
Medium-term - fuel cell Aircraft			
Design Mission			
Take off	1400	0.33	23
Climb	1400	13.21	872
Cruise	1275	103.33	6212
Descent	60	12.33	235
Second Climb	1400	10.31	600
Alternate	1400	15.87	681
Second Descent	60	5.67	108
Loiter	1400	30.00	1124
Landing	55	1.57	32
		Total	**9888**
Typical Mission			
Take off	550	0.32	13
Climb	786	11.57	561
Cruise	477	22.84	820
Descent	60	12.33	235
Second Climb	1400	10.30	600
Alternate	1400	15.88	681
Second Descent	60	5.67	108
Loiter	1400	30.00	1124
Landing	55	1.57	32
		Total	**4174**

3.5. SOFCs operational behavior

3.5.1. Cell & stack & fuel cell plant operating behaviour

SOFCs are mainly described according to their characteristic curves such as voltage, power, and efficiencies as function of the surface current density. The specific operating curves of SOFCs used in 20 years are not available yet, however, extrapolating results from the latest research is found to be the most suitable way to predict performances. The goal of the fuel cells is to replace the gas-turbine system and the need for kerosene. Figure 28 depicts the operating behavior of a SOFC based on current performances found in laboratory in a technologically relevant cell format. It shows the Beginning of Life (BoL) and End of Life (EoL) polarization curves (after 10'000 hours), the thermal and voltage efficiencies as well as the power of the cell. Additionally, the surface maximum current density achievable is expected to be 3 A/cm^2 which would lead to a maximum power of 2.36 W/cm^2. It is believed that these performances will be transferable commercially by 2040. Figure 29 shows the thermal and voltage efficiencies during operation as a function of the surface current density. At the maximum operation rate (3 A/cm^2) , the voltage and thermal efficiency will be 68% and 52% respectively.
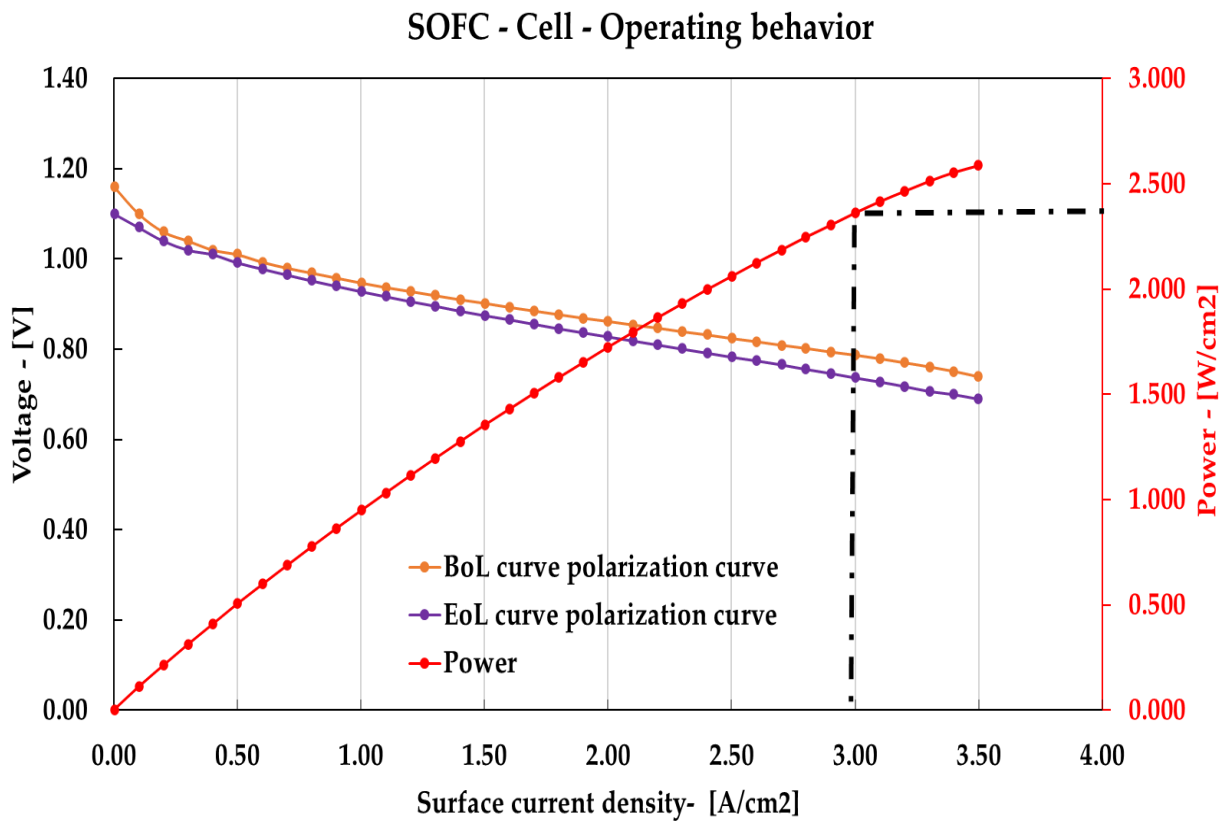
Figure 28. Solid-oxide fuel cell operating behavior in for the medium term.

SOFC - Cell - Efficiencies
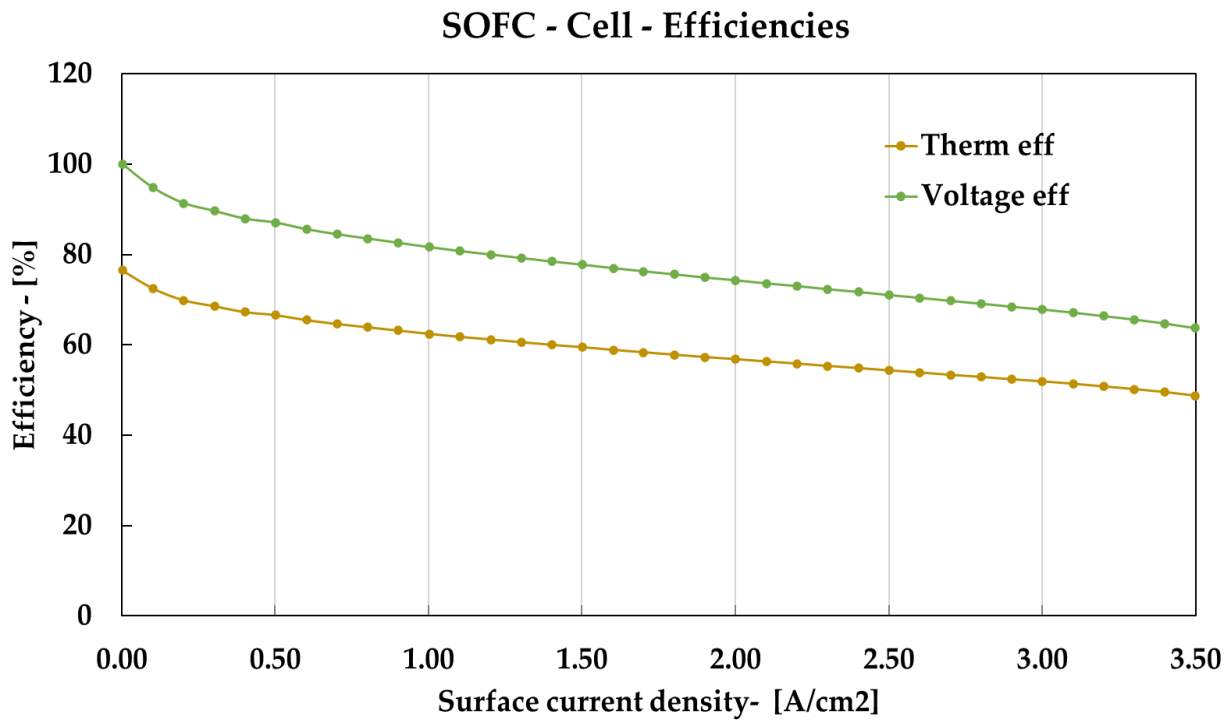
Figure 29. Solid-oxide fuel cell efficiency for the medium term.

Practically, it is easier to assemble SOFCs connected in series to increase the voltage than to increase the number of stacks in parallel as it requires additional components such as gas inlets and sensors. Therefore, it was decided to scale the system to reach higher voltages with 1200 cells connected in series (maximum voltage of 1380 V) and the surface area of a single cell is set to be 100 cm² as it is a common size found in industry. The behavior of a single stack can be seen in Figure 30. It can be seen that when the maximum current of 300 A is reached the stack provides a power of 284 kW. One stack would weight 190 kg and occupy a volume of 142 Ll. The maximum voltage is 1380 V and the minimum voltage is 950 V
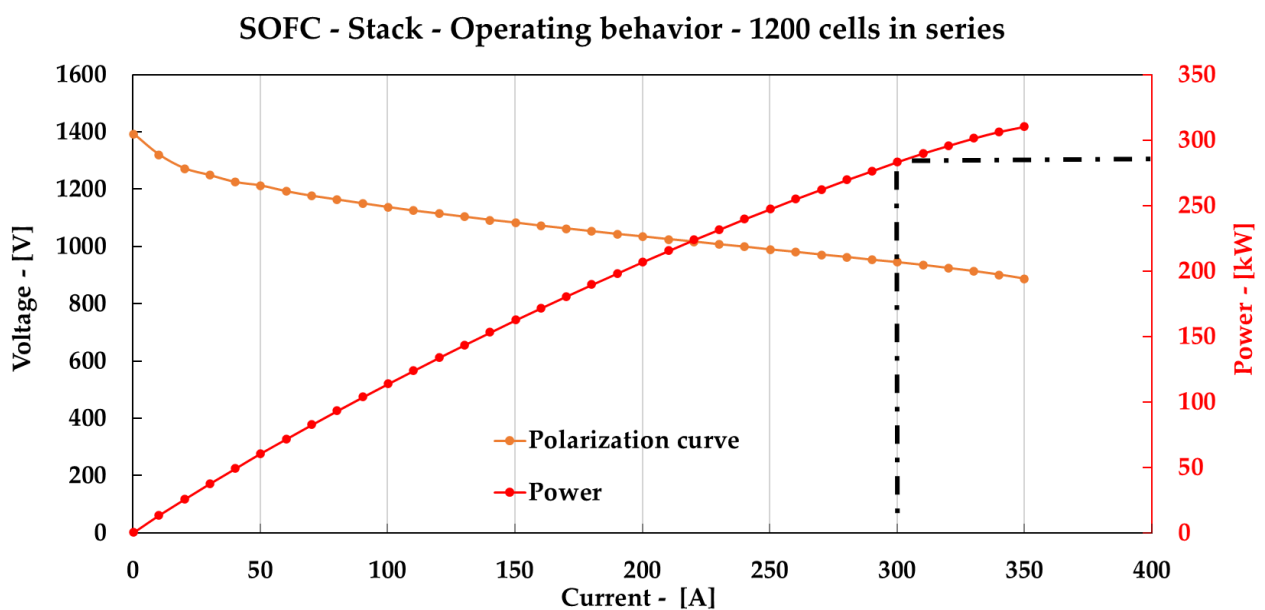
Figure 30. SOFC stack operating behavior

In order to provide 1400 kW peak power, the fuel cell plant will be composed of 5 modules connected in parallel. Figure 31 shows the behaviour of the fuel cell plant for the 2040/2050-FC scenario.
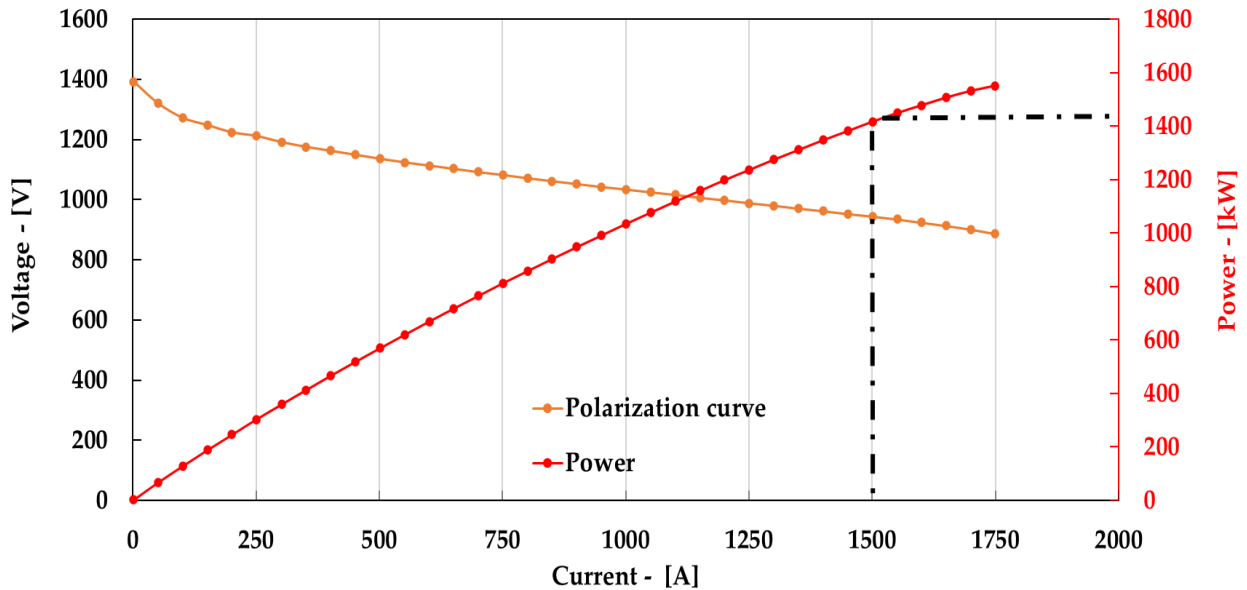
Figure 31. SOFC plant behavior

Currently, we consider that the modules are separated but it could very well be assembled by juxtaposing different cells into one structure as an array like seen in Figure 32 to increase the active surface and have a bigger stack that is equivalent to nine stacks in parallel.
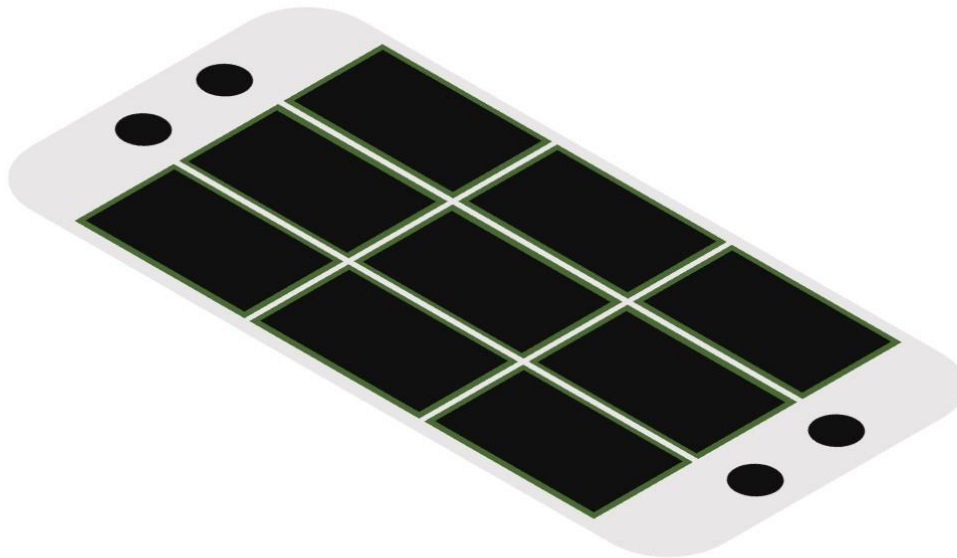
Figure 32. Cell arrays connected in parallel to form a single stack.

With 5 modules in parallel, the fuel cell plant would produce a maximum power of 1420 kW for a weight of 1262 kg and a volume of 1420 l excluding the storage of hydrogen. Indeed, concerning the upscaling from stack to module, the gravimetric and volumetric efficiencies are estimated at 75% and 50% respectively.

Table 20. Fuel cell stack and system values.

Parameter	Max Power [kW]	Weight [kg]	Volume [l]
Stack	190	190	142
System	1420	1262	1420

3.6. PEM Fuel Cell Technology

3.6.1. Introduction

When considering the medium-term technological analysis of LT-PEM (Low temperature Polymer Electrolyte Membrane Fuel Cells) it is assumed that the general stack and system architecture will not change. This means that the individual components of the stack, as well as the Balance of Plant (BOP) and peripheral components will still be the same as described in D2.1 (short-term technological analysis). Of course, „game changing" new developments can take place but their impact on the future's technology is not predictable. However, a considerable development is expected on many components, leading to better performance, extended lifetime, and lower costs. These improvements can be grouped mainly in three different areas: 1 – Improvement in materials and material combinations, e.g., in the catalyst, the membrane or bipolar plate coatings. 2 – Technological improvement of complex periphery components, e.g., compressor or DC/DC converter. 3 – Improvement in production processes and scale-up effects, e.g., bipolar plate or membrane electrode assembly. Scale-up effects not only come from reduced costs through automated production processes and higher volume orders, but also from an increasing number of suppliers, leading to more market competition and thus lower prices.

3.6.2. Technological Development

Based on several investigations, the following are considered as key technologies for the further development of PEMFCs and hence strong progresses are expected. Detailed information will be given in the following section.

FC stack:

- Improved components (materials), e.g. membranes
- Reduction of ageing/degradation
- lowering Platinum Group Material (PGM) content
- Improved joining technology/sealing materials

FC system:

- Peripheral components (BoP)
- Sensor technology (smart sensors, virtual sensors))
- Reduction of complexity
- Advanced safety technology
- Diagnostic methods in the system (e.g. enhancing lifetime by avoiding negative impacts, predictive maintenance etc.)

Hybrid components (not described in detail in the following section):

- Downsizing/new development
- Higher integration capability
- New control concepts

Overall system:

- General operating concepts
- Advanced design to manufacture (& design to serviceability)
- Improved start/stop capability
- Advanced Break-In procedures

Below are given performance curves of state-of-the-art fuel cell stacks (based on Proton Motor system technology). These are taken as basis for the description of the future improvements. All given curves are comparable in principle to other fuel cell stack/system manufacturers.

As shown in Figure 33 the system power generated by the fuel cell (blue curve) increases with increasing stack current. This follows the polarisation curve (U/I) shown in Figure 34 amd also described in the previous GENESIS Deliverable D2.1 (Short-term Technology Analysis) in more detail. This curve is a general characterisitc of a fuel cell. At the same time, the efficiency of the system (red curve) decreases from about 60% to 40%.

This means that a fuel cell system can be designed in such a way that either a high efficiency (with better utilisation of the hydrogen but with a correspondingly lower power density) is achieved or an operating point with an optimised power-to-weight/volume ratio (but lower efficiency in relation to H_2) is aimed for. Both, system power and stack current depend on the individual fuel cell but are scalable to the target application
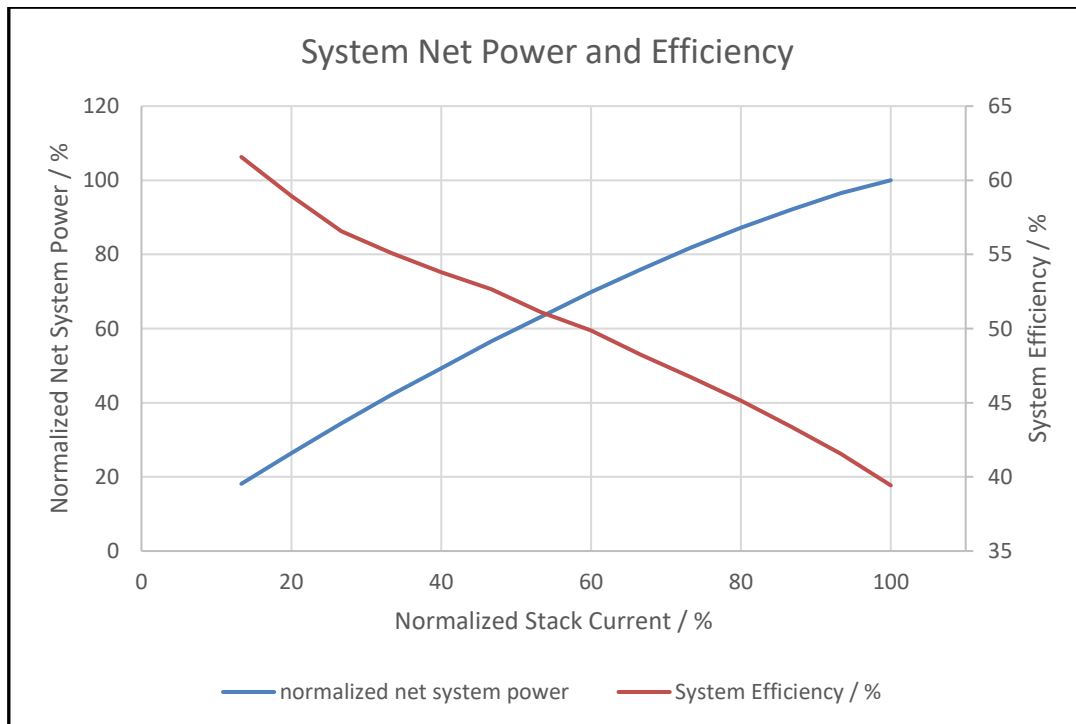
Figure 33: System performance (state-of-the-art PM system).
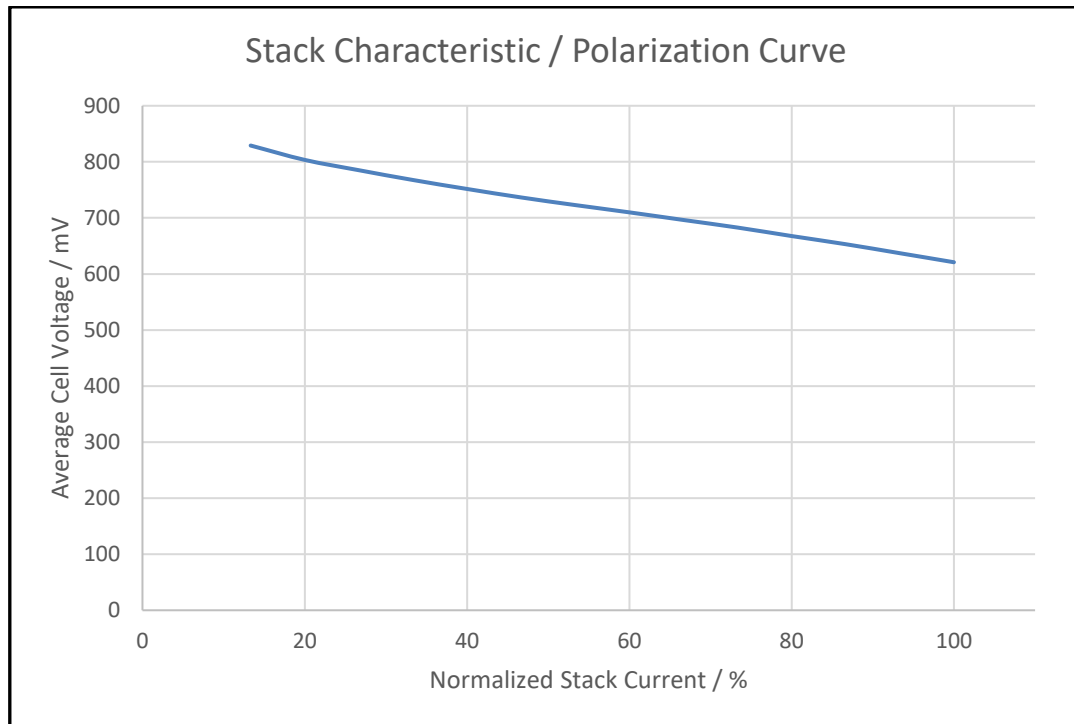
Figure 34: Stack performance curve (state-of-the-art PM stack).

Considering the improvements described below and projecting from current values, the following Table 21 gives details about the power densities of the stack and the system. In order to reach the required power levels and take into account redundancy, three stacks per system are considered.

Table 21: PEMFC performance evolution

Parameter	Horizon 2025-2035	Horizon 2035-2045	Horizon 2050+
Grav. power density (stack) – [kW/kg]	1	1.8	3
Vol. power density (stack) – [kW/l]	1	1.5	2.5
Grav. power density (system) – [kW/kg]	0.5	1.5	2
Vol. power density (system) – [kW/l]	0.3	0.8	1.5

Table 22 gives the details of the stack and system that were used as basis for the preceding Table 21.

The values presented here are based on well-founded expert opinions within the PEFC sector as well as on an extrapolation of previous trends.

Here, the comparison of these values in Table 21 with the values of SOFC technology given in Table 18 shows some differences, although the trend is going in the same direction. In principle, both gravimetric and volumetric power densities are slightly lower with PEM. However, it is also important to define the exact scope of the stacks and systems considered. Different manufacturers

have different definitions of this. In addition, the given values are subject to a great deal of uncertainty. These two factors should be taken into account in the interpretation

Table 22: PEMFC stack and system values medium-term

Parameter	Max Power [kW]	Weight [kg]	Volume [L]
Stack	180	75	120
System	540	360	360

3.6.3. Cost Development

A detailed cost forecast is difficult to do as reliable numbers and cost analyses are hard to come by and can vary considerably, depending on supplier or research institute consulted. This can lead to predicted system costs (€/kW) ranging several orders of magnitude. In Literature target costs are discussed in a very broad variety from below 50 $/kW (passenger cars) to >5.000 $/kW (portable applications) [52]. From our point of view total system costs in the range of 1000 – 3000 €/kW are realistic.

Part of the difficulty is that industrial production processes are in the middle or beginning of being developed and installed and there is still unclear or insufficient data available to make a reliable forecast. For example, there are different technologies for producing graphitic bipolar plates, e.g. hot pressing or injection moulding and the price of the component varies considerable, depending on which technology is used. When considering that for metallic bipolar plates there are even more and completely different production processes with completely different machinery and costs behind them, the issue becomes clearer. This example then only relates to one component of the stack and is exacerbated by the many other stack and system components.

Even though it might be a momentary effect, it should also not be neglected that geopolitical aspects like supply chains and production locations can drastically influence prices. Given the current situation it is likely that in the mid-term more production and supply chains will be shifted to the European and American market, resulting in higher production overhead costs, ultimately counterbalancing other price reduction trends.

In general, however, there are certain aspects that are clear and may be extrapolated from current price situations. For a PEMFC system today roughly 50 – 60% of the total cost is due to the fuel cell stack and the rest comes from BOP and periphery components. It is projected to shift towards 28% stack cost and 72% BOP cost in 2040 [53].

Considering that the electrical power is generated in the stack, it is not surprising that the largest potential for improvement in power density and lifetime lies in its components. Considering also that the stack has a high degree of high-tech materials and components still closest to research and development, it is also not surprising that these offer the largest potential for improvement in costs. More details with respect to the individual components will be given below. The BOP components on the other hand are mainly off-the-shelf, commercial products, like piping and hosing, valves, sensors and pumps. It is not expected that these can contribute to a significant increase in performance or lifetime, as well as a reduction in cost. An exception are the two largest BOP components: air compressor and power converters. Both offer development potential, mainly in terms of size and weight, as discussed further in the following paragraphs. The production of the PEMFC itself is

expected to be a significant factor in reducing the overall system costs. In addition to the expected economies of scale through the reduction of individual component costs, the mass production of the FCS is a key factor in this regard. here, a potential reduction in manufacturing costs of up to 66% is predicted, primarily through largely automated production [54, 55].

A concise and very rough summary of the cost situation of PEMFC is shown in Figure 35. This shows the assumption of a relatively progressive cost development of PEMFC stacks and systems. In addition to the wide range of uncertainties discussed, it shows that a significant reduction can be expected over the next 30 years to reach a system cost of $750/kW (system) in 2050. The reduction potential in the fuel cell stack is seen as even greater. Of course, even greater cost savings are possible in principle.
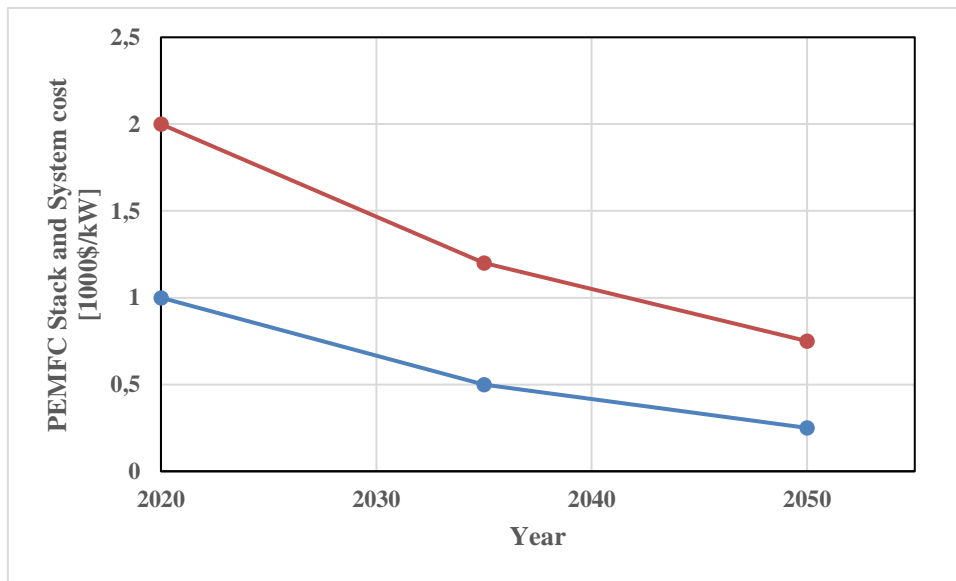
Figure 35. Cost evolution of PEMFC stack and system (optimistic scenario)

3.6.4. Stack Components

The heart of any fuel cell system is the stack, i.e. the electrochemical energy conversion unit. Here, the chemical energy of the fuel (e.g. hydrogen) and an oxidant (oxygen from air) is converted to electrical energy and waste heat, which can also be utilized via heat exchangers and secondary cooling liquid loops. Following is a closer look at each of the main components.

3.6.4.1. Bipolar Plate (BPP)

Given the immense importance of the BPP for the stack performance, lifetime and cost, it is one of the two critical components when it comes to future development. As mentioned in the last deliverable, there are two different technologies: Graphitic compound plates and metallic plates. Each offers unique points of improvement and cost reduction. For graphitic plates the main challenges are finding ways to reduce the overall thickness and thus increasing power density (volumetric and gravimetric). However, lower thickness makes the issue of H_2-crossover through the plate more pressing, resulting in the need to change the properties of the compound accordingly. The chemical properties of the compound then determine the production process. Several suppliers and research institutes are also looking for ways to reduce production cycle times, thus decreasing costs, for example via injection moulding. Additionally, a large price reduction potential for the BPP results from installation of large-scale production lines, at the same time increasing quality. Extrapolating current price indications, it is likely that the BPP subcomponent will decrease in cost by up to 70%.

For metallic plates there is little potential for a thickness reduction. On the other hand, the most pressing issue here is the low lifetime of the plates, due to corrosion issues. This problem is currently handled with special coatings that are costly because of noble metal content and expensive coating machinery. Consequently, the lifetime extension potential for the medium-and long term future stems from improvement of coatings (high electrical conductivity and high corrosion stability). With these improvements it can be expected that lifetimes of 20,000 – 40,000 operating hours might be achieved. Moreover, a price reduction potential is due to coatings with low or no noble metal content and scale-up effects of coating machines.

Great progresses are expected in the field of both, graphite and metallic bipolar plates. Although, according to the state-of-the-art (SoA), the use of metallic bipolar plates is the only option for aviation is favoured due to their more advantageous power density, this question cannot be conclusively clarified for the mid-term period. Whether and if so, one of the two technologies will prevail in the market in the future remains open. However, since both technologies are moving in the same direction (long service life, low volume, high conductivity), this question is ultimately irrelevant.

A strong improvement is also expected in manufacturing technologies. Today, there are a large number of different methods for manufacturing both variants of the bipolar plates, each of which has advantages and disadvantages [56]. Here too, depending on the improvements in the respective bipolar plate technology, a significant further evolution will emerge with regard to the individual production process (cycle times, complexity, manufacturing costs). It is primarily in this respect that the greatest reduction in the cost drivers for bipolar plates is to be expected.

3.6.4.2.   Catalyst Coated Membrane (CCM)

In the light of the CCM being the exact location of the electrochemical conversion reactions and its content of highly engineered materials and coatings, it is the second critical component for future development. Certainly, also since it offers improvement potential in all three main aspects: Higher performance, longer lifetime and reduced cost.

Per definition the CCM consists of an ion-permeable membrane and a catalyst coating. The function is described in D2.1 in more detail.

Enhancements of the catalyst can have a positive influence on all three aspects. A reduction in catalyst loading is one possibility to reduce cost and can be achieved from better catalyst supports, offering smaller and more stable particles. There are also considerable research activities in core-shell and alloy catalyst particles. Lastly, completely noble metal free catalysts on the basis of activated carbon and transition metal compounds are also possible, although this will likely only result in a significant cost reduction without being able to increase performance (maybe even reduce performance). For optimisation of catalyst and support a huge variety of investigations can be found in literature [57, 58, 59]

Another subcomponent is the membrane itself and there are trends to progressively thinner membranes. Since this will increase gas crossover and reduce lifetime, they must be chemically and physically strengthened. Given the recent development and research trends, membrane engineering will most likely lead to higher lifetimes. As already mentioned for the BPP, a scale-up in production lines will also significantly reduce costs in the CCM sector, but likely not as much as for the BPP. This is due to the fact that large lines handling thin foils and coating machines are already part of

industrialized production. Altogether, a price reduction of around 40% might be expected. As one example electrospinning is one of the most discussed technologies for producing PEMFC membranes in the future but also total new developments such as Nafion-free hydrocarbon membranes are under scientific investigation [60, 61].

In this respect, too, a strong improvement in production can be expected in the manufacture of membranes and catalyst inks, but especially in the application process of the catalyst layer to the membrane. For example, the related application methods of photovoltaics are considered, which implement similar requirements in mass processes. This will lead to a higher quality, homogeneity of the catalyst layer and thus, in addition to the cost reduction effects, to a further improvement in stability and service life.

3.6.4.3. Gas Diffusion Layer (GDL)

The GDL is needed for a homogeneous distribution of media to the catalyst layer and a uniform current distribution across the active area of the fuel cell. Lifetime and performance are already quite high at the current state-of-the-art and there is only a small potential for improvement in the future. Thickness and special coatings can be adapted for higher performance, e.g. for higher operating temperatures and pressures or for more effective water removal. A larger potential lies in scale-up effects relating to raw materials and production lines potentially in the range of 20% - 30%. Also here an advancement in improved manufacturing technologies can be assumed, which may lead to additional cost reduction and higher service life for the FCS due to according higher product quality (more uniform thickness and fibre distribution, higher QA etc.).

3.6.4.4. Sealing

Sealing material is needed to prevent all three media lines (H_2 or other fuel, air, cooling liquid) to mix with each other and to be released into the surroundings. Material improvement is mainly focused on increasing lifetime. Moreover scale-up effects, as well as advanced machines and concepts for sealing application onto the BPP or Membrane-Electrode-Assembly (MEA) will likely lead to decreasing costs, again projected to be around 50%. The effects of the corresponding improvements are not to be expected on the side of the manufacturing costs of the entire FCS due to the relatively low cost share of the individual components, but on the side of the increase in the reliability of the system (and thus, of course, also the total cost of ownership TCO).

3.6.4.5. Stack-Compression and Media Adaptation

Other stack related components are the compression system, as well as media adaptation and connection solutions. These will not play a role in determining performance or lifetime but can increase gravimetric power density when more lightweight materials are used. Additionally cheaper production processes like injection moulding and use of standard components will lead to lower costs, boosted by scale-up effects of higher volume supply chains. It is harder to make a prediction of cost reduction, as there are quite different systems possible, but they can range from 10 – 50%.

3.6.4.6. Stack Assembly, Break-In and FAT

Apart from the individual components of the stack, the process of assembling the stack and making sure it passes the quality/performance checks (Factory Acceptance Test, FAT) can be examined on its own. Especially the stacking/assembly process of the stack is mainly done manually at the moment, or the first machines are in the validation process. There is still much to be learned and not yet a

proven concept that can be easily adapted and scaled up. Consequently, the price point of assembly of the stack will decrease significantly once the stacking automation is implemented. Assembly can be also improved by integration of components and functionality in order to reduce the number of individual components and their complexity. A prime example is the trend to combine CCM and GDL into a so-called 7-Layer MEA, which is already starting to become state-of-the-art.

After assembly, each stack has to be conditioned to make sure each cell reaches its intended performance point. This process is usually referred to as the break-in procedure and currently takes several hours per FC stack. An optimisation of this break-in, which is being worked on in several scientific groups and projects (e.g. within the framework of the German Hy-Fab project), will not only save time, but also considerably reduce costs through a reduction in personnel expenditure, hydrogen costs and an increase in service life through the avoidance of life-critical processes already at the BoL. The conditioning procedure consists of certain physico-chemical processes in the cells that offer limited ways to accelerate. Therefore, another possibility to deal with this step is to implement advanced analytics to detect stacks with inadequate performance early in the process and to be able to tell if a stack will pass the FAT criteria before it actually reaches them.

Both steps will lead to large decreases in production time of the stack and can thus reduce its price considerably. Potential price savings of more than 50% are realistic.

3.6.5. BOP Components

Balance of Plant (BOP) refers to any additional component that is needed to operate the stack itself and can be divided into the three media lines (H_2/fuel, air and cooling liquid) as well as the power electronics and the fuel cell control with according safety system. As already mentioned above there are mainly two BOP components that are a major focus of development in the medium-future. Due to the higher relevance to the overall system the converters will be described in a separate section by the according experts.

A) Air compressor

In view of the high power density of the fuel cell a large amount of reactant has to be delivered to the active area, especially taking into account that atmospheric air only consists of 20% oxygen. This leads to the compressor being a large/heavy and expensive part of the BOP. Constant high power operation also leads to high degradation and therefore low lifetime. Technical development in the direction of turbochargers with low resistant/low wear air bearings can help extending the lifetime as well as being much smaller and more lightweight. Since these are in the early stages of commercialization the medium-term forecast might not offer cost savings here. On the contrary, the turbo-compressors might be more expensive for a while before scale-up effects take effect and the balance between power and cost has to be evaluated carefully.

The compressor itself has been one of the most critical components in the PEM fuel cell system for years, since an extremely high purity of the reaction air is opposed to the problem of bearing the high-revving compressor shafts (poisoning through the introduction of lubricants). A currently disputed approach to a solution envisages air-bearing or magnetic air-bearing compressors, which represent a considerable share of the total costs of the FCS, as they are (still) custom-made in relatively small quantities. However, this is precisely where there is an enormous cost-saving potential of up to 80%.

B) Fuel cell control and safety system

Significant improvements can be expected in those area as well. Beside the hardware development (control systems, sensor technology etc.) especially the development of advanced control and safety strategies may result in improved service life and broader operation windows and higher safety of the overall system.

3.6.6. Operating strategy

This aspect also has implications that are not easy to describe. Due to the fact that the operating window of the fuel cell systems can be extended, the links with the hybrid strategy are also variable. Each individual component in the hybrid system (battery, power electronics, motors, fuel cell) can have an impact on the design of the others. This makes the overall concept very complex. However, an improvement in terms of efficiency of the overall system and tailor-made solutions to the respective target application can be expected to lead to a cost and performance advantage. The overall consideration of the concepts takes place at a higher level.

Another significant improvement can be found e.g. in the development of virtual sensors: here, material parameters that cannot be measured directly in a simple way or whose sensors are complex and expensive are calculated by algorithms and the fuel cell control can react immediately to them, e.g. in order to avoid undesirable conditions or conditions that affect the service life. In addition to saving on sensors (weight, cost, complexity), this also improves service life (and thus also again the TCO). The operating strategy can also be increased in terms of (electrical) efficiency, which is extremely valuable, especially in aviation applications.

3.6.7. Conclusion

Hydrogen and fuel cells have great potential for sustainable aviation. A large number of research and industry groups worldwide are working on the development and implementation of such solutions.

However, the challenges are extremely high, especially for the case of aviation, since in no other application weight in terms of gravimetric power density is of more significance (also valid in the overall system context with Hydrogen storage, motors and power electronics as described in other sections).

From a cost perspective, the use of fuel cell in aviation is certainly less critical. As this requirement is also important in other fields of fuel cell applications huge efforts will be a strong driver for cost reduction in general. Above all, cost advantages through market penetration and mass production are expected to bring the benefits of economies of scale of PEMFC in automotive, heavy duty, rail and marine applications. The message will be: Capital Expenditures (CAPEX) of the fuel cell system will not be a barrier. (Considering the current situation and developments, also the hydrogen costs and hence the Operating Expenses (OPEX) are expected to get very competitive in the upcoming years.)

For the scenario of a 50 PAX aircraft taken up in the GENESIS project with the mission profiles developed therein, the defined goals are difficult to achieve, based on our projected development, at least for the mid-term range. This does not mean, however, that they are completely out of reach. On the contrary, the predicted specifications are quite close to what is needed. Big game changers in terms of both, the political framework conditions and technologically unforeseeable developments might strongly influence these developments and future trends.

The defined targets in the long-term scenario are very much likely achievable (insofar as these targets do not also change by then).

Likewise, the assumptions made here are of course not valid for all applications in the field of aviation but refer to the scenario defined here. In other scenarios, a dedicated analysis of the specific framework conditions must be carried out carefully.

3.7. Hydrogen storage

3.7.1. Introduction

While storing hydrogen, the main challenges are volume and weight efficiency. To tackle the first one the main storage technologies, increase the hydrogen density through high pressure for compressed hydrogen tanks and through cryogenic temperature for liquid hydrogen tanks. These processes, though energy-demanding, are already mastered.

These methods induce additional requirements of pressure bearing and temperature holding to the tanks, which constitutes the technical challenges for the design of hydrogen storage.

3.7.2. Technological challenges

3.7.2.1. Liquid hydrogen

The technological challenges of liquid hydrogen are temperature related. At low temperature, most materials experience changes in mechanical properties. Below the glass-transition temperature, polymers lose their resilience and go from ductile to brittle. Thus, most polymers cannot be used in liquid hydrogen tanks. Metals are also subject to cold embrittlement at cryogenic temperature, so materials have to be carefully chosen in regard to temperature rather than weight and are typically made of metal alloys such as stainless steel, aluminium, copper, brass, and monel. Among these, stainless steel is the most commonly used for cryogenic applications, but in terms of weight aluminium is the best candidate for hydrogen storage. In particular, low-density alloys, such as Al-Li which would offer lower density and higher elastic modulus than standard aluminium alloys [62]. Some of them, like 8090 alloy, show density as low as 2.54 kg/dm^3, almost 10% lighter that conventional aluminium alloys (2.66–2.84 kg/dm^3) [63] but quality improvements in composition and process still need to be done before we can produce materials up to the regulations for applications as critic as aviation.

The next challenge is to minimise heat transfer. The liquid state of liquid hydrogen is only reached at cryogenic temperature of approximatively 19 K. The heat coming from outside the tank vaporizes the liquid H_2 into a gas, which needs to be vented and released, used, or reliquefied to prevent overpressure in the tanks that are usually designed to withstand only low pressures under 10 bar. So naturally, the key technology of liquid hydrogen storage is the insulation.

The 3 modes of thermal transfer conduction, convection, and radiation, can be weakened by the use of materials that present low thermal conductivity, low emissivity at thermal wavelengths, and low mobility fluids (vacuum).

Multi-layer insulation is a good candidate as it consists of a succession of metal sheets that hinders radiative transfer, separated by a low conductivity filler material put under extremely low pressure, typically <1 Pa, to reduce the convection.

Aerogels, i.e. gels in which the liquid part has been replaced with gas, making it a light and porous material, are also good candidate. Silica aerogels can be as light as 3 kg/m^3 as the solid only represents around less than 10% of the volumes, the rest being gas trapped in nanopores. Which reduces the conductive and convective transfers and in normal conditions apparent conductivity can reach as low as 30 mW·m^{-1}·K^{-1} down to 13 mW·m-1·K-1 with soft vacuum [64].

It is worth mentioning that with insulation the surface-to-volume ratio is essential, and in that regard, larger spherical tanks offer a great advantage. But with further development of low conductivity

materials such as aerogels, small to medium size liquid hydrogen tanks (<300 m^3) could have low input heat flux (1 W/m2) without requiring high vacuum [65].

3.7.2.2.   Gaseous Hydrogen

Gaseous hydrogen tanks are rather simple of use compared to liquid hydrogen tanks as the fluid is stored at a stable state. The only functions are gas-tightness, pressure-bearing reinforcement, and interface between the tank and the system, respectively handled by the liner, the reinforcement, and the bosses.

The weight repartition between these 3 components varies largely depending on the pressure, and the dimensions of the tank. However, for mobile applications where the volume is a constraint and requires compact tanks with high storage pressure, the reinforcement represents the biggest part of the mass, followed by the liner.

For gaseous storage the challenge is clear using the lightest material to withstand pressure and reduce the impact of the non-load bearing functions.

3.7.3. Forecasts

Since the first high pressure hydrogen tanks introduced in the late 19th century, high pressure tanks design has gone through different types of technology, each more weight- and volume- efficient than the previous one.

the previous one.

The first ones were entirely made of metal (type I) and incredibly heavy. The use of continuous fibres enabled first as a reinforcement of the cylindrical part of the tank (type II) and then as the only pressure-bearing component (type III & IV) empowered the reduction of the mass in tanks. These two technologies differ in the material of the liner: type III uses a single part metallic liner, whereas type IV uses a polymer liner tightly assembled with metallic bosses. As polymers are lighter than metals, type IV is more weight-efficient. Nevertheless these two technologies still coexist, for matters of cost and environmental condition: the type IV is more sensitive to temperature, for example. The next step would be to store the hydrogen directly in the pressure-bearing composite shell and suppress the liner altogether. This technology of linerless tanks is often referred to as type V.

Since the liner also acts like a mandrel for filament winding, the need for removable mandrels arises. Several processes were developed to tackle this issue:

- Dissolvable tooling: after winding and curing, the mandrel is chemically dissolved. This technology is suitable for small series as the mandrel can only be used once.
- Extractable tooling: before winding the tooling encased in a bladder is pressurized to the wanted mandrel size, after curing vacuum is applied so that the mandrel collapse into itself and can be extracted from the tank. It can then be pressurized again to produce the next tank.
- Although it is not commonly used, patents have been issued for such technologies and several companies already produce and commercialize this type of tanks. The applications are usually small series and specific developments and guidelines for FCEV do not allow this type of tank yet. But we can imagine that the hydrogen economy and its need for lighter tanks will bring up an evolution of regulations.
- The manufacturer announces a gain on mass efficiency going from 15 to 22% compared to the type IV counterparts.

- Carbon fibre is made of a carbon allotrope graphite, in which the carbon atoms are arranged in a lattice of hexagonal structure.
- In bulk graphite, this lattice structure gives the soft properties that allow it to be used as pencil or as lubricant. Because the different layers are weekly bonded, via Van der Waals bonds, one

layer can slide past another. However, the hexagonal structured elements in each individual layer, also called graphene, are strongly bonded, via covalent bond, and give the material high strength.

- Carbon fibres are long, thin, narrow strips of graphite, therefore its properties depend on the quality of the structure but cannot surpass the properties of the graphite layer. The better the orientation of the lattice layer in the fibre the higher the tensile modulus.

a   b   c
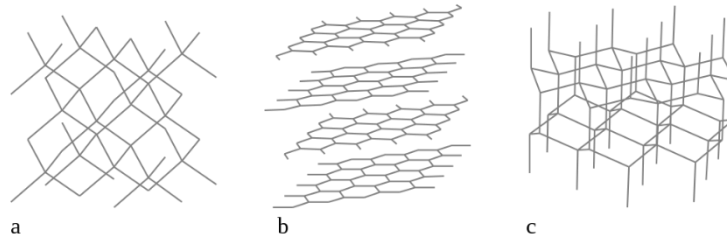
Figure 36. Some allotropes of carbon: a) diamond; b) graphite; c) ionsdaleite

The estimated maximum Young's modulus is around 1000 GPa for a theoretical perfect graphene, along with a tensile strength of 100 GPa. In reality, the maximum achievable values are generally one order of magnitude below, and tensile strength as high as 19.6 GPa [66] has already been observed in lab graphite materials with particular structures (whiskers) [67].

Although such material could not be used for hydrogen tanks for composite it gives limit of the maximum attainable strength for the continuous carbon fibres.
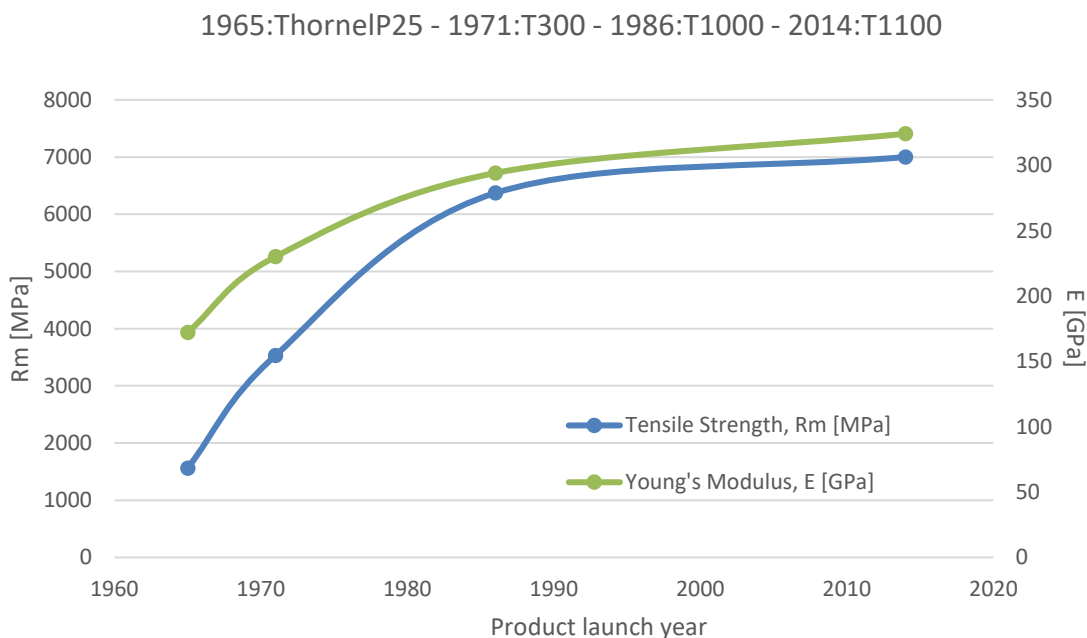
Figure 37. Evolution of industrial carbon fibre properties

Since the fortunate discovery of carbon whiskers in 1960 the research on carbon fibre resulted in a quick progression of carbon fibre production.The first mass produced fibre, Solvay Thornel P25, obtained a tensile strength of 1560 MPa in 1965 [68].

Nowadays, mass-produced fibres used for manufacturing of lightweight hydrogen tanks have a tensile strength of 5000 MPa on average, already 25% of the maximum observable for graphite materials. The current strongest industrial grade fibre is the T1100 by Toray, launched in 2014 and commercially available [69]. It has a tensile strength of 7000 MPa, a Young's modulus of 324 GPa and an elongation at break of 2%, which make it a good material for filament-winding [70]. Nevertheless, its price is still a liability for large usage and very few, if not any, high pressures tank manufacturers use it.

The initial fast development of fibre has now somehow slowed down since the T1100 launch. Though several industrial grade fibres with similar properties were developed by other manufacturer, no further improvement has been made in carbon fibre tensile strength. The development of hydrogen economy and the need of lighter tanks should make the prices drop in the decade and democratised the use of this type of fibre.

Compared to the standard fibre for high pressure tanks, T1100 fibre this typeshows an increase of 20-40% of the tensile strength, that translates in the composite into a 10-20% of reduction of the mass, based on datasheets. Since the composite is, by weight, the most important part of the high-pressure tank, especially for large volumes we can expect nearly 10-20% of mass reduction on the whole structure as well.

3.7.4. Sizing and designing of the system for the mission.

For medium term the design and typical mission respectively require respectively 250.94 kg andet 105.91 kg of usable hydrogen. Gaseous hydrogen storage is considered.

To dimension the hydrogen storage, a few parameters and hypothesis have to be considered:

- Maximum storage pressure: higher pressure means smaller volume but thicker tank walls, so a compromise has to be made between compactness and lightness.
  - ➢ Suggestion: 30 MPa.
- Safety coefficient: is the ratio between the design pressure to failure of the tanks and the maximum storage pressure. It is dictated by codes and regulation between 1.5 and 3.
  - ➢ Suggestion: 2.25 in accordance with current directives for FCEV.
- Minimum required pressure: is the minimum pressure required to guarantee the fuel cell operating pressure and flowrate with pressure loss in the piping. This will determine the mass of hydrogen remaining at the end of the mission and thus the minimum hydrogen to carry.
  - ➢ Suggestion: 5 MPa
- Allowed storage space: is the maximum dimension allowed in terms of length and diameter and will condition the number of storage tanks needed.
  - ➢ Suggestion: Limits of 10 m long and 2 m wide, in accordance with aircraft integration.

For the design of the tanks, type V is chosen along with Toray T1100 carbon fibre. Tanks are usually cylindrical or spherical. The former is easier to scale up by adjusting the length, which usually gives more leeway than diameter, and it is usually preferred for common application. The latter is more efficient but difficult to produce and stack, and it is left for high-end applications where the mass is crucial like spacecraft and aircraft.

In carbon composites, though the matrix plays a key role in the structure of the material, the fibre accounts for most of the material resistance. In order to put aside the choice of the matrix we will use an energy method for its dimensioning, as introduced by Kim et al [71].

Table 23. Material properties for energy-based design method

Properties	
Fibre	Toray T1100
Tensile strength	7000 MPa
Fibre volume fraction	50%*

* Corresponds to the standard low of 60% fibre mass fraction)

Assuming a constant temperature of 15°C the density of the hydrogen inside would be 21.2 kg/m^3 when full at 30 MPa and 4.09 kg/m^3 when emptied to the system minimum operating pressure. This means that only 81% of hydrogen is usable and therefore to fulfil both missions' hydrogen requirements, a mass of 311.09 kg should be embarked. The maximum diameter imposes a configuration with 4 tanks for the chosen pressure. Once the tank inner volume is set, we can easily determine the inner diameter, and then the minimum wall thickness via the energy method [71] To take into account the thickening of the composite shell around the bosses due to the manufacturing process and the defects of fibre placement, a 1.2 coefficient is applied to determine the wall thickness. Finally, we can estimate the total mass of the tank of 423 kg per tank, considering 5 kg for the bosses yet to be designed, resulting in 1692 kg total empty storage mass for 250.9kg of usable hydrogen.

Table 24. Storage system configuration

Properties		Units
Total hydrogen mass	311.09	kg
Number of tanks	4	
Tank inner volume	3.68	m^3
Shape	Sphere	
Inner diameter	1.91	m
Wall thickness	22.16	mm
Tank empty mass	422.96	kg
Outer diameter	1.94	m

Compared to tanks designed and produced at this time, the energy-based design method seems a little optimistic but the further improvement of process and the use of local reinforcement would make it more achievable.

The technological maturity on hydrogen tanks is already high, reaching TRL 8 - 9 for mass-procuded small volume tanks used in the automitive field. However the weight efficiency is under 8%.

The linerless tank technology is TRL 8 - 9.

The high resistance fibre techlogy is TRL 8 - 9.

The making of spherical high pressure tank is TRL 8 - 9.

But the making of spherical, linerless tanks using ultra-high resistance fiber is TRL 2 - 3. Mainly due to the high cost of the fibres and the complexity of manufacturing spherical or linerless tanks which, as of now, is not really suitable for mass production.

4. Turbine / ICE generator set analysis

This chapter aims at providing an overview of the work that was performed for the GENESIS project regarding the modelling and the technological analysis of gas turbine engines for the three time perspectives considered by the project. In particular, the results of the analyses reported in this chapter are mainly focused on the medium-term scenario (2035-2045 timeframe, with 2040 selected as the representative year), with a quick digression concerning the short-term, to amend some preliminary results presented in D2.1.

In particular, this chapter has been structured in the following way:

- Section 4.1 provides a short introduction to the technology, as well as a quick description of the reference gas turbine configuration selected for the technological analysis of GENESIS.
- Section 4.2 deals with the description of the methodology that was adopted in order to model the main characteristics of a gas turbine engine (e.g., fuel consumption, mass, dimensions, and costs) as a function of assumptions related to the technological level, as well as to link them to main engine design parameters, such as the design burner exit temperature (T_4), the overall pressure ratio (OPR), and the shaft power delivered (SPD) at sea-level static (SLS) take-off (T/O) condition. This methodology was already detailed in D2.1. Section 4.2 provides a recap on the main characteristics of this approach, as well as a description of the changes that were applied to it, in light of several suggestions and feedback received during the past months. Moreover, the overall approach for the modelling of gas turbine engines was also enriched with new equations allowing to describe the characteristics of the remaining components of a conventional powerplant (e.g., gearbox and propellers). These were essential in order to try to provide a full picture of the powerplant characteristics to the LCA analyses.
- Section 4.3 includes a small digression on the short-term, which was necessary especially in light of the modifications that occurred regarding the overall approach.
- Section 0 provides a description of the preliminary analysis carried out for the medium-term scenario, including results in terms of expected specific fuel consumption (SFC), NO_x emission index (EI), engine dry mass, overall size, and costs.
- Finally, section 4.6 provides a brief recap of the main achievements regarding the gas turbine technology analysis.

4.1. Introduction to the technology

In order to generate the amount of power/thrust required by an airplane to take-off from the ground, climb at the desired cruise altitude, and fly the cruise phase at the selected design speed, quite different solutions have been adopted throughout the years, both for civil and military planes. For a commuter or a regional airplane (i.e., aircraft covering relatively short distances, typically connecting small to medium/large airports of a certain region), turboprop engines are preferred in general over turbofan or reciprocating engines. This selection is typically the result of trade-off analyses, including considerations on ground performance, reliability, and, of course, operating costs.

A turboprop engine includes three main components:

- The gas turbine core, which, in terms of general architecture, is not very different from the one of a turbojet/turbofan engine and is the portion of the engine in which mechanical power is actually produced. This part of the engine includes one or more compressors, a combustion chamber, and one or more turbines.
- The reduction gearbox, which allows reducing the rotational speed of the output shaft of the engine to the desired value.
- The propeller, which allows transforming the power generated by the gas turbine core to thrust, and operates at a reduced rotational speed, according to the gear ratio of the gearbox, with respect to the output shaft of the engine.

With regards to the architecture of the core of the engine, different choices can be made regarding the compressors and the turbines groups. In order to reach the desired OPR, one or more compressors can be used. The compressors can be of two types:

- axial compressors, in which the air flows along the same direction of the axis of the rotation;
- centrifugal/radial compressors, in which air is pushed to flow in the orthogonal direction with respect to the inlet flow.

The choice between these two types is affected by many factors, which are well summarized in [72]. For entry mass flow rate values higher than 10 kg/s, radial compressor units are no longer competitive with respect to axial compressors, due to the much higher frontal area and weight, which overturn the benefit of lower costs. For values comprised between 1.5 and 10 kg/s, both the solutions can be taken into account and the selection may be essentially driven by considerations on costs (radial units have lower unit cost for the same mass flow rate and pressure ratio), frontal area (axial compressors have a lower diameter at mass flow rate and pressure ratio parity), weight (axial compressors tend to weigh less due to the reduced diameter), and pressure ratio (single-stage centrifugal compressors can grant pressure ratios up to 9, while axial compressors would need up to 12 stages to provide the same level of compression).

Concerning the turbine group architecture, there are several available options. These options mainly differ in terms of number of stages of each turbine (which is determined according to the expected loading of each stage), cooling system (which determines the number and how the different turbine stages are cooled in order to withstand the extreme temperatures of the exhaust gases), and in the way the power generated by the core is transferred to the gearbox and to the propeller. In some engine designs, the turbine linked to the gearbox is on the same shaft as one of the compressors. Another solution consists in linking the gearbox to a so-called power turbine, leading to what is usually called a free turbine turboprop engine.

For the GENESIS project, the Pratt & Whitney PW127 engine [73] was selected as the reference model in terms of gas turbine configuration and for performance comparison, with respect to the advanced models designed for the three time perspectives of the project. This is the engine equipped on the ATR 42 turboprop airplane, which is the reference aircraft model selected for GENESIS. This engine features a three-shaft configuration, with:

- a single-stage low-pressure (LP) radial compressor, driven by a single-stage LP turbine;
- a single-stage high-pressure (HP) radial compressor, driven by a single-stage HP turbine;
- a two-stage power turbine (PT) moving the propeller through a reduction gearbox.

A visual representation of this engine is provided in Figure 38. Its configuration was assumed as the starting point for the application of the methodology already reported in D2.1, which is recapped and amended here in section 4.2. Small deviations were eventually applied with respect to this general layout especially in terms of turbine cooling system. Most of the PW127 models feature a cooling system only for the stator and rotor stages of the HP turbine. But, for the technology analyses of the medium and long-term scenarios, it was supposed that also the turbine stages of the LP turbine could be eventually cooled. A more detailed description of this aspect is provided in section 4.2.
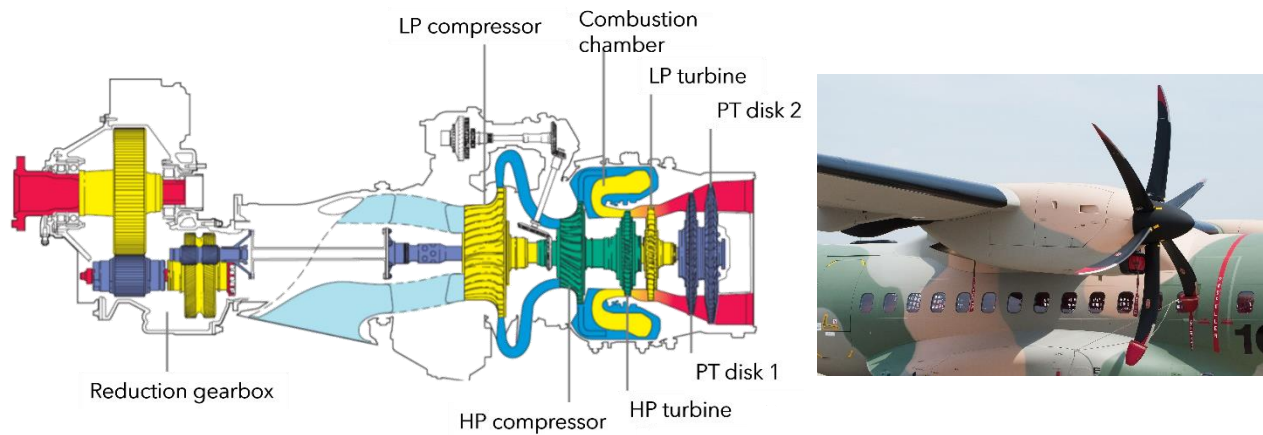
Figure 38. Pratt & Whitney PW127 engine configuration. Images taken and adapted from [74] (left) and from [75] (right).

4.2. Gas turbine preliminary design methodology definition

An integrated approach for the design of the airframe and of the powerplant system has become, especially during the last decades, an important requirement for the aircraft and the engine design specialists. During the conceptual design phase of a hybrid-electric aircraft, several levels of hybridization are typically investigated, based on technological assumptions and future trends for the performance of batteries and fuel cells [76]. The requirement in terms of gas turbine shaft power at this point is still not precisely set, but it is adjusted during parametric analyses, in order to detect the best promising combinations between conventional and advanced propulsive solutions. Typically, during these studies, the characteristics of the gas turbine in terms of size, weight and performance are simply scaled, based on empirical or semi-empirical calibrations taking into account power ratios. However, a more systematic approach, including physics-based considerations derived from actual gas turbine performance models, would surely lead to much more accurate results.

For this purpose, the approach depicted in Figure 39, which is a particularization to the case of turboprop engines of the general approach reported in [77], was adopted for GENESIS. This approach was already outlined in D2.1 and consists in four main steps:

- Generation of a *rubber* (i.e., conveniently scalable) engine model for the description of the performance of a gas turbine engine similar, in terms of layout and general characteristics, to the Pratt & Whitney PW127 model. A set of design laws and automatic update rules would be implemented in a gas turbine performance tool, such as GasTurb [78], to *rubberize* (i.e., make scalable) the selected reference engine model. A set of limitations was elaborated too, in order to further ensure the feasibility of each engine designed with this approach. This rubberized model would be then tested, calibrated and validated against available data of existing engine models with the same (or similar) characteristics of the reference engine.
- Definition of the set of input variables to be used for the generation of a surrogate engine model. This set of input variables would be used to drive a parametric study, at engine design point cycle (selected as the maximum take-off condition), in order to derive all the output variables required for the estimation of fuel consumption, emissions, engine dry mass, engine overall size, and costs. For all the quantities not directly provided by GasTurb standard output (essentially all the ones listed above, with the exception of the specific fuel consumption), a dedicated model was picked from the literature or was eventually elaborated.
- Generation of a surrogate engine model, by means of the dataset produced at the previous step through the execution of parametric studies at the design point, and by means of the MATLAB

Regression Learner App [79]. The latter would be used to train several regression models (one for each of the output variables of interest of the thermodynamic cycle of the engine).

- Implementation of this gas turbine engine surrogate model in the aircraft design framework elaborated for GENESIS.
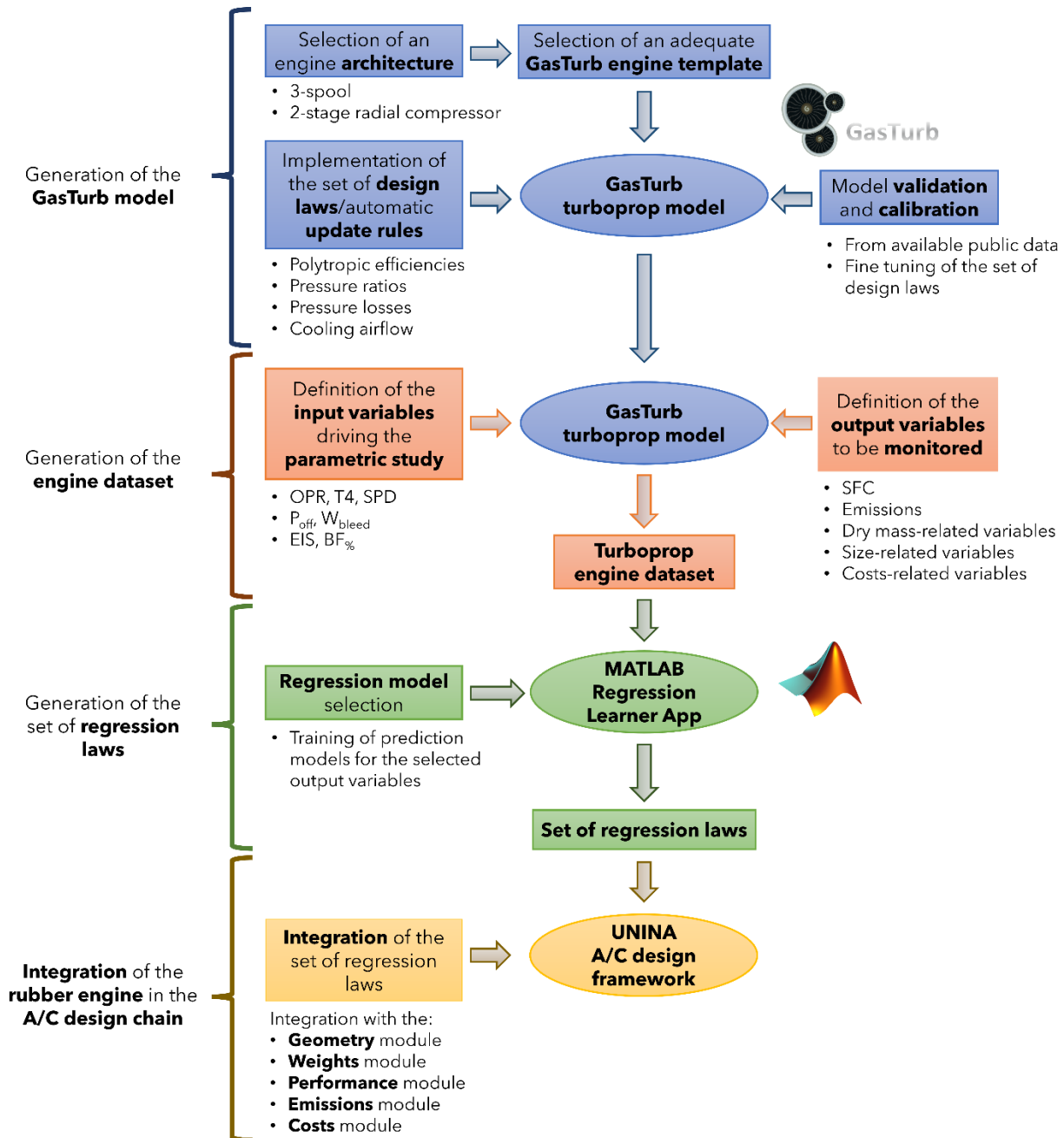
Figure 39. Set of steps elaborated for the development of a new tool for the rubberization of gas turbine engines for turboprop applications.

In order to match the objectives of GENESIS in terms of analysis of the gas turbine technology for the three time perspectives selected for the project, the rubber engine model implemented in GasTurb first, and then the surrogate engine model included in the aircraft design chain, were made sensitive to improvements in terms of technology level. This was accomplished by:

- Linking the efficiencies of the radial compressors, of the axial turbines and of the burner to one of the input variables, set as the expected entry into service (EIS) of the engine. This link was created thanks to the adoption of several prediction models, essentially gathered from [80] and [81]. A description of these models was already provided in D2.1.
- Linking the efficiencies of the radial compressors and of the axial turbines to an additional input variable, set as the technology level (f_{tech}). Again, this tie was created starting from the statistical data reported in [82], and details of its application were provided in D2.1.
- Linking the required amount of cooling air by each turbine stage to the characteristics of their materials (i.e., essentially maximum allowable temperature) and to the characteristics of the cooling system (i.e., the type of cooling technology adopted for the blades of each rotor and stator stage). Turbine materials characteristics (both for currently adopted materials and more advanced solutions) were mainly collected from [83] and [84]. Whereas distinct values of cooling efficiency were gathered from [85], which also provided the methodology for the estimation of the required amount of cooling air, based on output data coming from the thermodynamic cycle in terms of cooling air and hot gas temperatures. The abovementioned characteristics of the cooling system were linked to the input variable f_{tech}.

As previously mentioned, a detailed description of the overall methodology for gas turbine modelling was already presented in D2.1. The following sub-sections focus on providing an overview of some major modifications and additions that were implemented after the finalization of D2.1. It should be highlighted that the modifications just slightly affected the results that were presented in the first deliverable regarding the short-term scenario. And that these modifications were applied in order to generate more reasonable results for each time horizon. Nonetheless, the effect of these modifications on the predictions for the first scenario of GENESIS is accounted in section 4.3.

4.2.1. GasTurb-implemented rubber engine model

In order to simplify the subsequent integration in the aircraft design chain of a surrogate model based on the rubber engine model implemented in GasTurb, the number of input variables required by the model was reduced from eight to seven, by tying the f_{tech} variable to the EIS one and by slightly recalibrating some of the original assumptions reported in D2.1. This led to the set of input parameters of the model reported in Table 25. In this way, for each time perspective of GENESIS, there is now one and only choice in terms of:

- Normalized polytropic efficiency (i.e., the starting value depending on average stage loading, which is then eventually corrected for engine size, Reynolds number, EIS, and cooling air) of the turbines, polytropic efficiency of the radial compressors;
- Maximum allowable material temperature of cooled and uncooled turbine stages;
- Cooling factor (i.e., the c_{cool} parameter of D2.1, setting the efficiency of the cooling system) of cooled turbine stages.

Dealing with the last two items, Table 26 and Table 27 provide the new assumptions regarding their values. Table 26 links a specific material to each time horizon (last column), and also provides the original assumptions in terms of the f_{tech} variable reported in D2.1 (penultimate column). The usage of single crystal superalloys was supposed for the stators and rotors of the HP and LP turbines of the short and medium-term scenarios. Whereas ceramic matrix composites (CMC) were supposed to be applicable for the long-term. Similarly, Table 27 links a specific technology for cooling air flow to each of the scenarios investigated in GENESIS.

Finally, for the polytropic efficiency of the turbomachineries, almost identical assumptions were performed in terms of binding between the f_{tech} variable and the expected EIS of the engine. It should be remarked here that, according to the methodology reported in D2.1, the f_{tech} variable impacted the calculation of the normalized polytropic efficiency of the turbines and the polytropic efficiency of the

compressors, leading to different values (higher values of the technology factor implied higher values of the efficiency) for the same average stage loading.

Table 25. Updated set of input variables of the surrogate gas turbine engine model of GENESIS.

Input variable	Symbol/Abbreviation	Unit
Shaft power delivered	SPD	kW
Burner exit temperature	T_4	K
Overall pressure ratio	OPR	-
Power off-takes	P_{off}	kW
Overboard bleed	W_{bleed}	kg/s
Biofuel blending ratio	$BF_\%$	%
Entry into service	EIS	year

Table 26. Maximum limiting temperature assumptions for the calculation of the required amount of cooling air, mainly assumed from [83] and [84].

	Maximum temperature (uncooled)	Maximum temperature (cooled)	f_{tech} (as in D2.1)	EIS
Inconel 792	1250 K	1550 K	0.2	Reference (1990)
PWA 1480	1300 K	1750 K	0.4	2030 (short-term)
PWA 1492	1350 K	1950 K	0.6	2040 (medium-term)
CMC	1400 K	2050 K	0.8	2050 (long-term)

Table 27. Cooling factor reference values, according to [85], adopted to define a technological trend within the GasTurb rubber engine model.

	Cooling factor c_{cool}	f_{tech}	EIS
Film with convection (50-75 % trailing edge ejection)	1.25	0.2	Reference (1990)
Film with convection (25 % trailing edge ejection)	1.1	0.4	2030 (short-term)
Transpiration with convection	0.9	0.6	2040 (medium-term)
Transpiration	0.8	0.8	2050 (long-term)

Dealing with the remaining variables that were affected by f_{tech} in the original methodology reported in D2.1, namely:

- Burner pressure losses,
- Inter-ducts pressure losses,
- Spools mechanical efficiencies,

constant values, i.e., independent of the expected EIS of the engine, were assumed for the three time scenarios of GENESIS. This occurred since, from a closer analysis of the original approach, it was determined that it would have been more reasonable to unbind those variables from the EIS/f_{tech} dependency. In fact, even from statistical data reported in [86], there seems not to be a clear link between the burner pressure loss and the technology level of the gas turbine (at least from a certain EIS on). Whereas the information reported in [72] mostly links the inter-ducts pressure losses to the average Mach number, and the spools mechanical efficiency to the type of bearings. Nonetheless, values comprised between the plausible ranges for these variables indicated in D2.1 were adopted:

0.985 for the pressure losses along the compressors and turbines ducts, 0.99 for the pressure loss at the free turbine exit duct, 0.96 for the burner pressure loss, and 0.995 for the mechanical efficiencies of the spools.

As a further improvement to the original approach presented in D2.1, it was supposed that, at least for the medium-term and long-term scenarios, also the rotor and stator stages of the LP turbine could be eventually cooled, allowing to reach much higher T_4 values, thus higher core efficiency and lower SFC. In case of cooled LP turbine stages, the values reported in the second column of Table 26 (cooled maximum temperatures) would be used to perform a feasibility check on the temperature at the entry of the power turbine.

No other major modifications occurred with respect to the set of design laws and update rules that were implemented directly into GasTurb and that were already documented in D2.1. Here there is a brief recap:

- The approach suggested in [86] was adopted for the estimation of the efficiencies (polytropic) of the turbines.
- Statistical data reported in [86] were used to determine the pressure split between LP and HP radial compressors, whereas the set of equations reported in [72] was used to set the efficiencies (polytropic) of the radial compressors, as well as the rotational speeds of the spools.
- The approach described in [85] was implemented for the estimation of the amount of relative cooling air for the turbines.

4.2.2. Powerplant system mass calculation

Dealing with the dry mass of the engine, the approach reported in D2.1 was improved, to allow the inclusion of the effect of additional input parameters in the calculation. A reference dataset, including an increased number of engines with respect to those used for the generation of the semi-empirical approach of D2.1, was considered. This dataset was derived from data provided in [87]. A correlation was found between the dry mass of a turboprop engine (also including the contribution of the gearbox) and a custom parameter, defined as:

$$P_{eng} = W_2^{1.15} \cdot OPR^{0.1} \cdot SPD^{0.3},$$

in which P_{eng} is the engine dry mass parameter, W_2 is the engine entry mass flow rate given in kilograms per second, OPR is the engine overall pressure ratio, and SPD is the maximum shaft power of the engine expressed in kilowatts. This correlation reads as:

$$M_{eng} = -2 \cdot 10^{-10} \cdot P_{eng}^4 + 1.36 \cdot 10^{-6} \cdot P_{eng}^3 - 3.39 \cdot 10^{-3} \cdot P_{eng}^2 + 3.53 \cdot P_{eng} + 37.7 \ (P_{eng} \leq 700),$$

$$M_{eng} = 1.7 \cdot P_{eng} - 1610 \ (P_{eng} > 700),$$

in which M_{eng} is the dry mass of the engine expressed in kilograms. A visual representation of this regression law is provided in Figure 40. With this new approach, the dry mass of the engine is not affected by the entry mass flow rate only, but also by the shaft power and by the pressure ratio. Thus, two engines with the same characteristics in terms of entry mass flow rate and OPR but different maximum power output will weigh differently. Similarly, two engines with the same entry mass flow rate and power but different OPR will also have a different weight, which is physically motivated.

To estimate the mass of the reduction gearbox of the gas turbine, which, according to preliminary analyses, will be always required to reduce the rotational speed of the output spool to acceptable values for the propellers, the semi-empirical equation provided in [88] was adopted. This equation was developed at NASA by means of actual gearbox weight data coming from different types of aircraft (e.g., rotorcraft, tiltrotors and airplanes) and links the weight of the gearbox to a parametric value, expressed as:

$$P_{gbox} = (SPD/RPM_{out})^{0.75} \cdot (RPM_{in}/RPM_{out})^{0.15},$$

in which P_{gbox} is the gearbox mass parameter, RPM_{in} is the free spool rotational speed, and RPM_{out} is the propeller rotational speed, both expressed in routes per minute. At this point, the mass of the gearbox can be written as:

$$M_{gbox} = -37.4262 + 116.3297 \cdot P_{gbox},$$

where M_{gbox} is the mass of the gearbox given in pounds.

For the calculation of the masses of the remaining gearboxes of the powerplant, eventually required to reduce the rotational speed of the electric motors, the equations reported in [89] were adopted:

$$W_{e-gbox} = a \cdot T_{e-eng} + b,$$

in which W_{e-gbox} is the weight in kilograms of the gearbox of the electric motor, T_{e-eng} is the torque of the electric motor expressed in Nm, and:

$$a = -0.001647 \cdot (RPM_{in}/RPM_{out})^2 + 0.03692 \cdot (RPM_{in}/RPM_{out}) - 0.05811,$$

$$b = -0.490700 \cdot (RPM_{in}/RPM_{out})^2 + 7.64900 \cdot (RPM_{in}/RPM_{out}) - 13.5000.$$
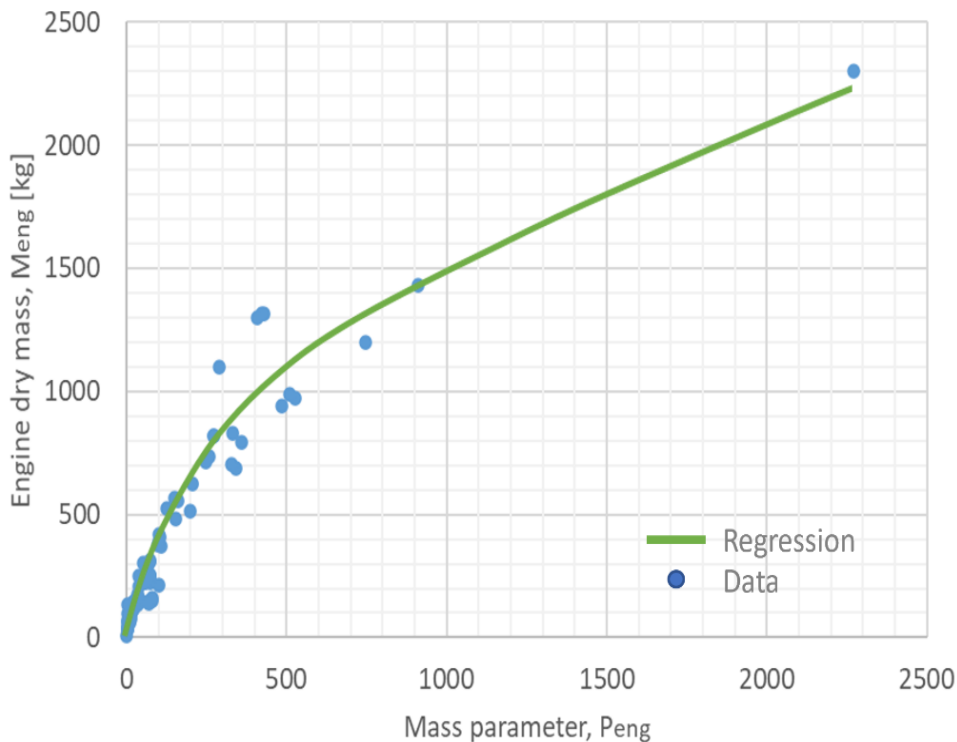
Figure 40. Updated engine dry mass regression law, along with reference data from the literature [87].

For the propeller mass, the equation reported in [90] was considered:

$$W_{prop} = K_p \cdot N_{blades}^{0.391} \cdot \left(d_{prop} \cdot SPD/1000\right)^{0.782},$$

where: W_{prop} is the mass of the propeller expressed in pounds, K_p is a parameter essentially depending on the shaft power of the engine, N_{blades} is the number of blades of the propeller, and d_{prop} is the propeller tip diameter given in inches. SPD should be expressed in imperial units (horsepower) as well. This equation can be reasonably applied to the propellers of both the thermal and the electric motors.

Dealing with the fuel system mass, the equation suggested in [91] was adopted:

$$W_{fuel-sys} = 2.405 \cdot V_t^{0.606} \cdot (1 + V_i/V_t)^{-1.0} \cdot \left(1 + V_p/V_t\right) \cdot N_t^{0.5},$$

in which: $W_{fuel-sys}$ is the mass of the fuel system given in pounds, V_t is the total fuel volume expressed in gallons, V_i is the overall volume of integral tanks given in gallons, V_p is the self-sealing tanks volume also given in gallons, and N_t is the number of fuel tanks. For the applications considered for GENESIS, integral fuel tanks (i.e., the fuel tank volume is provided by the sealed wing structure) are going to be considered.

Finally, the mass of the nacelle, both for thermal and electric machines, can be approximated by the following equation, taken from [92], which is valid for wing-mounted nacelles:

$$W_{nac} = 6.5 \cdot SPD,$$

in which W_{nac} is the nacelle weight given in pounds, and SPD is expressed in horsepower.

4.2.3. Powerplant system size calculation

In some circumstances, especially for high rotational speeds of the free turbine, the dimensions of the thermal engine nacelle could be driven by the gearbox size, rather than the gas turbine dimensions. In D2.1, an *almost* component-based approach was proposed for the estimation of the gas turbine width and height, relying on the calculation of the tip diameters of the LP radial compressor and of the power turbine. In order to improve this approach, the estimation of the maximum width and height of a split torque double reduction gearbox, like the one used by the PW127 engine, was implemented, by following the semi-empirical approach outlined in [93].
This approach is essentially based on a chart relating the output torque of each stage of the gearbox to the center distance between spur gear reducers. This allows to perform an approximate but rather realistic estimation of the final size of the gearbox, and to correctly size the thermal engines nacelles.

With regards to the gearboxes of electric motors, the usage of single or double-stage planetary gears can be supposed, leading to reduced volume requirements. For this reason, it could be still reasonable to size the nacelles of the electric motors based on the dimensions of the electric units.

4.2.4. Powerplant system costs calculation

An approach for a rough estimation of production cost, development cost and development time was reported in D2.1, based on the methodology for military turbojet and turbofan engines illustrated in [94]. This approach required the application of a strong calibration based on the f_{tech} variable, as well as the introduction of an assumption regarding the profit margin, in order to obtain reasonable prices for a turboprop engine.
In order to overcome this issue, the approach reported in [95] was selected as an alternative to the engine cost-related equations already included in D2.1. This approach allows to calculate the price of a turboprop engine according to the following equation:

$$EP_{year} = CEF_{1989-year} \cdot 10^{[2.5262+0.9465 \cdot log_{10}(SPD)]} \ (SPD < 5000 \ hp)$$

where EP_{year} is the engine price at the selected year in US dollars, and $CEF_{1989-year}$ is the cost escalation factor, which can be calculated as the cumulative inflation rate from 1989 (the reference year for which the above equation was determined) to the selected year. Engine shaft power should be provided in horsepower. The above equation should be valid for ranges of SPD between 400 and 5000 hp. According to [95], the prices estimated with this formula include the price of the gearbox, but not the one of the propellers.

However, the same reference also provides a similar equation for estimating the price of the engine rotor. Due to the lack of sufficient data, this relationship does not take into account the number of propeller blades, but the engine SLS T/O power alone again:

$$PP_{year} = CEF_{1989-year} \cdot 10^{[0.7746+1.1432 \cdot log_{10}(SPD)]} \ (200 \ hp < SPD < 20000 \ hp)$$

in which PP_{year} is the propeller price at the selected year in US dollars. This equation in particular applies to composite propellers, for engine power values comprised between 100 and 20000 hp.

4.3.   Amendment to the short-term results

In light of the modifications applied to the methodology and discussed above, the results provided for the short-term scenario (2025-2035, with 2030 as the representative year) were checked again, leading to the minor updates reported in Table 28. As for the previous analyses (i.e., the ones reported in D2.1) it was assumed:

- OPR equal to 18, for reasons linked to technology limitations (higher pressure ratios of the radial compressors are theoretically possible, but are not easy to achieve and may result in a high decrease of the efficiency), NO_x emissions (the higher the OPR, the higher the NO_x EI, the higher the grams of NO_x emissions per kilograms of fuel burn), and core efficiency gain (the increase in weight and complexity of the engine due to the higher OPR may not justify the possible further decrease in terms of SFC).
- Burner exit temperature set as the maximum allowable value compatible with the limitations provided in Table 26, and assuming a -30 K safety margin for the temperature of the uncooled turbine stages, to guarantee about 35000 life hours to the blades airfoils according to [96]. For the selection of a feasible sizing point of the engine, mechanical and design limitations already listed in D2.1 were accounted as well.
- Maximum SLS T/O power equal to 1800 kW, as indicated by preliminary analyses for the short/medium-term scenario performed by WP1.
- Power off-takes equal to 14 kW and overboard bleed equal to 0.25 kg/s, as for the reference aircraft.
- Biofuel blending ratio from 0 to 100 %.
- EIS 2030.

In this case, the analysis was carried out for a single hypothesis on the technology level f_{tech}, which was assumed equal to 0.4 for this 2030 EIS, in line with the considerations reported in the previous sections. Only the stator and the rotor of the HP turbine were supposed to be cooled, in accordance with the hypothesis on the short-term scenario reported above.

Table 28 shows how the gas turbine engine of the short-term scenario would guarantee SFC reductions (SFC values are for SLS T/O rating) between 20 and 22 %, depending on the selected blending ratio of conventional kerosene with biofuel. As already stated in D2.1, the fuel blending ratio would have a very limited impact on engine key characteristics other than power-specific fuel consumption, and for this reason only the effect on this variable was reported in Table 28. The mass and the size of the engine benefit from the improvements in terms of turbomachineries efficiency and cooling system technology and materials. The price of the engine, reported in 2022 US dollars, is now much more in line with expectations (the PW127, which has a maximum SPD close to the value considered here, had a price tag of $920,000 US in 2010 [97], without the need of further calibrations. No further assumptions were performed for the short-term scenario in terms of f_{tech}, as anticipated. More optimistic hypotheses on the turbomachineries efficiencies, on the cooling technology and on the turbine materials were retained for the medium and the long-term scenarios.

Table 28. Short-term updated results for the gas turbine engine.

Variable	Short-term	Reference (PW127)	% Difference
SFC (0 % biofuel)	0.2436 kg/(kWh)	0.3080 kg/(kWh)	-20.91 %
SFC (50 % biofuel)	0.2415 kg/(kWh)	-	-21.60 %
SFC (100 % biofuel)	0.2393 kg/(kWh)	-	-22.30 %
Engine dry mass	379 kg	481 kg	-21.22 %
Engine max. diameter	655 mm	770 mm	-14.93 %
Engine price (2022)	M$1.24 US	-	-

4.4. Medium-term preliminary analysis

By following the example of the short-term analysis, a similar one was carried out for the medium-term scenario. Assumptions were performed regarding the input values of the surrogate engine model created with GasTurb and through the MATLAB Regression Learner App:

- An OPR value equal to 19 was selected. This choice derived from assuming to have an improvement in terms of compressor group technology with respect to the 2030 EIS engine. The same considerations reported in the previous section were of course accounted.
- Maximum SLS T/O power was taken equal to 1800 and 1400 kW, in accordance with the requests coming from the WP1 for the preliminary analyses on the medium and long-term horizons.
- For the power off-takes and the overboard bleed, the same values used for the short-term case, corresponding to the assumed values valid for the reference aircraft, were applied.
- Blending ratios up to 100 % of conventional kerosene with biofuel were considered.
- The EIS was set to 2040.

As for the short-term analysis, the burner exit temperature was determined as the maximum reachable temperature, compatible with both limitations of Table 26 regarding maximum cooled and uncooled material temperatures. The same assumptions reported in the previous section regarding the turbine blade airfoils life was also performed in this case. Unlike the short-term analysis, the stator and rotor stages of the LP turbine were assumed to be cooled, adopting the same materials and cooling technology of the HP turbine. For the power turbine, the material characteristics of Table 26 were used as well.

In addition to thermal limitations, mechanical constraints linked to circumferential tip and average speeds of compressors and turbines (as reported in D2.1) as well as manufacturing considerations for radial compressors (also included in the same deliverable), were checked during the selection process of the design point.

Table 29 provides the results for the first analysis, carried out for an SPD value equal to 1800 kW. This engine provides an SFC reduction (still estimated for SLS T/O rating) comprised between 26 % and 28 %, with respect to the PW127 model, depending on the biofuel blending ratio. This reduction is approximately 5 % greater than the one granted by the short-term model. Moreover, it is worth to highlight that the direct impact of biofuel blending on the SFC is not affected by other parameters than the blending ratio itself. In fact, the effect of $BF_\%$ remains the same, if differences in Table 28 and Table 29 for different blending ratios are compared: a $BF_\%$ equal to 50 % grants an SFC reduction of about 0.6 % with respect to conventional kerosene, whereas a 100 % blending (i.e., pure biofuel) leads approximately to 1.3 % reductions.

The engine dry mass would benefit from a further reduction with respect to the short-term engine, due again to the effect of improvements to the turbomachineries efficiencies and to the cooling system

technology. The same consideration also applies to the engine size. It should be noted that for this analysis, the size of the gearbox (which was estimated supposing a rotational speed of the propellers equal to 1200 rpm, as for the reference engine and aircraft) is still not the one sizing the transversal dimension of the engine, but it is quite close to be, due to the reduced size of the engine core.

Finally, with regards to the engine price, the same value of the short-term engine expressed in 2022 US dollars is obtained. This descends from the fact that the new adopted approach is not sensitive to any engine parameter other than the shaft power. This makes the engine price independent of any kind of consideration regarding the level of technology of the gas turbine. However, this approach actually returns price values close to the expected ones for the turboprop category. Moreover, it is reasonable to assume that the engine price should not be affected too much by assumptions regarding the level of the technologies, if these are applied for a time perspective for which it is reasonable to assume that they will be sufficiently mature.

Table 30 provides the results for the medium-term perspective, assuming a SLS T/O SPD value equal to 1400 kW. As expected, the SFC is slightly increased with respect to the case reported in Table 29, due to core size effect on efficiencies. Due to the lower request in terms of maximum shaft power, the dry mass, the engine maximum transversal dimension and the price are beneficially affected, with respect to the 1800 kW scenario. It is worth to mention that in this case the maximum diameter of the engine is actually driven by the gearbox size, rather than by the gas turbine transversal dimensions.

Table 29. Medium-term results for the gas turbine engine, for a SLS T/O shaft power of 1800 kW.

Variable	Medium-term	Reference (PW127)	% Difference
SFC (0 % biofuel)	0.2266 kg/(kWh)	0.3080 kg/(kWh)	-26.43 %
SFC (50 % biofuel)	0.2246 kg/(kWh)	-	-27.08 %
SFC (100 % biofuel)	0.2226 kg/(kWh)	-	-27.73 %
Engine dry mass	260 kg	481 kg	-45.95 %
Engine max. diameter	530 mm	770 mm	-31.17 %
Engine price (2022)	M$1.24 US	-	-

Table 30. Medium-term results for the gas turbine engine, for a SLS T/O shaft power of 1400 kW.

Variable	Medium-term	Reference (PW127)	% Difference
SFC (0 % biofuel)	0.2333 kg/(kWh)	0.3080 kg/(kWh)	-24.25 %
SFC (50 % biofuel)	0.2313 kg/(kWh)	-	-24.90 %
SFC (100 % biofuel)	0.2293 kg/(kWh)	-	-25.55 %
Engine dry mass	203 kg	481 kg	-57.80 %
Engine max. diameter	490 mm	770 mm	-36.36 %
Engine price (2022)	M$0.98 US	-	-

4.5. Technology readiness level assumptions

Gas turbine engine is a mature technology, adopted on airplanes since the 1940s. Low technology readiness levels can be assumed for gas tubine concepts implementing disruptive core technologies, which are not considered for the thermal engines of GENESIS. The expected improvements of this technology, according to the scalable model described in the previous sections, can be addressed to:

- An improvement of the aerodynamics of the blades of the compressors, leading to improved performance of the whole compressors group, which should imply higher OPR values and higher efficiency.
- The use of high technology materials for the turbines, which allows to increase the operating temperatures and the thermal efficiency of the engine.
- The implementation of more sophisticated cooling concepts, which allows to reduce the relative amount of air needed to cool the stator and rotor stages of the turbines.
- An improvement of the aerodynamics of the blades of the turbines, allowing to increase the efficiency of the turbines group.
- Improvements in the manufacturing of the turbomachineries, granting reduced tip clearances and improved efficiency.

The technologies enabling for the abovementioned improvements are already available, and some of them are already applied on high-end gas turbines for turbofan applications (i.e., CFM International LEAP-1, Pratt & Whitney PW1000, General Electric Aviation GEnx families of turbofan engines). For this reason, it is appropriate to assume high TRL values for the gas turbine engine concepts of GENESIS. These values are reported in Table 31 for the short and medium-term scenarios. The first column of this table provides the current TRL. The second column indicates the expected TRL by each GENESIS timeframe. A slightly lower TRL, comprised between 7 and 8, is indicated for the gas turbine engines of the medium-term scenario, warranted by the assumed lower readiness level of its materials, compressors and turbines design, cooling technology, and manufacturing.

Table 31. TRL assumptions for the gas turbine engines of the short and medium-terms scenarios of GENESIS.

TRL assumptions	Today's TRL	Expected TRL
Short-term (2025-2035)	8	8 - 9
Medium-term (2035-2045)	7-8	8 - 9

4.6. Conclusions

The previous sections provided a brief description of the approach that was defined and adopted, to model the set of advanced gas turbine engines for turboprop applications to be equipped on the hybrid-electric aircraft of GENESIS. The surrogate engine models built with this approach are sensitive to technology changes, linked to the expected EIS of the advanced aircraft.

In order to improve the approach, several modifications and additions were implemented during the past months. Section 4.2 included a description of these improvements, to provide an update with respect to the information already reported in D2.1.

In light of these modifications, the results for the short-term analysis were corrected and reported in section 4.3.

Section 0 provided the results for the medium-term analysis, which is the main outcome of this chapter. These results already took advantage of the improvements applied to the engine preliminary design methodology. Two different hypotheses were made regarding the shaft power request to the engine, leading to different results in terms of engine SFC, dry mass, transversal size, and price. For the highest SPD request, an SFC reduction greater than 25 % was predicted, with respect to nowadays engine. Sensible reductions were predicted also in terms of size and weight, which will allow the aircraft models of the medium-term scenario to benefit even further from the application of these new engines. Slightly lower values in terms of SFC reduction were predicted for the engine model with the lower power request, but this downside is followed by a reduced mass and size, which could compensate for the previous negative effect at aircraft level.

5. Power electronics technology analysis

5.1. Introduction

This chapter deals with the medium-term (2035-2045) technology analysis for all power electronics converters in the GENESIS project. In this report, two different scenarios are examined and explained more in detail. The GT/hybrid scenario still considers the gas turbine (GT), the FC/hybrid scenario describes the power electronics in the aircraft when the gas turbine is replaced by a fuel cell system. Figure 41 shows the basic electric architecture of the regional aircraft and all possible existing power electronics converters for the first scenario with a gas turbine.
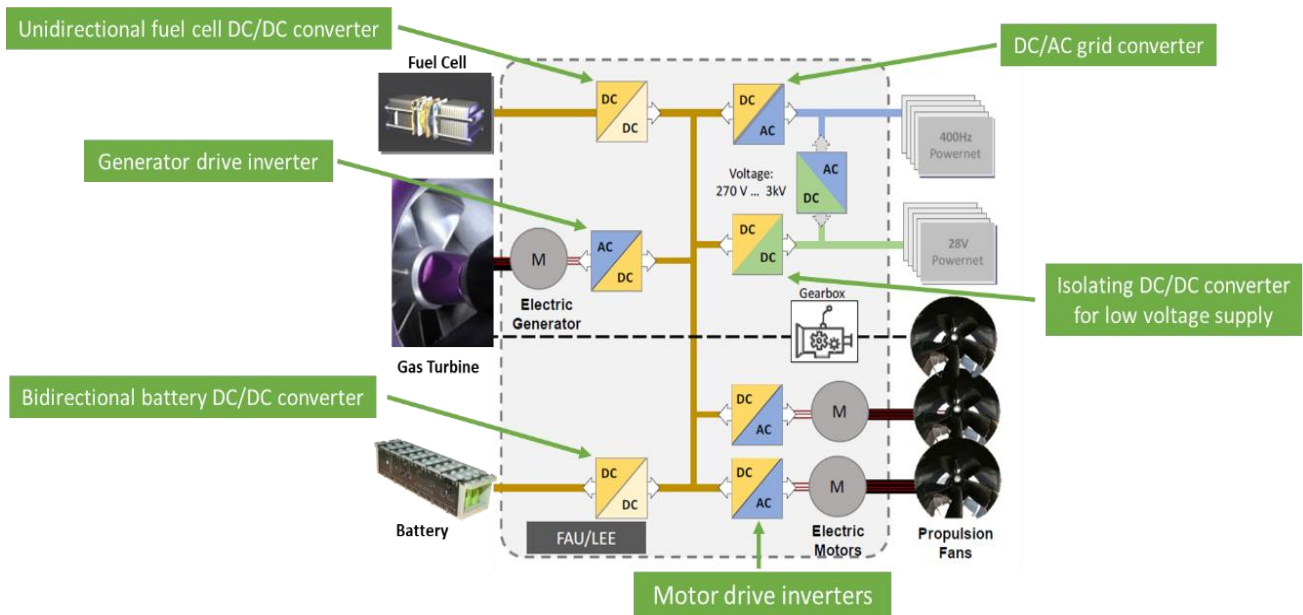
Figure 41. Overview of possible power electronics converters for all time frames

Scenario with the gas turbine (GT):

The electric generator (primary electric machine) is driven by the gas turbine and converts mechanical power into electrical power. The output voltage of the electric generator is actively rectified by the generator drive inverter, which will supply the internal (high voltage) HV DC bus. For the HV DC bus, a voltage between 270 V and 3 kV is conceivable. This topic is analyzed in depth in Chapter 5.2 and the end, also a voltage of 800 V was chosen for the medium-term horizon like in the short-term. The generator and motor inverters drive the primary and electric motors by generating sinusoidal currents. The electric motors convert electrical into mechanical power and drive the propulsion fans to generate thrust. The bidirectional battery DC/DC converter transfers in the medium-term time frame power between the battery pack with a maximum voltage of 681 V and the internal 800 V DC bus. Depending on the power flow direction, the bidirectional battery DC/DC converter charges or discharges the battery pack. The DC/AC grid converter transfers power from the internal 800V DC bus to the 400 Hz Powernet, which is used to power different aircraft electric consumers like heaters and hydraulic pumps. The isolating DC/DC converter for low voltage supply transfers power from the internal 800V DC bus to the 28 V powernet. Depending on the redundancy concept of the aircraft, there could also be an AC/DC grid to low voltage (LV) converter. It can transfer power directly between the 400 Hz and 28 V Powernet if there is an outage of the DC/AC grid converter or the isolating DC/DC converter for low voltage supply. For the medium-term report, the AC/DC grid to LV converter is neglected because, at the moment, it is planned to have two DC/AC grid converters and two isolating DC/DC converters for low voltage supply. So, a single outage of a converter can already be compensated.

Scenario with the fuel cells (FC):

For the fuel cell scenario, the electric generator (primary electric machine) is not needed anymore as the fuel cell will supply the internal (high voltage) HV DC bus. Five e-drive electric machines are assumed which will provide the same power for five propellers. For the HV DC bus, a voltage between 270 V and 3 kV is also in the FC/hybrid scenario conceivable however a voltage of 800 V was chosen for the medium-term horizon. The functionality of the motor inverters is the same as in the GT/hybrid scenario, with the difference that no generator is needed anymore. The electric motors convert electrical into mechanical power and drive the propulsion fans to generate thrust. The bidirectional battery DC/DC needs approximately 200 kW less power in the scenario for the FC because the FC power for each wing is in the second scenario higher than in the scenario with the GT. The maximum voltage of the battery is also 681 V and the internal 800 V DC bus is the same as in the first scenario. Depending on the power flow direction, the bidirectional battery DC/DC converter charges or discharges the battery pack. The power flow of the FC is unidirectional to the HV DC bus. The DC/AC grid converter and the isolating DC/DC converter for low voltage supply have the same parameters and workspaces as in the scenario with the GT. Table 32 shows the considered power electronics components for the medium-term horizon. It is assumed that all converters are like in the short-term horizon liquid-cooled to increase the power density.

Table 32. Power electronics components for the medium-term period

Power electronics component	Number of units	Reference power in kW
Generator drive inverter (Scenario GT)	2	1200
Motor drive inverter	8	600
Bidirectional battery DC/DC converter (Scenario GT)	2	1185
Bidirectional battery DC/DC converter (Scenario FC)	2	900
Unidirectional fuel cell DC/DC converter (Scenario FC)	2	1407
DC/AC grid converter	2	30
Isolating DC/DC converter for low voltage supply	5	11.2

5.2. Choice of HV DC bus voltage

The internal HV DC bus voltage is a very important parameter for all power electronics converters. It influences many different topics, which are briefly discussed below. Four different voltage levels (800 V, 1500 V, 2000 V, 3000 V) have been chosen for the analysis. A HV DC bus voltage of 800 V is a popular choice for the newest battery electric vehicle (BEV) generation. Many experience and field data are already available for this voltage class. Higher voltage levels above 1 kV would be discussed by many aircraft manufacturers and also in the project, but there are safety concerns and empirical values are missing. Another reason is, that higher voltages aren´t very good for the efficiencies of power electronics and other components. The only advantage of a higher voltage is that less current is required for the same power demand. This advantage is only really noticeable through lower cable weights. Due to the continuous development of cables and the fact that superconducting cables may be used in the near future, it makes sense to keep the HV DC bus voltage at 800 V. The higher the HV DC bus voltage, the higher the creepage and clearance distances have to be. Consequently, the physical size of the power electronics converters can be negatively affected

if the creepage and clearances distances become too high as discussed for the short-term horizon in chapter 5.2 [98].

5.3. Choice of power semiconductors

The main components for all power electronic converters are power semiconductors. For low voltage applications, silicon (Si) Metal Oxide Semiconductor Field-Effect Transistors (MOSFET) and for high voltage applications, silicon Insulated-Gate Bipolar Transistors (IGBT) were used. Roughly ten years ago, the first wide bandgap (WBG) power semiconductors based on silicon carbide (SiC) and gallium nitride (GaN) came on to the market [99] [100].

SiC and GaN are wide bandgap materials with a comparably larger bandgap than other semiconductor materials. This enables the realization of transistors with high blocking voltages and low on-resistance, especially compared to silicon-based semiconductors. Table 33 compares the properties of the semiconductor materials Si, SiC, and GaN (see also Figure 42). The higher critical field of SiC and GaN underlines their usability at high voltages, the higher thermal conductivity of SiC facilitates the thermal management. SiC and GaN power semiconductors enable the realization of power electronic systems with the highest power densities, efficiencies, and switching frequencies. This is due to the significantly reduced switching and conduction losses of these wide bandgap semiconductors compared to state-of-the-art silicon-based IGBTs and MOSFETs.

Table 33. Comparison of material properties

Materials property	Si	SiC	GaN
Band gap (eV)	1.12	3.2	3.43
Critical field (10^6 V/cm)	0.3	3.0	3.3
Electron Mobility (cm^2/(Vs))	1500	700	2000
Peak Electron velocity (10^7 cm/s)	1	2	2.5
Relative Dielectric Constant	11.9	10	9.5
Thermal conductivity (W/(cmK))	1.5	3.7	1.3
Baliga Figure of merit – BFOM (W/ cm^2)	1	392*	1416*

*Normalized to Si
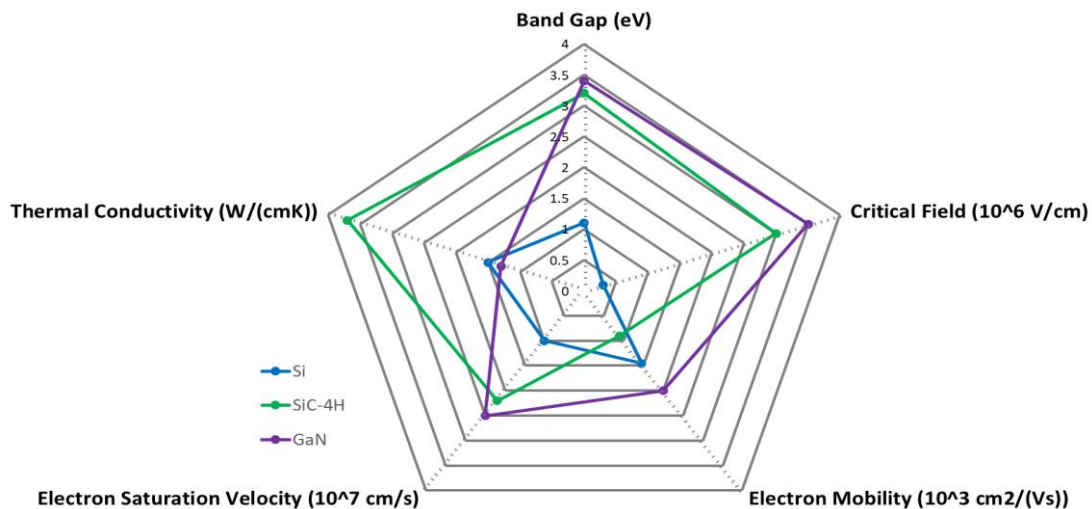
Figure 42. Comparison of material properties [98]

For the chosen 800 V DC bus voltage of the aircraft, it should be noted that only silicon IGBT can (normally) be considered for this voltage class. Silicon MOSFETs are only used for lower DC bus voltages. However, for wide bandgap materials, the situation is different. For these materials, power semiconductors are only used in a MOSFET structure nowadays. As of today, there is no GaN IGBT available, and there is some ongoing research work regarding SiC IGBTs and GaN IGBTs. Still, there is no commercial product available due to the intrinsic defects and immature fabrication process [101].

GaN is the newest class of market-available semiconductors with ongoing R&D work and technical improvement. All currently available GaN-transistors are lateral semiconductors as vertical GaN-technology is still in a research state with unknown readiness for market. The Baliga Figure of Merit (BFOM) is a unified performance metric for power semiconductor devices that takes into account the critical electric field and the mobility properties of the materials simultaneously. In Table 33 it can be seen very well that GaN is more than 1000 times better than Si and more than 3 times better than SiC. The BFOM value describes how well the component is able to operate at higher voltages and frequencies. The technology leap to vertical GaN would offer huge benefits like significantly reduced specific on-resistance, higher current densities, more even heat distribution, increased efficiency, and reduction in the size of passive components at a higher frequency. These advantages reduce overall the system size, weight, and costs. In order to take advantage of the full potential of GaN's material properties, homoepitaxially grown GaN substrates are a very good approach for the fabrication of vertical power devices. The main disadvantage of epitaxial growth of GaN on Si or SiC wafers arises from a lack of agreement between the lattice constants of the materials. This causes high stresses in the epitaxial layer. These high stresses, in turn, lead to defects in the crystalline structure known as dislocations. These dislocations alter and degrade the electrical properties of GaN and are the cause of low breakdown voltages and are often the cause of poor device reliability. Therefore, it would be best if GaN-on-GaN can be produced as in Table 34 to circumvent this physical barrier. However, GaN-on-GaN is still very expensive at this stage. For 2 inch GaN-on-GaN the costs are currently 55-93 €/cm². In comparison, an 8-inch GaN-on-Si costs about 1 €/cm² [102], [103].

Table 34. Comparison of different types of GaN substrate [9]

	GaN	GaN	GaN
Device Area →			
Carrier Wafer →	Si	SiC	GaN

Attribute	GaN-on-Si	GaN-on-SiC	GaN-on-GaN
Defect Density (cm^{-2})	10^9	5×10^8	10^3 to 10^5
Lattice Mismatch (%)	17	3.5	0
CTE Mismatch (%)	54	25	0
Layer Thickness (µm)	1-2	2-6	>40
Reliability	Low	LoW	High
Device Types	Lateral	Lateral	Vertical & Lateral

Transistors have three terminals, namely gate, drain and source. The source connection is the source of the electrons. At the gate terminal, the power flow (electron flow) between source and drain is controlled by creating a potential barrier for electrons. The electrons then arrive at the drain terminal accordingly. The $R_{DS,on}$ (Designation for the switch-on resistance or a minimum contact resistance of a field effect transistor) is specified between the drain and source, which determines the amount of current that can flow between the source and drain. The lower the $R_{DS,on}$, the more current can flow (simplified: Ohm's law). With the new GaN-on-GaN scheme, a junction-fet (JFET) transistor can be

built vertically, which is many times smaller than a lateral GaN-on-SiC transistor shown in the Figure 43. With the vertical design, the GaN buffer layer can be bypassed, as explained above. For the same $R_{DS,on}$, the GaN-on-GaN is 4 times smaller than a GaN-onSi at a breakdown voltage (BV) of 600V and 7 times smaller at a BV of 1200V. Due to the fact that no GaN-on-Si HEMT is specified above a BV of 650V, the estimation for 1200V is purely fictitious. The limitations are as follows. As soon as the reverse voltage of the device exceeds the breakdown voltage, the electric field becomes too large and displaces free charge carriers from the lattice during collisions. These displaced charge carriers generate new charge carriers when colliding with lattice atoms. This snowball effect causes a sudden increase of free charge carriers, which causes an avalanche breakdown [102], [103].
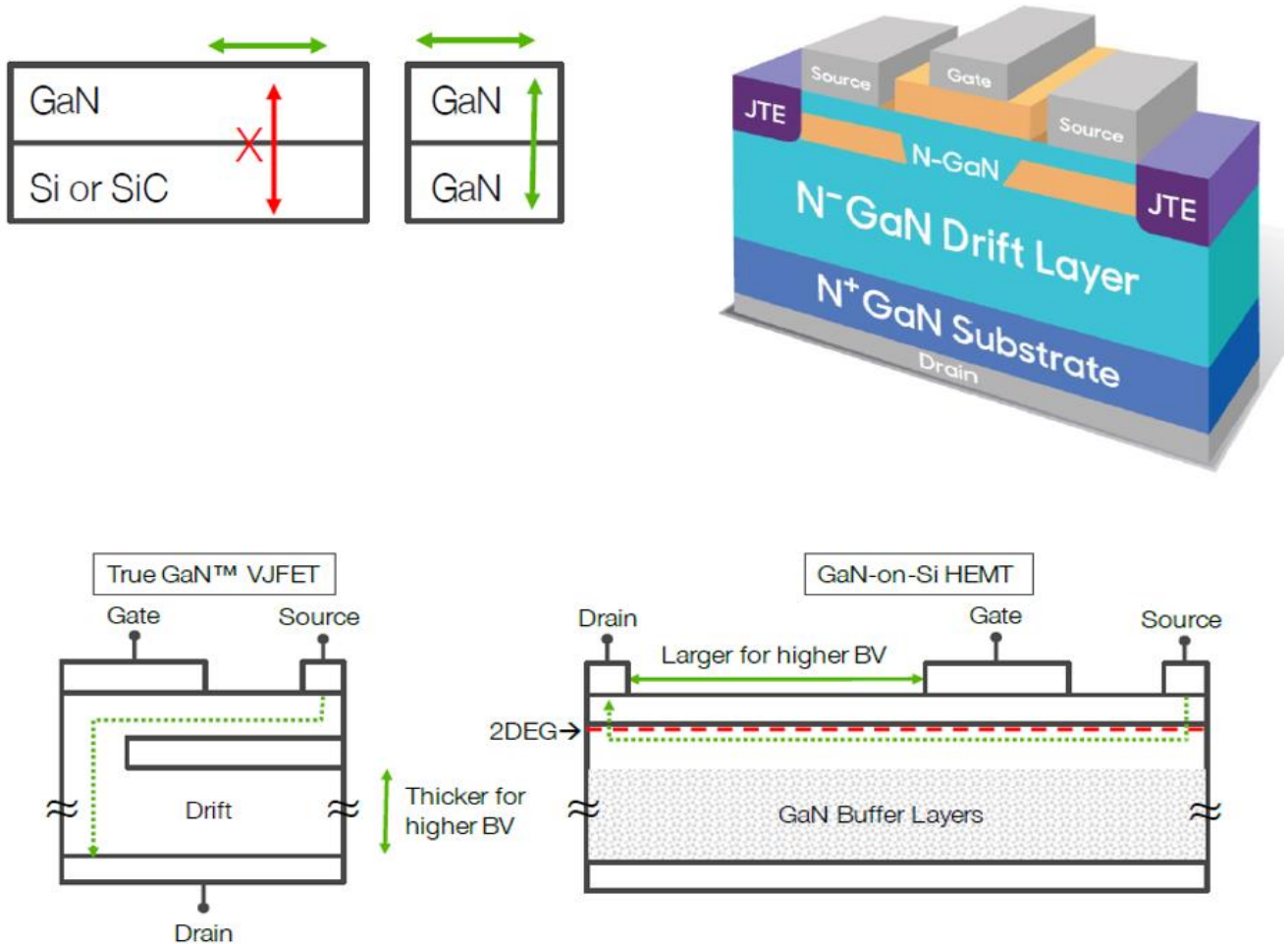
Figure 43. GaN-on-GaN vertical, schematic of an true GaN VJFET transistor [103].

Overall, the competitiveness of GaN will strongly depend on its technological advancement within the next years. If it is possible to replace silicon devices with GaN devices in the near future, it would be possible to build more compact converters with a much higher density, as the electron mobility in GaN is 10 times higher than in Si and 2.5 times higher than in SiC [103].

In Figure 44 is a performance comparison of true GaN VJFET with respect to other devices is shown. In this diagram, the BV is plotted over the $R_{DS,on}$. The ideal device would be in the lower right quadrant with a low $R_{DS,on}$ and a high BV. These measurements prove that GaN fulfils the best prerequisites for this and has a high justification for further research.
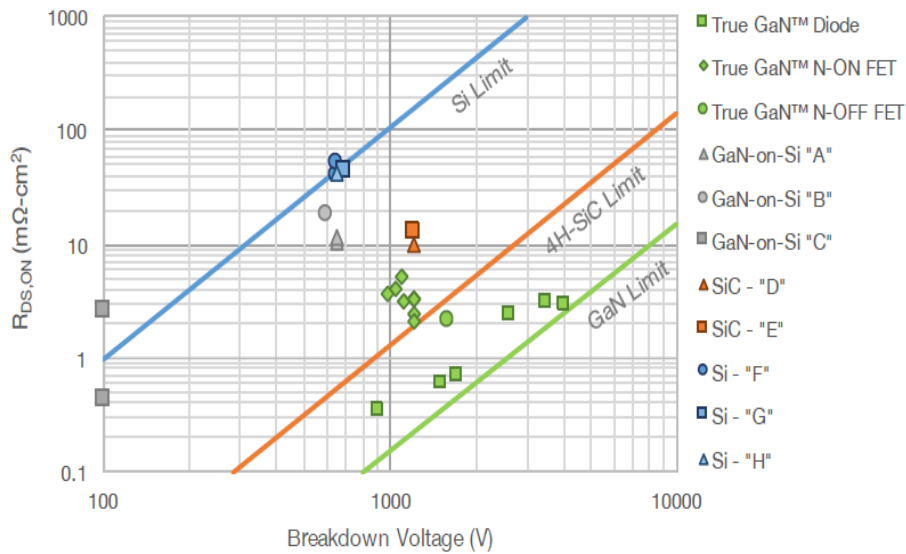
Figure 44. Performance comparison of true GaN with respect to other devices [103].

Today, only a few GaN devices are available with blocking voltages of 900 V and 1200 V. They cannot compete with Si and SiC devices regarding the specific on-resistance. Therefore, it was decided that for the medium-term (2035-2045) technology analysis, GaN devices are not considered in detail. But a rough estimate of the possible power density for the use of GaN devices in the converters is nevertheless given. For the long-term horizon, they will be an interesting alternative to SiC devices. SiC devices will be used for higher voltage, higher power, and medium frequency (<100 kHz) applications [104]. In addition, the new specifications for the GENESIS project were transferred to the converters and designed with the SiC MOSFETS already available on the market.

Overall, it can be concluded that silicon carbide and gallium nitride devices have many advantages regarding electrical properties compared to silicon devices (see Table 35). In view of the insufficient voltage and lack of components on the market, it can be concluded that for the medium-term analysis (2035-2045) in the GENESIS project, silicon carbide power semiconductors (SiC MOSFETs) are the best option for all power converters. However, as already mentioned a roughly estimation could provide for a power density with the GaN MOSFETS in the nearly future.

Table 35. Comparison of Si MOSFETs, Si IGBTs, and SiC MOSFETs properties [105]

Parameter	Si MOSFET	Si IGBT	SiC MOSFET	GaN MOSFET
Device type	unipolar	bipolar	unipolar	unipolar
Breakdown voltage	12 V to 650 V	400 V to about 12 kV	600 V to several kV	12V to 650 V
Current density	medium	high	very high	Very high
On-resistance $R_{DS(on)}$	medium	medium	low	Low
Conduction losses	medium	medium	low	low
Switching speed	high	low	very high	Very high
Switching losses	medium	high	low	Low
Cost	low	medium	high	Very high
Thermal conductivity	low	low	high	low

5.4. Motor and generator traction drive inverters

5.4.1. Introduction

This chapter deals with the technology analysis for the motor and generator traction drive inverters in the medium-term horizon. For the scenario with the GT is the same possibility as described in Chapter 6.3 of deliverable D.2.1 [98]. For the primary machines (generators), two secondary machines (motors) are stacked together and connected with a common rotor shaft. Accordingly, two motor drive inverters will be used as generator drive inverters. The secondary machine will be a six-phase machine, which will be driven by a six-phase motor drive inverter. The primary machine will be a two-times stacked six-phase machine, which will be driven by two six-phase motor inverters. For the scenario with the fuel cell, the secondary motors are sufficient and are therefore referred to as e-drive motors in the following. The calculation and simulation procedure can be found in D.2.1 in Chapter 5.4.2-5.4.4 [98]. In the medium term deliverable, only the results for the medium-term horizon are given and possible improvements are discussed.

First, the losses have been calculated and simulated for a three-phase inverter used in a classic three-phase motor system belonging to the secondary electric machines. Also, as in the D.2.1 the primary electric machines are supplied by two identical inverters, also used for the secondary electric machines. The analysis showed that, for this system configuration, two power modules per phase would have to be connected in parallel to reduce the losses and not to exceed the current capability of the power modules. To avoid the parallel connection of two power modules, it is also possible to use a six-phase motor system with two separated star points (see Figure 45). Half-bridges can be used as an example for the selection of devices, as described in the next chapter and presented in Table 36.
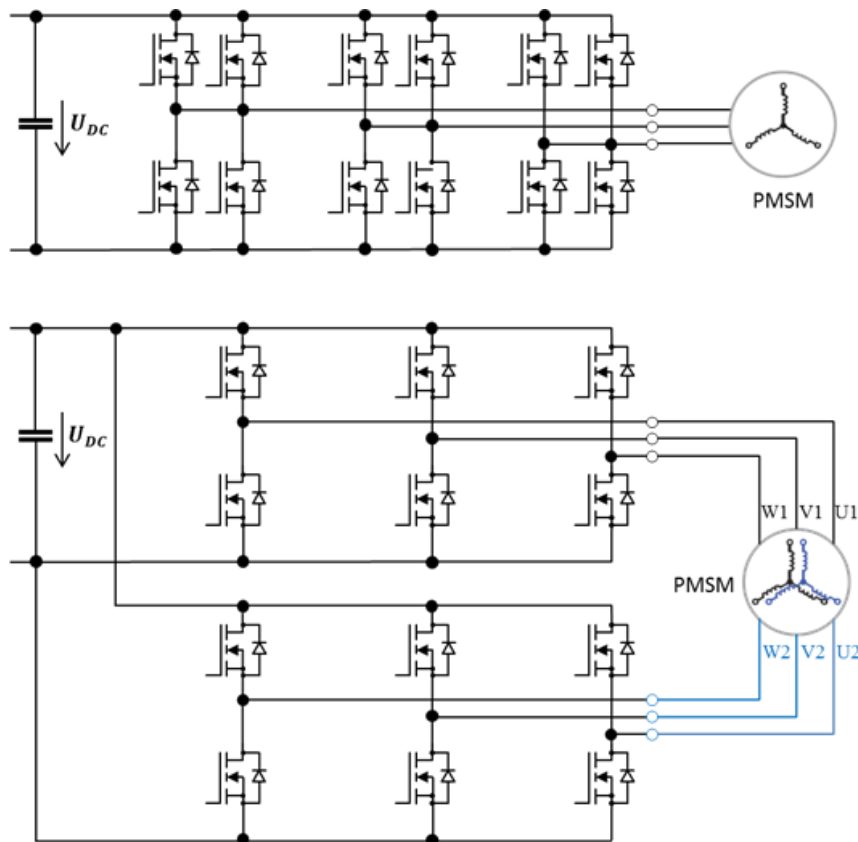
Figure 45. Three-phase topology with parallel devices (top) and six-phase topology (bottom)

5.4.2. Design results for the motor and generator inverter systems

The following tables are showing the results for the simulated power losses with the "SpeedFit Design Simulator" and the calculated DC link parameters for the motor inverters for the scenario with the GT and the FC. The secondary electric machines and the generator inverters for the primary electric machines for the first scenario are listed in Table 37 and Table 38. As explained in the introduction (Chapter 5.4.1), the generator inverter with a nominal power of 1200 kW consists of two motor drive inverters, each having a nominal power of 600 kW. Different SiC power modules were investigated, and the low-inductance half-bridge power module, CAB760M12HM3 from Wolfspeed (see Table 36), was chosen as the best option, because it is the best option today to simulate the inverter. The 6-phase motor inverter will consist of six half-bridge power modules, and the two-times 6-phase generator inverters will consist of twelve half-bridge power modules. For both inverter systems, efficiencies greater than 99 % can be achieved.

Table 36. Characteristics of half-bridge power module CAB760M12HM3 from Wolfspeed

Parameter	Value
Blocking voltage	1200 V
Current rating	765 A
On-resistance $R_{DS(on),25°C}$	1.33 mΩ
Turn-on switching energy $E_{on,25°C}$	20.3 mJ
urn-off switching energy $E_{off,25°C}$	17.9 mJ
Reference voltage U_{ref} for switching energies	600 V
Reference current I_{ref} for switching energies	760 A

Table 37. Results of technology analysis for secondary electric machine and inverter with 600 kW nominal power for medium-term horizon (2035-2045) - GT scenario

			Take off	Climb	Cruise	Data Origin
Secondary propeller	Definition	Mission time in min	0.34 / 0.37	21 / 24	12 / 97	from TLAR
	Mechanical power	$P_{Propeller}$ in kW	428	196	--	from TLAR
	Tourque	$T_{Propeller}$ in Nm	2044	936	--	from TLAR
	Rotational speed	$n_{Propeller}$ in rpm	2000	2000	--	calculated
	Efficiency	$\eta_{Propeller}$ in %	79	72	--	from TLAR
Secondary electric motor	Efficiency	$\eta_{Gearbox}$ in %	100	100	--	from TLAR
	Gearbox ratio	Gearbox ratio	1:1	1:1	--	determined
	Mechanical Power	$P_{Motor,mech}$ in kW	542	272	--	calculated
	Tourque	T_{Motor} in Nm	2587	1300	--	calculated
	Rotational speed	n_{Motor} in rpm	2000	2000	--	calculated
	Efficiency	η_{Motor} in %	96	96	--	from TLAR
	Motor configuration	Motor configuration	6-phase	6-phase	--	determined
Inverter for secondary electric motor	Inverter configuration	Inverter configuration	6-phase	6-phase	--	determined
	Electrical Power	$P_{Inverter,total}$ in kW	564	116	--	calculated
	Electrical Power	$P_{Inverter,3-phase}$ in kW	282	29	--	calculated
	Phase to phase current	$I_{LL,eff} = I_{str,eff}$ in A_{RMS}	376	39	--	calculated
	DC voltage	V_{DC} in V	800	800	--	determined
	DC current	I_{DC} in A_{RMS}	712	145	--	calculated
	Pulse-Width Modulation Switching frequency	f_{PWM} in kHz	20	20	--	determined
	Conduction losses	$P_{cond,total}$ in W	1996	235	--	simulated
	Switching losses	$P_{sw,total}$ in W	2900	32	--	simulated
	Inverter losses total	$P_{losses,total}$ in W	4896	267	--	simulated
	Efficiency	$\eta_{Inverter,total}$ in %	99.14	99.54	--	simulated
	Junction temperature	Tj in °C	132.7	68.7	--	simulated
	DC link capacitor capacity	$C_{DC-link,min}$ in µF	339	35	--	calculated
	DC link capacitor current	$I_{DC-link}$ in A_{RMS}	124	13	--	calculated

Table 38. Results of technology analysis for primary electric machine and inverter with 1200 kW nominal power for medium-term horizon (2035-2045) – GT scenario

			Take off	Climb	Cruise	Data Origin
Primary propeller	Definition	Mission time in min	0.34 / 0.37	21 / 24	12 / 97	from TLAR
	Mechanical power	$P_{Propeller}$ in kW	340	1266	1136	from TLAR
	Tourque	$T_{Propeller}$ in Nm	1624	6045	5424	from TLAR
	Rotational speed	$n_{Propeller}$ in rpm	2000	2000	2000	calculated
	Efficiency	$\eta_{Propeller}$ in %	60	81	81	from TLAR
Primary electric motor	Efficiency	$\eta_{Gearbox}$ in %	100	100	100	from TLAR
	Gearbox ratio	Gearbox ratio	1:1	1:1	1:1	determined
	Mechanical Power	$P_{Motor,mech}$ in kW	1130	121	156	calculated
	Tourque	T_{Motor} in Nm	5637	577	746	calculated
	Rotational speed	n_{Motor} in rpm	2000	2000	2000	calculated
	Efficiency	η_{Motor} in %	96	96	96	from TLAR
	Motor configuration	Motor configuration	2x 6-phase	2x 6-phase	2x 6-phase	determined
Inverter for primary electric motor	Inverter configuration	Inverter configuration	2x 6-phase	2x 6-phase	2x 6-phase	determined
	Electrical Power	$P_{Inverter,total}$ in kW	1185	116	150	calculated
	Electrical Power	$P_{Inverter,3-phase}$ in kW	271	29	38	calculated
	Phase to phase current	$I_{LL,eff} = I_{str,eff}$ in A_{RMS}	362	39	50	calculated
	DC voltage	V_{DC} in V	800	800	800	determined
	DC current	I_{DC} in A_{RMS}	1368	145	188	calculated
	Pulse-Width Modulation Switching frequency	f_{PWM} in kHz	20	20	20	determined
	Conduction losses	$P_{cond,total}$ in W	5528	235	437	simulated
	Switching losses	$P_{sw,total}$ in W	3555	32	74	simulated
	Inverter losses total	$P_{losses,total}$ in W	9083	584	511	simulated
	Efficiency	$\eta_{Inverter,total}$ in %	99.17	99.54	99.49	simulated
	Junction temperature	Tj in °C	128.5	68.7	72.1	simulated
	DC link capacitor capacity	$C_{DC-link,min}$ in µF	595	65	82	calculated
	DC link capacitor current	$I_{DC-link}$ in A_{RMS}	239	26	33	calculated

Table 39. Results of technology analysis for e-drive electric machine and inverter with 600 kW nominal power for medium-term horizon (2035-2045) - FC scenario

			Take off	Climb	Cruise	Data Origin
Propeller	Definition	Mission time in min	0.34 / 0.37	21 / 24	12 / 97	from TLAR
	Mechanical power	$P_{Propeller}$ in kW	304	316	289	from TLAR
	Tourque	$T_{Propeller}$ in Nm	1451	1509	1380	from TLAR
	Rotational speed	$n_{Propeller}$ in rpm	2000	2000	2000	calculated
	Efficiency	$\eta_{Propeller}$ in %	69	80	90	from TLAR
Electric motor	Efficiency	$\eta_{Gearbox}$ in %	100	100	100	from TLAR
	Gearbox ratio	Gearbox ratio	1:1	1:1	1:1	determined
	Mechanical Power	$P_{Motor,mech}$ in kW	441	395	321	calculated
	Tourque	T_{Motor} in Nm	2104	1886	1533	calculated
	Rotational speed	n_{Motor} in rpm	2000	2000	2000	calculated
	Efficiency	η_{Motor} in %	96	96	96	from TLAR
	Motor configuration	Motor configuration	6-phase	6-phase	6-phase	determined
Inverter for electric motor	Inverter configuration	Inverter configuration	6-phase	6-phase	6-phase	determined
	Electrical Power	$P_{Inverter,total}$ in kW	459	411	334	calculated
	Electrical Power	$P_{Inverter,3-phase}$ in kW	229	206	167	calculated
	Phase to phase current	$I_{LL,eff} = I_{str,eff}$ in A_{RMS}	306	274	223	calculated
	DC voltage	V_{DC} in V	800	800	800	determined
	DC current	I_{DC} in A_{RMS}	578	518	421	calculated
	Pulse-Width Modulation Switching frequency	f_{PWM} in kHz	20	20	20	determined
	Conduction losses	$P_{cond,total}$ in W	1215	957	687	simulated
	Switching losses	$P_{sw,total}$ in W	2292	2032	1714	simulated
	Inverter losses total	$P_{losses,total}$ in W	3507	2988	2400	simulated
	Efficiency	$\eta_{Inverter,total}$ in %	99.24	99.28	99.32	simulated
	Junction temperature	T_j in °C	114	107	99	simulated
	DC link capacitor capacity	$C_{DC-link,min}$ in µF	276	247	201	calculated
	DC link capacitor current	$I_{DC-link}$ in A_{RMS}	101	91	74	calculated

To give some idea how a possible 600 kW motor traction inverter for the medium-term horizon (2035-2045) could look like, an inverter reference design CRD600DA12E-XM3 from the manufacturer Wolfspeed with SiC power modules and a custom foil capacitor should be mentioned again in Deliverable 2.2 [106]. The key parameters of this inverter system are listed in Table 40. The reference design can meet the requirements for the proposed GENESIS motor traction drive inverter. Two of these inverter systems can be used to drive the generator (primary electric machine) for the scenario with the GT.

Table 40. Key parameters of the 6-phase 600 kW inverter from Wolfspeed [106]

Parameter	Value
SiC power modules	6x CAB450M12XM3
DC link capacitance in µF	600
Nominal output power in kW	600
Nominal output current in A_{RMS}	360
External length in mm	267
External width in mm	204
External thickness in mm	157
Total weight in kg	9.7
Volume in liter	8.6
Volumetric power density in kW/liter	70.0
Gravimetric power density in kW/kg	62.9

Table 41. Key parameters of the 6-phase 600 kW inverter for 2035-2045

Parameter	Value
GaN power modules	6x
Nominal output power in kW	600
Nominal output current in A_{RMS}	360
External length in mm	178
External width in mm	136
External thickness in mm	104.5
Total weight in kg	6.5
Volume in liter	5.7
Volumetric power density in kW/liter	105
Gravimetric power density in kW/kg	94.2

Based on the research perspective adopted in Chapter 5.3, a rough estimate can be given for a 600 kW inverter for 2035-2045 with GaN MOSFETs. Firstly, the $R_{DS,on}$ at 600V decreases by a factor of 4 for the same $R_{DS,on}$. In addition, the switching speed and the switching frequency increase with GaN devices. Due to a higher switching speed, there are fewer losses, which in turn leads to higher efficiency. Due to the higher efficiency, the cooling of the inverter can be reduced. In addition, the DC-link capacitance is reduced by increasing the switching frequency, which also reduces the size of

the DC link capacitor. However, the overall system should be considered to select the optimal switching frequency. For the medium-term with GaN MOSFETS, 30 kHz can be considered.

For all these reasons, a hypothesis can be made, that the size of the motor-dive inverter with the SiC devices in Table 40 will reduce quite safely by using GaN devices in Table 41 by the same power demands, and thus 1.5 times the power density can be achieved.

5.5. Bidirectional battery DC/DC converter

There are several suitable topologies for the bidirectional battery DC/DC converters. The main challenge is to choose the optimal solution for every individual application. The main requirements for the battery DC/DC converter in the GT/hybrid scenario are:

- The maximum output power is 1185 kW
- The battery voltage range is between 681.08 V and 454.05 V
- The HV DC bus voltage is assumed to be constant 800 V
- There is no galvanic isolation needed

The main requirements for the battery DC/DC converter in the FC/hybrid scenario are:

- The maximum output power is 900 kW
- The battery voltage range is between 681.08 V and 454.05 V
- The HV DC bus voltage is assumed to be constant 800 V
- There is no galvanic isolation needed

The battery voltage ($U_{battery}$)is always lower than the HV DC bus voltage (U_{HV_DC}). From the battery to the HV DC bus, the converter will work as a boost-converter and from the HV DC bus to the battery as a buck-converter. In order to briefly explain the individual components, the illustration (Figure 46) should be viewed from the left-hand side first. There are two modes of operation, MOSFET (M1/M2) "ON" or MOSFET "OFF". If the MOSFET is "ON", the current increases or the current can flow. If the MOSFET is turned "OFF", the current drops. The inductance (L_{boost}, Lbuck) wants to maintain the current flow due to Lenz's law, and the inductance continues to conduct the current for a short time. Therefore, however, the current decreases again. For the next switching period the MOSFET is switched "ON" again, and the current rises again. This produces a triangular signal of the current. The capacitor ($C_{battery}$)now forms the average value of this current by charging and discharging, whereby the average output voltage decreases. The switching time (also the switching frequency of the MOSFET) can be used to adjust the level of the output voltage. Switching on the MOSFET for a longer time increases the output voltage. Switching it on for a shorter time reduces it. The capacitor C_{HV_DC} is used for capacitive coupling and represents the transfer of energy between two physically unconnected conductors due to the mutual different electrical potential.

Due to this limitation, a simple half-bridge converter is the also in the medium-term horizon an optimal topology. Figure 46 shows the proposed topology. It provides a simple, low-cost and highly efficient solution due to the low number of semiconductors and passive components.
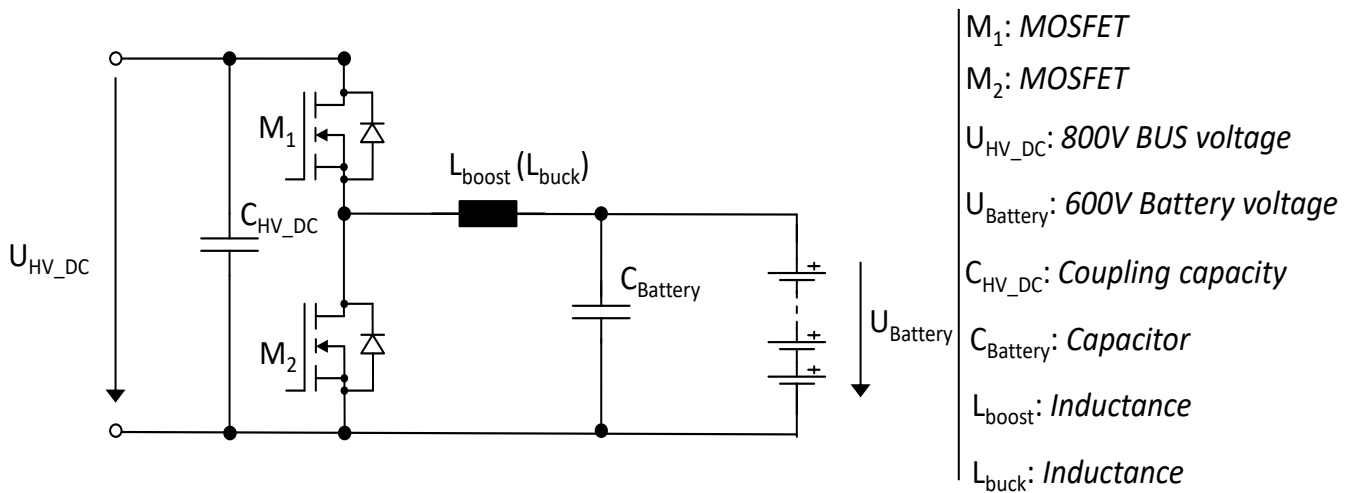
Figure 46. Half-bridge DC/DC converter

M_1: *MOSFET*

M_2: *MOSFET*

U_{HV_DC}: *800V BUS voltage*

$U_{Battery}$: *600V Battery voltage*

C_{HV_DC}: *Coupling capacity*

$C_{Battery}$: *Capacitor*

L_{boost}: *Inductance*

L_{buck}: *Inductance*

Furthermore, in the medium-term horizon it is proposed to use three DC/DC converters in an interleaved configuration (see Figure 47) to decrease the ripple current and, therefore, the losses in the inductors and capacitors. The size of the capacitors can also be reduced by using interleaved technology. Moreover, the number of parallel MOSFETs for a single converter without interleaving would be too high to construct a MOSFET module.

U_{HV_DC}: *800V BUS voltage*

$U_{Battery}$: *600V Battery voltage*

C_{HV_DC}: *Coupling capacity*

$C_{Battery}$: *Capacitor*

$L_{1,2,3}$: *Inductance*
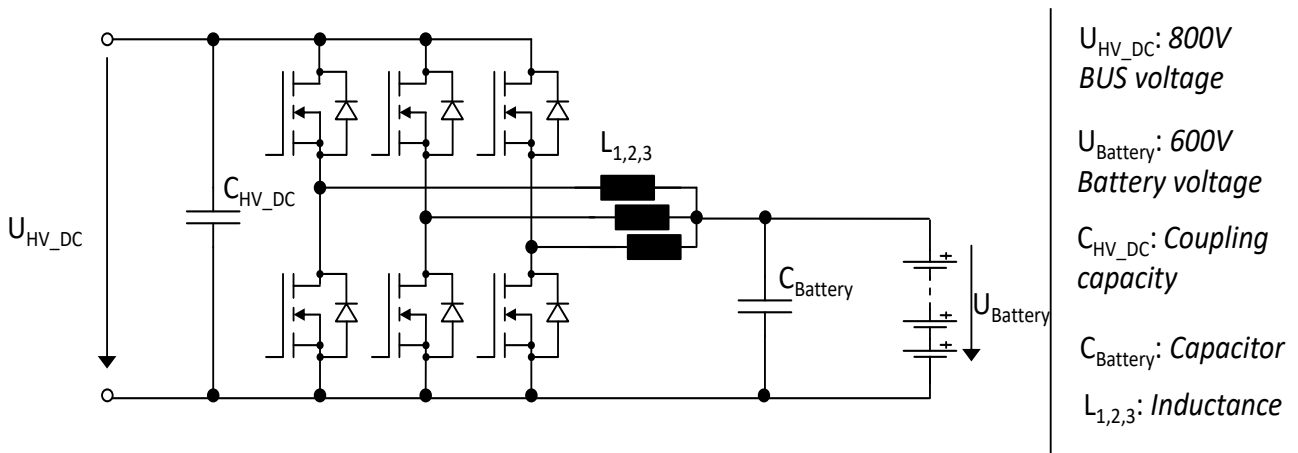
Figure 47. Three times interleaved halfbridge DC/DC converter

The converter will be operated in continuous conduction mode for better efficiency. The value of the inductor in a half-bridge converter depends on both possible directions of energy flow. It is necessary to calculate the minimum inductor value for buck (L_{Buck}) and boost operation (L_{Boost}). The calculations are the same as in the short-term Deliverable 2.1, because the physic laws are the same. [98]

For the medium-term DC/DC converter f is the PWM switching frequency, K is the estimated inductor ripple, V_{out} is the output voltage, I_{out} is the output current, V_{in_max} is the maximum input voltage. With an estimated 20 % inductor current ripple per converter, the inductance must be at least 28.04 µH for the scenario with the GT and 21.18 µH for the scenario with the FC. The voltage ripple ΔV_{max} is also assumed to be less than 1 %. The capacitance and the ESR (equivalent series resistance) of the capacitor determine the voltage ripple. For an assumed ESR of 1 mΩ, the capacitances for the scenario with the gasturbine are calculated to $C_{out_{Boost},GT} = 28.04$ µF and $C_{out_{Buck},GT} = 908.41$ µF. A

maximum temperature increase of $\Delta T, GT = 60$ K was assumed to calculate the necessary amount of parallel MOSFETs. For the scenario with the FC, the capacitances are calculated to $C_{out_{Buck},FC} = 21.18\ \mu F$ and $C_{out_{Boost},FC} = 636.75\ \mu F$. A maximum temperature increase of $\Delta T, FC = 65$ K was assumed to calculate the necessary amount of parallel MOSFETs. The losses consist mainly of conduction losses and switching losses.

One of the main factors that determine the switching losses is the switching frequency. There is a tradeoff between the size of passive components and switching losses. With a high switching frequency, the size of the capacitors and inductors can be reduced, but the switching losses will increase. A switching frequency of 100 kHz offers a reasonable tradeoff between size and losses. To estimate the resulting temperature rise, the losses are multiplied by the thermal resistance. Assuming a small thermal resistance between MOSFET and heat sink, the minimum number of parallel MOSFETs in the scenario with the GT is seven for M1 and six for M2 (see Figure 46). The minimum number of parallel MOSFETs in the scenario with the FC is 5 for M1 and 4 for M2. Table 42 gives a summary of the MOSFET losses and the resulting temperature increases for the scenario with the gasturbine. In Table 14 are the values for the scenario with the FC are listed.

Power semiconductors with a minimum breakdown voltage of 1200 V have to be used due to the given maximum battery voltage of 681.08 V. Different options were considered and, in the end, the 8.6 mΩ 1200 V SiC MOSFETs UF3SC120009K4S from UnitedSiC were chosen for the battery DC/DC converters.

Table 42: Summary of MOSFET losses for the GT scenario

Operation mode	Switch	P_{sw}	P_{con}	ΔT
Buck-Mode	M1	221.95 W	66.9 W	60.6°C
	M2	258.9 W	23.86 W	59.4°C
oost-Mode	M1	221.9 W	37.6 W	54.5°C
	M2	258.9 W	22.6 W	59.1°C

Table 43: Summary of MOSFET losses for the FC scenario

Operation mode	Switch	P_{sw}	P_{con}	ΔT
Buck-Mode	M1	236 W	75.65 W	65.45°C
	M2	295 W	30.96 W	68.45°C
Boost-Mode	M1	236 W	42.55 W	58.5°C
	M2	295 W	29.3 W	68.1°C

The theoretical calculated efficiency of the DC/DC converters for both scenarios is around 99.69 % for buck operation and around 99.70 % for boost operation. For the calculation, neither the inductor nor the capacitor losses were included. The actual reachable efficiency, in a realistic application, should be about 98 % to 99 %. Using zero voltage switching to decrease switching losses might result in higher efficiency. This would require further investigation. Depending on the size of the inductors and capacitors, highly sophisticated designs of the battery DC/DC converter should enabled to reach a power density of about 50 to 65 kW/kg.

Based on the research outlook assumed in Chapter 5.3, a rough estimate for an 1185 kW DC/DC converter can be given for 2035-2045 with GaN-MOSFETs. Compared to motor drive inverters, there is a positive influence on the choke inductances, which are reduced. This results in greater savings

on the DC/DC converter. Therefore, compared to the motor drive inverter, GaN components can be scaled by a factor of 2.

To sum it up, it can be estimated that a factor of 2 can almost certainly be achieved in the time frame 2035-2045 and the power density could be about 100 to 130 kW/kg.

5.6.　Unidirectional fuel cell DC/DC converter

For the medium-term horizon (2035-2045) a fuel cell system is planned as an energy source. Therefore, there is a unidirectional fuel cell DC/DC converter required. However, the basic topology for such a converter would be a multiple times interleaved boost-converter. Therefore, the same topology and design rules from Chapter 5.5 are used.

The main requirements for the battery DC/DC converter for this specific scenario of the in the GENESIS project are:

- The maximum output power is 1407 kW
- The Fuel Cell voltage range is between 400 V and 500 V
- The HV DC bus voltage is assumed to be constant 800 V
- There is no galvanic isolation needed

Furthermore, in the medium-term horizon it is proposed to use three DC/DC converters in an interleaved configuration (see Figure 48).
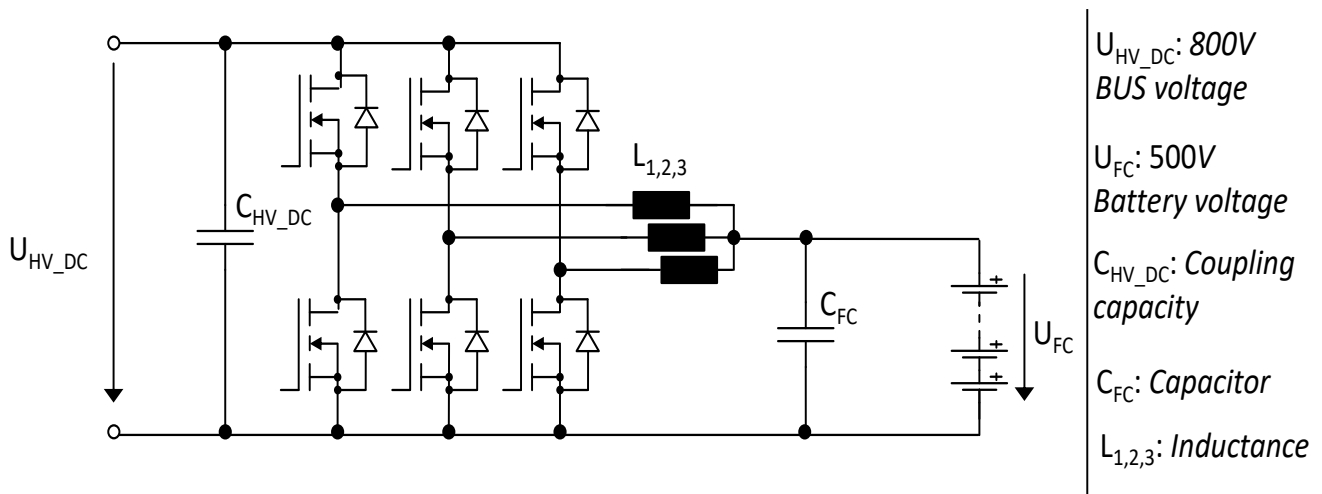
Figure 48. Three times interleaved half-bridge DC/DC FC converter

The converter will also be operated in continuous conduction mode for better efficiency. The value of the inductor in a half-bridge converter depends on one possible direction of energy flow, from the FC to the HV DC bus. But it is necessary to calculate the minimum inductor value boost operation (L_{Boost}),too. The calculations are the same as in the short-term deliverable 2.1, and in chapter 5.5 [98].

For the medium-term FC-DC/DC converter the PWM switching frequency, the estimated inductor ripple, V_{out}, I_{out}, V_{in_max} are also necessary parameters like for the DC-DC converter. With an estimated 20 % inductor current ripple per converter, the inductance was calculated at least 9.45 µH. For an assumed ESR of 1 mΩ, the capacitances for the scenario are calculated to $C_{out_{Boost,FC}} = 1.60$ mF. A maximum temperature increase of $\Delta T = 60$ K was assumed to calculate the necessary amount of parallel MOSFETs. The losses consist mainly of conduction losses and switching losses.

One of the main factors that determine the switching losses is the switching frequency. There is a tradeoff between the size of passive components and switching losses. With a high switching frequency, the size of the capacitors and inductors can be reduced, but the switching losses will increase. A switching frequency of 100 kHz offers a reasonable tradeoff between size and losses. To estimate the resulting temperature rise, the losses are multiplied by the thermal resistance. Assuming a small thermal resistance between MOSFET and heat sink, the minimum number of parallel MOSFETs is 12 for M1 and 11 parallels for M2 (see Figure 46). Table 44 gives a summary of the MOSFET losses and the resulting temperature increases.

For the FC DC/DC converter also power semiconductors with a minimum breakdown voltage of 1200 V should be used due to the given maximum FC voltage of 500 V. Different options were considered and, in the end, the 8.6 mΩ 1200 V SiC MOSFETs UF3SC120009K4S from UnitedSiC were chosen for the battery DC/DC converters.

Table 44: Summary of MOSFET losses for FC converter

Operation mode	Switch	P_{sw}	P_{con}	ΔT
Boost-Mode	M1	204.9 W	19.9 W	47.21°C
	M2	223.6 W	16.6 W	50.4°C

The theoretical calculated efficiency of the unidirectional FC DC/DC converters is around 99.69 % for buck operation and around 99.62 %. For the calculation, neither the inductor nor the capacitor losses were included. The actual reachable efficiency, in realistic application, should be about 98 % to 99 %. Using zero voltage switching to decrease switching losses might result in higher efficiency. This would require further investigation. Depending on the size of the inductors and capacitors, high sophisticated designs of the unidirectional FC DC/DC converter should be enabled to reach a power density of about 60 to 70 kW/kg.

Based on the research outlook assumed in Chapter 5.3, a rough estimate for a 1407 kW DC/DC converter can be given for 2035-2045 with GaN-MOSFETS. It can be estimated that a factor of 2 can almost certainly be achieved in the time frame 2035-2045 and the power density could be about 120 to 140 kW/kg.

5.7. DC/AC grid converter

The DC/AC grid converter has the basic topology of a two-level inverter, as described in Chapter 5.4 (see Figure 49). Therefore, the same design rules from Chapter 5.4 apply to calculate the inverter losses and to size the DC link capacitor, like in the short-term horizon. The only difference is that filter inductors have to be connected between the DC/AC grid converter and the 400 Hz 115 V powernet to reduce the output current ripple. Depending on the requirements of the 400 Hz power net (harmonics current limits), it could also be necessary to increase the filter effort and to install a three-phase LC-filter or LCL-filter instead of only three inductors. The topic of electromagnetic compatibility (EMC) and net filters is rather complex and needs extensive analysis and is not part of this report. However, a rough estimation of the filter inductance value is given here. The inductance value L_{filter} can be approximated to [107]:

$$L_{filter} \cong \frac{V_{DC} \cdot m}{2 \cdot \sqrt{3} \cdot f_{PWM} \cdot \Delta i_{max}} = \frac{800\ V \cdot 0.144}{2 \cdot \sqrt{3} \cdot 16\ kHz \cdot 5\ A} = 416\ \mu H$$

with V_{DC} the DC bus voltage, m the modulation index, f_{PWM} the PWM switching frequency and Δi_{max} the maximum allowed current ripple value. If required, a LCL-filter can, for example, be sized according to [108]. Table 45 shows the analysis results for the DC/AC grid inverter. The power semiconductor losses have been simulated with the "SpeedFit Design Simulator" from Wolfspeed.

For the power semiconductors, the Wolfspeed power module CAB425M12XM3 was chosen. Sophisticated designs of DC/AC grid converters can reach a power density of at least 30 kW/kg.

Based on the research outlook assumed in Chapter 5.3, a rough estimate for a 30 kW DC/AC converter can be given for 2035-2045 with GaN-MOSFETS. It can be estimated that a factor of 1.7 can almost certainly be achieved in the time frame 2035-2045 and the power density could be about 51 kW/kg.
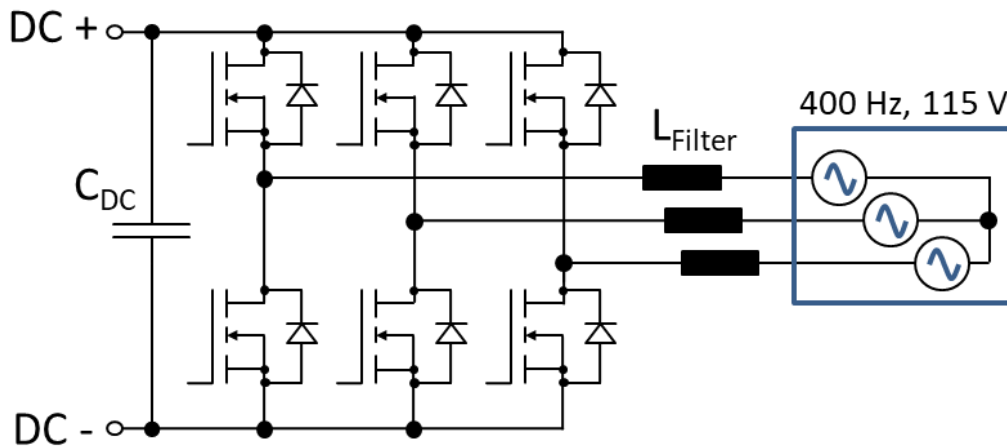
Figure 49. DC/AC grid converter

Table 45. Results of technology analysis for the DC/AC grid inverter

	Parameter	**Value**	**Data Origin**
Definition	Inverter configuration	3-phase	determined
Electrical Power	$P_{Inverter,total}$ in kW	30	from TLAR
DC current	I_{DC} in A_{RMS}	37.5	calculated
DC voltage	V_{DC} in V	800	determined
Phase to phase voltage	$V_{out,LL}$ in V_{RMS}	115	from TLAR
Powernet frequency	f_{out} in Hz	400	from TLAR
Pulse-Width Modulation Switching frequency	f_{PWM} in kHz	16	determined
Phase to phase current	$I_{LL,eff} = I_{str,eff}$ in A_{RMS}	150.6	calculated
Conduction losses	$P_{cond,total}$ in W	244.5	simulated
Switching losses	$P_{sw,total}$ in W	240.5	simulated
Inverter losses total	$P_{losses,total}$ in W	485.0	simulated
Efficiency	$\eta_{Inverter,total}$ in %	98.40	simulated
Junction temperature	Tj in °C	84.2	simulated
DC link capacitor capacity	$_{DC-link,min}$ in µF	60.0	calculated
DC link capacitor current	$I_{DC-link}$ in A_{RMS}	90.4	calculated

5.8. Isolating DC/DC converter for low voltage supply

The isolating DC/DC converter for low voltage supply transfers power from the 800 V DC bus to the 28 V consumers of the aircraft. The total 28 V power demand or power demand per converter can differ for various regional aircraft. Table 46 shows two examples. The difference can be explained by the electric consumers inside the aircraft. The Bombardier CRJ100 has many more electric consumers, which run on the 400 Hz power net, than the Embraer ERJ145. Therefore, the Bombardier CRJ100 has a higher power demand regarding the 400 Hz power net. The Embraer ERJ145, by contrast, has a higher power demand regarding the 28 V power net. For this case study, a maximum output current of 400 A and a maximum output power of 11.2 kW for the isolating DC/DC converters were assumed.

Table 46. Examples for 28V power demand for two regional aircraft [98]

Regional aircraft	Number of units	Rated Voltage	Maximum Current	Maximum Power
Embraer ERJ145	5	28 V	400 A	11.2 kW
Bombardier CRJ100	5	28 V	100 A	2.8 kW

For the isolation between the high voltage and low voltage sides, a transformer is necessary. The transformer adds a significant amount of weight, decreases the system efficiency, and increases the system complexity. The isolating DC/DC converter for low voltage supply is the most challenging converter to design compared to the other presented power electronics converters. There are non-resonant, partial-resonant and resonant topologies.Fifteen different implementation possibilities of isolating DC/DC converters are described in [109].

For the given application, an LLC resonant converter or a phase-shifted full bridge (PSFB) converter are the two most promising candidates. The two topologies are shown in Figure 50 and Figure 51. They have the same number of power semiconductors, and both can use the same output stage (e.g., full bridge rectifier) on the low-voltage side. For higher efficiency, the diodes in the output stage are replaced by low-voltages silicon MOSFETs or, for very high switching frequencies, by low-voltage GaN-MOSFETs. The main difference between the two topologies is the control strategy. The output voltage of the LLC converter is controlled by changing the switching frequency, while the one of the PSFB converter is controlled by a phase shift of the PWM signals for the second half-bridge. Both topologies have distinct advantages and disadvantages. A short comparison of the properties is presented in Table 47 and more details can be found in [109] or [110].
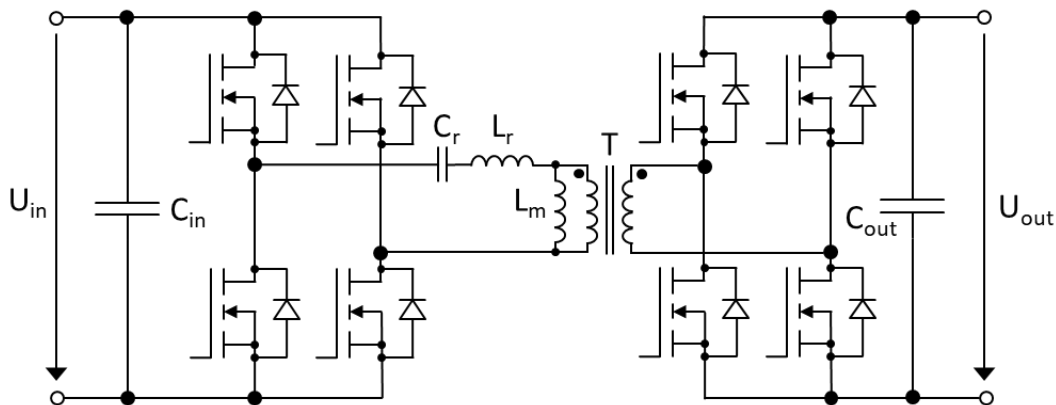
Figure 50. LLC resonant converter
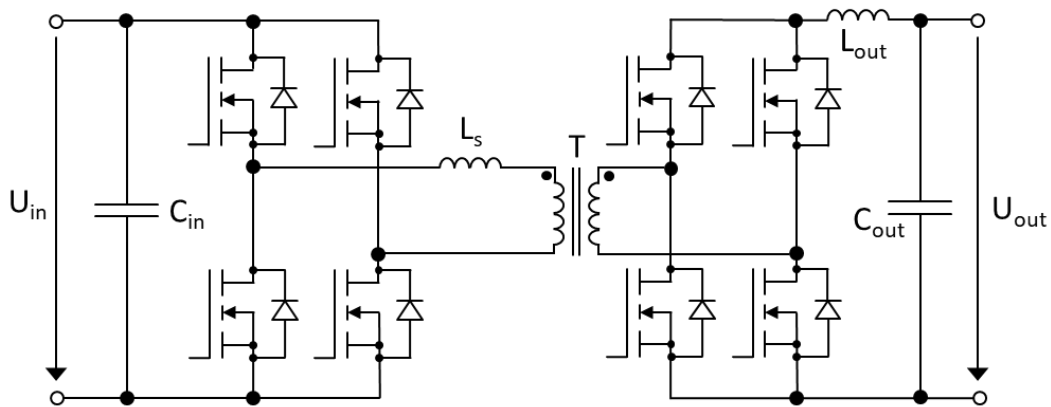
Figure 51. Phase-shifted full-bridge (PSFB) converter

Table 47. Comparison between LLC and PSFB converter [110]

Parameter	LLC converter	PSFB converter
Switching frequency	variable	fixed
Synchronization, current share	poor	good
Output voltage range	medium	wide
EMI	low level of noise generation	medium level of noise generation
Efficiency	good, best at resonance	good, minimizes body diode conduction
Transformer	operates over a wider frequency range	fixed frequency range

An isolated 10 kW HV/LV DC/DC converter is presented, which serves as a reference design for this converter class for the short-term horizon (2025-2035) and also for the medium-term horizon (2035-2045). Fraunhofer IISB developed the converter for the LuFo V-3 project "GETpower 2", which is (partially) funded by the German federal ministry BMWi [111]. The main parameters of the converter are listed in Table 48. Regarding the power density, the developed reference design has a 2.5-times higher gravimetric power density than comparable state-of-the-art converters and a 2.3-timer higher volumetric power density. The basic structure of the converter is shown in Figure 52 The converter is split into two identical building blocks. The HV input stage is connected in series to consider the breakdown voltage derating, which must be applied due to cosmic radiation and high altitudes. For the high voltage input stage, 1000V SiC MOSFET are used. The LV output stage is connected in parallel to increase the output current rating. The topology of the converter is a LLC resonant converter with a full-bridge rectifier output stage. In the output stage, silicon 100 V MOSFETs are used instead of diodes to increase efficiency. The mechanical design is shown in Figure 53. For the medium term, this converter is more than sufficient, because to develop this converter. For the medium term, it is expected that this converter would then be available for purchase and could be installed. For the long-term scenario a optimistic estimation could be a power density of 5 kW/kg feasible for this DC/DC converter.
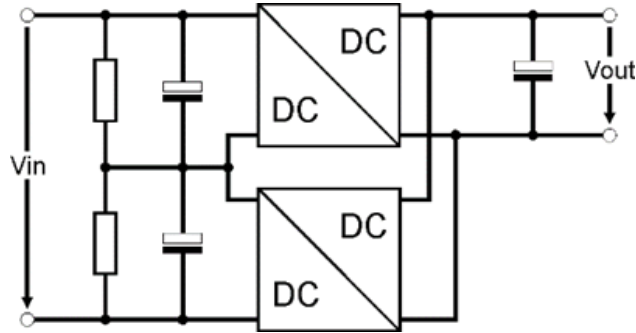
Figure 52. Basis structure of the 10 kW isolating DC/DC converter for low voltage supply

Table 48. Key parameters of the 10 kW isolating DC/DC converter for low voltage supply

Parameter	Value	Unit
Input voltage range	540…840	V
Output voltage range	24…28	V
Maximum output current	400	A
Nominal output current	360	A
Maximum output power	11.2	kW
Nominal output power	10.0	kW
Volume	4	dm^3
Weight	5	kg
Volumetric power density	2.5	kW/dm^3
Gravimetric power density	2	kW/kg
witching frequency	120…240	kHz
Efficiency	94…97	%
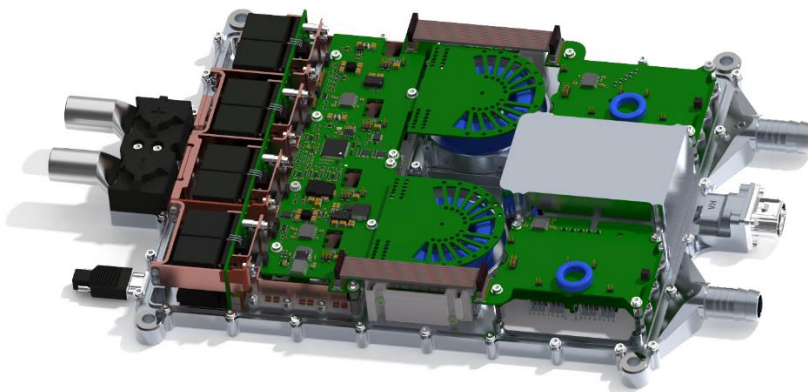
Figure 53. Mechanical design of the 10 kW isolating DC/DC converter for low voltage supply without housing

5.9. Conclusions

The technology analysis for all power electronics converters in the GENESIS project for the medium-term horizon (2035-2045) has been presented. The influence of the HV DC bus voltage was investigated. It was concluded that the bus voltage should be set to 800 V also for the medium-term perspective. Power semiconductors have the biggest influence on the design of power electronics systems. The properties of silicon, silicon carbide, and gallium nitride power semiconductors have been compared. The analysis has shown that silicon carbide power semiconductors (SiC MOSFETs) are the best option for all power electronic converters in the medium-term because manufacturers still have too few GaN devices insight. However, a rough estimate with potential GaN devices was given for the converters considered. All different power electronics converters, i.e, motor traction drive inverter, generator traction drive inverter, bidirectional battery DC/DC converter, unidirectional fuel cell DC/DC converter, DC/AC grid converter, and isolating DC/DC converter for low voltage supply, have been investigated in detail for both scenarios. The converters were sized for the application and efficiency and power density values have been provided. The results of the investigation and the estimations with GaN devices are summarized in Table 49. These parameters and interpretations in this chapter were verified in expert discussions with Dr.-Ing Bernd Eckardt [112] and Dr.rer.nat. Elke Meißner [113].

Another potential with GaN devices could be to increase the DC link voltage, provided that the appropriate devices were available and the fuel cell and battery voltages were increased.

Table 49. Results of the technology analysis for all power electronics converters for the medium-term horizon (2035-2045)

Converter	Topology	Rated power	Efficiency	Power density SiC	Power density GaN	TRL SiC/GaN
Motor drive inverter	6-phase two-level inverter	600 kW	99 %	63 kW/kg	94.2 kW/kg	SiC: 7 – 8; Expected: GaN: 6 – 7;
Generator drive inverter (Scenario GT)	2x 6-phase two-level inverter	1200 kW	99 %	63 kW/kg	94.2 kW/kg	SiC: 7 – 8; Expected: GaN: 6 – 7;
Battery DC/DC converter (Scenario GT)	3-times interleaved half-bridge converter	1085 kW	98 - 99 %	50 - 65 kW/kg	100 - 130 kW/kg	SiC: 7 – 8; Expected: GaN: 6 – 7;
Battery DC/DC converter (Scenario FC)	3-times interleaved half-bridge converter	900 kW	98 - 99 %	50 - 65 kW/kg	100 - 130 kW/kg	SiC: 7 – 8; Expected: GaN: 6 – 7;
Fuel cell DC/DC converter	3-times interleaved half-bridge converter	1407 kW	98 - 99 %	50 - 65 kW/kg	120 - 140 kW/kg	SiC: 7 – 8; Expected: GaN: 6 – 7;
DC/AC grid inverter	3-phase two-level inverter	30 kW	98.4 %	30 - 40 kW/kg	45 - 55 kW/kg	SiC: 7 – 8; Expected: GaN: 6 – 7;
Isolating DC/DC converter	2x LLC converter	11.2 kW	94 - 97 %	2 kW/kg	2 kW/kg	SiC: 7 – 8; Expected: No GaN

6. Electric drive technology analysis

6.1. Introduction

This chapter deals with the medium-term (2035-2045) technology analysis for the electric drives in the GENESIS project. For the medium-term horizon, there are two different suggested scenarios. As described in chapter 5, the GT/hybrid scenario consist of a hybrid system with gas turbines and batteries.The FC/hybrid scenario consist of a hybrid system consisting of a fuel cell and battery.

Scenario with the gas turbine (GT):
The mechanical power of the gas turbine is delivered to a gearbox, which drives the primary propulsion fan. The gas turbine also drives the electric generator via the gearbox. The electric generator (primary electric machine) converts mechanical power into electrical power. The electric motors (secondary electric machines) convert electrical power from the HV DC bus into mechanical power and drive the secondary propulsion fans to generate thrust. This scenario is also discussed in detail in the short-term horizon. An overview of this scenario is shown in Chapter 1.2 in Figure 5.

Scenario with the fuel cell (FC):
The electric generator (primary electric machine) is not needed anymore. Five e-drive electric machines are supposed to provide the same power to five seperate propellers. The electrical power comes from the FC and the batteries and supplies the e-drive electric machines via the HV DC bus An overview of this scenario is shown in Chapter 1.2 in Figure 9.

In the short-term horizon, it was already discussed, that, for a hybrid or all-electric aircraft application, the motor efficiency and the power density are more important than the cost in light of their direct effect on the aircraft mass and overall efficiency. If the motor efficiency increases, the battery size can be reduced, allowing weight savings. Considering the crucial role that weight plays, it was concluded that permanent magnet synchronous machines (PMSM) are the most suitable option for the electric drives in the GENESIS project for the short-term horizon (2025-2035) [98]. The PMSM was further developed and optimized for the medium-term horizon. For this purpose, the optimization was limited to two possibilities. Firstly, a Halbach array was considered and secondly, the machine could be developed with directly cooled stator windings.

In the long-term horizon (and in a scenario with FC in the medium-term horizon), hydrogen will be stored on the plane. The usage of partially (i.e., only with a superconduction rotor) or fully superconducting separately excited synchronous motor machines is possible with liquid hydrogen. This option will be investigated in the following deliverable D2.7.

6.2. Optimization Opportunities

6.2.1. Halbach Array

The Halbach arrangement of PMs is the combination of the radial and azimuthal PM arrangements. This combination results in a stronger magnetic field on one side of the arrangement, while the field on the other side cancels out to almost zero. That is why there is a big difference in the magnetic field around each magnet. Typically, the magnetic field is equally strong with a single magnet on both sides. For the Halbach arrangement, the magnets are arranged with all north poles facing upwards. From a magnetic point of view, this results in a single long magnet. Figure 54 on the left shows how the north pole of a single magnet always points upwards. The color scale estimates the field strength, which is just as strong on the upper side as on the lower side. The advantage of the Halbach arrangement is shown on the right side in Figure 54. The arrangement of the magnets creates a powerful field on the upper side. On the lower side, the field strength lines almost cancel each other out or generate no field.

In addition, Halbach arrays offer other advantages like:

- They have excellent magnetic field performance when certain gaps exists
- Their magnetic field exhibits sinusodiale distribution and drastically reduces harmonic waves.
- They pfovide an effective increase in power.
- They provide an xcellent magnetic shielding effect.

Halbach arrays can be mainly divided into the straight type and circular type based on their geometry. Circular type can be further classified into outer diameter (O.D.) iteration and inner diameter (I.D.) iteration based on the arrangement of the permanent magnet. Numerous directions and strengths will be yielded by different magnet configurations. According to numerical calculations, and harmonic analysis, the PMSM with Halbach magnet array provides higher torque and better performance than the classical radial PMSM [114], [115].
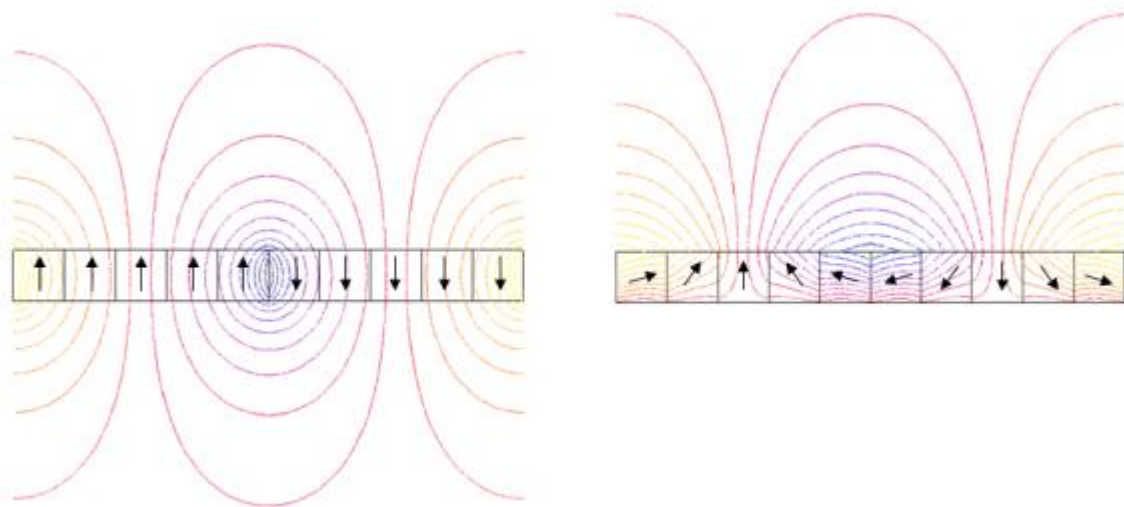
Figure 54. Conventional Magnet Arrangement Flux Lines (left) and Halbach Array Arrangement Flux Lines (right) [115]

6.2.2. Direct cooled stator windings

Due to the increasing demands on electrical machines, new cooling concepts have to be designed, so for some time now the focus has been on direct cooling concepts. These aim to shorten the existing heat path through the machine by cooling as directly as possible at the heat sources in the motor, usually the copper or aluminium windings and the stator laminations, thus improving the overall machine efficiency. For directly cooled stator windings, two methods should be widely used so far:

- Winding head and stator cooling by through a cooling medium flowing around the winding.

This concept aims at a total cooling of the large loss sources. The entire stator, including the winding, "floats" in the dielectric.

- Winding cooling by hollow wires or other conductor geometries

By using hollow copper wires for the stator winding, which carry the cooling medium this concept can also be used to cool the winding directly. Other geometries are possible from the hollow wire , like the ones in Figure 55 [116], [117].
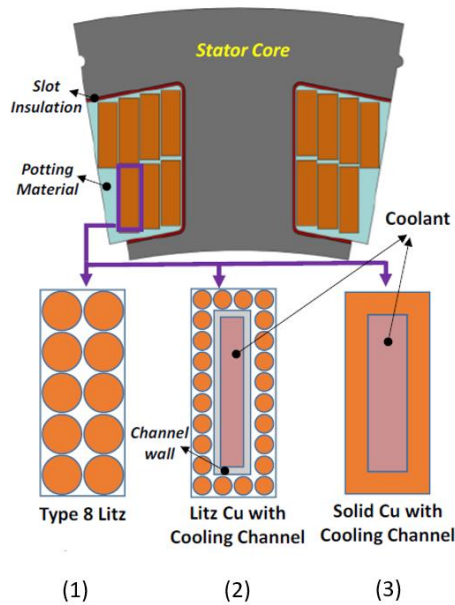
Figure 55 Cross-section of electric machine stator slot with alternative winding/cooling approaches [117]

First, a type 8 stranded coil with a rectangular shape is presented. The windings are filled with a highly heat-conductive potting material. The same applies to the stator slots. However, heat dissipation is limited by the thermal conductivity of the potting material and the surrounding slot insulation. This concept can be modified by inserting cooling channels into the potting material, as shown on the left in Figure 55 (1).

In the middle of Figure 55 (2), the stranded winding can also be cooled directly by wrapping the winding around the outside of a rectangular metallic cooling channel. This approach brings the strands in close thermal proximity to the coolant while maintaining the AC losses of the stranded construction. This type of stranded coil configuration is manufacturable with some trade-offs. The cooling channel has two important tasks in this configuration: It transfers heat from the stranded coils to the coolant and provides structural support for the strand winding and coolant flow. The metallic cooling channel is also exposed to, among other things, fluctuating alternating fields from the magnetic field within the stator slots. This can cause considerable eddy currents and Joule losses. In addition, the cooling channel takes up valuable space in the coil area, reducing the copper fill factor and increasing the DC electrical resistance and copper losses.

Therefore, the duct must be thoughtfully designed to minimize the cross-sectional area required for its walls while balancing structural strength, thermal conductivity, and electrical resistance. Stainless steel, for example, is a good material for this. The total losses of the winding are usually estimated to be twice higher than those for the type 8 stranded coil. However, this approach with the core channel achieves a much lower thermal resistance, which reduces the winding temperature despite the higher losses.

The third cooling option is shown on the right in Figure 55 (3). This solution uses a solid rectangular copper channel as a conductor with internal coolant flow. This allows an impressively low thermal resistance to be achieved, as the coolant is in direct contact with the walls of the conductor over the entire length of the channel. The copper fill factor is also higher than with the combination of stranded wire and core cooling channels (1) and (2), which reduces the DC resistance. As a disadvantage, it should be mentioned that the AC losses associated with the solid-wall channel are significantly higher due to the high operating frequency and the spatial harmonic content of the concentrated winding

distribution. According to FEA estimates, the total losses of the solid copper concept are approximately five times higher than the losses of the stranded coil type 8.

Clear electromagnetic trade-offs must be made between the individual cooling methods. The loss values and the thermal compromises from the basic structure of each cooling method are included in this decision. Therefore, the trade-offs between these three techniques should be made in terms of losses/efficiency and thermal effectiveness [116] [117].

6.3. Drive train components

Table 50 shows the power demand of the electric machines for different periods and the different scenarios (GT or FC). The configuration is the same as in Deliverable 2.1. The secondary electric machines always have half of the power demand of the primary electric machines. Therefore, it is suggested to reuse the components of the secondary electric machines in the primary machines. Two secondary machines are stacked together and connected with a common rotor shaft for the primary machines. For example, the motor manufacturers EMRAX and MagniX recommend this variant to double the motor power and torque. Figure 56 shows what such a configuration would, in principle, look like. Not only the secondary motors but also the motor drive inverters for the secondary machines can be reused. Two motor drive inverters will be used in combination as the generator drive inverter for the primary motors. As described in Chapter 5.4, multi-phase motors and inverters will be used to enable fail-operational capabilities and limit the current demand for single parts. The secondary machine will be a six-phase machine, which six-phase motor drive inverter will drive. The primary machine will be two stacked six-phase machines, each driven by two six-phase motor inverters. It has not been deined whether or not a gear box will required during the climb and cruise phase, thus, the efficiency losses from the gearbox were not considered, or the efficiency of the gearbox was assumed to be 100% for this preliminary assessment. To complete the drivetrain, the gearbox has been included in the illustrations.

Table 50. Power demand of electric machines for different time frames

Motor	Number of units	Reference Power in kW		
		Short-Term Year 2025-2035	Medium-Term Year 2035-2045	Long-Term Year 2045-2055
Primary electric machine (GT)	2	1200	1200	-
Secondary electric machine (GT)	8	600	600	750
e-drive electric machine (FC)	10	-	600	750
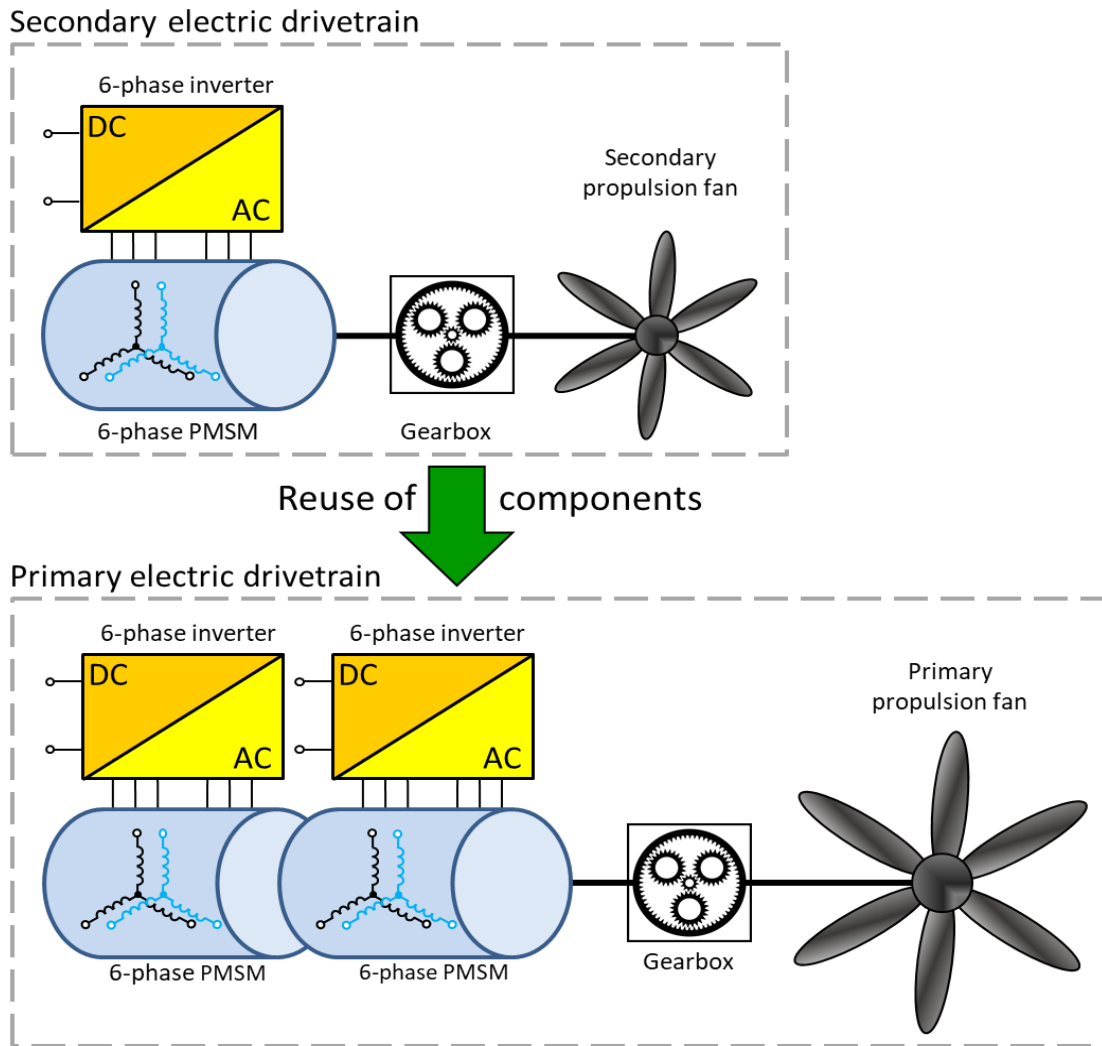
Figure 56. Reuse of secondary electric drive train components to build up the primary electric drive train

6.4. Design results for the electric drive train

A six-phase 600 kW liquid-cooled PMSM motor was designed in the short-term scenario to meet the requirements for the secondary electric machine. The design of an electric machine depends on many different parameters like stator current density, magnetic field density, pole pair number, number of slots, rotor diameter, rotor length, and the stator geometry defined by yoke thickness teeth height, and teeth width. The power density of an electric machine is given by [118]:

$$\frac{P}{m} = k_{geometry} \cdot B_g \cdot A \cdot n_{rot} \cdot \eta_{EM}$$

Where P is the electrical motor power, m is the motor mass, B_g is the magnetic field density in the air gap, A is the stator current density, n_{rot} is the motor speed, and η_{EM} is the motor efficiency. The geometry parameters $k_{geometry}$ include, e.g., the geometrical details of the teeth (e.g., width and height) and of the rotor, the winding geometry, etc.

The power density is directly proportional to the magnetic field density in the air gap B_g. Therefore, neodymium iron boron (NdFeB) magnets were chosen. They are expensive, but this material has the highest magnetic flux density and thus enables the highest power density. The power density also

increases with the stator current density A, which is limited by the cooling of the stator. A typical value of 10 A/mm^2 is possible for a water-jacked cooled motor.

With direct liquid-cooled windings used in the medium-term horizon. a value of 25 A/mm^2 can be reached. For superconducting machines, the current density can even be greater than 500 A/mm^2. This possibiliy should be researched in the subsequent deliverable D.2.7. However, the ohmic losses of the stator windings will also increase with higher current density leading to reduced efficiency.

For the motor design in the medium-term, presented at the end of the chapter, a direct liquid-cooled stator windings motor with a Halbach Array was chosen. With this motor, the baseline of the short-term scenario would be developed. The motor power density also increases with the rotational speed n_{rot}. For the GENESIS project in general, the rotational speed of the electric machines was set in the short-term by choosing a gearbox transmission ratio. A direct drive of the propulsion fans is possible in the medium-term. The gearbox ratio was chosen to 1:1 and limit the motor speed to 2,000 rpm during the "Cruise phase". As a result, we have higher torque than the engine can deliver. Alternatively two engines can afford.

This is a common value for machines for electric powertrains. The mechanical parameters of the primary and secondary drivetrain of the GT scenario are listed in Table 51 and Table 52. The mechanical parameters of the FC scenario are listed in Table 53. A high rotational speed positively influences the motor power density, but it negatively affects the AC motor losses. Moreover, a higher PWM switching frequency is necessary, leading to higher inverter losses. Overall, it can be said that if the rotational speed is increased too much, the motor efficiency will suffer. About this fact, the rotational speed in the medium-term motor would be decreased. Due to the rotational speed reduction, the torque had to be increased. Unfortunately, the huge torque density/current density that can be achieve in this motor, has to be paid for with a somewhat poorer efficiency.Table 54Table 54 shows the design results for the electric machine for the medium-term period (2035-2045). The motor efficiency was estimated to be about 92 %. The power density for active parts is about 23.7 kW/kg. With a total motor weight of 40-45 kg, the total power density is calculated to be 13.5-15.2 kW/kg. The continuous torque density for active parts is 112.9 Nm/kg [119].

Table 51. Mechanical minimum parameter requirements for the secondary drive train for the medium-term horizon (2035-2045) GT-Scenario

	Use Case	Take off	Climb	Cruise	Data Origin
Secondary propeller	Mission time in min	0.34 / 0.37	21 / 24	12 / 97	from TLAR
	$P_{Propeller}$ in kW	428	196	--	from TLAR
	$T_{Propeller}$ in Nm	2044	936	--	from TLAR
	$n_{Propeller}$ in rpm	2000	2000	--	calculated
	$\eta_{Propeller}$ in %	79	72	--	from TLAR
Secondary electric motor	$\eta_{Gearbox}$ in %	100	100	--	from TLAR
	Gearbox ratio	1:1	1:1	--	determined
	$P_{Motor,mech}$ in kW	542	272	--	calculated
	T_{Motor} in Nm	2587	1300	--	calculated
	n_{Motor} in rpm	2000	2000	--	calculated

Table 52. Mechanical minimum parameter requirements for the primary drive train for the medium-term horizon (2035-2045) GT-Scenario

	Use Case	Take off	Climb	Cruise	Data Origin
Primary propeller	Mission time in min	0.34 / 0.37	21 / 24	12 / 97	from TLAR
	$P_{Propeller}$ in kW	340	1266	1136	from TLAR
	$T_{Propeller}$ in Nm	1624	6045	5424	from TLAR
	$n_{Propeller}$ in rpm	2000	2000	2000	calculated
	$\eta_{Propeller}$ in %	60	81	81	from TLAR
Primary electric motor	$\eta_{Gearbox}$ in %	100	100	100	from TLAR
	Gearbox ratio	1:1	1:1	1:1	determined
	$P_{Motor,mech}$ in kW	1130	121	156	calculated
	T_{Motor} in Nm	5396	578	745	calculated
	n_{Motor} in rpm	2000	2000	2000	calculated

Table 53. Mechanical minimum parameter requirements for the e-drive electrical machine for the medium-term horizon (2035-2045) FC-Scenario

	Use Case	Take off	Climb	Cruise	Data Origin
Primary propeller	Mission time in min	0.34 / 0.37	21 / 24	12 / 97	from TLAR
	$P_{Propeller}$ in kW	304	316	289	from TLAR
	$T_{Propeller}$ in Nm	1452	1509	1380	from TLAR
	$n_{Propeller}$ in rpm	2000	2000	2000	calculated
	$\eta_{Propeller}$ in %	69	80	90	from TLAR
Primary electric motor	$\eta_{Gearbox}$ in %	100	100	100	from TLAR
	Gearbox ratio	1:1	1:1	1:1	determined
	$P_{Motor,mech}$ in kW	441	395	321	calculated
	T_{Motor} in Nm	2104	1886	1613	calculated
	n_{Motor} in rpm	2000	2000	2000	calculated

Table 54. Results of technology analysis for 6-phase electric machine for the medium-term horizon (2035-2045) [119]

Parameter	Value	Unit
DC link voltage	800	V
Nominal phase current 3-phase	1002	A_{RMS}
Nominal phase current 6-phase	530	A_{RMS}
Nominal power	607	kW
Nominal torque	2900	Nm
Nominal speed	2000	rpm
Estimated efficiency (part load)	92	%
part load Efficiency @	900 rpm/1580 Nm	
Estimated efficiency @Pmax	88	%
Length active parts	119	mm
Outer diameter housing	478	mm
Height housing	233	mm
Active parts weight	30,8	kg
Total weight	40-45	kg
Continuous power density for active parts	23,7	kW/kg
Continuous total power density	13.5-15.2	kW/kg
Continuous torque density for active parts	112.9	Nm/kg

We achieve approximately 88 % at maximum output and approximately 92 % in a partial load range in terms of the efficiency. Unfortunately, the huge torque density/current density that we achieve in this motor has to be paid for with somewhat lower efficiency. However, the waveguide cooling makes this possible in the first place. In addition, these efficiencies were explicitly defined and targeted for a particular application. The optimum for the GENESIS application is certainly in a different range and could be optimized. The high cooling performance allows defining the system precisely in the design with great freedom like in Figure 57. There is a cross-section of the coolant path through the conductor or a hollow-conductor-wound stator tooth. Especially with weight-optimized machines, this cooling concept makes other cooling methods obsolete [119].

To achieve high power densities, also high-end magnets are needed in the rotor with particularly high tolerance against demagnetization. Which could installed in a Halbach arrangement (Figure 58).

Figure 58 and Figure 59 show an external rotor, which could offer more performance. Our first calculations are based on an internal rotor. This is because a motor with the Halbach array and directly cooled stator windings has already been built in a smaller power class and is currently being tested on the test bench. However, as this is a different project, only selected data can be shared. This motor with its characteristics was adapted to the power class for the GENESIS project. This offers the advantage that the motor with the components is already tested and commissioned. The waveguide cooling technology for this motor is called capcooltech [119].
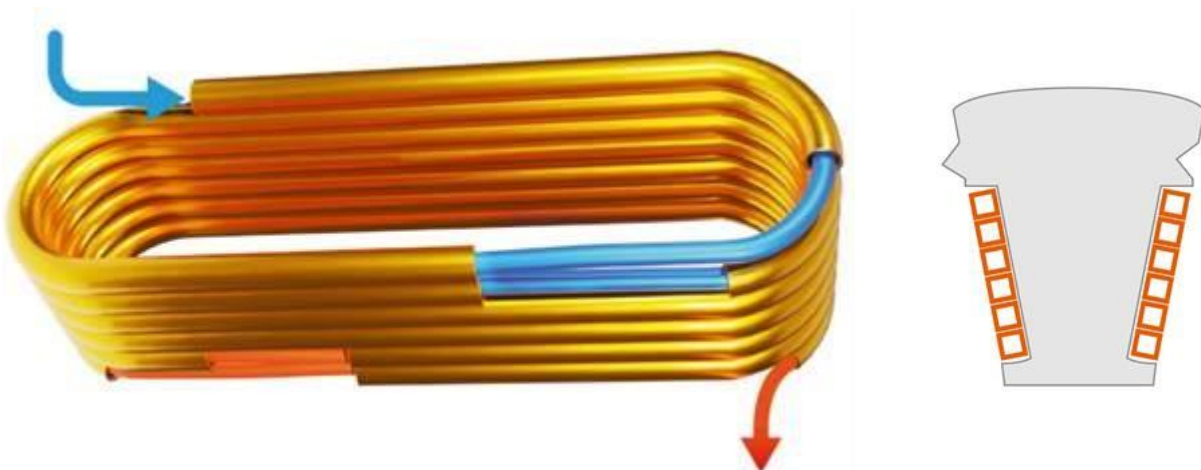
Figure 57. Path of the coolant through the conductor or a hollow-conductor-wound stator tooth in cross-section [119]
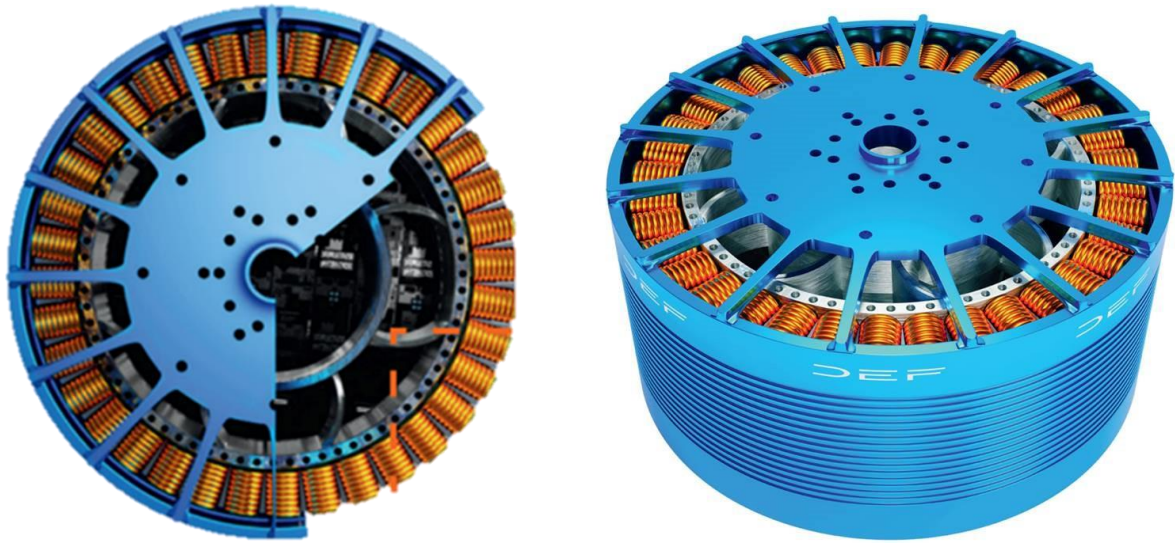
Figure 58. Halbach arrangement for a possible GENESIS Motor in medium-term horizon [119]
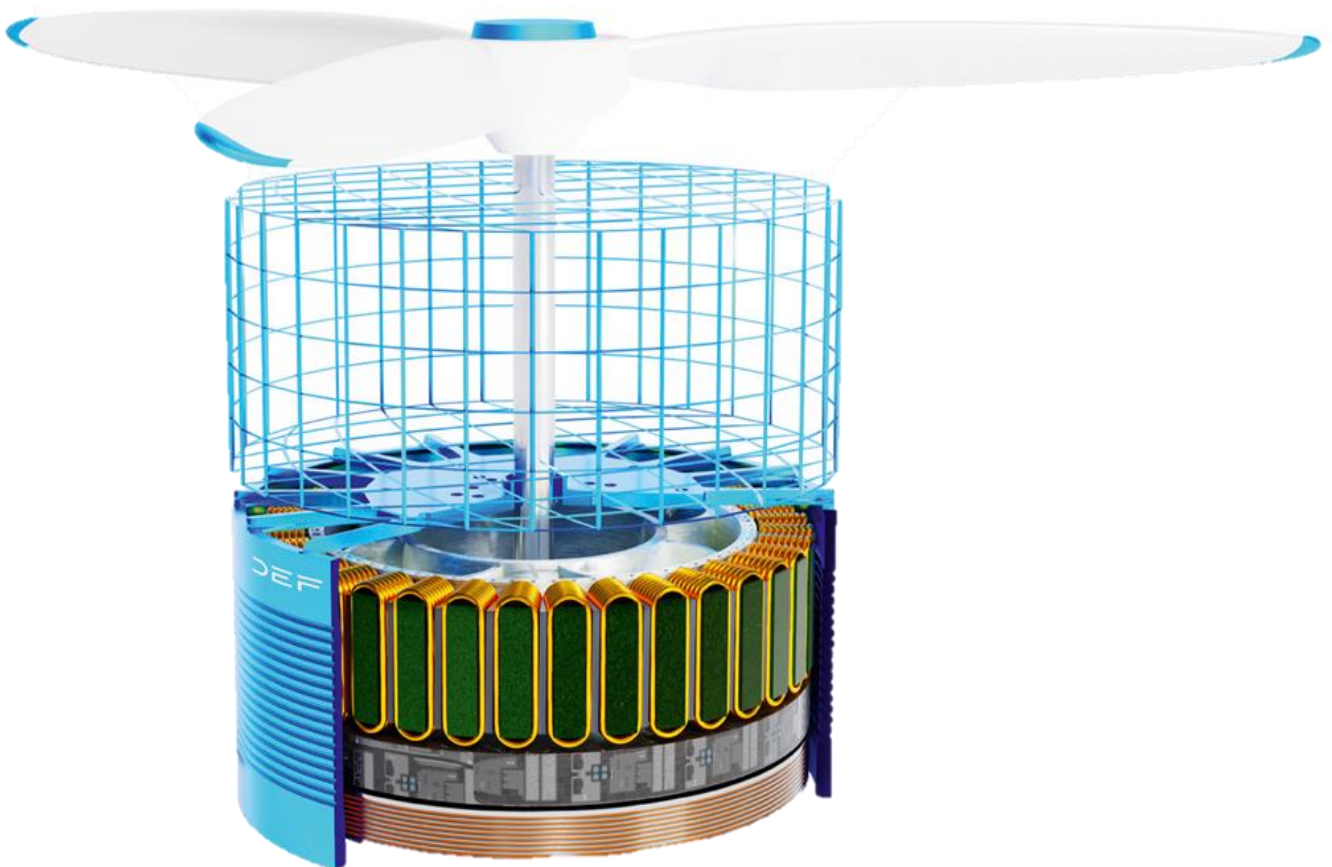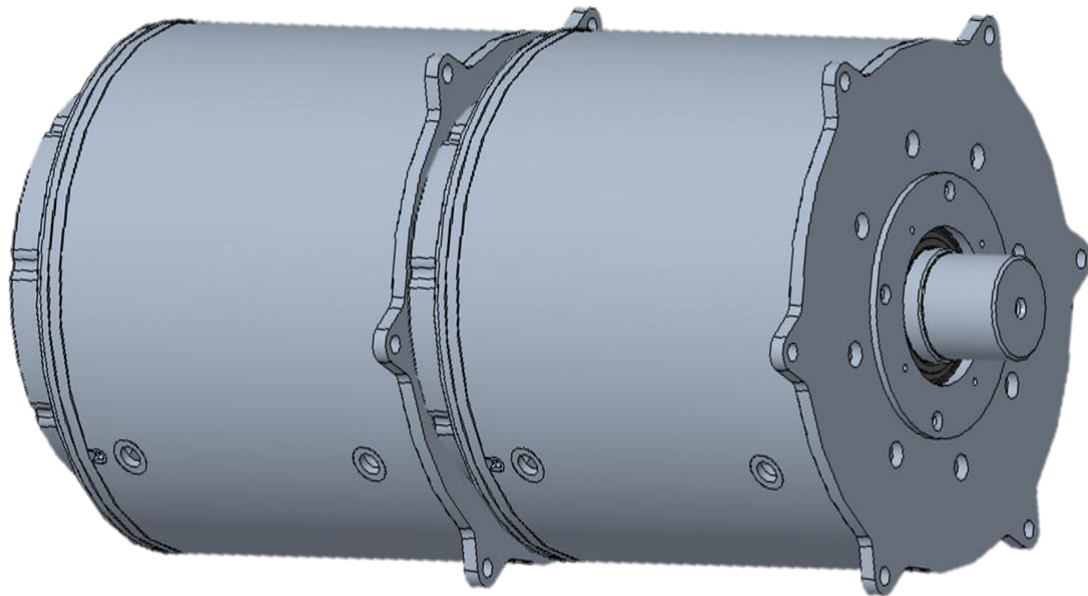

Figure 59. Mechanical design of the secondary electric machine with housing, rotor shaft and propeller [119]

Figure 60. Mechanical design of the primary electric machine as a stacked version of two secondary electric machines for GT-scenario in the medium-term horizon

In Figure 60, the mechanical design of the primary electric machine, as a stacked version of two secondary electric machines.

The motor design presented corresponds to further development of the state of the art used in many battery-powered electric vehicles today. The two topics Halbach array and direct-cooled copper windings are investigated in the new motor design. With a Halbach magnet array, a more sinusoidal magnetic field in the air gap can be achieved than a traditional PMSM. The magnet field density in the air gap is increased, and the iron losses are decreased. With direct-cooled copper windings, the current density and, therefore, the power density can be increased. A higher current density can lead to higher ohmic losses and, therefore, reduced motor efficiency. Hence, a sophisticated investigation is necessary. The primary electric machine can also be further optimized if a new motor housing is designed, which will enclose the active parts of two secondary machines. As a conclusion for the motor design and the comparison with the engine from the short-term scenario, the following statements can be made.

- The engine is in a similar power class
- The new engine weighs only half as much as the engine in the short-term horizon. A large part of this is due to the processing of the carbon material.
- The power density of the active components has more than doubled. The same applies to the power density of the entire engine.

A comparison of the most important engine parameters is shown in Table 55.

Due to the fact that this machine is already being built and tested on a smaller scale, a TRL of 9 can be assumed in the medium-term horizon.

Table 55. Comparison of the electrical machines short/medium-term

Parameter	Value short-term	Value medium-term	Unit
DC link voltage	800	800	V
Nominal phase current 3-phase	770	1002	A_{RMS}
Nominal phase current 6-phase	385	530	A_{RMS}
Nominal power	554	607	kW
Nominal torque	993	2900	Nm
Nominal speed	5633	2000	rpm
Estimated efficiency	96	92	%
Length active parts	180	119	mm
Outer diameter housing	265	478	mm
Active parts weight	52.3	30,8	kg
Total weight	86.5	40-45	kg
Continuous power density for active parts	10.6	23.7	kW/kg
Continuous total power density	6.4	13.5-15.2	kW/kg

7. On-ground energy supply technology analysis

7.1. Introduction

The on-ground energy supply technology analysis focuses on analyzing appropriate energy supply technologies for on-ground energy storage, grid connection, and energy transfer to aircraft Since this year, the regional airport Rotterdam The Hague Airport, through subcontractor RHIA, is involved in the Genesis project and provides specific data and modelling experience for the different energy supply systems. This includes the local systems and infrastructure for the supply of sustainably generated electricity and green hydrogen.

Therefore, the regional airport will be presented first. Then the grid structure and what is planned at the airport will be explained in detail. In addition, suggestions for fast charging stations will be given. The concepts will be further evaluated and concretized in the following Chapters. Open questions that could be answered include the total energy demand, the connection to the power grid, the number of hybrid/electric aircraft to be charged, the maximum available charging time, the possibilities for installing local photovoltaic systems, and energy storage units. A charging profile for the aircraft batteries was created, and the peak power demand could be determined. Suggestions are given for charging and refuelling the aircraft.

For the medium-term time frame (2035-2045), the aircraft will use a fuel-cell system, and therefore the on-ground hydrogen storage and supply will play an important role. This topic has been briefly introduced in Chapters 5 and 6 and will be examined and presented in the following for medium-term technology analysis for all important technologies.

7.2. Rotterdam The Hague Airport (RTHA)

Rotterdam The Hague Airport (RTHA) offers 24 hours a day, 365 days a year, a home base for airlines for scheduled and vacation flights, business flights, and social air transport (such as police helicopters). RTHA is the regional airport for the Rotterdam/The Hague area and facilitates air traffic for about two million passengers annually. This makes RTHA the third largest airport in the Netherlands in terms of passengers, connecting fifty European flight destinations from the region, mainly also regional airports.

The adaptation of RTHA to accommodate (hybrid)-electric and hydrogen aircraft will require adaptations in fleet and infrastructure, which impact safety and emissions at the airport.

Furthermore, it will definitely require large investments and high costs in the early years, but it could also bring a competitive advantage due to early adaptation to new technologies.

In the case of airports, technology is not only at the core of its business but is also interdependent with airlines´ and passengers' needs. As such, adaptation to the changing needs of customers will be key for the positioning of the 'RTHA in the future.

By adapting the HE and LH2 aircraft traffic early, RTHA can strengthen its position in the area. For instance, RTHA could gain market share in the early years due to its capability to accommodate HE and hydrogen traffic, leading to the airport being a main European hub for future, more sustainable aircraft. An overview of the Airport is given in Figure 61.

For RTHA, the number of hybridized and fully electrified aircraft has been forecasted based on the available technologies in 2030 (2025-2035), 2040 (2035-2045), and 2050 (2045-2050). In 2030 the first hybrid aircraft are introduced, while most of the fleet is still kerosene-fuelled. In 2040 the share of hybridized aircraft increases, and even some fully electric (battery) powered aircraft are introduced. In 2050, almost all movements on RTHA are assumed to be hybridized or fully electric [120].

Figure 61. Overview of RHTA [120]

7.3. Facts of RTHA and Status quo

RTHA has a Surface area of 220 ha and 110 Employees today. More details are listed in Table 56.

Table 56. Facts RTHA [120]

Flight movements	Year	Value
Line/Charter air traffic	2019	16.683
	2020	5.314
	2021	6.164
Aviation (>6 ton)	2019	21.049
	2020	7.964
	2021	10.642
General aviation (>6 ton)	2019	31.390
	2020	30.689
	2021	35.437
Passengers	2019	2.133.976
	2020	497.078
	2021	754.161

More than half of all flights at Rotterdam Airport are performed using a small 0 – 19 passenger aircraft over 0 – 1,000 km, many of which are training flights. Another group of frequent

flight/capacity combinations are flights with a seating capacity of 100 – 150 over 0 – 3,000 km, with the bulk of flights between 1,500 and 3,000 km. A smaller but significantly large group of flights is performed by aircraft with a seating capacity of 20 to 100 passengers over 0 – 1,000 km. Furthermore, it is estimated that around 10% of flights are helicopter flights [120].

*Electrical-Grid and Solarpark at the airport*

Electric energy can be drawn from the grid or the solar energy produced at the airport. When electric energy is drawn from the grid, this can be done on an as-needed basis. The public network around RTHA is managed by Stedin. They provide the connection of roughly 2.3 million households and business connections and are proactive in supporting sustainability. By integrating the previously separate energy flows of gas, heat and electricity, Stedin offers the flexibility needed to fit a large share of renewable energy into the energy system. For instance, the solar park at RTHA is directly connected to the Steding network. For example, if there is a surplus of electricity, this can be converted into hydrogen (power-to-gas).This, however, means that the electricity grid will deal with high peak powers, which must meet the demand. The option to avoid high peak loads to the grid is to implement battery swapping and optimize the swapping such that the electric power drawn is distributed more throughout the day. Additionally, RTHA produces solar electricity on site. An overview of the Airport Grid connection is shown in Figure 62. Also, an overview of the Solar Park is given in Figure 63 and Table 57 shows the current situation of the electricity production and consumption of the airport [120].
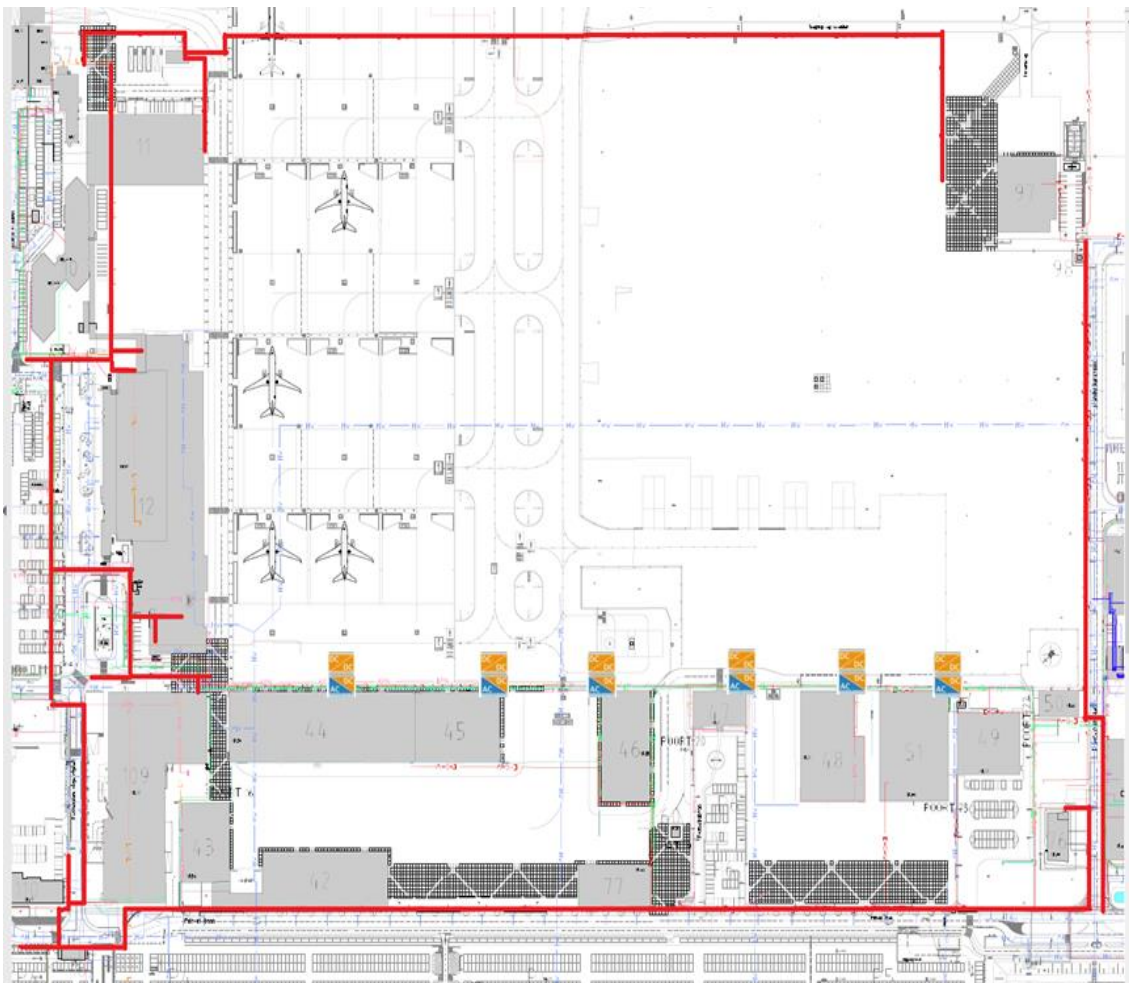
Figure 62. RTHA-Grid connections to the Stedin grid [120]

Table 57. Current Status RTHA [120]

Topic	Comment and Facts
Grid	Multiple connections (20+)
	Stedin grid (10kV / 400V)
	Combined Tree / Bus grid topology
Solar Farm	13,6 MWp solar farm - Airside, next tor runway
	870 kWp roof top solar – Buildings airside
Annual production electricity	12,5 GWh/year - Airside, next tor runway
	0,8 GWh/year – Buildings airside
Annual consumption electricity	6 GWh/year
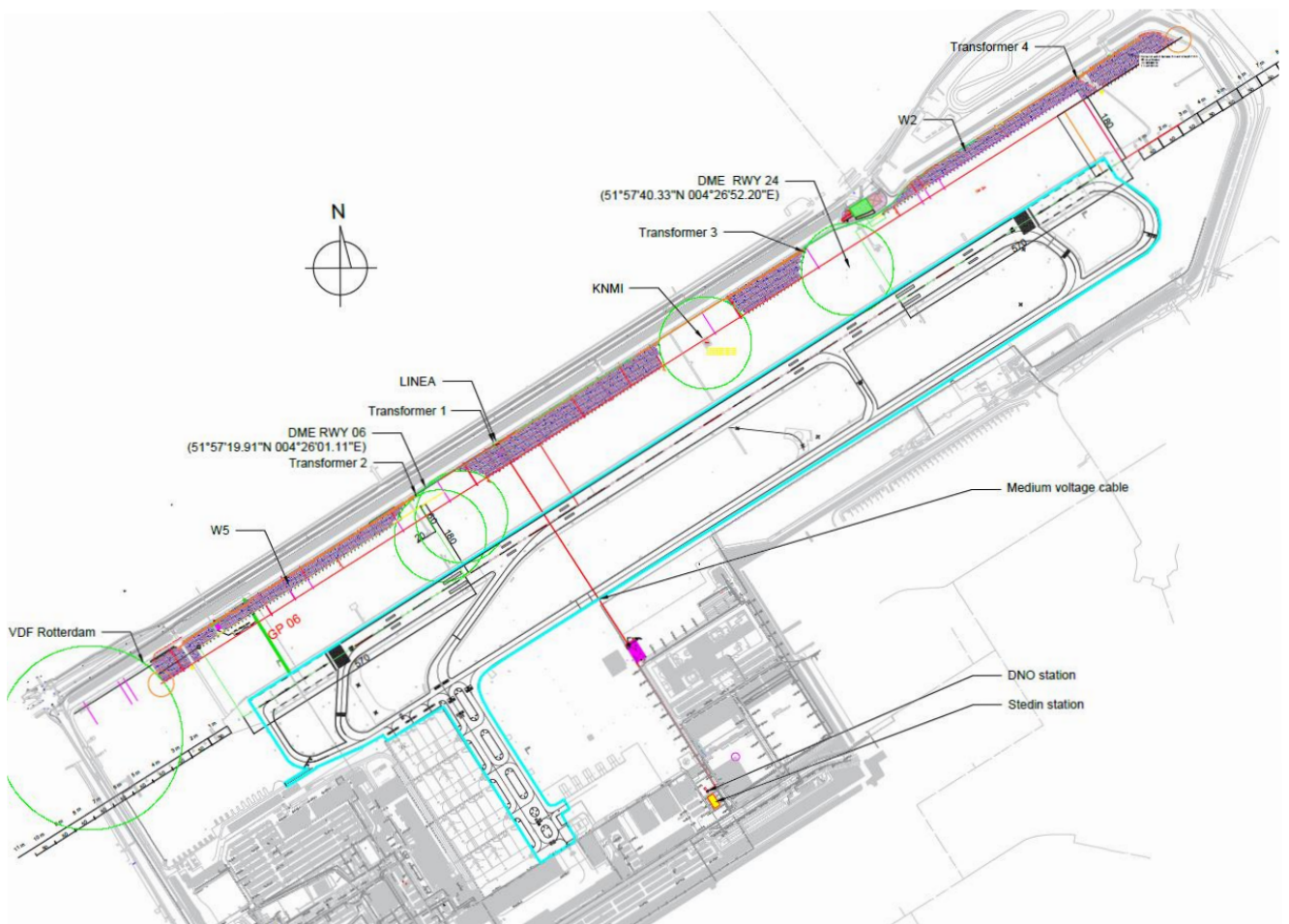
Figure 63. Solar Farm RTHA [120]

Electrical-Aircraft Energy supply

On RHA there is a limited amount of infrastructure and equipment for take-off, landing, taxiing, parking, handling and other activities. The infrastructure is partially built around existing aircraft types and changes to aircraft is bound to have effect on the infrastructural and equipment needs from airlines of airports. Smaller electric aircraft may ramp up aircraft numbers and movements on the ground putting strain on currently available airport capacity.

The network of of RTHA is strongly dependent of the airlines that operate on RTHA and the aircraft that they use in operation. If airlines like Transavia phase out some of their older aircraft and phase in the new Airbus models with different properties, this will have an impact on the network of RTHA on which that airline operates or will operateDuring the transition the airport's infrastructure will need adaptation to efficiently supply electric power to aircraft.

Alternate Current (AC) charging is not a feasible option due to the long time periods required for charging. Direct Current (DC) charging, also known as fast charging, is predicted to compete with turnaround times of smaller conventional aircraft up to 70 pax in case four to eight 120 kW charging stations are used for charging up to 80% SoC. For the short-term, it is expected that only small aircraft will be electrified. At this time only several very small (<5pax) aircraft are electrified. However, different companies have announced projects that should deliver hybrid or full electric passenger aircraft between 1 and 19 seats and that can fly up to 1500km before 2030. Due to many of the training flights at Rotterdam Airport being flown with aircraft with less than 5 seats over small distances there is a big potential for a (hybrid-)electric substitute aircraft with the earlier assumed properties (0-1500km 0-20pax) [120].

E-aircrafts under consideration :

- The hybrid e-heli has a battery capacity of **100 kWh** for flights up to 750 km.
- The Airbus helicopter type H130. Airbus Helicopters is also working on a high voltage "Start and Stop" electric system that should fly next year on the company's Rapid and Cost-Effective Rotorcraft (RACER) demonstrator
- For 0-20 PAX, the type of "small aircraft" is specified as
    - the Pipister Vilas Electric **27 kWh 2 PAX**
    - the Eviation Alice **820 kWh 11 PAX**.
- For 20-100 people, the "large aircraft" type is like a Venturi Echelon 01 **9 MWh 44 PAX**

Charging assumptions:
Until 2030, the charging speed is 1 MW. After that, 2 MW should be realized. Including the possibility to use 4-8 MW batteries for multiple connection charging. Table 58 shows the average daily amount of turnarounds for (hybrid) electric or hydrogen aircraft at RTHA in 2030, based on the fleet forecast to make the infrastructure forecast robust for busier peak days. The approximation of 1/3 more traffic on busy days was made based upon RTHA's 2019 flight data per month [120].

Table 58. Average daily turnarounds at RTHA in 2040 [120]

pax	Hybrid electric A/C	Hydrogen	Hybrid Helicopter
0-19	30.5	-	3.4
20-99	1.7	1.7	-
100-149	-	3.4	-
150-209	-	<1	-
210-299	-	<1	-

Table 59 Electric infrastructure in 2040 for two power supply options [120]

In case of electric charging at the gate	Average	Maximum
Gates equipped with chargers or A/C charge stations	7	45
Helicopter chargers	1	1
In case of battery swap		
Charge points	4	4
Spare batteries small	7	9
Spare batteries large	8	8
Helicopter chargers	1	

Plug-in battery charging (Table 59) :

Eight charge points would suffice for regular operations (under "average" in the table), seven for regular aircraft and one for helicopters. In the case of last-minute changes in the flight schedule or if flights are extremely concentrated around peak hours, 45 charge points would be needed to cover demand without delays. This number may seem high; the reason for this is that the model assumes that one battery can be charged by multiple chargers to speed up the turnaround time.

In the case of last-minute changes in the flight schedule, or if flights are extremely concentrated around peak hours, 45 charge points would be needed to cover demand without delays. The model assumes that one battery can be charged by multiple chargers to speed up the turnaround time.

Battery swapping:

In the case of battery swapping, four aircraft charge points would suffice (besides one helicopter charge point). For small aircraft, seven batteries were calculated to enable the airport to meet demand in the case of an average flight schedule, and nine would be sufficient on rare days of high demand. Eight spare batteries were calculated to meet the demand on both average and extreme days for larger aircraft.

Hydrogen supply to the airport:

Most airports are supplied with jet fuel by road transport (trucks). There are three main options for supplying to the airport for liquid hydrogen, namely cryogenic road transport, onsite electrolysis and liquefaction, and cryogenic pipeline.
The feasibility of liquid hydrogen supply:
- Delivering liquid hydrogen from A to B is feasible today and will be possible when hydrogen aircraft become available between 2025 and 2040.
- Both means of transport by cryogenic truck and electrolysis are commercially available technologies to supply hydrogen to the airport. Transport by cryogenic pipeline is a standard technology for offshore and space applications, so it is expected to be technically possible (although expensive) for airport applications [120].

Hydrogen storage:
Storage for liquid hydrogen would have to be in a cylindrical, cryogenic tank, either above or under ground. Whether the strict safety requirements and the operational efficiency of the airport environment can be maintained for these storage solutions has not yet been demonstrated.

Aircraft liquid hydrogen supply:

There is a choice to be made in terms of hydrogen supply to aircraft, which significantly influences the operation and scheduling aspects of an airport; direct fuelling of hydrogen to the aircraft or swapping of hydrogen canisters. The advantage of swapping canisters is that no hydrogen fuelling activities have to take place in the chaotic environment of the apron and airport airside in general. The concept is shown in Figure 64. The disadvantage is that the safety and quality of every individual tank must be ensured in some way, which makes it challenging from an airworthiness and certification point of view.

Liquid hydrogen refuelling is ready to be demonstrated in an airport environment, but a canister swap only exists on paper [120].
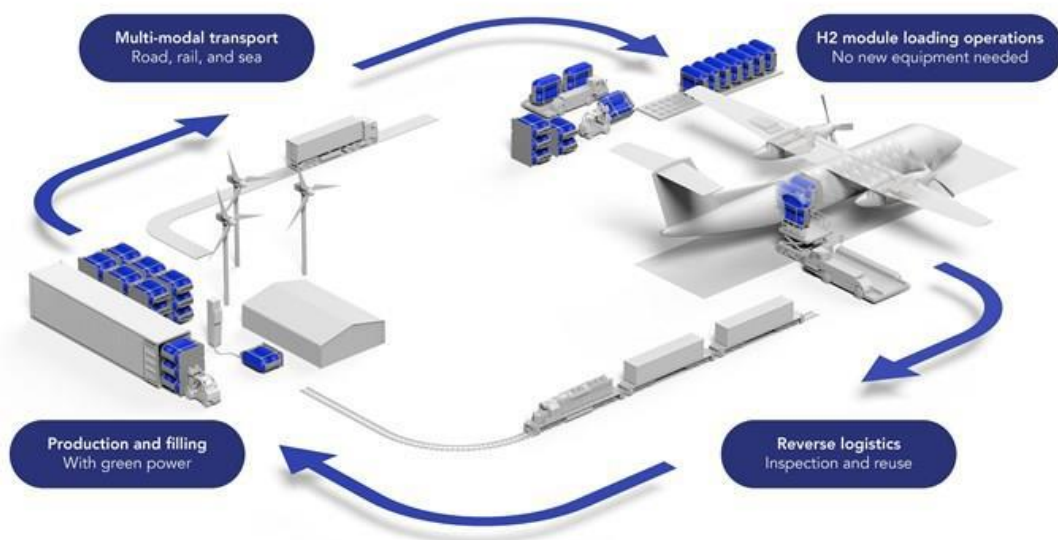
Figure 64. Hydrogen Tank swap system [121]

E-aircrafts under consideration:

- For the 20-100 PAX hydrogen aircraft, Universal Hydrogen's Bombardier Dash-8 was used, which is assumed to have two tanks.
- For the 100-150 PAX hydrogen aircraft, Airbus' ZEROe turboprop concept was taken, which is assumed to have eight tanks.

Charging assumptions:

- Hydrogen tanks have a volume of 2.5 m^3.
- Hydrogen fuelling takes 30 minutes per tank, based on the assumption that 5000 l/h will be realistic.

Hydrogen Infrastructure (Hydrogen refuelling):

If cryogenic refuelling at the gate is performed, two gates equipped with a cryogenic refuelling installation will suffice for average days. On extremely congested days, seventeen fuel points would ensure that demand is met. The assumption leading to this high number is that different fuelling installations can fuel an aircraft simultaneously to decrease turnaround time.

Table 60. Hydrogen fueling options [120]

| In case of hydrogen fuelling at the gate	Average	Maximum
Gates equipped with cryogenic fuelling installations	2	17
In case of a swap with hydrogen cartridges		
Cartridge refuelling station (on- or off-site)	1	2
Spare cartridges	21	25

Hydrogen canister swap:

In the case of canister swapping, one cartridge refuelling station and twenty-one spare tanks are required. To accommodate extreme congestion, two charge points and twenty-five spare cartridges would ensure that demand is met and delays are prevented.

Table 61. Overview of seat bands and comparable aircraft in 2019 for RTHA [120]:

Number of seats (pax)	Comparable 2019 aircraft type
0 – 19	E.g. P28A, C172, DR40, F900, E35L
20 – 99	E.g. E170, CRJ2, F100, AT75
100 – 149	E.g. B737, A319
150 – 209	E.g. A20N, A321, B752
210 – 299	E.g. A21N, A332, B762

The propulsion type of the aircraft differs from kerosene-fueled to hybrid- and fully electric. While it is realistic that higher blending ratios of SAFs will be mandatory soon, the focus is on the hybrid- and fully electric propulsion types. It should be noted that both battery and hydrogen-powered aircraft are considered. The range and capacity of aircraft are dependent on several elements like weight (during the whole flight), the amount of energy on board, aerodynamic aspects, size and power, and efficiency of the engines. The flight range and capacity differ from one aircraft to another. All airports receive a particular mix of aircraft types with differing ranges. For example, the distribution at Schiphol Airport has a great variety, with short, medium, and long-range aircraft. RTHA offers more space for mainly short or short to medium flight range aircraft. Table 61 gives an overview seat bands and comparable aircraft in 2019 for RTHA

Highlights of the transition study of Rotterdam The Hague Airport:
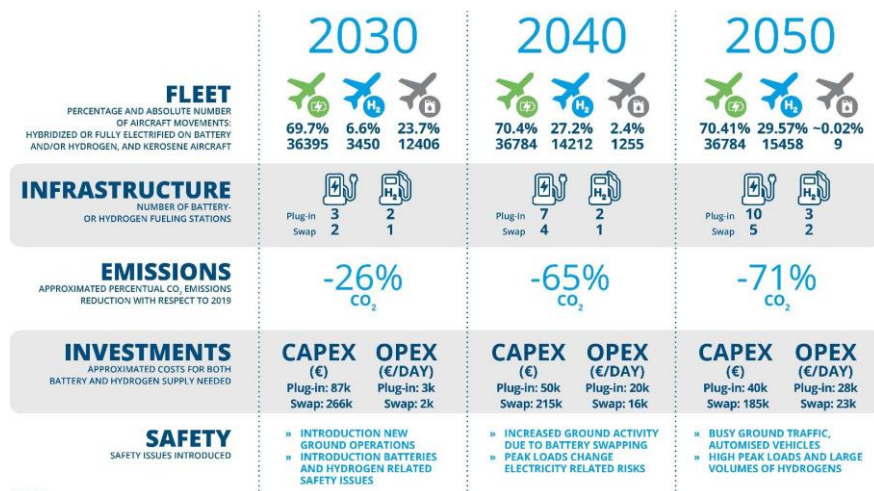
Figure 65. Infographic on transition through the years 2030, 2040 and 2050 for the fleet composition, infrastructure, emissions, investments and safety [120].

The numbers provided for investment costs are an estimation caveat several assumptions and limitations: (1) the calculations are infrastructure-focused, meaning that they not include costs associated with personnel or land/storage locations; (2)prices were estimated based on online sources and/or previous literature and are likely to change over time; (3) depreciation costs were not taken into account [120].

7.4. On-ground battery technology

The wide usage of hybrid or electric aircraft will require the airports to adapt and re-organize their infrastructure. For this reason, it was decided to investigate different energy storage solutions to answer the high demand for energy that the aircraft will require while on-ground.

7.4.1. Al-ion batteries

Despite the successful commercialization of LIBs, the limited lithium resources and safety related problems are hard to comply with the increasing energy storage requirements. As an alternative, metal-ion rechargeable such as Aluminum-ion batteries (AIBs) are also attracting recent interest [14].

AIBs are a promising candidate thanks to the abundant aluminum material and its low price. Additionally, Al metal anode can exchange 3 electrons during the process and thus, delivers superior theoretical specific volumetric and gravimetric capacity. Additionally, the ease of operation of Aluminum in an ambient environment greatly improves the AIB´2 safety.

However, the search for suitable cathode materials is still on going as graphite has a low specific capacity and other materials candidates suffer from cycling stability or poor kinetics. On the other side, Al anode suffers from dendrite growth and passivation layer formation, similarly to Lithium metal anodes. Additionally, costly electrolytes are currently needed to prevent commercial applications. However, such technologies could become great options for the airport´s on-ground energy storage approach. Indeed, such technology would feature good performances (~200-300Wh/kg), high safety, low costs, and more sustainability.

7.4.2. Sodium-ion batteries

Due to the natural abundance and low-cost of sodium resources, sodium-ion batteries (SIBs) are becoming one of the most investigated alternatives to LIBs to fulfil the demand for residential or large energy storage systems. SIBs are not a new concept [122], however, research focused mainly on LIBs thanks to their high theoretical performances. Although SIBs do not show comparable performances, they still provide a scalable solution for large scale energy storage systems with high adaptability and high efficiency, such as the on-ground electrical system that an airport could present.

SIBs could profit greatly from the mass commercialization of LIBs as most of the knowledge and experience are directly transferrable to SIBs, which could significantly decrease the time to market needed for the mass commercialization of technology. It was also shown that the SIB electrodes could deliver a specific capacity comparable to or even higher than their corresponding LIB counterparts. They also demonstrated impressive ultra-long cycle performance [14]. These achievements provide hope for developing SIBs for grid-scale energy-storage applications. The main challenge to handle with SIBs is the large ionic diameter of Na, which leads to the need for particular cathode materials (large interstitial space in the structure). Sodium-ion batteries would feature good performances (~200 Wh/kg), low cost and sustainable materials.

7.4.3. 2nd life batteries

Another approach to designing a fraction of the energy storage system of the airport could also gain interests. Indeed, it is possible to integrate second-life batteries from other applications such as EV's. These batteries are usually still in a good state (~80/90% SOH) and still offer many cycles before there is the need for them to be recycled. Considering the increasing volume of EVs sold every year,

second-life batteries for stationary energy storage could represent a cheap and sustainable solution to designing airport energy storage systems.

7.5. Dimensioning of fast-charging stations

A short introduction is needed to design fast-charging stations for aircraft further. In terms of the lower voltage levels of the battery system in the medium-term, which is also discussed in chapter 5.5, higher supply currents are necessary to provide the high power demand for a charging time of 45 minutes.

The limits of the combined charging system (CCS) standard for electric vehicles should also be used as a reference in the short-term horizon. The CCS is the preferred charging standard used in Europe and Northern America. It currently allows charging with up to 350 kW and a maximum voltage of 1000 V. For the medium-term analysis, it is a reasonable estimate that market-available DC fast chargers will suffice to charge a regional aircraft to 80 % state-of-charge (SoC) within half an hour.

For the aircraft charger, the WP2 battery design is taken into consideration. The parameters of the battery are summarized in Table 62.

Table 62 Electrical parameters of the aircraft battery system

Parameter	System-level
Upper voltage limit	681 V
Nominal voltage level	600 V
Lower voltage limit	454 V
Capacity	410 kWh
Charging current	683,3 A (1C), 1025 A (1,5C) 1366,67 A (2C)

The battery's voltage limits set the output range of the charger, while the 2C rate defines the maximum output current. Because of the lower battery voltage, a much higher current is considered. Due to the very high charging currents, charging the aircraft with two charging stations in parallel is suggested. The reason for this is that the currents of the individual cables can be reduced, the cables can be cooled, and the battery system can be charged at full power. A better overview is provided in Figure 66.

Therefore, a DC fast-charging station for one GENESIS aircraft with at least a power of 820 kW is needed to charge the aircraft in one hour. The aircraft has two identically 410 kWh battery packs. As a result, four DC fast-charging stations per aircraft are needed. Overall, the charging requirements and the size of the battery pack are comparable to battery-electric trucks like the Tesla Semi. A new charging standard, called the "Megawatt Charging System" (MCS), for high power charging of commercial vehicles is under development by CharIN (Charging Interface Initiative e.V). The maximum charging power will be 3.75 MW with a voltage limit of 1250 V and a current limit of 3000 A [123]. Once this megawatt charging system is ready for the market, a charging station could theoretically be used to charge the aircraft. However, the security of supply via the local grid at the airport must always be guaranteed. The MCS standard will meet the charging requirements for the aircraft in the GENESIS project for all time horizons.

Due to safety concerns, a galvanically isolated charger has to be used. While there are currently no standards that would prevent using non-isolated converters, the application is comparable to the current standards for road vehicles. Each charging point needs to be isolated due to safety concerns.

Figure 66. Fast Charging with two parallel stations per wing [124] [125]

Due to the high power demand, building a modular charging system with single modules in the < 100 kW range is recommended to reduce the strain on single components. Using the same modules but with a different total number for the aircraft charger and the other chargers for airfield support vehicles is viable. Topology-wise, the power requirement alone disqualifies simple switching converter topologies, like the Flyback converter, since they would require a bulky transformer and filter components. To utilize the entire operating range of the transformer and reduce the strain on the semiconductors, a full bridge topology should be used on the primary side. The most common topologies resulting from that would be the Dual-Active-Bridge (DAB) and the resonant LLC converter in full-bridge implementation, as shown in Figure 67 and Figure 68.
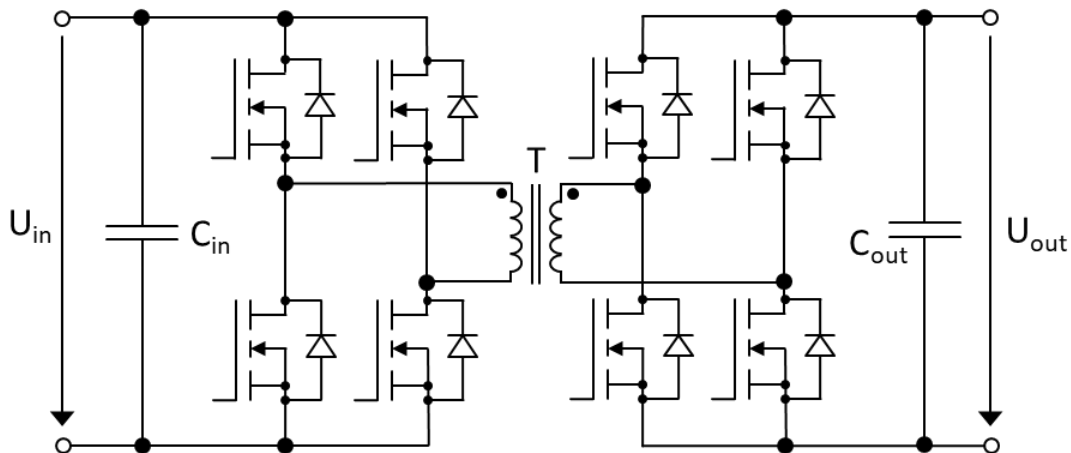

Figure 67. Dual-Active-Bridge converter
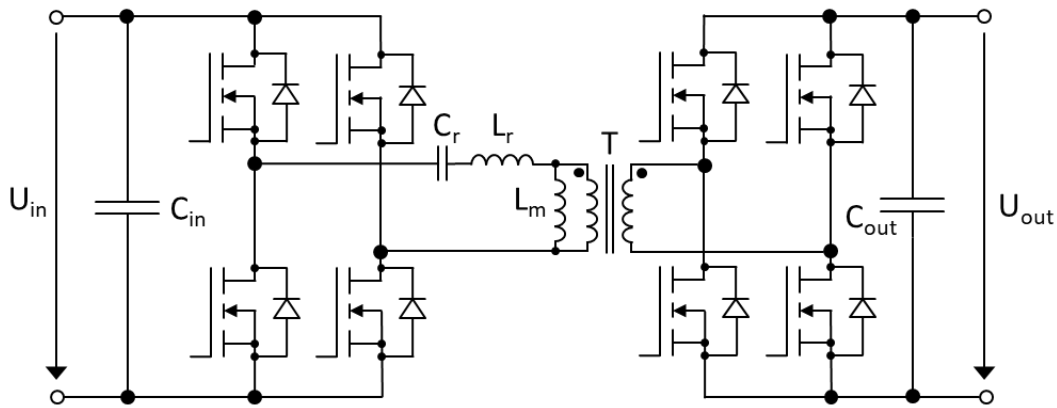
Figure 68. LLC resonant converter

As it can be seen, the primary switching circuits are the same, but the transformer path is different. With both topologies, ZVS (Zero-Voltage-Switching) and ZCS (Zero-Current-Switching) can be achieved to increase the switching frequency, optimize the magnetic components, and increase the efficiency. The LLC offers good EMC behaviour and high efficiency at its nominal operating point, but its efficiency falls considerably outside the nominal area. The efficiency of the DAB is high over a broader operating area, although it does not meet the peak efficiency and the EMC performance of the LLC. Depending on the modularization, both topologies can be used for realizing the charging systems.

A possible arrangement or construction of a potential 615 kW fast-charging station coul already be realized with ABB´s 175 kW power units. The proposal would be to connect four power units in parallel, as shown in Figure 69. This would allow a maximum power of 700 kW [126].
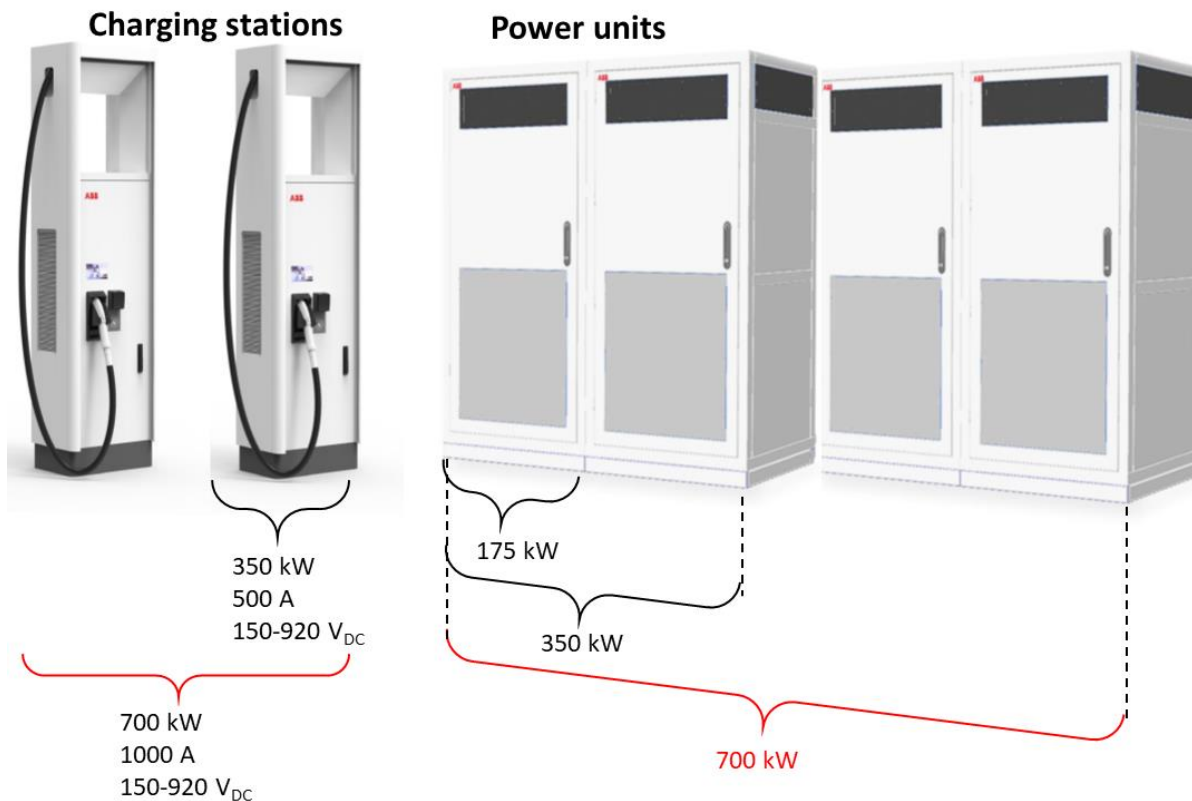
Figure 69. Possible arrangement of fast-charging stations for required GENESIS power, according to [126]

ABB already offers 350 kW fast-charging stations for electric vehicles. One of these charging stations or power modules is located at Fraunhofer IISB in Erlangen and is shown in Figure 70 with the corresponding components. The components of the power unit are also visible. The transformer, which serves as galvanic isolation, is also important here [126].
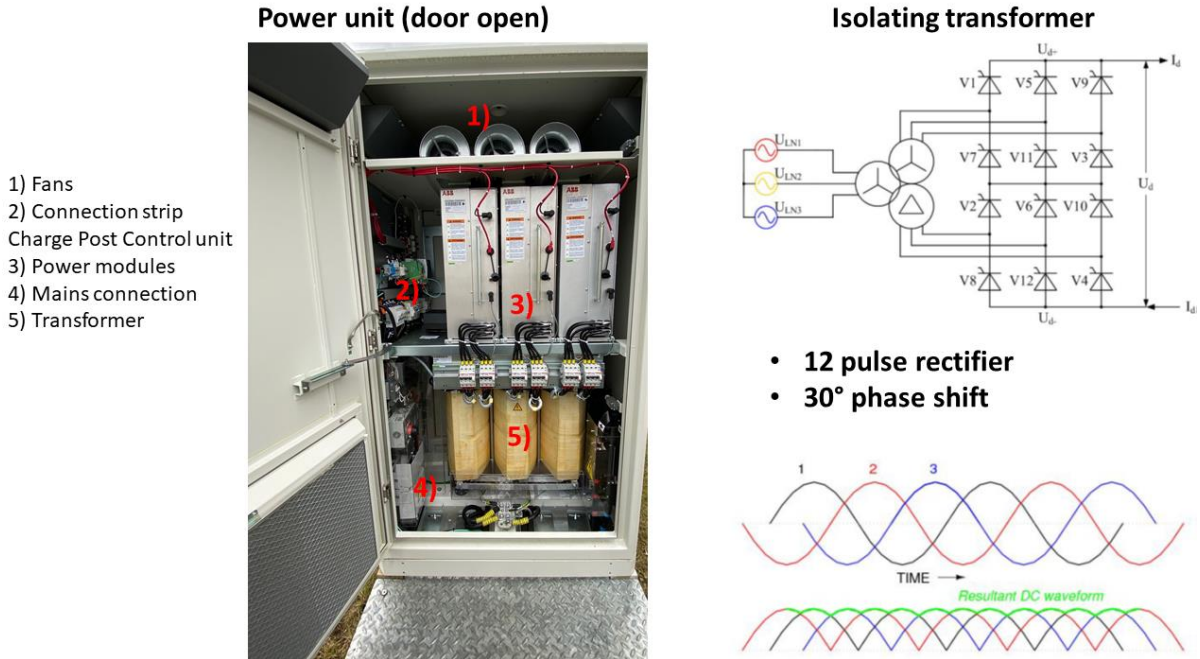
Figure 70. Opened power unit and transformer for galvanic isolation at Fraunhofer IISB in Erlangen

175 kW cable from power unit

1) DC +
2) DC -
3) Protective conductor
4) Liquid tube to the plug
5) Communication lines

Figure 71. Opened fast charging station (350 kW) and cable for EV charging at Fraunhofer IISB in Erlangen

In Figure 71, on the left, the opened quick charging station is illustrated. Two parallel DC cables from the power unit, which can deliver 350 kW of power, are connected to the fast-charging station. Therfore, it would be possible to connect another of these charging stations in parallel. With four power modules and two fast-charging stations, the charging capacity would reach 700 kW.

However, the cable design is not yet designed for such high power, which has already been discussed. If one were to think further, it would already be possible today to charge the GENESIS aircraft with four fast-charging stations and eight power units in 45 minutes using ABB's design.

Since only trained specialists should be considered for connecting the charging stations to the aircraft, the connecting cables between the aircraft and the charging station can be developed lightly differently and do not have to meet the high safety standards of the charging cables for electric cars for example. The cables and the high currents they transmit make cooling, the safety concept and the cable design very complex. If only trained personnel can do this, other cable designs could be considered, and a charging station for an aircraft might be feasible. This will be further investigated in the long-term horizon.

7.6.   Simulations and results of modelling an on-ground-energy-supply-system

Matlab-Simulink is used to build a simulation model for the airport's on-ground energy supply system. The load profiles of the airport, the fast-charging stations, and other consumers are to be integrated into this simulation model to simulate and estimate the power flows and the network utilization at the airport due to the considerable increase in the required electrical energy. FAU-LEE created a model of the current situation at Rotterdam Airport. The two fast-charging stations are currently being planned but will be implemented in the simulations. The fast-charging stations in Figure 72 can be used to charge one GENESIS aircraft. On each wing could be made one connection to the aircraft. The first step was to simulate airport´s performance, and therefore, the fast-charging stations were built as an ideal load. The load profile of the airport was determined for 24 hours and transferred to a table as a variable load. Since, in the Netherlands, the airport's PV system must first feed into the transmission grid, the PV system is not included in the simulation for the medium-time horizon.
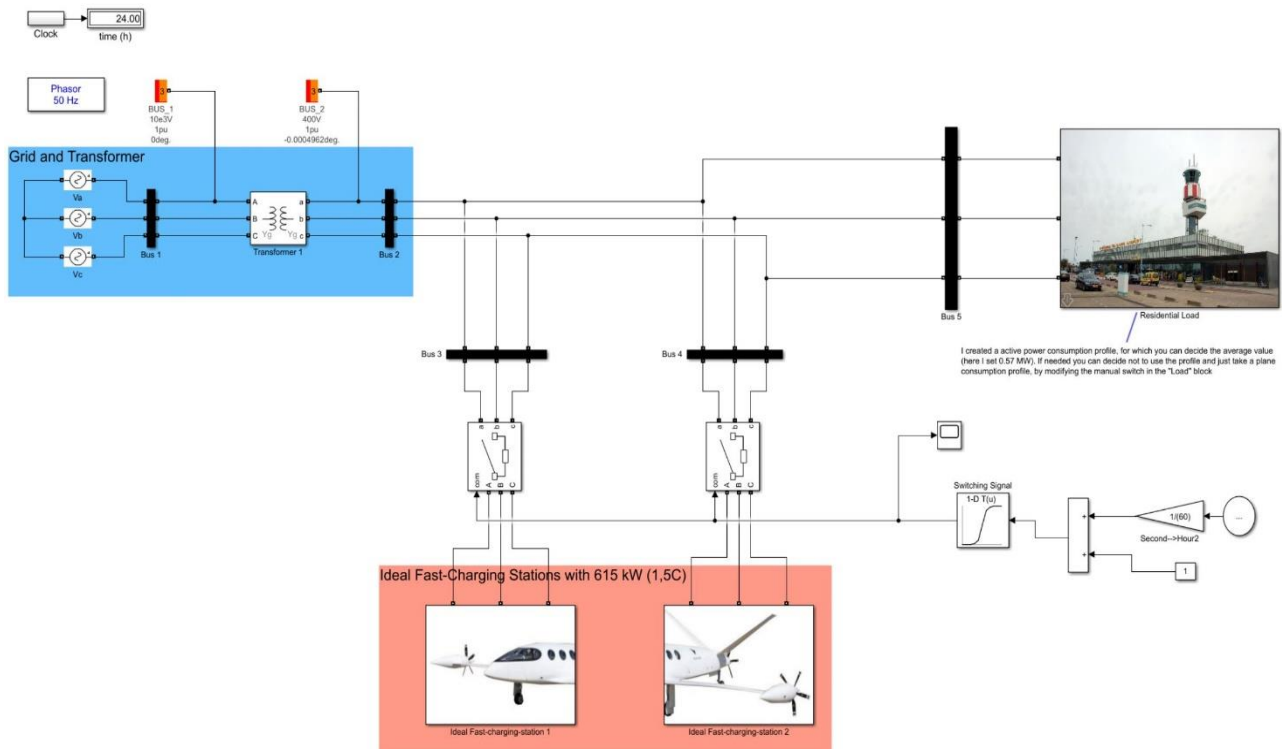

Figure 72. Overview of the first model for RTHA Airport

A switching signal was added to the model to determine the charging cycles of the aircraft with ideal switches. As already mentioned, the planned charging time for an aircraft is 45 minutes. This switching signal itself is given by a logic table generated by a function written in Matlab.

The input and output of this function are defined as:

```
function switch_table = chargePwmTable(sim_time, charge_time, buffer_time, start_time, end_time)
%    This funtion creates a variable time table with boolean expressions for a switch in an pwm fashion.
%    Inputs:
%      sim_time:      Simulation Time [min] (integer)
%      charge_time:   Time of a single battery charge [min] (integer)
%      buffer_time:   Time between a battery charge [min] (integer)
%      start_time:    Time to start charging processes [h] in 24h format (integer/double)
%      end_time:      Time to stop charging processes [h] in 24h format (integer/double)
%    Output:
%      switch_table:  Time table with boolean values
```

The inputs of this simulation example were selected as:

"charger1_table = chargePwmTable(24*60, 46, 14, 6, 16);"

Due to programmability, the charging time is 46 minutes, as the increase in power is delayed by 1 minute compared to the logic signal. For a short-term horizon solution to reach the charging capacity of 45 minutes, the logic signal was extended by 1 minute. The buffer time was set to 14 minutes for convenience so that the pattern repeats after 1 hour. The resulting power flow for chargers 1 and 2 can be seen in Figure 73. This clearly shows that 615 kW active power (P: active power/charging power) is delivered to the aircraft, which makes sense in the other modelling, as the aircraft is charged with DC power. Due to the DC charge, the reactive power (Q) is zero, because in a DC charging, could´t be measured a reactive power.
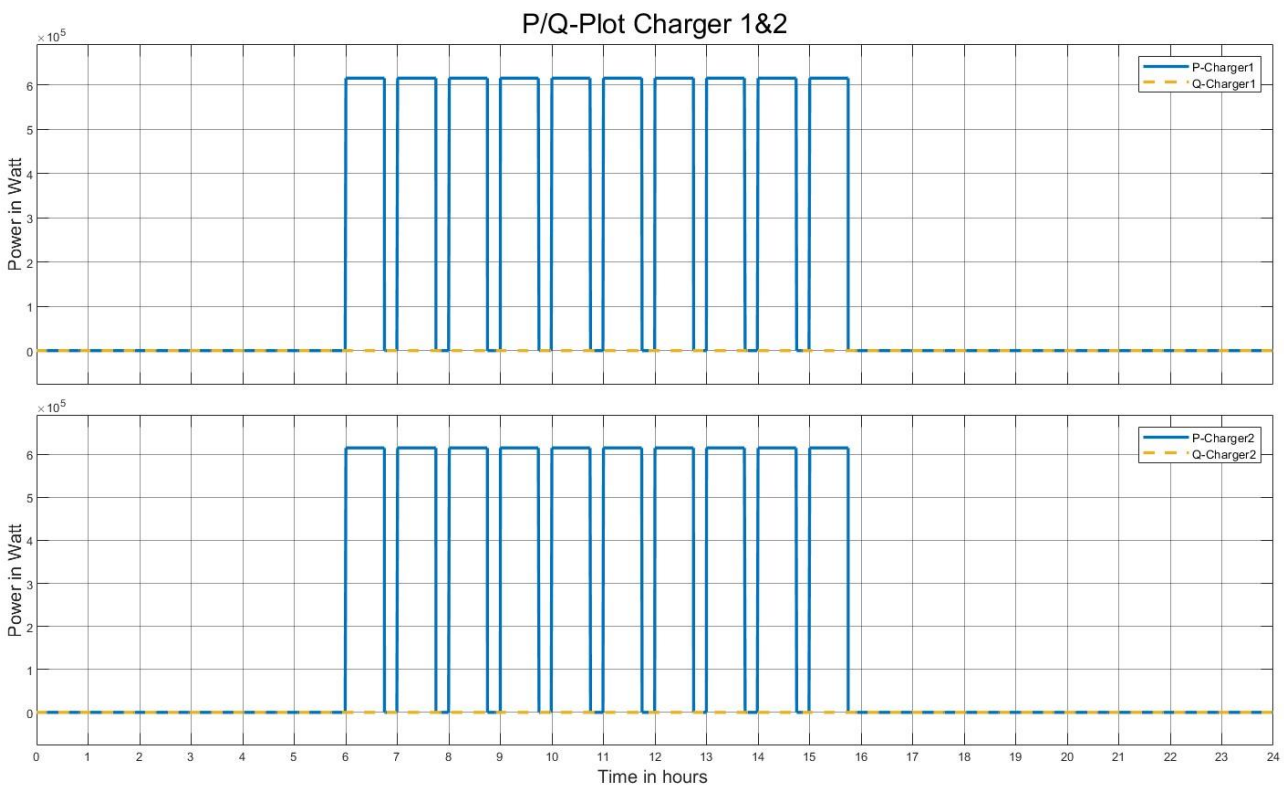
Figure 73. Power of ideal fast-charging stations

The charging stations are used during these 24 hours from 6 am to 4 pm. Switching signals appear simultaneously for chargers 1 and 2, representing the charging an aircraft´s left and right wings. Figure 73 can be derived like the others in the measurement section of the Simulink model.

Calculations were performed with the input signals from Figure 73 and Figure 75 to show the trend of the summed active powers.A discrete-time integrator was necessary for the two sine wave inputs. as a delay element. For the load values of the airport, a conversion from MWs to Wh was made for the charger from Ws to Wh.

The sum signals of the airport and the charger were added to obtain a sum of the active power consumption over one day for the entire system.

In addition, the gains of 365.25 were added to each signal to give an estimated power consumption value over a whole year with the same profile on each day.

The results can be seen in Figure 76, and it can be seen from the watt-hours per year that the simulation reaches 6 GWh/year just from the residential load. It can be seen that two fast-charging stations require 3.37 GWh/year for a daily charging period from 6 am to 4 pm.

In addition, Figure 77 shows the sum of the active power consumption over one day for the entire system. It is easy to see that 25.6 MWh/day and 9.373 GWh/year (Figure 76) would be consumed by Rotterdam Airport with two charging stations of 615 kW each. A GENESIS aircraft could currently be charged and operated in a medium-term design with these two charging stations.
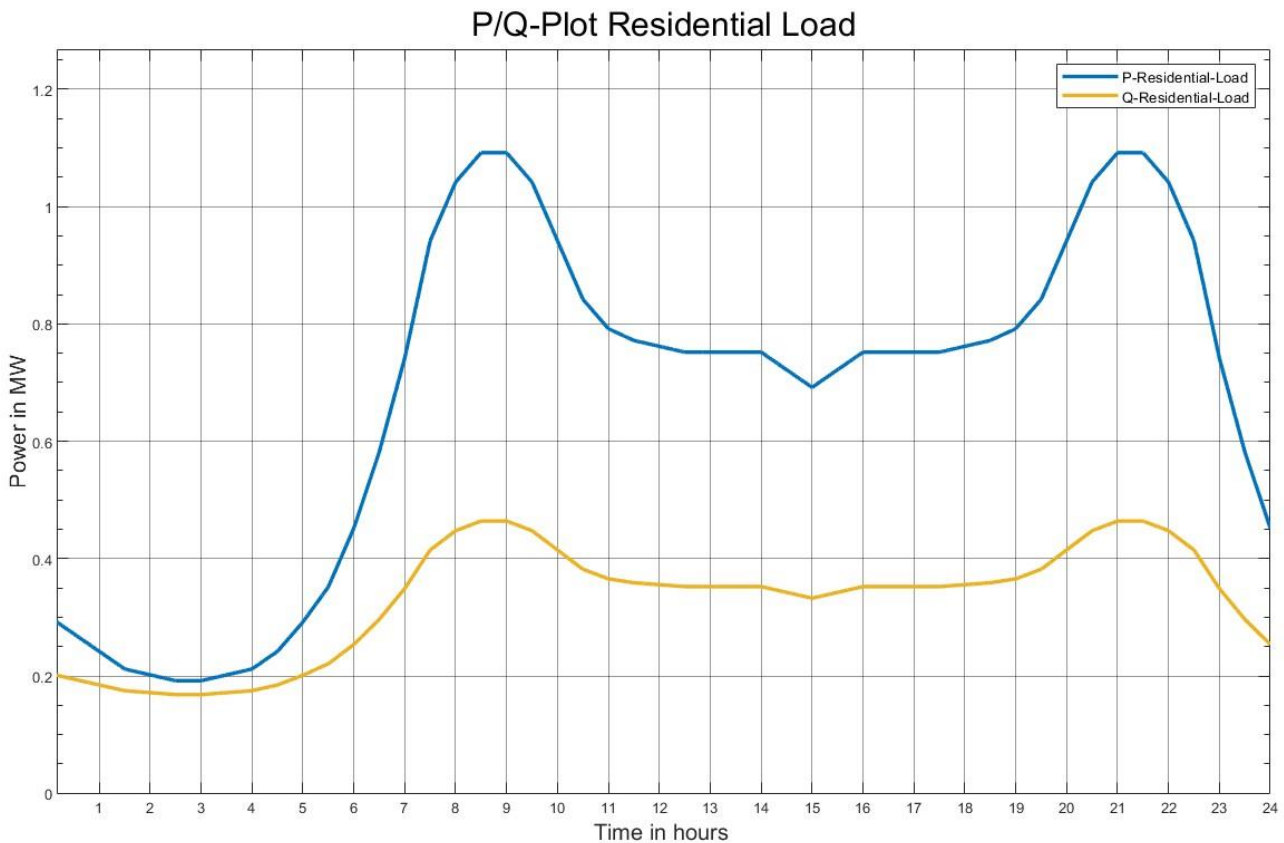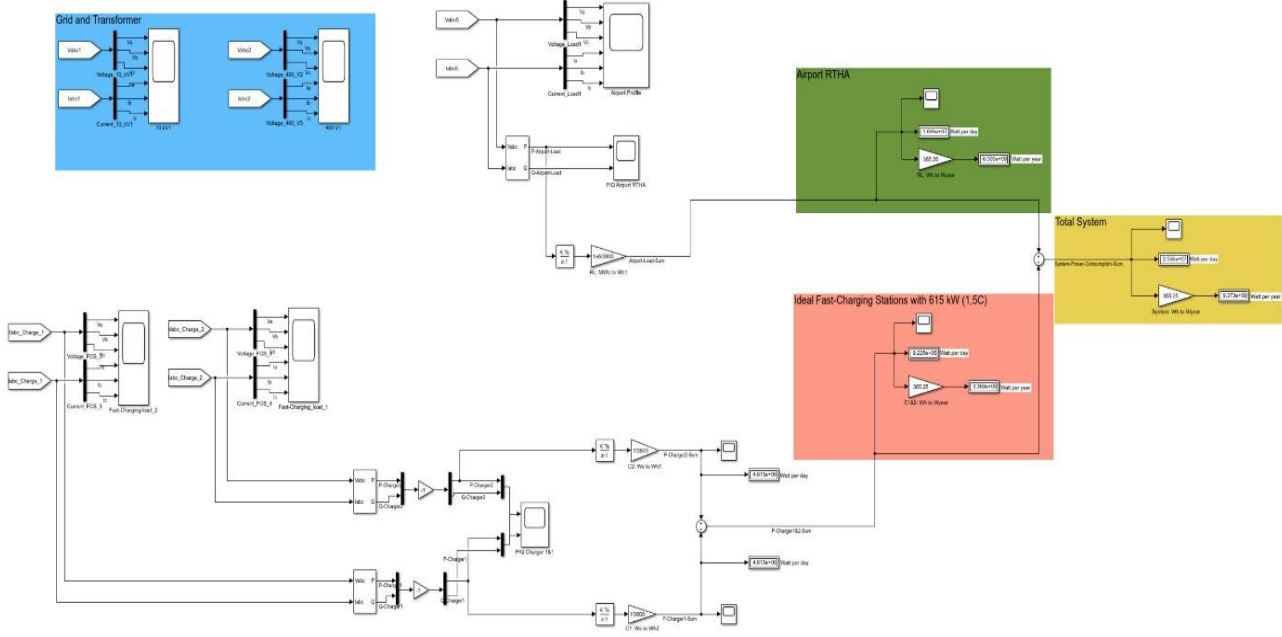

Figure 74. Variable load at Rotterdam airport

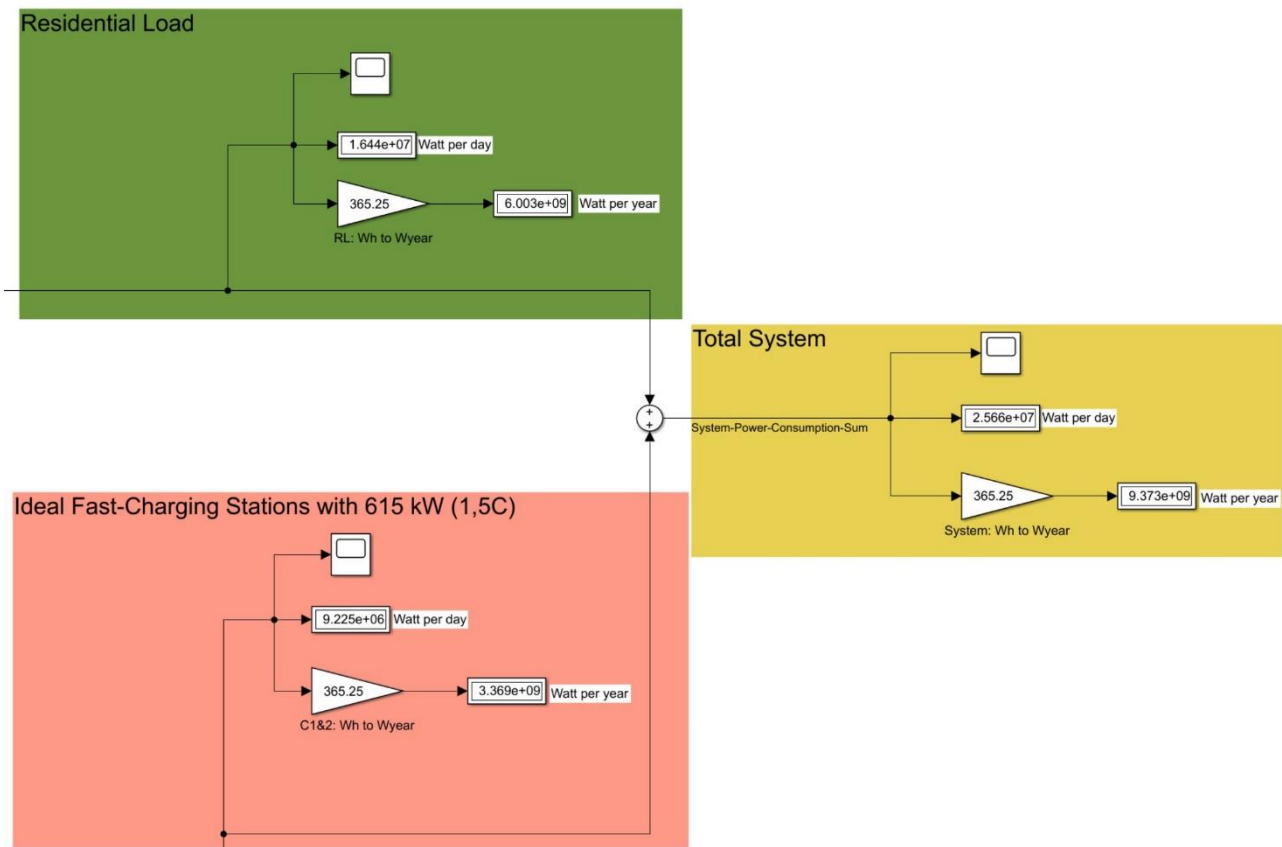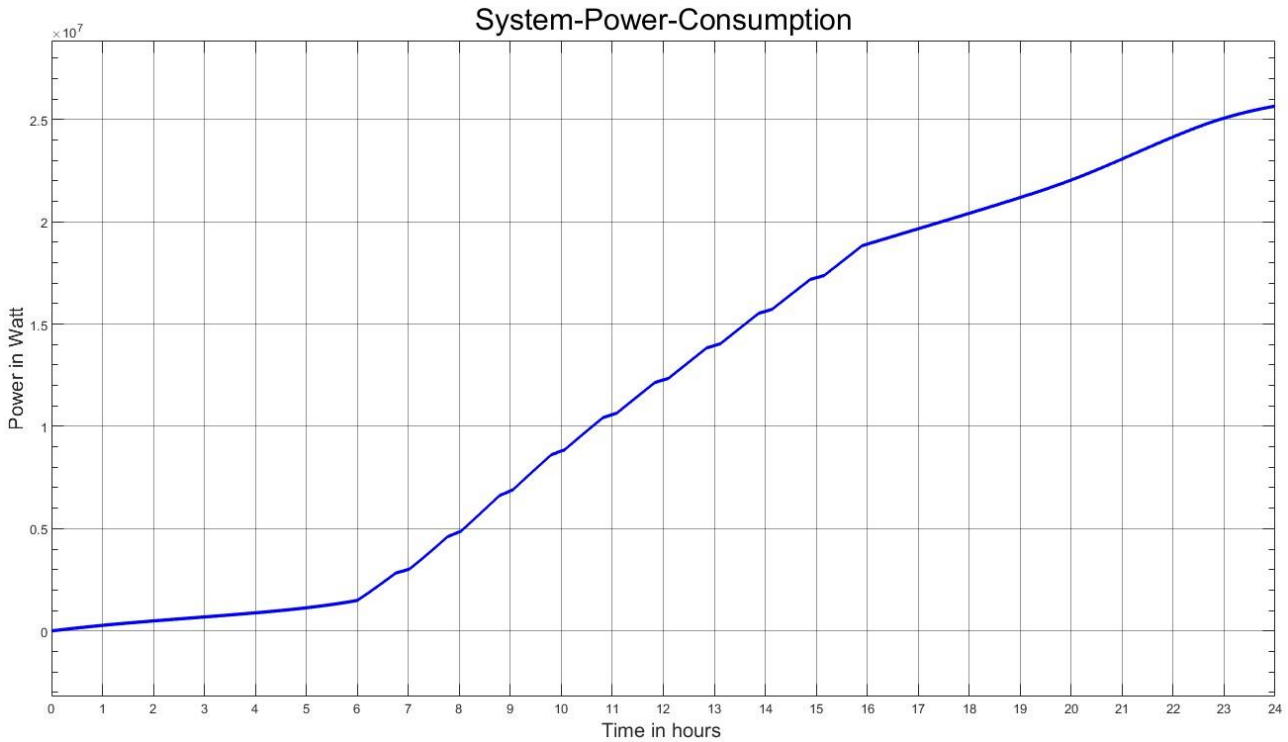**Figure 75. Overview signals and load flow**

Figure 76. Simulation results at Rotterdam airport including the contribution of fast-charging stations

Figure 77. Sum of the active power consumption over 24 hours

For the further development of the infrastructure, the model is extended by including two additional fast-charging stations. This would allow two GENESIS aircraft to be charged simultaneously.

The results and modelling can be seen in Figure 78. From the watt-hours per year, it can be seen that the simulation provides the same 6 GWh/year of load for the airport. It can be seen that the two additional fast-charging stations, at 3.37 GWh/year for a daily charging time from 6 am to 4 pm, require an increase in the consumption to 6.73 GWh/year, exactly doubling it as expected.
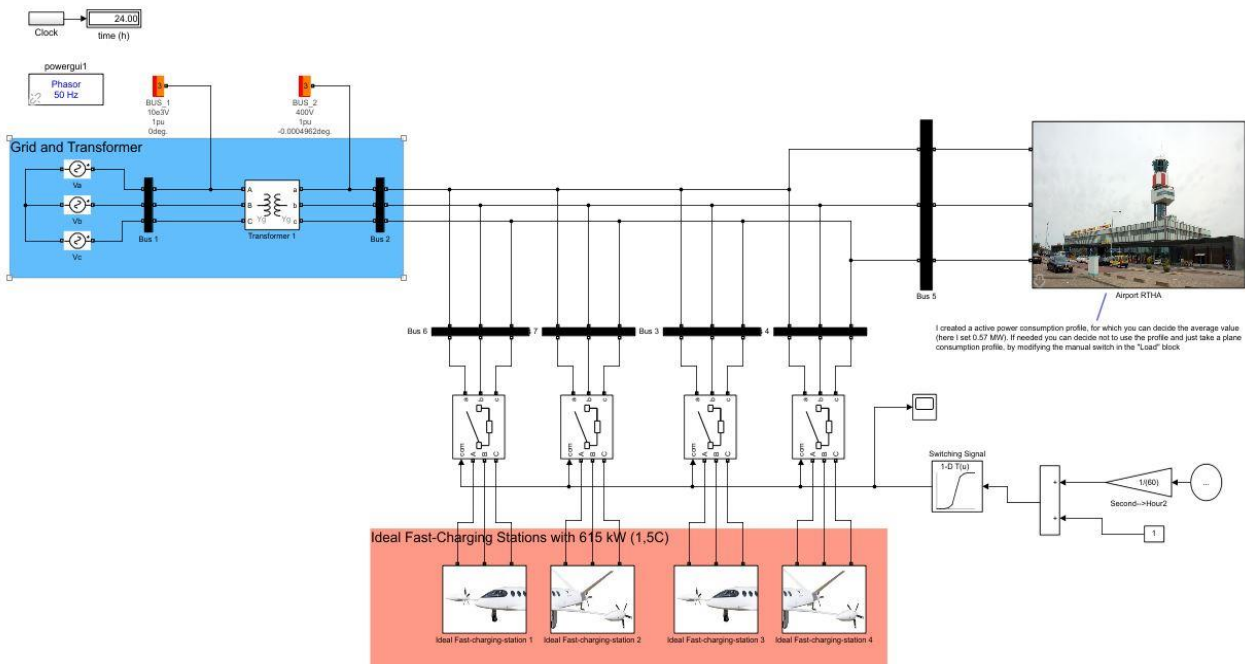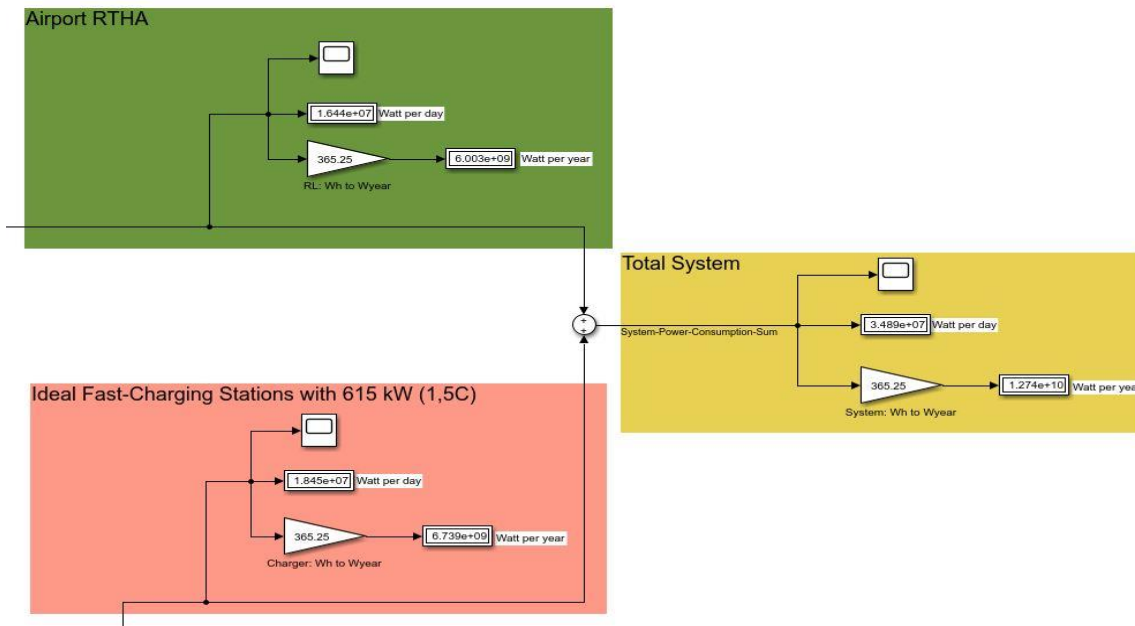
Figure 78. Simulation results of fast-charging stations for two GENESIS aircrafts

This is accompanied by an increase in load for the entire system. Two GENESIS aircraft could currently be charged and operated in the medium-term design with these two additional charging stations. It should also be noted here that a charging time of 45 minutes is very optimistic. There are two main issues for this topic:

- Connect and disconnect the cables to the aircraft
- Parking and unparking of the aircraft between landing and the next take-off.

However, it still makes sense for a real observation, as the aircraft battery and the tanks are never empty and are normally always 30 percent full. Therefore, it is legitimate to carry out these simulations in the time frame of 45 minutes.

In the further course of the project, the simulation model is to be expanded to include an electrolyzer and possibly a battery storage system. In addition, a PV system should be implemented in the simulation model. The background to this is that it can be assumed that the agreement with the transmission grid operators could be overturned in the long-term scenario. This agreement implies that all plants with higher outputs must feed into the transmission grid for 20 years. The PV electricity could thus be used directly or stored in hydrogen form via an electrolyser. This hydrogen can then be converted back into electrical energy or even used to fuel the aircraft.

PEM and alkaline electrolyzers, the hydrogen infrastructure and hydrogen tanks are currently in discussions for the on-ground-energy-supply system.

The battery storage for the on-ground-energy supply system could be implemented, for example, from old EV batteries or aircraft batteries with a second life as a sustainable solution. These proposals should be further researched and discussed in Deliverable D.2.8.

8. Conclusions and outlook

The previous chapters presented the medium-term (2035-2045) technology foresight analysis for the powertrain components, energy storage, and on-ground energy supply. Each chapter of the deliverable was dedicated to one specific task and key element in the aircraft system (batteries, fuel cells, gas turbines, power electronics, electric drives, and on-ground infrastructures).

Li-S- and SSB-Batteries are possible options for the medium-term horizon. The specific energy density for SBB is expected to rise from 400 Wh/kg in 2035 to 650 Wh/kg in 2045. This allows a significant weight reduction over the years. However, that is to low for a fully electric aircraft in the regional class. Therefore, two hybrid electric solutions with a gas turbine or a fuel cell are needed for the medium-term horizon.

Solid oxide fuel cells and polymer electrolyte membrane fuel cells are the two most promising candidates for the fuel cell technology. . However, with a power density of 1 kW/kg, they lay below the minimum value of 2 kW/kg at which fuel cells can be utilized for an aircraft application. Some opportunities for technological development are given in Chapter 3.

A surrogate model for a gas turbine engine for the medium-term horizon with performance, emissions, weight, main dimensions, and cost evaluation was provided. Validation of the model has been provided. Additionally, the consequences of using different biofuel blending ratios have been investigated.

For the power electronics converters, the motor traction drive inverter, generator traction drive inverter, bidirectional battery DC/DC converter, fuel cell DC/DC converter, DC/AC grid converter, and isolated DC/DC converter for low voltage supply have been investigated in detail. For each converter type, the efficiency and power density values were determined. The choice of the HV DC bus voltage and power semiconductors was discussed. The voltage was set to 800 V and it was illustrated that silicon carbide wide-bandgap power semiconductors should be used for all power electronics converters. For the medium time horizon, it can be achieved to replace SiC with GaN devices and make them partially marketable. An early estimation for the converters is given in the power electronics chapter.

For electric drives, optimization possibilities for the PMSM of the medium-term horizon are mentioned with the result that a Halbach magnet arrangement and direct cooled stator windings are the best options for the medium-term horizon. Furthermore, a possible design of the primary and secondary electric machines is presented.

Finally, the on-ground energy supply possibilities focus on the electric on-ground energy supply at RTHA airport, battery storage possibilities and ultra-fast DC charging stations. To develope a good charging infrastructure for the on-ground-energy supply and evaluating it beforehand in simulations was started. PEM and alkaline electrolyzers, the hydrogen infrastructure, and hydrogen tanks are currently in discussions for the on-ground-energy-supply system and should provide in the following deliverable D2.8. The DC ultra-fast chargers need to provide a maximum output power of 820 kW, and they will be built with silicon carbide-based building blocks of 100 kW power. If possible, it is recommended to use a DC-based distribution network in a (zonally structured) ring topology to save converters and thus losses. Two different scenarios were considered in the medium-term, and data was collected for each scenario. The first scenario deals with the gas turbine and battery as a hybrid drive system. In the second scenario, the gas turbine is replaced by the fuel cell and forms the hybrid propulsion system for the aircraft together with the battery. Table 63 summarizes the recommended main technologies for all key technology components for the medium-term horizon. The requirements for the powertrain components of the suggested scenarios are summarized in Table 64

Table 63. Summary of the main recommended technologies for the medium-term horizon

Key technology components	Recommended technologies for the medium-term perspective	Main technical parameters and values	Technology readiness level (TRL)
Batteries (Task 2.1)	Li-S, SSBs and Semi-integrated structural Batteries are possible opinions	Li-S: Expected specific energy densitiy: 750 Wh/kg SBB Expected specific energy densitiy: 650 Wh/kg LiFePO$_4$ based chemistry with carbon fiber electrode and glass fiber seperator. Expected specific energy densitiy: 106 Wh/kg	Li-S: Current TRL: 5; Expected TRL: 8 – 9; SSBs: Current: TRL: 4; Expected TRL: 8 – 9; Structual batteries: Current TRL: 1 – 2; Expected TRL: 3 – 4;
Fuel cells (Task 2.2)	Low temperature Polymer Electrolyte Membrane (LT-PEM) Fuel Cell	Actual power density: 1 kW/kg Needed power density: > 2 kW/kg	SOFC: Current TRL: 5 - 6; Expected TRL: 8 – 9; SO-Electrolyzer: Current TRL: 4 - 6; Expected TRL: 8 – 9; PEMFC: Current TRL: 7 – 8; Expected TRL: 8 – 9;
Gas turbines (Task 2.3)	Conventional gas turbine (shaft power of 1800 kW) sized according to the application with the usage of up to 100 % biofuel	Fuel consumption: 0.223 kg/(kWh)-max. take-off-rating Dry mass: 260 kg Maximum diameter: 530 mm	Current TRL: 7 - 8; Expected TRL: 8 – 9;
Power electronics converters (Task 2.4)	Silicon carbide (SiC) power semiconductors, multi-phase/interleaved topologies, estimation of Gallium nitride (GaN)-MOSFETs	HV DC bus voltage: 800 V Inverter efficiency: ≈ 99 % SiC: Inverter power density: 63 kW/kg GaN: Inverter power density: 94.2 kW/kg	SiC: Current TRL: 7 - 8; Expected TRL: 8 – 9; GaN: Current TRL: 6 - 7; Expected TRL: 8 – 9;
Electric drives (Task 2.5)	Multiphase permanent magnet synchronous machine (PMSM) with Halbach array and direct cooled stator windings	Efficiency: ≈ 92 % Total power density: 13.5-15.2 kW/kg Mass for 600 kW motor: 40 - 45 kg	Current TRL: 6 - 7; Expected TRL: 9;
On-ground infrastructure (Task 2.6)	AC-based distribution grid in a (zonal structured) ring topology, silicon carbide-based DC fast charges	DC charging power: 2x 820 kW Hydrogen infrastructure and tanks under discussion – no TRL could be provided in this deliverable.	Fast-charging-station: Current TRL: 9; Expected TRL: 9;

Table 64. Power demand of powertrain components for different time frames [1]

Powertrain Component	Number of units	Reference Power in kW	
		Short-Term GT/Hybrid	Medium-Term GT/Hybrid
Gas turbine	2	1800	1400
Battery pack	2	550	950
Primary electric machine	2	1200	1500
Secondary electric machine	8	600	750
Powertrain Component	Number of units	Reference Power in kW	
		Medium-Term FC/Hybrid	Long-Term FC/Hybrid
Fuel cell system	2	1400	1400
Battery pack	2	1000	1000
E-drive-power machine	10	500	500

[1] M. Ruocco, M. Di Stasio, V. Marciello, S. Corcione, F. Orefice and F. Nicolosi, "GENESIS Deliverable D1.1 - Overall Requirements for (hybrid) electric 50 pax regional class A/C," CLEAN SKY 2 JTI-CS2-2020-CFP11-THT-13, Naples, 2021.

[2] Y. Gibbs, "X-57 Maxwell - Electric Propulsion Airplane," 7 August 2017. [Online]. Available: https://www.nasa.gov/centers/armstrong/multimedia/imagegallery/electric_propulsion_aircraft/X-57_maxwell_water.html. [Accessed 15 November 2021].

[3] D. Z. f. L.-. u. R. e. (. Raumfahrt, "Auf dem Weg zu einer emmisonsfreien Luftfahrt," DLR, 2021.

[4] J. Dahl, "Jet engine.svg CC BY-SA 4.0," <https://creativecommons.org/licenses/by-sa/4.0>, via Wikimedia Commons, 2007.

[5] D. B. S. Y. A. H. J. L. M. F. &. Z. C. Zachary P. Cano, "Batteries and fuel cells for emerging electric vehicle markets," Nature Energy 3, pages279–289 , https://www.nature.com/articles/s41560-018-0108-1, 2018.

[6] H. R. L. C. C. A. M. B. A. G. Benveniste, "Comparison of the state of Lithium-Sulphur and Lithium-ion batteries applied to electromobility," https://upcommons.upc.edu/bitstream/handle/2117/121911/comparison_state.pdf;jsessionid=EAFD7FC8182729558B0920CE7806C36D?sequence=1.

[7] K. T. R. S. D. D. L. J. H. S. D. H. A. S. K. C. P. S. A. Alberto Varzi, "Current status and future perspectives of lithium metal batteries," Science Direct, https://doi.org/10.1016/j.jpowsour.2020.228803, 2020.

[8] Y. L. Y. C. Dingchang Lin, "Reviving the lithium metal anode for high-energy batteries," Nature Nanotechnology, https://www.nature.com/articles/nnano.2017.16, 2017.

[9] Z. P. C. A. Y. J. L. Z. C. Yuanli Ding, "Automotive Li-Ion Batteries: Current Status and Future Perspectives," Springer Link, https://link.springer.com/article/10.1007/s41918-018-0022-z, 2019.

[10] P. L. J. Y. ,.-D. Z. L. K. ChenYang, "Approaching energy-dense and cost-effective lithium–sulfur batteries: From materials chemistry and price considerations," Science Direct, https://www.sciencedirect.com/science/article/abs/pii/S0360544220308252?via%3Dihub, 2020.

[11] OxisEnergy, "Building pilot cell manufacturing facilities: The commercialisation scale up plan is to build cells in pilot facilities and prove them in a number of applications.," Oxis Energy, [Online]. Available: https://oxisenergy.com/products/. [Accessed 28 04 2022].

[12] F. Instights, "High-energy battery technologies," The Faraday Institution, https://faraday.ac.uk/wp-content/uploads/2020/01/High-Energy-battery-technologies-FINAL.pdf, 2022.

[13] P. H. A. v. J. A. Y. Yu Miao, "Current Li-Ion Battery Technologies in Electric Vehicles and Opportunities for Advancements," https://www.mdpi.com/1996-1073/12/6/1074, 2019.

[14] Y. L. N. S. G. J. B. G. Y. C. L. G. Z. P. X. Q. F. Y. L. Q. Jianmin Ma, "The 2021 battery technology roadmap," Journal of Physics D: Applied Physics, https://iopscience.iop.org/article/10.1088/1361-6463/abd353, 2021.

[15] F. Insights, "Solid-State Batteries: The Technology of the 2030s," The Faraday Institution, https://faraday.ac.uk/wp-content/uploads/2020/04/Faraday-Insights-5_Updated.pdf, 2020.

[16] OxisEnergy, "Building pilot cell manufacturing facilities: The commercialisation scale up plan is to build cells in pilot facilities and prove them in a number of applications.," [Online]. Available: https://oxisenergy.com/products/ . [Accessed 28 04 2022].

[17] D.-I. S. R. P. S. W. D. J. A. A. F. V. Knap, "Reference Performance Test Methodology for Degradation," in *Journal of The Electrochemical Society*, https://45uevg34gwlltnbsf2plyua1-wpengine.netdna-ssl.com/wp-content/uploads/2020/07/website-Knap_2018_J._Electrochem._Soc._165_A1601.pdf, 2018.

[18] S. M. H. L. F. S. J. L. Rui Xiong, "Toward a Safer Battery Management System: A Critical Review on Diagnosis and Prognosis of Battery Short Circui," iScience, https://www.researchgate.net/publication/340168273_Toward_a_Safer_Battery_Management_System_A_Critical_Review_on_Diagnosis_and_Prognosis_of_Battery_Short_Circuit, 2020.

[19] A. M. O. R. A. Hossam A. Gabbar, "Review of Battery Management Systems (BMS) Development and Industrial Standards," https://doi.org/10.3390/technologies9020028, 2021.

[20] A. Brunner, "NTBatteryManagementSystem," [Online]. Available: https://www.newtec.de/loesungen/plattformen/ntbatterymanagementsystem/. [Accessed 28 04 2022].

[21] H. S, "Overview of cell balancing methods for Li-ion battery technology," https://doi.org/10.1002/est2.203, 2020.

[22] F. D. J. L. Lukas Mauler, "Economies of scale in battery cell manufacturing: The impact of material and process innovations," Applied Energy, https://www.sciencedirect.com/science/article/pii/S030626192100060X, 2021.

[23] S. W. C. O. M. K. J. R. H. H. a. A. K. H. Löbberding, "From Cell to Battery System in BEVs: Analysis of System Packing Efficiency and Cell Types," 2020.

[24] F. D. W. G. Z. J. L. Lukas Mauler, "Battery cost forecasting: a review of methods and results with an outlook to 2050," Energy & Environmental Science, https://pubs.rsc.org/en/content/articlelanding/2021/EE/D1EE01530C, 2021.

[25] T. F. institution, "Lithium-sulfur batteries: lightweight technology for multiple sectors," FARADAY INSIGHTS, no. 8, 2020 July, 8.

[26] L. E. Asp, K. Bouton, D. Carlstedt, S. Duan, R. Harnden, W. Johannisson, M. Johansen, M. K. G. Johansson, G. Lindbergh, F. Liu and others, "A structural battery and its multifunctional performance," *Advanced Energy and Sustainability Research,* vol. 2, p. 2000093, 2021.

[27] S. R. H. B. K. D. L. M. D. A. R. G. R. S. A. O. A. P. S. a. A. J. T. A. W. Schäfer, "Technological, economic and environmental prospects of all-electric aircraft," in *Nature Energy, vol. 4, p. 160–166*, 2019, 2019.

[28] J. Xu, Z. Geng, M. Johansen, D. Carlstedt, S. Duan, T. Thiringer, F. Liu and L. E. Asp, "A multicell structural battery composite laminate," *EcoMat,* p. e12180, 2022.

[29] J. Xu, G. Lindbergh and J. Varna, "Carbon fiber composites with battery function: Stresses and dimensional changes due to Li-ion diffusion," *Journal of composite materials,* vol. 52, p. 2729–2742, 2018.

[30] J. Xu, W. Johannisson, M. Johansen, F. Liu, D. Zenkert, G. Lindbergh and L. E. Asp, "Characterization of the adhesive properties between structural battery electrolytes and carbon fibers," *Composites Science and Technology,* vol. 188, p. 107962, 2020.

[31] S. Yin, Z. Hong, Z. Hu, B. Liu, X. Gao, Y. Li and J. Xu, "Fabrication and multiphysics modeling of modified carbon fiber as structural anodes for lithium-ion batteries," *Journal of Power Sources,* vol. 476, p. 228532, 2020.

[32] S. K. Martha, J. O. Kiggans, J. Nanda and N. J. Dudney, "Advanced lithium battery cathodes using dispersed carbon fibers as the current collector," *Journal of The Electrochemical Society,* vol. 158, p. A1060, 2011.

[33] D. Carlstedt, F. Rittweger, K. Runesson, A. M. Navarro-Suárez, J. Xu, S. Duan, F. Larsson, K.-R. Riemschneider and L. E. Asp, "Experimental and computational characterization of carbon fibre based structural battery electrode laminae," *Composites Science and Technology,* p. 109283, 2022.

[34] W. Johannisson, D. Carlstedt, A. Nasiri, C. Buggisch, P. Linde, D. Zenkert, L. E. Asp, G. Lindbergh and B. Fiedler, "A screen-printing method for manufacturing of current collectors for structural batteries," *Multifunctional Materials,* vol. 4, p. 035002, 2021.

[35] J. S. Sanchez, J. Xu, Z. Xia, J. Sun, L. E. Asp and V. Palermo, "Electrophoretic coating of LiFePO4/Graphene oxide on carbon fibers as cathode electrodes for structural lithium ion batteries," *Composites Science and Technology,* vol. 208, p. 108768, 2021.

[36] L. M. Schneider, N. Ihrner, D. Zenkert and M. Johansson, "Bicontinuous electrolytes via thermally initiated polymerization for structural lithium ion batteries," *ACS Applied Energy Materials,* vol. 2, p. 4362–4369, 2019.

[37] I. M. Daniel, O. Ishai, I. M. Daniel and I. Daniel, Engineering mechanics of composite materials, vol. 1994, Oxford university press New York, 2006.

[38] A. Baker, D. S and K. D, Composite Materials for Aircraft Structures, Virginia: AIAA, 2004.

[39] "Gillfab® 4009 and 4017T Product Data Sheet," Gillfab, [Online]. Available: www.thegillcorp.com. [Accessed 24 04 2022].

[40] E. F. Gmbh, "Composite Solutions," [Online]. Available: https://www.elbeflugzeugwerke.com/en/composite-solutions/. [Accessed 20 05 2022].

[41] embraercommercialaviation, "embraercommercialaviation," [Online]. Available: https://www.embraercommercialaviation.com/wp-content/uploads/2017/02/APM_ERJ145.pdf.. [Accessed 24 04 2022].

[42] S. N. Nguyen, A. Millereux, A. Pouyat, E. S. Greenhalgh, M. S. P. Shaffer, A. R. J. Kucernak and P. Linde, "Conceptual multifunctional design, feasibility and requirements for structural power in aircraft cabins," *Journal of Aircraft,* vol. 58, p. 677–687, 2021.

[43] K. B. D. C. S. D. R. H. W. J. M. J. M. K. G. J. G. L. F. L. a. o. L. E. Asp, "A structural battery and its multifunctional performance," in *Advanced Energy and Sustainability Research, vol. 2, p.2000093*, 2021.

[44] M. G. J. Y. R. J. Braun, "System Architectures for Solid Oxide Fuel Cell-Based Auxiliary Power Units in Future Commercial Aircraft Applications," The American Society of mechanical Engineers, https://asmedigitalcollection.asme.org/electrochemical/article/6/3/031015/470248/System-Architectures-for-Solid-Oxide-Fuel-Cell, 2009.

[45] L. C. GA Whyatt, "Electrical Generation for More-Electric Aircraft Using Solid Oxide Fuel Cells," U.S. Department of Energy, https://www.pnnl.gov/main/publications/external/technical_reports/PNNL-21382.pdf, 2012.

[46] D. Jeffrey M.Collins, "All-electric commercial aviation with solid oxide fuel cell-gas turbine-battery hybrids," Science Direct, https://www.sciencedirect.com/science/article/abs/pii/S0306261920302993?via%3Dihub, 2020.

[47] "Fuel Cell Technology Elcogen," Elcogen, [Online]. Available: https://elcogen.com/. [Accessed 28 04 2022].

[48] R. M. K. K. K. Y. H. T. K. Y. N. K. T. M. T. T. T. H. K. S. T. N. H. I. T. K. K. O. Shin-ichi Hashimoto, "A New Development Strategy of Light Wight Solid Oxide Fuel Cells for Electrified Airplane System," Aerospace Research Central, https://doi.org/10.2514/6.2019-4470, 2019.

[49] Å. H. P. T. T. M. K. B. Jimmi Nielsen, "Towards High Power Density Metal Supported Solid Oxide Fuel Cell for Mobile Applications," Journal of The Electrochemical Society, https://iopscience.iop.org/article/10.1149/2.0741802jes, 2018.

[50] J. R. R. N. C. B. F. T. W. S. N. H. M. L. G. d. H. A. N. A. K. O. G. M. David Udomsilp, "Metal-Supported Solid Oxide Fuel Cells with Exceptionally High Power Density for Range Extender Systems," ScienceDirect, https://www.sciencedirect.com/science/article/pii/S2666386420300679?via%3Dihub, 2020.

[51] I. M. A. S. L. C. S. K. S. W. a. J. F. W. M. M. Whiston, "Meeting U.S. Solid Oxide Fuel Cell Targets," Joule , p. 6, 2019.

[52] "Wasserstoff und," [Online]. Available: http://www.fvee.de/fileadmin/publikationen/Themenhefte/th2004/th2004.pdf. [Accessed 03 05 2022].

[53] "Impact oFuel Cell Technology on the Machinery and Component Supplier Industry, FEV Final Consulting report," FEV Final Consulting report,VDMA report, 2020.

[54] T. W. R. Sebastian Porstmann, "Overcoming the Challenges for a Mass Manufacturing Machine for the Assembly of PEMFC Stacks," https://www.mdpi.com/2075-1702/7/4/66, 2019.

[55] "Hydrogen Council," [Online]. Available: https://hydrogencouncil.com/wp-content/uploads/2020/01/Path-to-Hydrogen-Competitiveness_Full-Study-1.pdf. [Accessed 03 05 2022].

[56] T. W.-G. S.Porstmann, "A comprehensive comparison of state-of-the-art manufacturing methods for fuel cell bipolar plates including anticipated future industry trends," Science Direct, https://www.sciencedirect.com/science/article/pii/S152661252030709X?via%3Dihub, 2020.

[57] D. Y. J. R. S. J. Y. Y.-E. Namgee Junga, "Pt-based nanoarchitecture and catalyst design for fuel cell applications," Science Direct, https://www.sciencedirect.com/science/article/abs/pii/S1748013214000863?via%3Dihub, 2014.

[58] T. K. Z. S. K. B.-I. O. Y. I. S. Y. DUSTIN BANHAM, "Critical advancements in achieving high power and stable nonprecious metal catalyst–based MEAs for real-world proton exchange membrane fuel cell applications," Science Advances, https://www.science.org/doi/10.1126/sciadv.aar7180, 2018.

[59] S. L. C. P. Q. S. G. W. Yanghua He, "Atomically dispersed metal–nitrogen–carbon catalysts for fuel cells: advances in catalyst design, electrode performance, and durability improvement," Royal Society of chemestry, https://pubs.rsc.org/en/content/articlehtml/2020/cs/c9cs00903e, 2020.

[60] R. W. P. N. Krysta Waldrop, "Application of electrospinning for the fabrication of proton-exchange membrane fuel cell electrodes," Science Direct, https://www.sciencedirect.com/science/article/abs/pii/S2451910320300648?via%3Dihub, 2020.

[61] J. N. Y. C. G.H.Byun, "Molecular engineering of hydrocarbon membrane to substitute perfluorinated sulfonic acid membrane for proton exchange membrane fuel cell operation,"

Science Direct, https://www.sciencedirect.com/science/article/abs/pii/S2468606920301027?via%3Dihub, 2020.

[62] D. E., "Materials for cryogenics applications," in *12th International science conference achievements in mechanical & materials engineering*, Gliwice, 2006.

[63] Kloeckner, "WHY IS THE DENSITY OF ALUMINUM IMPORTANT?," 26 Juillet 2021. [Online]. Available: https://www.kloecknermetals.com/blog/why-is-the-density-of-aluminum-important/. [Accessed 26 Avril 2022].

[64] K. S. Prakash C. Thapliyal, "Aerogels as Promising Thermal Insulating Materials: An Overview," *Journal of Materials- Hindawi,* vol. 2014, 2014.

[65] K. I. K. T. K. A. Y. Y. T. Shoji Kamiya, "Technologies of hydrogen liquefaction, transport and storage - paving the way to a hydrogen fueled future," *Kawasaki Technical Review,* no. 176, pp. 51-58, 2016.

[66] D. J. Johnson, "Structure-property relationships in carbon fibres," *Journal of Physics D: Applied Physics,* vol. 20, no. 3, pp. 286-291, 1986.

[67] R. Bacon, "Growth, Structure, and Properties of Graphite Whiskers," *American Institute of Physics- JOURNAL OF APPLIED PHYSICS ,* vol. 31, no. 2, p. 283, 1960.

[68] J. Gorss, *High Performance Carbon Fibers,* Washington DC: American Chemical Society, 2003.

[69] Toray Industries, Inc., "Toray Subsidiaries to Exhibit at Composites Europe," 2 Septembre 2019. [Online]. Available: https://www.toray.com/global/news/details/20190902000531.html. [Accessed 26 04 2022].

[70] Toray Composite Materials America, Inc, "T1100S Data Sheet," [Online]. Available: https://www.toraycma.com/wp-content/uploads/T1100S-Technical-Data-Sheet-1.pdf.pdf. [Accessed 2022 04 26].

[71] C.-R. J. Byung-Sun Kim., "Filament Wound Spherical Composite Pressure Vessel Design by an Energy Method," in *Composite Technologies for 2020-Proceedings of the Fourth Asian–Australasian Conference on Composite Materials*, Woodhead Publishing, 2004, pp. Pages 299-304.

[72] P. F. P. Walsh, "Gas Turbine Performance 2nd," in *Blackwell Science*, 1998.

[73] [Online]. Available: https://www.pwc.ca/en/products-and-services/products/regional-aviation-engines/pw100-150. [Accessed 26 04 2022].

[74] [Online]. Available: https://www.mitma.gob.es/recursos_mfom/comodin/recursos/in-052-2019_final_report_nm2.pdf. [Accessed 26 04 2022].

[75] [Online]. Available: https://commons.wikimedia.org/wiki/File:RAFO_EADS_CASA_C-295_901_PAS_2013_04_PW127G_turboprop_engine.jpg. . [Accessed 26 04 2022].

[76] F. O. C. D. o. H.-E. Aircraft, *Conceptual Design of Hybrid-Electric Aircraft,* PhD Thesis, University of Naples Federico II, 2022.

[77] M. D. Stasio, *Efficient Gas Turbine Modeling for Low Emissions Aircraft Preliminary Design Workflows,* PhD Thesis, University of Naples Federico II., 2022.

[78] [Online]. Available: https://www.gasturb.de/index.php. [Accessed 26 04 2022].

[79] [Online]. Available: https://it.mathworks.com/help/stats/regression-learner-app.html. [Accessed 26 04 2022].

[80] H. Grieb, "Projektierung von Turboflugtriebwerken," Springer, Basel, 2004.

[81] H. H. T. P. J. Mattingly, "Aircraft engine design 2nd edition," in *AIAA*, 2002.

[82] H. H. T. P. J. Mattingly, "Aircraft engine design 2nd edition," in *AIAA*, 2002.

[83] A. G. R. F. Yin, "Performance analysis of an aero engine with inter-stage turbine burner," in *Aeronautical Journal*, 2017.

[84] K. Kyprianidis, "Future Aero Engine Designs: An Evolving Vision," in *IntechOpen.*, 2011.

[85] J. Gauntner, "Algorithm for calculating turbine cooling flow and the resulting decrease in turbine efficiency," in *NASA Technical Memorandum.*, 1980.

[86] H. Grieb, "Projektierung von Turboflugtriebwerken," Springer, Basel, 2004.

[87] T. Bose Airbreathing Propulsion: An Introduction, "Airbreathing Propulsion: An Introduction," Springer Aerospace Technology, 2012.

[88] M. T. E.S. Hendricks, "Performance and Weight Estimates for an Advanced Open Rotor Engine," in *48th Joint Propulsion Conference and Exhibit*, 2012.

[89] V. M. F. N. Q. Z. G. W. J. M. V. C. F. Orefice, "Design of Hybrid-Electric Small Air Transports," in *IOP Conference Series: Materials Science and Engineering*, 2022.

[90] G. C. L.M. Nicolai, "Fundamentals of Aircraft and Airship Design," in *AIAA Education Series.*, 2010.

[91] D. Raymer, "Aircraft Design: A Conceptual Approach – Sixth Edition," in *AIAA Education Series*, 2018.

[92] A. Kundu, "Aircraft Design," in *Cambridge University Press*, 2010.

[93] Z. Z. A. Maciejczyk, "Design basic of industrial gear boxes," in *Technical University of Lodz.*.

[94] M. A. R. M. M. L. J. M. J. G. O. Younossi, "Military Jet Engine Acquisition: Technology Basics and Cost-Estimating Methodology," in *RAND*, 2002.

[95] J. Roskam, *Airplane Design – Part VIII: Airplane cost estimation,* Roskam Aviation and Engineering Corp., 1990.

[96] J. Gauntner, "Algorithm for calculating turbine cooling flow and the resulting decrease in turbine efficiency," in *NASA Technical Memorandum.*, 1980.

[97] Vv.Aa., "he Market for Aviation Turboprop Engines: 2010-2019," in *Forecast International.*, 2010.

[98] T. W. (. N. (. A. G. (. Z. W. M. D. (. M. R. C. B. (.-L. Bruno Lemoine (BFH), "Short-term technology analysis covering all main," https://www.genesis-cleansky.eu/deliverables/, 2021.

[99] S. Dixon-Warren, "TechInsights," 31 October 2019. [Online]. Available: https://www.techinsights.com/blog/evolution-sic-mosfet-technology-retrospective.

[100] S. Davis, "Power Electronics," 1 März 2010. [Online]. Available: https://www.powerelectronics.com/technologies/discrete-power-semis/article/21857697/enhancement-mode-gallium-nitride-mosfet-delivers-impressive-performance. [Accessed 15 October 2021].

[101] L. Han, L. Liang, Y. Kang and Y. Qiu, "A Review of SiC IGBT: Models, Fabrications, Characteristics, and Applications," *IEEE Transactions on Power Electronics, vol. 36, no. 2,* pp. 2080-2093, 30 June 2020.

[102] K. Patel, "GaN is Great, True GaN TM is Beter!," Avogy Inc., https://nexgenpowersystems.com/wp-content/uploads/2016/06/GaN-is-Great-v4.pdf, 2016.

[103] Y. B. E. B. M. B. ,. T. B. P. R. C. ,. M. C. ,. K. J. C. ,. N. C. R. C. ,. C. D. S. ,. M. M. D. S. S. D. ,. L. D. C. ,. B. E. T. E. P. F. ,. H Amano, "The 2018 GaN power electronics roadmap," IOP Publishing, https://doi.org/10.1088/1361-6463/aaaf9d, 2018.

[104] A. B. Slimane and P. Chiu , "GaN Power 2021: Epitaxy, Devices, Applications and Technology Trends report," Yole Development, 2021.

[105] E. Dogmus, A. B. Slimane and P. Chiu, "Power SiC Materials, Devices and Applications," Yole Development, 2020.

[106] "600 kW XM3 High Performance Dual Three-Phase Inverter," [Online]. Available: https://www.wolfspeed.com/products/power/reference-designs/crd600da12e-xm3. [Accessed 21 October 2021].

[107] G. Grandi and J. Loncarski, "Evaluation of current ripple amplitude in three-phase PWM voltage source inverters," in *2013 International Conference-Workshop Compatibility And Power Electronics*, Ljubljana, Slovenia, 2013.

[108] R. N. Beres, X. Wang, M. Liserre, F. Blaabjerg and C. L. Bak, "A Review of Passive Power Filters for Three-Phase Grid-Connected Voltage-Source Converters," *IEEE Journal of Emerging and Selected Topics in Power Electronics, vol. 4, no. 1,* pp. 54-69, March 2016.

[109] Y. Ting, "DC-DC Converters with a Wide Load Range and a Wide Input-Voltage Range," TU Delft, Delft, 2015.

[110] C. Gillmor, "Comparison of PSFB and FB-LLC for high power DC/DC conversion," Texas Instruments, 2018.

[111] K. H. Passand Johannes, "Gallery energy trolley operation 2 (GETop2) : Abschlussbericht zum LuFo-V.3 Projekt : zum Diehl Aerospace GmbH geführten Verbundvorhaben: Gallery energy trolley power 2 (GETpower2) : Projektlaufzeit: 01.04.2019-31.10.2021 / Projektleitung: Dr. Johannes Pa," Technische Universität Braunschweig, 25 02 2022. [Online]. Available: https://katalog.ub.tu-braunschweig.de/vufind/Search2Record/1802102086 . [Accessed 20 05 2022].

[112] B. Eckardt, Interviewee, *Dr.-Ing..* [Interview]. 15 04 2020.

[113] E. Meißner, Interviewee, *Dr. rer. nat..* [Interview]. 15 04 2020.

[114] Bouloukza Ibtissam, Mordjaoui Mourad, Medoued Ammar & Guerboussa Fouzi, "Magnetic Field Analysis of Halbach Permanent Magnetic Synchronous Machine," International Conference on Control, Engineering & Information Technology (CEIT'14), 2014.

[115] X. Y. J. M. Y. C. K. H. Andy Yoon, "A High-Speed, High-Frequency, Air-Core PM Machine for Aircraft Application," IEEE, 2016.

[116] Z. X. P. A. S. J. P. C. N. E. C. G. S. B. A. La Rocca, "Thermal management of a high speed permanent magnet machine for an aeroengine," in *2016 XXII International Conference on Electrical Machines (ICEM)*, https://ieeexplore.ieee.org/stamp/stamp.jsp?tp=&arnumber=7732908&isnumber=7732494, 2016.

[117] Z. Y. J. S. R. M. P. M. T. J. B. S. Dheeraj Bobba, "Multi-Physics Based Analysis and Design of Stator Coil in High Power Density PMSM for Aircraft Propulsion Applications," in *AIAA Propulsion and Energy Forum*, IEEE Explore, 2021.

[118] M. Filipenko, S. Biser, M. Boll, M. Corduan, M. Noe, and P. Rostek, "Comparative Analysis and Optimization of Technical and Weight Parameters of Turbo-Electric Propulsion Systems," *Aerospace, vol. 7, no. 8,* p. 107, 27 July 2020.

[119] M. H. (.-d. E. f. GmbH and www.dynamicEflow.com), Interviewees, *Motorauslegung GENESIS Motor.* [Interview]. 25 04 2022.

[120] C. D. Ruiter, Interviewee, *Energy supply of Rotterdam Airport.* [Interview]. 25 04 2022.

[121] G. GARDINER, "Universal Hydrogen uses dry braided carbon preform tanks as part of plan to decarbonize aviation," Aerospace, 24 09 2020. [Online]. Available:

https://www.compositesworld.com/news/universal-hydrogen-uses-cfrp-tanks-as-part-of-plan-to-decarbonize-aviation . [Accessed 25 04 2022].

[122] J.-P. Parant, R. Olazcuaga, M. Devalette, C. Fouassier and P. Hagenmuller, "Sur quelques nouvelles phases de formule Na xMnO 2 (x ⩽ 1)," https://ui.adsabs.harvard.edu/abs/1971JSSCh...3....1P/abstract, 1971.

[123] "Megawatt Charging System (MCS)," [Online]. Available: https://www.charin.global/technology/mcs/. [Accessed 18 November 2021].

[124] D. Z. f. L.-u. R. (DLR), "Klimafreundlicher fliegen mit hybrid-elektrischen Antrieben-DLR Portal," [Online]. Available: https://www.dlr.de/content/de/artikel/news/2021/04/20211122_klimafreundlicher-fliegen-mit-hybrid-elektrischen-antrieben.html. [Accessed 25 04 2022].

[125] A. E.-m. GmbH, "https://webcache.googleusercontent.com/search?q=cache:hvcUXk7CKFAJ:https://library. e.abb.com/public/628804a4a649461cb348a07ce8114c51/ABB%2520EVCI%2520Preisliste _Oktober%2520bis%2520Dezember_2021.pdf%3Fx-sign%3DN3ww0GoZlNaC96/ey72rTnQpuno2xwHJ9d1cdsdFs/EQR," 04 2022. [Online]. Available: https://webcache.googleusercontent.com/search?q=cache:hvcUXk7CKFAJ:https://library.e. abb.com/public/628804a4a649461cb348a07ce8114c51/ABB%2520EVCI%2520Preisliste_ Oktober%2520bis%2520Dezember_2021.pdf%3Fx-sign%3DN3ww0GoZlNaC96/ey72rTnQpuno2xwHJ9d1cdsdFs/EQR. [Accessed 2025 04 2022].

[126] ABB, "High Power Schnellladestation," ABB, 2022. [Online]. Available: https://new.abb.com/ev-charging/de/produkte/ladestationen-pkws/high-power-schnellladestation . [Accessed 25 04 2022].

[127] K. Kyprianidis, "Future Aero Engine Designs: An Evolving Vision,," in *IntechOpen*, 2011.

[128] "embraercommercialaviation," [Online]. Available: https://www.embraercommercialaviation.com/wp-content/uploads/2017/02/APM_ERJ145.pdf. [Accessed 24 04 2022].